Direct and Indirect probes of New Bosonic Physics at the Large Hadron Collider

A Thesis

Submitted to the
Tata Institute of Fundamental Research, Mumbai
for the Degree of Doctor of Philosophy
in Physics

by

Disha Bhatia

Tata Institute of Fundamental Research
Mumbai
September 2018
Final Version Submitted in June, 2019

DECLARATION

This thesis is a presentation of my original research work. Wherever contributions of others are involved, every effort is made to indicate this clearly, with due reference to the literature, and acknowledgement of collaborative research and discussions. The work was done under the guidance of Professor Sreerup Raychaudhuri, at the Tata Institute of Fundamental Research, Mumbai.

Disha Bhatia

[Disha Bhatia]

In my capacity as supervisor of the candidates thesis, I certify that the above statements are true to the best of my knowledge.

[Sreerup Raychaudhuri]

Date: 18th September 2018

Preface

Welcome to my journey into the field of particle physics: a field which is at once rich, dense, puzzling, and yet amazing. Our understanding of particles and their interactions has evolved over several years and has resulted into a phenomenological model viz., the Standard Model, which till date explains the interactions between particles very well. However there are strong motivations — the choice of the gauge group, number of fermionic generations, stability of the Higgs mass, hierarchy between fermion masses, neutrinos masses and mixings, particle nature of dark matter, strong CP problem — for us to believe that physics beyond the Standard Model must exist.

Given the lack of experimental evidence, however, almost all new physics models (with a few notable exceptions) can be made consistent with the present data by tuning the free parameters suitably, making the overall search strategy haphazard and difficult to steer using objective criteria. In such a scenario, simple extensions of the Standard Model and effective field theories are currently favoured as a classic bottom-up approach when elegant UV-complete theories seem to falter. In fact, data can provide direct or indirect hints for the presence of new physics, depending upon its nature. For example, while the lighter particles may be observed directly as resonances in the invariant mass spectrum, such a method would not work for heavier particles due to energy limitations. One would then have to rely upon indirect clues where the presence of such a heavier resonance could lead to deviations in well-measured/predictable observables.

In this thesis work, a similar approach has been adapted, wherein we have considered simple bosonic extensions of the Standard Model to probe and predict direct and indirect signals – or hints – in the data. A multitude of 'clean' final states have been analyzed, ranging from $\gamma\gamma$ to di-muons to $W\gamma$, where leptonic decays of W are considered, for different new physics scenarios. The interesting regions/channels, which could be probed in future runs of LHC have been identified. The reader is invited to share in these explorations, and ultimately, to share in the hope that some of these studies may eventually prove useful when and if new physics is discovered.

List of publications:

1. Neutrino mixing and R_K anomaly in $U(1)_X$ models: a bottom- up approach: Disha Bhatia, Sabyasachi Chakraborty and Amol Dighe. JHEP 1703, 117 (2017).
2. Dissecting Multi-Photon Resonances at the Large Hadron Collider: B. C. Allanach, D. Bhatia and A. M. Iyer. Eur. Phys. J. C 77, no. 9, 595 (2017).
3. Discovery prospects of Light Higgs at LHC in Type-I 2HDM: D. Bhatia, U. Maitra and S. Niyogi, Phys. Rev. D 97, no. 5, 055027 (2018).
4. Pinning down anomalous $WW\gamma$ couplings at the LHC: D. Bhatia, U. Maitra and S. Raychaudhuri, Phys. Rev. D **99**, no. 9, 095017 (2019).

Conference proceedings:

1. Addressing R_K and neutrino mixing in a class of $U(1)_X$ models: Disha Bhatia, Sabyasachi Chakraborty and Amol Dighe. PoS CKM **2016**, 064 (2017).
2. Hints on neutrino mixings from flavour data: Disha Bhatia, Springer Proc. Phys. **203**, 881 (2018).

If you haven't found it yet, keep looking— Steve Jobs

So here I am, a final year PhD student hoping to decipher the laws of nature. So did I succeed in my venture? The answer is perhaps no, but hopefully I became wiser!

Acknowledgements

Like many other schoolchild, my fascination in science arose due to interest in Astronomy. Although, I didn't end up doing Astrophysics, the motivation was strong enough for me to choose physics for higher studies.

In this journey of mine, there are many people who have helped, encouraged and supported me in various ways. I begin by first thanking my supervisor, Prof. Sreerup Raychaudhuri, for his guidance and support. He, through his excellent teaching skills, laid down a good baseline for me to start research in particle physics. I have been fortunate to learn loop calculations and Monte Carlo simulations for cross-section calculations from him, in which he is an expert.

In the same way, I would also like to acknowledge Prof. Amol Dighe. Although he was not my official supervisor, but he has been just like a supervisor for me. Discussing physics was always fun with him and the best part was that he has this amazing trick by which he would never answer the question which we asked, rather used to get the answer out from us. His ability to simplify complicated things, insights and patience with which he deals with students never cease to amaze me.

I have been also extremely fortunate to have a few years of overlap with Dr. Tuhin Roy. Interacting with him has not only helped in increasing my knowledge about other fields but has also helped in making me more confident and independent.

During my Ph.D. period, our HEP group had a large number of post-docs namely, Abhishek Iyer, Sabyasachi Charkraborty, Ushoshi Maitra, and Amit Chakraborty. I have been extremely fortunate to discuss, learn and collaborate with all of them.

I am also grateful to other faculty members viz., Profs. Gobinda Mazumdar, B.C. Allanach, Monoranjan Guchait and Kajari Majumdar for being always ready to discuss statistics and experiment related queries. I also had a great opportunity to work for some time in the Indian Neutrino Observatory laboratory under the supervision of Prof. Naba K. Mandal. I am grateful to him for allowing me to have a hands-on experience with resistive-plate-chambers to detect muon tracks.

I would also like to thank all the members of our HEP group at TIFR for enlightening discussions during our journal club sessions.

I really had a great time studying in TIFR simply because of the kind of platform which we have got with so many experts present in every field. I would like to thank all the departmental members for being extremely helpful and motivating.

I would also like to acknowledge Raju Bathija, Rajan Pawar, Kapil Ghadiali, Aniket Surve, Ajay Salve, Bindu Jose and members of the TIFR Establishment Section for their constant efforts in helping me through any non-academic hurdles.

I would also like to acknowledge my school teachers — Harleen ma'am and Amit sir; my Hansraj and IIT teachers — Santhalin ma'am, Ranganathan sir, Ajit sir, Ghatak sir and Thyagrajan sir, for all the help, support, care and for making physics so interesting through their awesome teaching skills. I am doing physics primarily because of these people.

I had not imagined that I would make so many friends in TIFR. I was really lucky to be surrounded by so many crazy but awesome people. I will begin by acknowledging Ankita and Ananya, for their unconditional love and care, and for being just like family. Shafali, for having the extra-ordinary capability to turn serious discussions into lighter ones, Melby, for all our late night chat sessions about changing the world, Manibrata, for listening to all my cribbing and torturing me with his stories, Ahana, for our weight-loss and walk sessions, Tousik, for all the help in teaching Shankar, Jacky, for all black-board discussions, Umesh, for being always concerned about my health and work, Debjyoti, for being himself, Sarath and Mangesh, for making C-338 lively, Sarbajaya, for all the enlightening discussions, and all the members of C-338 for making the atmosphere friendly. I must also thank Debanjan, for his love for songs, Ajay and Palas, for all the movie sessions, Jasmine and Dipankar, for their frequent invitations for *rajma* parties, Deepanwita, for becoming vegetarian just for me and Sandhya, for being just like the elder sister which I never had. I would also like to mention Pallabi, Suman, Aravind, Nairit, Soureek, Sanmay, Moon Moon, Neha, Namrata and Saurabh for being invariably cordial.

Words would be inadequate to express my gratitude towards Adhip. I could not have imagined my thesis getting completed without him. He stood by me in the hardest times, motivated me and helped me to fight back in every situation possible. He was in some sense my backbone for all these years.

Finally I am extremely grateful to my family members — parents, brother and my uncle for their unconditional love, sacrifice and support for all my decisions. My late grandfather, who was quite close to my heart, is unfortunately not here to witness the completion of my Ph.D. work. I, therefore, dedicate my thesis to my family, to my late grandfather.

Disha Bhatia

Contents

Chapter 1

The Standard Way

1.1 Introduction

In this chapter, we discuss the central ideas which underlie the *Standard Model* (SM) of particle interactions. The theoretical and experimental advancements in the field of particle physics over the past century or so have led to this successful phenomenological model which describes the interactions among the fundamental particles in a systematic framework. The quest for such a systematic description began around the middle of 20^{th} century when many new particles were discovered with additional interactions which were different from the well-known electromagnetic and gravitational forces. Subsequently, four types of particle interactions were identified viz. electromagnetic, gravitational, weak and strong. Historically, the names weak and strong were given based on their observed interaction strengths, but now that we now know that these strengths are scale/energy dependent in a quantum theory, the names are to be understood just as labels.

The SM is actually a combination of the Glashow-Salam-Weinberg (GSW) theory of electroweak (EW) interactions [1–3] and quantum chromodynamics (QCD) which describes strong interactions. Around the EW scale i.e. $\mathcal{O}(100$ GeV$)$, the electromagnetic and weak forces unify and can be described within a single framework, which is the GSW model. The gravitational interaction lies outside the domain of the SM as it is too feeble to matter in laboratory experiments. It is dominant only near the Planck scale, i.e. $\mathcal{O}(10^{19}$ GeV$)$, so that we may regard the SM as a low-energy effective field theory of a full ultra-violet complete theory describing the gravitational interactions as well.

The matter content of the SM comprises of three classes of elementary particles

1. spin-1 gauge bosons,
2. spin-$\frac{1}{2}$-fermions, and
3. a scalar Higgs boson.

There are 12 gauge bosons, viz. 8 gluons g, $W^{\pm}$ and Z bosons and the photon γ. The fermions are further classified as quarks (which participate in both strong and electroweak interactions) and leptons (which participate only in the electroweak interactions). There exist a total of 6 quarks: up (u), down (d), charmed (c), strange (s), top (t) and bottom (b), and 6 leptons: electron (e), electron-neutrino (ν_e), muon (μ), muon-neutrino (ν_μ), tau (τ) and tau-neutrino (ν_τ) which are grouped into three generations each, as follows.

$$\begin{pmatrix} \nu_e \ (1955) \\ e \ (1896) \end{pmatrix} \qquad \begin{pmatrix} \nu_\mu \ (1962) \\ \mu \ (1937) \end{pmatrix} \qquad \begin{pmatrix} \nu_\tau \ (2001) \\ \tau \ (1975) \end{pmatrix}$$

$$\begin{pmatrix} u \ (1969) \\ d \ (1969) \end{pmatrix} \qquad \begin{pmatrix} c \ (1974) \\ s \ (1969) \end{pmatrix} \qquad \begin{pmatrix} t \ (1994) \\ b \ (1977) \end{pmatrix}$$

where the date of experimental discovery has been given in parentheses next to each fermion.

The discovery of the SM as a consistent theory of particle interactions has been a long journey filled with many direct and indirect evidences. A brief timeline of ideas is given below [4].

1927 Foch, London and Weyl propose a gauge theory of electromagnetism.

1932 Heisenberg discovers isospin and constructs a theory of the strong interaction.

1934 Fermi's theory of beta decay explains the weak interaction.

1935 Yukawa's theory of the strong interaction predicts pions.

1947 Schwinger, Feynman, Tomonaga and Dyson create quantum electrodynamics (QED).

1953 Yang and Mills introduce nonAbelian gauge theory.

1956 Schwinger introduces the intermediate vector boson hypothesis in weak interactions.

1957 Parity violation is discovered in the weak interactions by Yang and Lee. The V-A theory is suggested by Marshak & Sudarshan, Feynman & Gell-Mann and Sakurai.

1960 Nambu and Jona-Lasinio suggest spontaneous symmetry-breaking in elementary particle theory.

1961 Glashow constructs the first electroweak theory with massless particles and Gell-Mann constructs the eight-fold way .

1963 Cabibbo introduces the idea of flavour-mixing in u, d and s quarks.

1964 Englert & Brout, Higgs and Guralnik, Hagen & Kibble discover the Higgs mechanism. Gell-Mann and Zweig propose the quark model.

1966 Kibble constructs the Higgs mechanism in nonAbelian gauge theories.

1967 Weinberg publishes the Standard Model for the lepton sector. Similar ideas are independently proposed by Salam.

1971 t'Hooft prove that the Standard Model is renormalisable.

1973 Gell-Mann and Fritzsch & Leutwyler develop quantum chromodynamics (QCD) as a gauge theory.

1973 Kobayashi & Maskawa predict the third generation and explain the origin of CP-violation.

1973 Politzer and Gross & Wilczek discover asymptotic freedom of QCD.

By the mid-1970s, the Standard Model as we know it was more or less complete as a theory, though some of the particles were discovered later, such as the $W^\pm$ in 1982, the Z^0 in 1983, the t quark in 1994, the ν_τ in 2001 and, finally, the Higgs boson H in 2012. The interplay between direct and indirect evidences, and theoretical advancements have played a crucial role in defining the *standard* of particle interactions. With the SM turning out to be the underlying theory of particle physics, it is to be seen whether this is an ending or a mere beginning towards new expeditions.

1.2 Foundations of the Standard Model

The Standard Model of particle physics is built on the ideas of gauge invariance and spontaneous symmetry breaking [5–8] . The idea of gauge invariance was first discovered in classical theory of electrodynamics, when it was realized that the different kinds of the vector potentials A_μ, related by

$$A_\mu \to A_\mu + \partial_\mu \alpha \ , \tag{1.2.1}$$

could give rise to the same physical electric and magnetic fields. The above transformation on A_μ (vector/gauge field) is known as the gauge transformation. Mathematically this amounts to saying that the action

$$S = \int d^4x \ \mathcal{L} = -\frac{1}{4}\int d^4x \ F_{\mu\nu}F^{\mu\nu} = -\frac{1}{4}\int d^4x \ \left(\partial_\mu A_\nu - \partial_\nu A_\mu\right)^2 \ . \tag{1.2.2}$$

stays invariant under the gauge transformation in equation 1.2.1.

In quantum electrodynamics (QED), the excitation of the A_μ field corresponds to photons. An $A_\mu A^\mu$ term is forbidden in equation 1.2.2 due to gauge invariance. Therefore, zero mass of photons can be understood in terms of invariance of the Lagrangian under the gauge transformations.

Now we consider the scenario where a spin-$\frac{1}{2}$ field (ψ) interacts with the photon field. The Lagrangian for such a system is given as

$$\mathcal{L} = -\frac{1}{4}F_{\mu\nu}F^{\mu\nu} + i\bar{\psi}\left(\partial_\mu - i\,A_\mu\right)\psi \ . \tag{1.2.3}$$

It can be seen that the Lagrangian is invariant under the global phase rotations of the field ψ i.e.

$$\psi(x) \to e^{i\alpha}\psi(x) \ , \tag{1.2.4}$$

but is not invariant under the gauge transformation of the A_μ field as given in equation 1.2.1. Since photons are observed to be massless, the theory must respect gauge invariance.

Note that if we make the transformations in equation 1.2.4 local, then for the combined transformations

$$A_\mu(x) \to A_\mu(x) + \partial_\mu\alpha(x) \ , \ \psi(x) \to e^{i\alpha(x)}\psi(x) \ , \tag{1.2.5}$$

the Lagrangian in equation 1.2.3 stays invariant. The continuous symmetry transformations in equation 1.2.5 can be mapped to the $U(1)$ Lie group, where the field ψ transforms in the fundamental representation and A_μ transforms in the adjoint representation. The quantum field theory of electrodynamics hence corresponds to a $U(1)$ gauge theory. As an aside, note that the symmetry operations in equation 1.2.5 with constant α are referred to as the global symmetry transformations and correspond to a conserved current, J^μ and conserved charge (Nöther's theorem).

While a successful field theory for QED existed, attempts made to formulate a coherent quantum theory for weak interactions were less successful. The first theory was given by Fermi, where the interactions were written as four-fermion operators with the operator structure same as QED. While it fitted some of the low energy data, there were issues with unitarity and renormalisation as the theory was really an effective theory in terms of higher dimensional operators (dim > 4) and it failed at high energies. Since the weak interactions were observed to be short-ranged unlike the electromagnetic interactions, it was thought that a massive gauge particle could in principle serve as a consistent theoretical explanation at high energies. This was the idea implemented in Intermediate Vector Boson theory, whose Lagrangian is

$$\mathcal{L}_{\text{weak}} = -\frac{1}{4}W_{\mu\nu}W^{\mu\nu} + i\bar{\psi}\gamma^{\mu}\partial_{\mu}\psi + i\bar{\psi}'\gamma^{\mu}\partial_{\mu}\psi' + \bar{\psi}\gamma^{\mu}\psi' W_{\mu} + M_W^2 W^{\mu}W_{\mu} + h.c. \,. \tag{1.2.6}$$

The weak interactions at that time were observed only in the charged current processes before 1970's, as a result only massive charged gauge bosons viz., $W^{\pm}$ were postulated [1]. Although the Intermediate Vector Boson theory apparently looked renormalizable due to absence of higher-dimensional operators, it was actually non-renormalizable at higher energies. This can be understood by considering the W propagator,

$$\frac{1}{q^2 - M_W^2}\left(-g_{\mu\nu} + \frac{q_{\mu}q_{\mu}}{M_W^2}\right) \,. \tag{1.2.7}$$

This scales as $1/q^2$ at low energies but becomes constant at higher energies taking us back to the same situation as the Fermi theory. The naive counting of divergences hence breaks at higher q's. On the other hand, if the W propagator was coupled to a conserved current J^{μ}, such that $q_{\mu}J^{\mu} = 0$, then a scaling as $1/q^2$ could be achieved. However, the mass term of weak boson W in the equation 1.2.6 explicitly breaks gauge invariance and M_W cannot be set to zero because the weak interaction is short-range. The solution to write a consistent theory for weak interactions came with the idea of spontaneous symmetry breaking (SSB) of the gauge symmetries.

The concept of spontaneous breaking of the symmetry is quite different from that of explicit breaking. While the symmetry of the Lagrangian is completely broken at all energy scales for the latter case, in the former case the symmetry is broken only by the ground state of the system but the Lagrangian still preserves the symmetry. It just gets hidden due to expansion of the fields around the true minimum. If the symmetry transformation is described by the unitary operator U, then SSB implies

$$\mathcal{L} = U\mathcal{L}U^{\dagger} \,,\; U|0\rangle \neq |0\rangle \,. \tag{1.2.8}$$

Note that due to Lorentz invariance, only scalar fields can aid in the phenomena of spontaneous symmetry breaking.

To explain the idea of SSB in detail, we consider a simplistic example of scalar field $\phi = \dfrac{\rho + i\eta}{\sqrt{2}}$ theory, which is invariant under $U(1)$ global transformations[2].

$$\mathcal{L} = \partial_{\mu}\phi^{\dagger}\partial^{\mu}\phi + m^2\phi^{\dagger}\phi - \lambda(\phi^{\dagger}\phi)^2 \,. \tag{1.2.9}$$

[1]Here the fermions ψ and ψ' have a relative charge difference of ± 1.

[2]We will come to gauge symmetries shortly, after analyzing the repercussions of breaking a global symmetries spontaneously.

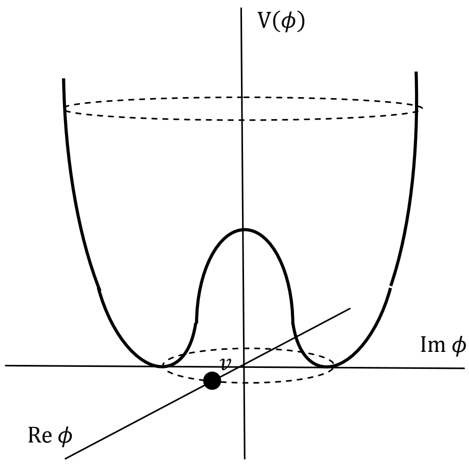

Figure 1.1: The scalar potential of the scalar field ϕ. Expansion of the field around one of its true minima breaks the symmetry spontaneously.

In above Lagrangian, note that the complex scalar field ϕ has an opposite mass-squared terms which corresponds to imaginary massive or unphysical particles ρ and η. In fact this term is crucial for generating multiple vacua for ϕ. The schematic potential of ϕ is shown in Fig. 1.1. Clearly because of $m^2 > 0$, the ground state here does not corresponds to a single state with zero vacuum expectation, rather to a plethora of states with non-zero expectation values i.e. $\langle \Phi \rangle = \frac{|v|}{\sqrt{2}} e^{i\theta}$ [3], which are obtained by solving

$$\frac{\partial V}{\partial \phi} = 0 \, , \quad \text{where } v = \sqrt{\frac{m^2}{\lambda}} \, . \tag{1.2.10}$$

The choice of choosing one minima over others breaks the symmetry spontaneously.

Suppose we choose the ground state of the potential to be $\langle \Phi \rangle = \frac{v}{\sqrt{2}}$ by fixing $\theta = 0$. Clearly this does not remain invariant under $U(1)$ symmetry transformations. Re-expressing the field around its true ground state i.e. $\phi \to \frac{\rho + i\eta + v}{\sqrt{2}}$, the Lagrangian in equation 1.2.9 gets modified to

$$\mathcal{L} = \frac{1}{2}\partial_\mu \rho \partial^\mu \rho + \frac{1}{2}\partial_\mu \eta \partial^\mu \eta - m^2 \rho^2 + \ldots \, . \tag{1.2.11}$$

Here dots represent trilinear and quartic scalar interaction terms. Note that the Lagrangian in equation 1.2.11 looks symmetry violating only because of the expansion of field ϕ around the true minimum, the symmetry has got hidden. Now the expansion of field around its one of the minima in equation 1.2.11 has results in physical particles — a massless and massive scalar η and ρ respectively. The appearance of massless particle can be explained by Goldstone's theorem which states that the number of broken generators in SSB corresponds to massless

[3]Here θ denotes the redundancy in choosing the ground state

particles which are known as Goldstone bosons in literature. Any global symmetry which is broken spontaneously will inevitably yield massless fields. However absence of these scalars in nature put such theories into serious trouble.

Thus far we have not addressed the solution of writing consistent broken gauge theories and have discovered a new problem of massless particles associated with spontaneous breaking of global symmetry. It was then realized that if a local gauge symmetry is broken spontaneously instead of a global one then the massless boson can be absorbed as the longitudinal degree of freedom of the gauge boson. This comes under the name of Brout-Englert-Higgs mechanism [9, 10], which is popularly known as Higgs mechanism. The triumph in incorporating Higgs mechanism is that the spontaneous broken gauge theories are renormalizable [11]. Hence one can write massive gauge field theories in a consistent manner.

To illustrate the procedure of SSB in gauge theories, we again consider a scalar field ϕ but now charged under a gauged $U(1)$ symmetry. The Lagrangian in equation 1.2.9 now gets modified to,

$$\mathcal{L} = -\frac{1}{4}F_{\mu\nu}F^{\mu\nu} + (\partial_\mu - igA_\mu)\phi^\dagger(\partial_\mu + igA_\mu)\phi + m^2\phi^\dagger\phi - \lambda(\phi^\dagger\phi)^2 \,. \tag{1.2.12}$$

As before, minimizing the potential and expressing the field around its ground state results in a massless field η and a massive degree of freedom ρ. Rewriting the above Lagrangian in terms of new fields:

$$\mathcal{L} = -\frac{1}{4}F_{\mu\nu}F^{\mu\nu} + \frac{g^2v^2}{2}A_\mu A^\mu + \frac{1}{2}\partial_\mu\rho\partial^\mu\rho + \frac{1}{2}\partial_\mu\eta\partial^\mu\eta - m^2\rho^2 + gvA_\mu\partial^\mu\eta + \dots \,, \tag{1.2.13}$$

where dots represent the trilinear and the quartic terms. Notice the bilinear term which is an admixture of the gauge field and the massless field. The term can be interpreted as a gauge transformation on A_μ field.

$$\frac{g^2v^2}{2}A_\mu A^\mu + \frac{1}{2}\partial_\mu\eta\partial^\mu\eta + gvA_\mu\partial^\mu\eta \to \frac{g^2v^2}{2}\left(A_\mu + \frac{\partial_\mu\eta}{gv}\right)^2 \,. \tag{1.2.14}$$

Hence $\partial_\mu\eta$ appears as the longitudinal degree of mode the massive gauge field. However in the Lagrangian η field still enters in the cubic and the quatic interactions. To make the physical particle content explicit, we write fields in the non-linear parameterization i.e.

$$\phi = \frac{\rho + i\eta + v}{\sqrt{2}} = e^{i\eta'}\left(\frac{\rho' + v}{\sqrt{2}}\right) \,, \tag{1.2.15}$$

where for small field expansions $\rho' \sim \rho$ and $\eta' \sim \eta$. In terms of these new fields ρ', η' and $A'_\mu = A_\mu + \frac{\partial_\mu\eta}{gv}$, the Goldstone mode disappears from the theory leaving the massive scalar and the vector field.

$$\mathcal{L} = -\frac{1}{4}F'_{\mu\nu}F^{\mu\nu\prime} + \frac{g^2v^2}{2}A'_\mu A^{\mu\prime} + \frac{1}{2}\partial_\mu\rho'\partial^\mu\rho' - m^2\rho^{2\prime} - \lambda v\rho^{3\prime} - \frac{\lambda}{4}\rho^{4\prime} \,. \tag{1.2.16}$$

The above Lagrangian can be interpreted by the means of performing a special gauge transformation viz., the unitary gauge transformation i.e.

$$\phi(x) \to \phi'(x) = e^{-i\frac{\eta'}{v}}\phi = \frac{(\rho' + v)}{\sqrt{2}} \text{ ,and } A_\mu \to A'_\mu = A_\mu + \frac{\partial_\mu\eta}{gv} \,. \tag{1.2.17}$$

Hence our twin problems — mass of gauge bosons and massless scalar — gets solved by invoking the spontaneous breaking of the gauge symmetry. To conclude, gauge invariance and spontaneous symmetry breaking mechanism are powerful tools for expressing the theories with massive gauge bosons in a consistent manner.

1.3 The Electroweak part of the Standard Model

The electroweak part of the SM is often popularly known as the Glashow-Salam-Weinberg model. In the previous section 1.2, we had discussed that the difficulties in describing weak interactions could be resolved if the gauge symmetry was broken spontaneously. Now the task is to determine the underlying symmetry associated with weak interactions. To do that, let us consider the interaction part of the Intermediate Vector Boson theory

$$\mathcal{L}^{\rm int}_{\rm weak} = \bar{\psi}\gamma_\mu \psi' W^\mu \ . \tag{1.3.1}$$

The simplest possible gauge group which we can consider to describe the weak interactions is $SU(2)$ with ψ and ψ' transforming as a doublet under $SU(2)$. Note that only left chiral fermions[4] could be charged under this $SU(2)$ due to observation of maximum parity violation in charged currents [12] to which $V - A$ structure provides a good fit [13, 14]. Among the three generators of the $SU(2)$ group, two of them can be associated with $W^\pm$ i.e. the charged current and the third one with the neutral current. Since both electromagnetism and weak forces were mediated by spin-1 particles, there were many efforts to unify these two forces. Note that one could not have simply considered the third generator of $SU(2)$ with the photon since the interactions mediated in electromagnetism were parity conserving. It was realized that the simplest possible gauge group for electroweak unification was $SU(2)_L \times U(1)_Y$. The charges associated with $U(1)_Y$ gauge group were termed as hypercharges. Since the low energy theory preserves $U(1)_{\rm em}$, therefore the electroweak gauge group should spontaneously break to electromagnetism. The generator which remains conserved after the symmetry breaking is a linear combination of T_3 and hypercharge and is given as $Q = T_3 + \frac{Y}{2}$.

The gauge group of the Standard Model is the direct product of strong interactions i.e. $SU(3)_c$ and electroweak interactions i.e. $SU(2)_L \times U(1)_Y$, where c, L and Y stands for colour, left chiral and hypercharge respectively. The $SU(3)_c$ symmetry results in eight gauge bosons i.e. the gluons and the electroweak gauge group corresponds to the four gauge bosons —W^μ_{1-3} for $SU(2)$ and B^μ for $U(1)_Y$ with the gauge couplings g_3, g and g' respectively. Amongst the matter content, there exist three generations of quarks and leptons each which are listed in Table 1.1. The characterization of the generation is based on the mass hierarchies — the first generation corresponds to the lightest fermions and the third generation to the heaviest[5]. The conservation of $SU(2)_L \times U(1)_Y$ along with Lorentz invariance not only necessitates the

[4]Apart from the gauge symmetries, SM Lagrangian should also be invariant under the Lorentz transformations. Correspondingly the fermionic fields in the Lagrangian can be projected onto their chiral basis ($\psi = \psi_L + \psi_R$) as the chirality operator i.e. γ_5 commutes with the Lorentz transformations.

[5]However it is still not known whether the neutrinos follow the same hierarchical patterns or not.

Generation	I	II	III
Quarks	up (u), down (d)	charm (c), strange (s)	top (t), bottom (b)
Leptons	electron (e), e-neutrino (ν_e)	muon (e), μ-neutrino (ν_μ)	tau (τ), τ-neutrino(ν_τ)

Table 1.1: The three generations of quarks and leptons.

SM gauge bosons, but also the fermions to be massless. After symmetry breaking, using the Higgs mechanism, the SM particles acquire mass. To break the symmetry spontaneously into $U(1)_{\rm em}$, a scalar doublet Φ carrying a hypercharge $Y = 1$ is introduced. The SM Lagrangian in presence of the scalar doublet is given as

$$\begin{aligned}
\mathcal{L}_{\rm SM} &= -\frac{1}{4}B_{\mu\nu}B^{\mu\nu} - \frac{1}{4}W^i_{\mu\nu}W_i^{\mu\nu} - \frac{1}{4}G^a_{\mu\nu}G_a^{\mu\nu} + |D_\mu\Phi|^2 + \overline{Q_L}i\not{D}Q_L \\
&+ \overline{u_R}i\not{D}u_R + \overline{d_R}i\not{D}d_R + \overline{L_L}i\not{D}L_L + \overline{e_R}i\not{D}e_R \\
&+ \overline{Q_L}\,\mathcal{Y}^d\Phi d_R + \overline{Q_L}\mathcal{Y}^u\Phi^c u_R + \overline{Q_L}\mathcal{Y}^e\Phi^c e_R + h.c. \\
&+ \mu^2\Phi^\dagger\Phi - \frac{\lambda}{2}|\Phi^\dagger\Phi|^2 \,, \qquad (1.3.2)
\end{aligned}$$

where $\mathcal{Y}^{u,d,e}$ are 3×3 Yukawa matrices for up, down and charged-lepton sectors respectively and D_μ is the covariant derivative, μ is the Higgs mass parameter and λ is the Higgs self interaction coupling. Note the wrong-sign mass parameter μ^2 helps in generating the infinite number of vacuum states and the choice of one over others breaks the symmetry. We choose the vacuum state as $\begin{pmatrix} 0 & \frac{v}{\sqrt{2}} \end{pmatrix}^T$ and define the scalar field in the unitary gauge as before.

$$\Phi' = e^{-i\frac{\theta_i\sigma_i}{v}}\Phi = \begin{pmatrix} 0 \\ \frac{h+v}{\sqrt{2}} \end{pmatrix} \,. \qquad (1.3.3)$$

In this gauge, the scalar potential becomes

$$\begin{aligned}
V(\Phi) &= -\mu^2\Phi'^\dagger\Phi' + \frac{\lambda}{2}\left(\Phi'^\dagger\Phi'\right)^2 \\
&= m^2h^2 + \lambda v h^3 + \frac{\lambda}{4}h^4 \,. \qquad (1.3.4)
\end{aligned}$$

Hence we see that the process of SSB has generated a Higgs mass, $m_h = \sqrt{2}m = \sqrt{2\lambda}v$ and additional Higgs cubic and quartic interactions.

The effect of SSB in gauge sector, as discussed before, is essentially to generate the masses of gauge bosons in a consistent manner. This can be seen by considering the kinetic part of the scalar Lagrangian

$$\begin{aligned}
|D_\mu\Phi'|^2 &= |\left(\partial_\mu - igW_\mu - ig'B_\mu\right)\Phi'|^2 \,, \\
&= \frac{1}{2}\partial_\mu h\partial^\mu h + M_W^2 W^{\mu+}W^-_\mu\left(1+\frac{h}{v}\right)^2 + \frac{1}{2}M_Z^2 Z^\mu Z_\mu\left(1+\frac{h}{v}\right)^2 \,. \qquad (1.3.5)
\end{aligned}$$

where,

$$
\begin{aligned}
W^{\pm}_{\mu} &= \frac{W_{1\mu} \pm i W_{2\mu}}{\sqrt{2}} \ , & M_W &= \frac{1}{2} g v \ , \\
Z_{\mu} &= \cos\theta_W W_{3\mu} - \sin\theta_W B_{\mu} \ , & M_Z &= \frac{1}{2} v \sqrt{g^2 + g'^2} \ , \\
A_{\mu} &= \sin\theta_W W_{3\mu} + \cos\theta_W B_{\mu} \ , & M_A &= 0 \ . \qquad (1.3.6)
\end{aligned}
$$

Here θ_W is referred as the Weinberg angle and is given as $\tan\theta_W = \frac{g'}{g}$. Since the electroweak symmerty gets broken to electromagnetism, the three broken generators are absorbed as the longitudinal modes for $W^{\pm}$ and Z, the unbroken generator corresponds to the massless photon. The masses and W and Z bosons can be expressed in terms of ρ parameter as

$$
\rho = \frac{M_W^2}{M_Z^2 \cos^2\theta_W} = 1 \ . \qquad (1.3.7)
$$

This parameter is exactly equal to unity at tree-level in Standard Model.

Similar to gauge bosons, Higgs mechanism also helps in generating the mass terms of the SM fermions. Let us consider the Yukawa part of the Lagrangian viz.,

$$
\begin{aligned}
\mathcal{L}_{\text{Yuk}} &= \overline{Q^i_L} \mathcal{Y}^d_{ij} \Phi d^j_R + \overline{Q^i_L} \mathcal{Y}^u_{ij} \Phi^c u^j_R + \overline{Q^i_L} \mathcal{Y}^e_{ij} \Phi^c e^j_R + h.c. \\
&= \overline{u_L} M_u \left(1 + \frac{h}{v}\right) u_R + \overline{d_L} M_d \left(1 + \frac{h}{v}\right) d_R + \overline{\ell_L} M_\ell \left(1 + \frac{h}{v}\right) \ell_R + h.c. \ . \qquad (1.3.8)
\end{aligned}
$$

The Yukawa matrices $\mathcal{Y}$'s are in general non-diagonal and non-hermition. They are diagonalized by performing bi-unitary transformations i.e.

$$
M_u = \frac{v}{\sqrt{2}} V^\dagger_{uL} \mathcal{Y}^u V_{uR} \ , \ M_d = \frac{v}{\sqrt{2}} V^\dagger_{dL} \mathcal{Y}^d V_{dR} \ , \ M_\ell = \frac{v}{\sqrt{2}} V^\dagger_{\ell L} \mathcal{Y}^\ell V_{\ell R} \ . \qquad (1.3.9)
$$

Here V's are the rotation matrices, $M_u = \text{diag}(m_u, m_c, m_t)$, $M_d = \text{diag}(m_d, m_s, m_b)$ and $M_\ell = \text{diag}(m_e, m_\mu, m_\tau)$. Note that the absence of right handed neutrinos lead to massless neutrinos in Standard Model framework. The above mass diagonalization modifies the structure of interactions of gauge bosons with fermions and leads to flavour changing interactions in charged currents mediated by W

$$
\mathcal{L}_{\text{cc}} = \frac{g}{\sqrt{2}} \bar{u}_i \gamma^\mu P_L [V_{\text{CKM}}]_{ij} d_j \ W^+_\mu + h.c. \ , \qquad (1.3.10)
$$

where $V_{\text{CKM}} = V^\dagger_{uL} V_{dL}$. Note that the flavour changing matrix V_{CKM} is also unitary and can be described in terms of nine parameters — three rotation angles and six complex phases. Out of these six phases, five can be absorbed by the rotation of the quark fields. The remaining phase is the sole source of CP violation in weak interactions.

In contrast with the charged current, flavour changing interactions mediated by Z and γ are absent at the tree-level because charges of all same-type fermions under $U(1)_Y$ symmetry are same. The Lagrangian corresponding to the neutral current interactions is given as

$$
\mathcal{L}_{\text{nc}} = e \overline{f} \gamma^\mu f \ A_\mu + \frac{g}{\cos\theta_W} \left(g^f_L \overline{f} \gamma^\mu P_L f + g^f_R \overline{f} \gamma^\mu P_R f \right) Z_\mu \ , \qquad (1.3.11)
$$

where, e_f is the electromagnetic charge of the fermion f, T_3 is the isospin of the fermion and $g^f_{L,R} = T_3 - e_f \sin^2\theta_W$. The electromagnetic charge of electron gets related to the $SU(2)_L$ gauge coupling g as $e = g\sin\theta_W$.

To conclude this section, we highlight the major predictions and findings of the electroweak sector of the Standard Model:

1. Unification of electromagnetism and weak forces via the electroweak gauge group $SU(2)_L\times U(1)_Y$. This is the minimal symmetry which would give rise to such a unification at high scales.
2. The electroweak theory predicts the presence of new kind of neutral currents coupling to heavy gauge boson, Z.
3. The electroweak structure along with three generations of fermions naturally incorporates the phenomena of CP violation.
4. Standard Model predicts ρ parameter to be exactly equal to unity at the classical level, with very small quantum corrections.

1.4 Current status of the SM

In the previous section, we considered the electroweak sector of the Standard Model. Due to its specific gauge group i.e. $SU(2)_L \times U(1)_Y$ definite interaction form exist between particles. Over past several years, these forms have been tested to a great degree of accuracy at electron-positron (LEP, SLAC, Belle, Babar), proton-antiproton (UA1, UA2, Tevatron), electron-proton (HERA) and proton-proton (LHC) colliders. The gauge sector was the first to be established with the discovery of $W^\pm$ and Z bosons at UA1 and UA2 [15, 16] followed by precision measurements of gauge boson interactions with fermions and self interactions at LEP-I, LEP-II and SLAC, where some of the interactions were tested upto a 0.1% level [17, 18]. The flavour sector has also been established at the B-factories by BABAR and BELLE collaborations [19].

Signal Strength $(\mu_j^{\mathrm{ggF}})^{\mathrm{exp}}$	ATLAS-CMS (7 – 8 TeV) (combined)	Signal Strength $(\mu_j^{\mathrm{VBF}})^{\mathrm{exp}}$	ATLAS-CMS (7 – 8 TeV) (combined)
$\mu^{\mathrm{ggF}}_{\gamma\gamma}$	$1.10^{+0.23}_{-0.22}$	$\mu^{\mathrm{VBF}}_{\gamma\gamma}$	$1.3^{+0.5}_{-0.5}$
μ^{ggF}_{ZZ}	$1.13^{+0.34}_{-0.31}$	μ^{VBF}_{ZZ}	$0.1^{+1.1}_{-0.6}$
μ^{ggF}_{WW}	$0.84^{+0.17}_{-0.17}$	μ^{VBF}_{WW}	$1.2^{+0.4}_{-0.4}$
$\mu^{\mathrm{ggF}}_{\tau\bar{\tau}}$	$1.0^{+0.6}_{-0.6}$	$\mu^{\mathrm{VBF}}_{\tau\bar{\tau}}$	$1.3^{+0.4}_{-0.4}$

Table 1.2: The combined measured values of $(\mu^i_j)^{\mathrm{exp}}$ from ATLAS and CMS using 7 and 8 TeV data [21].

Now with the Higgs discovery at LHC [20], we have just began our journey towards verifying the scalar sector. At tree level, Higgs couples with W^+W^-, ZZ, charged leptons and quarks.

Due to its dominant coupling with top, it couples with gg and $\gamma\gamma$[6] at one loop. The Higgs can be produced at the LHC via gluon fusion (ggF), vector-boson fusion (VBF), and in association with SM gauge bosons (Vh), as well as with a top pair ($t\bar{t}h$) and it can decay to $\gamma\gamma$, $ZZ^* \to \ell^+\ell^-\ell'^+\ell'^-$, $WW^* \to \ell^+\nu_\ell\ell'^-\nu'_\ell$, $f\bar{f}$ if ($m_h > m_f/2$). The accurate measurements of these couplings will hold a clues about the scalar sector and the nature of electroweak symmetry breaking. Table 1.2 shows combined ATLAS and CMS signal strengths measurements from run-I data for the observed Higgs Boson into various channels [21]. Although the uncertainties in measurements at the present moment are large $\mathcal{O}(10-20\%)$, we can clearly see that the SM is compatible with the data. Other Higgs couplings for instance the tri-linear and quartic at present are extracted using the information of the Higgs mass and the vacuum expectation value. Its independent measurement is yet to be made at the experiments and this will provide us a clear understanding of the nature of the electroweak symmetry breaking that whether it occurs because of a Higgs doublet or many more. Apart from Higgs studies, LHC is also actively probing other sectors and so-far have found no significant deviations from the Standard Model predictions, see for example [22].

Despite such phenomenal success of the SM, there are several reasons to believe the existence of the physics beyond Standard Model [23, 24]. The Higgs mass is thought to be one of the major reasons for existence of physics beyond Standard Model because it is unstable in the presence of new particles at scales much higher than the electroweak scales. Suppose a new particle is present scale $\Lambda >> \mathcal{O}_{\mathrm{EW}}$, then corrections to Higgs mass scales as

$$\delta m_h^2 \propto \Lambda^2 \ . \tag{1.4.1}$$

To arrange $m_h \approx 125$ GeV then requires large amount of fine tuning. The Higgs mass correction sets the scale of new physics to be roughly around a TeV to avoid large fine tuned cancellations. This problem is primarily associated with the fundamental scalars and do not arise for fundamental fermions and gauge particles. This can be simply understood based on symmetry arguments. If we have a theory with only fundamental fermions and no scalars, then the fermionic mass term viz., $\bar{\psi}\psi$ is symmetric under $U(1)_V$ transformations. In the limit of zero mass, there is an enhanced symmetry of the theory i.e. the chiral symmetry $U(1)_A$. If this symmetry is also preserved by the quantum fluctuations, then fermion remains massless even after performing higher order calculations. Notice this a phenomenal result because this implies that in presence of $m \neq 0$, the mass corrections are proportional to the symmetry breaking term which is m itself. The same result holds true for the gauge bosons. The gauge symmetry principles prevent the masses of gauge bosons from becoming too large. This is remarkable result in itself because the chiral/gauge symmetry argument prevents the fermions/gauge bosons mass term becoming dependent on the cut off scale. Notice that we cannot use such arguments of the SM Higgs. The mass term which arises from $\Phi^\dagger\Phi$ interaction is already invariant under all global and gauged symmetries. Therefore M_h^2 by no means is protected by any enhanced symmetry of the theory. It might still happen that due to fine tuned Higgs bare mass parameter, the actual mass of Higgs may be light and doesn't depend

[6] Here the coupling with W^+W^- also plays a crucial role

on the cut-off scale. But we strongly believe that just like fermions and gauge bosons, there may be some phenomena which prevents Higgs boson mass. There is also a counter-view that the issue associated with the stability of the mass of the fundamental scalar is more-or-less aesthetic and should be taken with a pinch of salt.

There have been numerous attempts to solve the Higgs hierarchy or rather fine tuning problem [25]. The most popular one has undoubtedly been supersymmetry, where there is an additional symmetry which relates the fermionic degree of freedom with the bosonic ones. Here the chiral symmetry of fermions protects the mass of the fundamental scalars. Alternatively, there are composite Higgs models, where Higgs is not a fundamental scalar but a bound state of fermions which are charged under a new gauge interaction similar to QCD. Therefore the problem associated with the elementary scalar at first place only doesn't arise. If the observed Higgs mass is protected by symmetry arguments then new particles should appear at the TeV-scale. But the continuous running of LHC has resulted in no sign of new particle at the TeV-scale. This has put the idea of naturalness and fine tuning into trouble and has resulted in a new problem of little hierarchy [26]. Experiments suggest that NP scales should atleast be greater than 2-3 TeV and for some models even 5 TeV, while Higgs mass stablization requires the scales to be present at a TeV. In the light of this, alternate models with the concept of neutral naturalness viz., where new particles do not have strong interactions have been hypothesized. Time will only tell that which of these models or any other variant of these models will survive.

Another issue which concerns Standard Model is the existence of the neutrino oscillations [27, 28]. The massless neutrinos in SM could not have given rise to this phenomenon. The problem may be easily alleviated by adding three right handed neutrinos and generating masses through Higgs mechanism, but the zero charge of neutrinos creates a dilemma over origin of neutrino masses. The fermions uncharged under electromagnetism are either Dirac-like or Majorana-like and the process of acquiring mass is completely different for the two cases. While Higgs mechanism works well with the Dirac-neutrinos, see-saw mechanism has been suggested as an alternative method for origin of mass for Majorana-like neutrinos. The data on the neutrino oscillation does hint towards new physics, but leaves its nature to be completely unknown.

Astronomically there are many compelling evidences of the existence of dark matter ranging from the proper velocities of galaxies clusters, rotation curve measurements of the galaxies, Cosmic Microwave Background Radiation etc [29]. However till date no interactions other than the gravitational ones have been reported for these particles. Attempts have been made in the past to determine the particle content of dark matter but all efforts so far have gone in vain. Since the existence of dark matter cannot be denied, some new physics should hold the explanation to this mystery.

There are few other aesthetic problems associated with the SM viz., why do we have $SU(3)_c \times SU(2)_L \times U(1)_Y$ gauge symmetry, why there are three generations of fermions and one Higgs doublet, why is the mass of an electron and top so different from each other?

These are few problems which have intrigued the theorist time and again. While there have been many theoretical breakthrough ideas as previously mentioned like supersymmetry, composite Higgs, extra dimensions which attempt to address some of the above problems, none of them have yet shown any observable effect at the detectors.

At present, SM fits the data well but it certainly cannot be the complete picture till all scales because around Planck scale the gravitational effects become strong and such effects would then have to be included in a consistent manner. Since data seems to be in agreement with the Standard Model predictions within the experimental uncertainties, the new physics may be either hidden under the large Standard Model backgrounds or may be present in an inaccessible part of the parameter space. Given the scenario where no model is being favoured by the experiments we choose to take an alternative and simplistic approach which we describe in detail in the next chapter.

Chapter 2

Small Expeditions out of the Standard Way

Experimental searches for physics beyond the Standard Model have – till date – yielded neither significant positive results nor specific directions or paths to follow. However it is clear from the discussions in the previous chapter, that physics beyond the Standard Model must exist. In the absence of any specific hint about the nature of new physics, various new physics models are current, and all being consistent with the present data, make the search strategies somewhat incoherent. Wide-reaching ideas encompassing all of particle physics, such as compositeness, supersymmetry or extra dimensions belong to this class, and one has only to look at the number of papers predicting signals for these to see the huge variety of possibilities which experimental physicists have to confront.

In such a situation, focused studies – often data-driven – have become extremely important. Thus, simple extensions of the Standard Model and effective field theories are being increasingly favoured to analyze the effects of new physics in data, as they have a small number of free parameters and hence greater predictivity. Similarly, one looks at simplified versions of the deeper models mentioned above where only a small sector of the full theory is relevant. In general, data can provide direct or indirect hints for the presence of new physics, depending upon its nature. For example, while the lighter particles may be observed directly as resonances in the invariant mass spectrum, such a method would not work for heavier resonances due to limited statistics. One would then have to rely upon the indirect clues where the presence of such a heavier resonance could lead to deviations in well measured/predictable observables.

The above approach has been adapted in this thesis work, wherein simple extensions of the Standard Model have been considered to probe and predict direct and indirect hints in the data. Our aim is not to address the problems listed in chapter 1 in a top-down fashion, but rather to understand the data and eventually make predictions in a bottom-up approach. The hope is that such studies would eventually guide us towards the UV-complete models, at some stage in future. We have, thus, chosen a few select areas, focussing on extensions of the Standard Model where extra bosons or additional couplings of the existing bosons are involved.

Recent flavour measurements in the neutral B decays concerning b to s flavour transitions [30–33] have hinted towards lepton flavour-universality violation. Although the individual deviations from the SM predictions are not more than 2-3σ, what is intriguing is the fact that so many observables are simultaneously pointing towards the need of a similar kind of new physics. Part of the thesis work has been devoted towards exploring a possible new physics explanation for a few of the above anomalies. In chapter. 3, we have presented the simultaneous solutions to the anomaly R_K and neutrino mixings. A class of $U(1)_X$ lepton flavour universality violating models have been identified in a bottom-up approach. Our solutions are consistent with the P_5' anomaly. At the time when the work was done, results for the R_{K^*} anomaly did not exist. We also analyze the implications of including R_{K^*} measurements towards end of chapter. 3.

The indirect effect of new physics may also affect the gauge boson self interactions. In another such study discussed in chapter 4, we perform a dedicated collider analysis for the process $pp \to W\gamma \to \ell\nu_\ell\gamma$, to study the new physics effects manifesting in the presence of anomalous $WW\gamma$ couplings. Instead of using the standard conventional variable i.e. the transverse momentum of the photon, we identify other kinematic variables which aid in better signal sensitivities.

The diphoton channel is perhaps one of the cleanest probes for searching for new physics at the LHC – witness the discovery of the Higgs Boson [20]. Owing to better signal and background distinctions, the sensitivity of these channels to detect new physics is much higher than that of other channels like $b\bar{b}$ or $\tau\bar{\tau}$. In chapter 5, we study the direct detection prospects of a light scalar (lighter than the Higgs Boson) in the di-photon channel in the context of a type-I 2HDM and find favourable regions where such a light scalar could be probed with the current luminosities at the LHC. We also briefly discuss the light scalar decays to $b\bar{b}$ final states.

The discovery of a diphoton resonance at the LHC would prompt various questions, which would hold true for any heavy resonance particle, e.g. does a heavy mass resonance corresponds to a two-photon final state or could that be an artefact of a multiphoton (three or more) final state appearing as an apparent diphoton state? or, what would be the spin of such a prototype resonance? We have attempted to address these questions in chapter 6 using an effective field theory approach in the context of a spin-0, spin-1 and spin-2 resonances. In fact, a couple of years back, an anomaly in the diphoton invariant mass around 750 GeV had been announced simultaneously by both ATLAS and CMS collaborations. Of course, it is well known that the anomaly disappeared with increased statistics [34, 35].

Most of the problems described above have been addressed by minimally extending the SM by, for example, (i) the addition of singlet scalars, (ii) $SU(2)_L$ doublet scalars, (iii) right handed neutrinos, (iv) additional gauge symmetries, (v) higher-dimensional operators. or some combinations of these. We describe the theoretical framework of these minimal extensions in the following sections.

2.1 Singlet Scalars

Introducing additional scalars S, uncharged under the SM gauge group, is perhaps the minimal way of going beyond the SM [36]. Such extensions are useful in explaining various problems, such as dark matter, smallness of neutrino mass masses through see-saw mechanism in presence of three right handed neutrinos, strong CP-problem, fermionic mass hierarchy through the Froggatt-Nielson mechanism, μ problem of supersymmetry and many more. The new SM-singlet scalar may be either charged under a Z_2 symmetry or some additional gauge symmetry depending upon the nature of the problem in consideration.

Let us consider two real scalar SM singlet fields S_1 and S_2 which transform under Z_2 and Z_2' symmetry operations respectively. The SM fields are not affected by these transformations. We choose to break Z_2 at scale v_{S_1} spontaneously and preserve Z_2' at all scales. To see the phenomenological consequences of this choice, consider the modified Higgs potential in presence of S_1 and S_2 fields

$$\begin{aligned} V(\Phi, S_1, S_2) \;\; = \;\; & -m^2\Phi^\dagger.\Phi + \lambda\left(\Phi^\dagger.\Phi\right)^2 + m_1^2 S_1^2 + \lambda_{S_1} S_1^4 \\ & -m_2^2 S_2^2 + \lambda_{S_2} S_2^4 + \lambda_{\Phi S_1} S_1^2 \left(\Phi^\dagger.\Phi\right) \\ & +\lambda_{\Phi S_2} S_2^2 \left(\Phi^\dagger.\Phi\right) + \lambda_{S_1 S_2} S_1^2 S_2^2 \end{aligned} \tag{2.1.1}$$

The spontaneous breaking of Φ and S_1 generates mixing between the the SM-Higgs and this new scalar. The observed Higgs hence is an admixture of the scalars h and S_1. The mixing between them is given by

$$\mathcal{L} = m_h^2 h^2 + m_{S_1}^2 S_1^2 + \lambda_{\Phi S_1}\, v_{EW}\, v_{S_1}\, h\, S_1 \tag{2.1.2}$$

Estimating orders of magnitude, $m_h \approx \mathcal{O}(v_{EW})$ and $m_{S_1} \approx \mathcal{O}(v_{s_1})$. Hence the mixing matrix becomes

$$\begin{pmatrix} v_{EW}^2 & \lambda_{\Phi S_1}\, v_{EW}\, v_{S_1} \\ \lambda_{\Phi S_1}\, v_{EW}\, v_{S_1} & v_{S_1}^2 \end{pmatrix} \tag{2.1.3}$$

In the limit when the symmetry Z_2 is broken at scales much larger than the electroweak scale, the eigenvalues are $v_{S_1}^2$ and $v_{EW}^2\left(1 - \lambda_{\Phi S_1}^2\right)$ and the mixing angle is $\dfrac{v_{EW}}{v_{S_1}}\lambda_{\Phi S_1}$. We want $\lambda_{\Phi S_1}$ to be at-least less than unity, such that Higgs mass remains of the order of electro-weak scale. Consequently the mixing angle generated is small. Nevertheless this mixing leads to the singlet scalar coupling with the SM particles. If mass of S_1 is of the order of TeV scale, then it could in principle be observed as a resonance at LHC provided its couplings are reasonable enough.

Howsoever simple this addition of SM scalar singlet S_1 may appear, it has rather powerful implications. In this thesis, we have studied the implications of adding such a scalar in the context of neutrino masses. The other scalar S_2 on the other hand doesn't mix with any other scalar field and is a stable particle due to preserved Z_2' symmetry. This could be a candidate for the unexplained dark matter content of the Universe.

2.2 Two-Higgs doublet models

Theoretically there is no physical reason why there should be only one scalar doublet in Nature. Just like the fermions, the scalar sector may well have more than one generation. Such a possibility is explored in various multi-Higgs doublet models [37]. We consider the two-Higgs doublet models, which are one of the simplest extensions of the SM with an additional $SU(2)_L$ scalar doublet carrying same hypercharge as the SM doublet. The Higgs potential in presence of Φ_1 and Φ_2 is

$$\begin{aligned} V(\Phi_1, \Phi_2) &= m_{11}^2\, \Phi_1^\dagger \Phi_1 + \frac{\lambda_1}{2}\left(\Phi_1^\dagger \Phi_1\right)^2 + m_{22}^2\, \Phi_2^\dagger \Phi_2 + \frac{\lambda_2}{2}\left(\Phi_2^\dagger \Phi_2\right)^2 - m_{12}^2 \Phi_1^\dagger \Phi_2 \\ &\quad + \lambda_3\, \Phi_1^\dagger \Phi_1\, \Phi_2^\dagger \Phi_2 + \lambda_4\, \Phi_1^\dagger \Phi_2\, \Phi_2^\dagger \Phi_1 - \frac{1}{2}\lambda_5 \left(\Phi_1^\dagger \Phi_2\right)^2 \\ &\quad - \frac{1}{2}\lambda_6\, \Phi_1^\dagger \Phi_2\, \Phi_1^\dagger \Phi_1 - \frac{1}{2}\lambda_7\, \Phi_1^\dagger \Phi_2\, \Phi_2^\dagger \Phi_2 + h.c.\,, \end{aligned} \tag{2.2.1}$$

where,

$$\Phi_1 = \begin{pmatrix} \frac{1}{\sqrt{2}}\left(\rho_1 + i\eta_1\right) \\ \frac{1}{\sqrt{2}}\left(\rho_2 + i\eta_2\right) \end{pmatrix} \quad \Phi_2 = \begin{pmatrix} \frac{1}{\sqrt{2}}\left(\rho_3 + i\eta_3\right) \\ \frac{1}{\sqrt{2}}\left(\rho_4 + i\eta_4\right) \end{pmatrix}\,. \tag{2.2.2}$$

The scalar potential above contains fourteen real parameters and eight real scalar fields. The parameters of the Lagrangian can be chosen appropriately such that both the doublets exhibit spontaneous symmetry breaking mechanism to yield masses to the fundamental particles of the theory. To avoid charge and CP-violating minimum of the potential, we chose minima at $\langle \rho_2 \rangle = v_1$ and $\langle \rho_4 \rangle = v_2$. For small expansions around the minima, the doublets in Equation.2.2.2 can be expressed in terms of non-linear representation as:

$$\Phi_1 \approx \exp^{i\frac{\tau.\xi_1}{v_1}} \times \begin{pmatrix} 0 \\ \frac{1}{\sqrt{2}}\left(\rho_2 + v_2\right) \end{pmatrix} \quad \Phi_2 \approx \exp^{i\frac{\tau.\xi_2}{v_2}} \times \begin{pmatrix} 0 \\ \frac{1}{\sqrt{2}}\left(\rho_4 + v_2\right) \end{pmatrix} \tag{2.2.3}$$

where τ are the Pauli matrices, $\xi_1 = (\eta_1, \rho_1, -\eta_2)$ and $\xi_2 = (\eta_3, \rho_3, \eta_4)$. The doublets in general can be rotated by different $SU(2)$ and $U(1)$ transformations. In the vector-axial basis, this amounts to

$$\begin{aligned} \Phi_1 &\to \exp^{i\tau.(\theta_V + \theta_A)}\, \Phi_1\,, \quad \Phi_2 \to \exp^{i\tau.(\theta_V - \theta_A)}\, \Phi_2 \qquad : SU(2) \\ \Phi_1 &\to \exp^{i\left(\theta'_V + \theta'_A\right)}\, \Phi_1\,, \quad \Phi_2 \to \exp^{i\left(\theta'_V - \theta'_A\right)}\, \Phi_2 \qquad : U(1) \end{aligned} \tag{2.2.4}$$

Only the vector part of these transformations is gauged and is identified with the Standard Model gauge group. The axial transformations on the other hand are already broken by the scalar potential in Equation. 2.2.1. After spontaneous symmetry breaking, a linear combination of ξ_1 and ξ_2 which transforms under $SU(2)_V$ results in three Goldston bosons which gets absorbed as the longitudinal polarization modes of the $W^\pm$ and Z bosons. The orthogonal axial combination results in the massive charged scalar and the pseudo-scalar. Consequently, the rotation angle which diagonalizes the mass matrix of the charged scalars and pseudo-scalars are same and is commonly denoted as β in the literature.

$$\begin{pmatrix} G^+\,, G^0 \\ H^+\,, A \end{pmatrix} = \begin{pmatrix} \cos\beta & \sin\beta \\ -\sin\beta & \cos\beta \end{pmatrix} \begin{pmatrix} \frac{1}{\sqrt{2}}(\rho_1 + i\eta_1)\,, \eta_2 \\ \frac{1}{\sqrt{2}}(\rho_3 + i\eta_3)\,, \eta_4 \end{pmatrix} \tag{2.2.5}$$

The masses of the charged scalar and the pseudoscalar are proportional to the terms in the scalar potential breaking $SU(2)_A$ and $U(1)_A$ symmetry respectively. The diagonalisation process of the neutral CP-even scalars on the other hand is independent and corresponds to the rotation angle α.

$$\begin{pmatrix} h \\ H \end{pmatrix} = \begin{pmatrix} \sin\alpha & -\cos\alpha \\ -\cos\alpha & -\sin\alpha \end{pmatrix} \begin{pmatrix} \rho_2 \\ \rho_4 \end{pmatrix} \tag{2.2.6}$$

Summarizing, the spontaneous breaking of the electroweak symmetry, $SU(2)_L \times U(1)_Y$ to the $U(1)_{\rm em}$, results in five physical scalar fields viz. light CP-even Higgs (h), Heavy CP-even Higgs (H), a pseudoscalar (A) and charged Higgs bosons ($H^\pm$) and three Goldstone fields — $G^\pm$ and G^0, which gets absorbed as the longitudinal modes for the $W^\pm$ and the Z boson in the unitary gauge. Expressing the doublets in terms of the physical degrees of freedom:

$$\begin{aligned} \Phi_1 &= \begin{pmatrix} G^+\cos\beta - H^+\sin\beta \\ \frac{1}{\sqrt{2}}\left[h\sin\alpha - H\cos\alpha + i\left(G\cos\beta - A\sin\beta\right) + v_1\right] \end{pmatrix}, \\ \Phi_2 &= \begin{pmatrix} G^+\sin\beta + H^+\cos\beta \\ \frac{1}{\sqrt{2}}\left[-h\cos\alpha - H\sin\alpha + i\left(G\sin\beta + A\cos\beta\right) + v_2\right] \end{pmatrix}, \end{aligned} \tag{2.2.7}$$

In this setup, the most general Yukawa interactions are given as

$$\begin{aligned} \mathcal{L}_{\rm Yuk} &= \overline{Q_L^i}\left(\mathcal{Y}^d_{1\,ij}\Phi_1 + \mathcal{Y}^d_{2\,ij}\Phi_2\right) d_R^j + \overline{Q_L^i}\left(\mathcal{Y}^u_{1\,ij}\Phi_1^c + \mathcal{Y}^u_{2\,ij}\Phi_2^c\right) u_R^j \\ &+ \overline{Q_L^i}\left(\mathcal{Y}^e_{1\,ij}\Phi_1^c + \mathcal{Y}^e_{2\,ij}\Phi_2^c\right) e_R^j + h.c.\,. \end{aligned} \tag{2.2.8}$$

This structure of couplings results in tree-level flavour changing neutral and charged currents mediated by the scalars since diagonalization of $\mathcal{Y}_1$ and $\mathcal{Y}_2$ matrices is different. To illustrate the point, we consider the Yuwaka interactions for down-type quarks:

$$\begin{aligned} \mathcal{L}_{\rm Yuk} &= \frac{v}{\sqrt{2}}\overline{d_L}\left(\mathcal{Y}_1^d\cos\beta + \mathcal{Y}_2^d\sin\beta\right) d_R \\ &+ \frac{1}{\sqrt{2}}\overline{d_L}\left(\mathcal{Y}_1^d\sin\alpha - \mathcal{Y}_2^d\cos\alpha\right) h\, d_R \\ &- \frac{1}{\sqrt{2}}\overline{d_L}\left(\mathcal{Y}_1^d\cos\alpha + \mathcal{Y}_2^d\sin\alpha\right) H\, d_R \\ &+ \frac{i}{\sqrt{2}}\overline{d_L}\left(\mathcal{Y}_1^d\sin\beta - \mathcal{Y}_2^d\cos\beta\right) A\, d_R \end{aligned} \tag{2.2.9}$$

The above interactions are written in the flavour basis. Diagonalizing the Yukawa matrices by bi-unitary transformations V_{d_L} and V_{d_R}

$$M_d = \frac{v}{\sqrt{2}} V_{d_L}^\dagger \left(\mathcal{Y}_1^d\cos\beta + \mathcal{Y}_2^d\sin\beta\right) V_{d_R}\,, \tag{2.2.10}$$

we can re-express the scalar interactions in the mass basis as

$$\begin{aligned} \mathcal{L}_{\rm Yuk} &= \frac{\sin\alpha}{\cos\beta}\overline{d_L}\left(M_d/v\right) d_R\, h - \frac{1}{\sqrt{2}}\frac{\cos(\beta-\alpha)}{\cos\beta}\overline{d_L}\, V_{d_L}^\dagger\, \mathcal{Y}_2^d\, V_{d_R}\, d_R\, h \\ &- \frac{\cos\alpha}{\cos\beta}\overline{d_L}\left(M_d/v\right) d_R\, H + \frac{1}{\sqrt{2}}\frac{\sin(\beta-\alpha)}{\cos\beta}\overline{d_L}\, V_{d_L}^\dagger\, \mathcal{Y}_2^d\, V_{d_R}\, d_R\, H \\ &+ i\tan\beta\,\overline{d_L}\left(M_d/v\right) d_R\, A - i\,\frac{1}{\sqrt{2}}\frac{1}{\cos\beta}\overline{d_L}\, V_{d_L}^\dagger\, \mathcal{Y}_2^d\, V_{d_R}\, d_R\, A \end{aligned} \tag{2.2.11}$$

Models	u^i	d^i	ℓ^i	Z_2
Type I	ϕ_2	ϕ_2	ϕ_2	$\phi_1 \to -\phi_1$
Type II	ϕ_2	ϕ_1	ϕ_1	$\phi_1 \to -\phi_1$, $\mathrm{d}^i \to -\mathrm{d}^i$,$\mathrm{e}^i \to -\mathrm{e}^i$
Lepton-specific	ϕ_2	ϕ_2	ϕ_1	$\phi_1 \to -\phi_1$, $\mathrm{e}^i \to -\mathrm{e}^i$
Flipped	ϕ_2	ϕ_1	ϕ_2	$\phi_1 \to -\phi_1$, $\mathrm{d}^i \to -\mathrm{d}^i$

Table 2.1: The doublets interacting with the fermionic fields for different kinds of two-Higgs models along with the fields transforming non-trivially under Z_2 symmetry.

Hence we have flavour-changing neutral current interactions at tree-level. Similarly, one could show the existence of flavour-changing charged current interactions mediated by the charged Higgs boson. Note that the bounds from K–$\bar{K}$ and B–$\bar{B}$ oscillations are quite stringent and restrict the allowed parameter space of the theory.

We have now witnessed the discovery of a scalar particle with mass 125 GeV at the Large Hadron Collider whose couplings are more-or-less Standard Model like. Due to large errors on the Higgs signal strength measurements, the possibility of the discovered scalar belonging to an enlarged scalar sector is still allowed. The measurement of CP properties of the observed scalar predicts it to be a CP-even scalar at 3-σ. We can therefore identify the observed scalar with any of the CP-even scalars in the enlarged framework. In the two Higgs doublet model set up — the natural choices are h or H. To suppress bounds from flavour oscillations, h is identified with observed scalar and other scalars — H, A and $H^\pm$ are considered to be heavy and decoupled from the theory. This limit in literature is popularly known as the *decoupling limit* but it is not interesting as its predictions cannot be tested at the current colliders.

Additional symmetries can be invoked at high scales in-order to have light scalars consistent with flavour oscillations leading to interesting phenomenological consequences. Z_2 symmetry being the simplest was the first one to be implemented and it categorized two Higgs doublet models into four kinds viz., type-I, type-II, lepton-specific and flipped. In all of these models, only one of the doublet coupled with the fermionic fields see Table 2.1 thus avoiding tree-level flavour-changing neutral currents. The tree-level charged currents mediated by charged scalars still exist and are CKM-like. We still get some bounds on the allowed parameter space depending on the type of 2HDM considered.

The Yukawa interactions as in Equation 2.2.8 for type-I and type-II models gets modified to

$$\mathcal{L}_{\text{Yuk}}^{\text{Type-I}} = \overline{Q_L^i}\,\mathcal{Y}_{1\,ij}^{d}\Phi_2 d_R^j + \overline{Q_L^i}\mathcal{Y}_{1\,ij}^{u}\Phi_2^c u_R^j + \overline{Q_L^i}\mathcal{Y}_{1\,ij}^{e}\Phi_2^c e_R^j + h.c.\,, \tag{2.2.12}$$

$$\mathcal{L}_{\text{Yuk}}^{\text{Type-II}} = \overline{Q_L^i}\,\mathcal{Y}_{1\,ij}^{d}\Phi_1 d_R^j + \overline{Q_L^i}\mathcal{Y}_{1\,ij}^{u}\Phi_2^c u_R^j + \overline{Q_L^i}\mathcal{Y}_{1\,ij}^{e}\Phi_1^c e_R^j + h.c. \tag{2.2.13}$$

Similar expressions can be written for lepton-specific and flipped models. The scalar potential with $\Phi_1 \to -\Phi_1$ under Z_2 gets modified to

$$\begin{aligned} V(\Phi_1,\Phi_2) &= m_{11}^2\,\Phi_1^\dagger\Phi_1 + \frac{\lambda_1}{2}\left(\Phi_1^\dagger\Phi_1\right)^2 + m_{22}^2\,\Phi_2^\dagger\Phi_2 + \frac{\lambda_2}{2}\left(\Phi_2^\dagger\Phi_2\right)^2 \\ &\quad +\lambda_3\,\Phi_1^\dagger\Phi_1\,\Phi_2^\dagger\Phi_2 + \lambda_4\,\Phi_1^\dagger\Phi_2\,\Phi_2^\dagger\Phi_1 - \frac{1}{2}\lambda_5\left(\Phi_1^\dagger\Phi_2\right)^2 + h.c.\,, \end{aligned} \tag{2.2.14}$$

which is same for the four types of the two Higgs doublet models listed in the Table. 2.1. Type-I model is more like the standard model as only one doublet has non-zero Yukawa coupling and Type-II 2HDM is similar to the supersymmetric extension of the standard model. In general there could be various other kinds of two Higgs doublet models like inert two Higgs doublet models, BGL models etc. which have slightly different phenomenology.

In one of the chapters 6, type-I 2HDM is considered for the analysis. There the phenomenology of a scalar h lighter than the observed scalar identified with H, in the mass range 70-110 GeV is discussed. In another chapter 3, a different kind of 2HDM is analysed, where the two doublets are charged differently under the abelian $U(1)_X$ symmetry. Since the motivation of the work was to explain the R_K anomaly using a Z', the additional scalars apart from the observed Higgs were considered to be heavy and hence decoupled from the theory. The additional doublet here helps to generate the correct structure of the CKM matrix, which otherwise would have been impossible owing to non-universal X-charge assignments of the quarks under $U(1)_x$

2.3 Additional $U(1)_X$ gauge symmetry

In this section, we study the implications of minimally extending the SM gauge group by an additional gauge symmetry $U(1)_X$ [38]. This addition results in a kinetic mixing between B_μ and X_μ fields. The gauge kinetic term in this set up gets modified as

$$\mathcal{L}_{\rm kin} = -\frac{1}{4}\widetilde{B}_{\mu\nu}\widetilde{B}^{\mu\nu} - \frac{1}{4}\widetilde{X}_{\mu\nu}\widetilde{X}^{\mu\nu} - \frac{k}{2}\widetilde{B}_{\mu\nu}\widetilde{X}^{\mu\nu} \,, \tag{2.3.1}$$

where k is the mixing strength between the two fields. The fields at present are not canonically normalized, and could be brought to their canonical basis by following transformation,

$$\begin{pmatrix} \widetilde{B}_\mu \\ \widetilde{X}_\mu \end{pmatrix} = P \begin{pmatrix} B_\mu \\ X_\mu \end{pmatrix} \,, \quad \text{where } P = \begin{pmatrix} 1 & -\dfrac{k}{\sqrt{1-k^2}} \\ 0 & \dfrac{1}{\sqrt{1-k^2}} \end{pmatrix} . \tag{2.3.2}$$

In the new basis, the kinetic term in Equation. 2.3.1 becomes

$$\mathcal{L}_{\rm kin} = -\frac{1}{4}B_{\mu\nu}B^{\mu\nu} - \frac{1}{4}X_{\mu\nu}X^{\mu\nu} \,. \tag{2.3.3}$$

The transformations in Equation. 2.3.2 changes the neutral current structure of the fields as follows

$$\begin{aligned} g\, J_3^\mu \widetilde{W}_{3\mu} + g_Y\, J_Y^\mu \widetilde{B}_\mu + g_X J_X^\mu \widetilde{X}_\mu \;\; \rightarrow \;\; & g\, J_3^\mu W_{3\mu} + g_Y\, J_Y^\mu B_\mu \\ & + \left(\frac{g_X}{\sqrt{1-k^2}} J_X^\mu - \frac{k}{\sqrt{1-k^2}} g_Y\, J_Y^\mu \right) X_\mu \end{aligned} \tag{2.3.4}$$

We note that the redefinition of fields at this stage has changed only the current structure of the $U(1)_X$ field.

Since the low energy symmetry of the nature is $U(1)_{em}$, therefore the $U(1)_X$ symmetry cannot remain conserved at all energy scales. If the SM particles, specifically quarks and leptons, are charged under this symmetry, then the bounds from LHC on mass of X can be quite stringent, typically around $\mathcal{O}(TeV)$. In such cases, the typical scales chosen to break $U(1)_X$ symmetry are much larger than the electroweak scale.

Another issue which concerns the X mass and more importantly Z–X mixing is the question whether the SM Higgs doublet or any additional doublet if any, are charged under $U(1)_X$ symmetry. If doublets transform as singlets under the action of $U(1)_X$, then there will not be any mass mixing between Z and X bosons and the kinetic mixing parameter k practically remains unconstrained. However, in presence of mass mixing, k will be constrained from various precision measurements at the LEP and the flavour factories. For example, let us consider the case where the SM Higgs Boson and an additional scalar S, carries equal charges, a_X (for simplicity) under $U(1)_X$ symmetry. The part of the Lagrangian containing the mass terms for the neutral gauge bosons can be given as:

$$\begin{aligned}\mathcal{L}_{\text{mass}} &= \Phi^{\dagger}.\left(\frac{g}{2}\widetilde{W}_{3\mu}\sigma_3 + \frac{g_Y}{2}\widetilde{B_\mu} + a_X\, g_X \widetilde{X_\mu}\right) \times \\ &\quad \left(\frac{g}{2}\widetilde{W}_{3\mu}\sigma_3 + \frac{g_Y}{2}\widetilde{B_\mu} + a_X\, g_X \widetilde{X_\mu}\right).\Phi + a_X^2 g_X^2 \widetilde{X}_\mu \widetilde{Z}'^{\mu} S^\dagger S\,. \end{aligned} \tag{2.3.5}$$

After spontaneous symmetry breaking the true minimum of the fields correspond to $\langle\Phi\rangle = \frac{v}{\sqrt{2}}$, and $\langle S\rangle = \frac{v_s}{\sqrt{2}}$. Redefining $a_X\, g_X \to g_X$, the Lagrangian in Equation. 2.3.5 can be written in a compact notation,

$$\mathcal{L}_{\text{mass}} = \frac{1}{2}\begin{pmatrix}\widetilde{W}_{3\mu} & \widetilde{B}_\mu & \widetilde{X}_\mu\end{pmatrix} M_V^2 \begin{pmatrix}\widetilde{W}_3^\mu \\ \widetilde{B}^\mu \\ \widetilde{X}^\mu\end{pmatrix}\,, \tag{2.3.6}$$

where

$$M_V^2 = \begin{pmatrix} \frac{1}{4}\, g^2 v^2 & -\frac{1}{4}\, g\, g_Y v^2 & -\frac{1}{2}\, g\, g_X v^2 \\ -\frac{1}{4}\, g\, g_Y v^2 & \frac{1}{4}\, g_Y^2 v^2 & \frac{1}{2}\, g_Y\, g_X v^2 \\ -\frac{1}{2}\, g\, g_X v^2 & \frac{1}{2}\, g_Y\, g_X v^2 & g_X^2\left(v_S^2 + v^2\right) \end{pmatrix} \tag{2.3.7}$$

This mass matrix doesn't account for the kinetic mixing. Incorporating the kinetic mixing will result in

$$\mathcal{L}_{\text{mass}} = \frac{1}{2}\begin{pmatrix}W_{3\mu} & B_\mu & X_\mu\end{pmatrix} P^T.M_V^2.P \begin{pmatrix}W_3^\mu \\ B^\mu \\ X^\mu\end{pmatrix}\,, \tag{2.3.8}$$

where matrix P is defined in eqn 2.3.2.

We first diagonalize the 1-2 component of the above mass matrix i.e. $W_{3\mu}$ and B_μ field to obtain massive Z_μ and massless A_μ fields,

$$\begin{pmatrix}Z^\mu \\ A^\mu \\ X^\mu\end{pmatrix} = \begin{pmatrix}\cos\theta_W & -\sin\theta_W & 0 \\ \sin\theta_W & \cos\theta_W & 0 \\ 0 & 0 & 1\end{pmatrix}\begin{pmatrix}W_3^\mu \\ B^\mu \\ X^\mu\end{pmatrix} \tag{2.3.9}$$

where, $\tan\theta_W = \frac{g_Y}{g}$. The mass matrix after this rotation is given as

$$\begin{pmatrix} Z^\mu & A^\mu & X^\mu \end{pmatrix} \begin{pmatrix} M_Z^2 & 0 & \Delta \\ 0 & 0 & 0 \\ \Delta & 0 & M_X^2 \end{pmatrix} \begin{pmatrix} Z^\mu \\ A^\mu \\ X^\mu \end{pmatrix} \tag{2.3.10}$$

where,

$$\begin{aligned} M_Z^2 &= \frac{1}{4}(g^2 + g_Y^2)v^2 \\ M_X^2 &= \frac{g_X^2}{1-k^2}\left(v_S^2 + v^2\right) + \frac{g_Y^2 v^2 k^2}{4(1-k^2)} - \frac{g_Y g_X k v^2}{1-k^2} \end{aligned} \tag{2.3.11}$$

$$\Delta = -\frac{g_X\sqrt{g^2+g_Y^2}v^2}{2\sqrt{1-k^2}} + \frac{k g_Y\sqrt{g^2+g_Y^2}v^2}{4\sqrt{1-k^2}} \tag{2.3.12}$$

and the Z–X mixing angle which diagonalizes the above mass matrix is given as

$$\tan 2\theta_{ZX} = \frac{2\Delta}{M_X^2 - M_Z^2} \tag{2.3.13}$$

The mixing is stringently constrained by the Z-pole measurements at LEP and SLC; therefore we can approximate it to be

$$\theta_{ZX} \approx \frac{\Delta}{M_X^2 - M_Z^2} \ . \tag{2.3.14}$$

The vacuum expectation values satisfying $v_s \gg v_{ew}$, renders small mixing angles naturally. The mass eigenstates of Z and X after mixing are given as

$$Z^m = Z - \theta_{ZX}X \ , \quad Z'^m = X + \theta_{ZX}Z \ . \tag{2.3.15}$$

The current in Equation. 2.3.4 gets modified to,

$$\begin{aligned} &e\,J_\mu^{em}A^\mu + \left[\frac{g}{\cos\theta_W} - \theta_{ZX}\left(\frac{g_X}{\sqrt{1-k^2}}J_X^\mu - \frac{k}{\sqrt{1-k^2}}g_Y\,J_Y^\mu\right)\right] Z^\mu \\ &+ \left[\left(\frac{g_X}{\sqrt{1-k^2}}J_X^\mu - \frac{k}{\sqrt{1-k^2}}g_Y\,J_Y^\mu\right) + \theta_{ZX}\frac{g}{\cos\theta_W}\right] Z'^\mu \ , \end{aligned} \tag{2.3.16}$$

where the superscript m is not written explicitly. The modifications in the current structure of Z boson, stringently constrains θ_{ZX} and k for a given value of g_X. The Z-pole observables will not only receive constraints due to the Z–X mixing, but will also be affected by the loop effects mediated by X. However for $\mathcal{O}$(TeV) scale Z', these effects are naturally small.

Another issue which concerns the additional gauge symmetry is anomalies. However if the fermions are assigned vector-like charges under $U(1)_X$, then the gauge symmetry by definition is anomaly free. Otherwise the X-charges of the new fermionic fields should be such that the anomaly coefficients are zero.

An additional $U(1)_X$ extension forms the backbone of the analysis reported in chapter 3.

2.4 Effective field theory

Effective field theory is a framework considering only those degrees of freedom which are relevant to the energy scales in the chosen problems [39]. For instance, for solving the hydrogen atom problem, we need not worry about the existence of quarks and similarly in the theory of weak interactions at low scales i.e. the Fermi theory, the knowledge of massive gauge bosons W and Z are not required simply because these particles cannot be produced on-shell. In the language of a quantum field theory, the basic idea is to integrate out the unimportant degrees of freedom and keep all the operators in the Lagrangian containing the relevant degrees of freedom.

There are two approaches of solving problems using an effective field theory viz. top-down and bottom-up. In a top-down approach, we begin with a well-motivated theory, and integrate out the irrelevant degrees of freedom. This approach is commonly used in flavour physics wherein, for most of the processes, the energy scales are much less than the electroweak scale. In contrast, the bottom-up approach is used when we are neither sure about the underlying high-scale symmetry nor about the new particles charged under it. Here the Lagrangian is expanded by writing all the possible terms which are consistent with the low-scale symmetry into consideration.

We begin by describing the top-down approach. To illustrate, we begin with a simplistic example of a semileptonic B decay, say $B \to K\ell\ell$, which, at parton level, is understood as a $b \to s\ell\ell$ transition. We are interested in computing the effects mediated by a heavy Z' massive particle with mass $m_{Z'} = \mathcal{O}(\mathrm{TeV})$, in the EFT framework. The energy scale at which this process is mediated is around the B-meson mass scale and is certainly well below $m_{Z'}$. Therefore we can safely integrate out Z' and obtain the effective Lagrangian. In order to do so, we have to follow a matching procedure where amplitudes of the full theory are matched with the effective theory. In this way we can be sure about the correctness of low-energy effective theory.

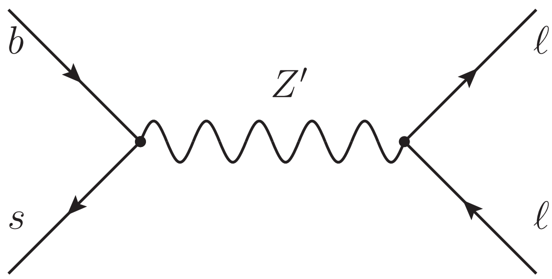

Figure 2.1: Feynman diagram depicting the tree level transition $b \to s\ell\ell$ mediated by a spin-1 particle.

For a top-down EFT, we should know the theory at high scale. Let us assume that the new physics interactions at a high scale are given by the following Lagrangian

$$\mathcal{L}_{Z'} = Z'_\mu \left(g_\ell \bar{\ell}\gamma^\mu \ell + g_{bs}\bar{b}\gamma^\mu s \right) \ . \tag{2.4.1}$$

To obtain the effective Lagrangian corresponding to $\mathcal{L}_{Z'}$, we compute the amplitude in the full theory following $+i$ convention for obtaining Feynman rules.

$$\begin{aligned} i\mathcal{M} &= \left(ig_\ell \times ig_{bs} \times \frac{-ig_{\mu\nu}}{q^2 - M_{Z'}^2} \right) \bar{\ell}\gamma^\mu \ell \, \bar{b}\gamma^\nu s \\ &= \left(ig_\ell \times ig_{bs} \times \frac{i}{M_{Z'}^2 \left(1 - \frac{q^2}{M_{Z'}^2}\right)} \right) \bar{\ell}\gamma^\mu \ell \, \bar{b}\gamma_\mu s \end{aligned} \tag{2.4.2}$$

In the limit $q^2 \ll m_{Z'}^2$

$$i\mathcal{M} = -i\,(g_\ell \times g_{bs}) \left(\frac{1}{M_{Z'}^2} + \frac{q^2}{M_{Z'}^4} + \dots \right) \bar{\ell}\gamma^\mu \ell \, \bar{b}\gamma_\mu s \tag{2.4.3}$$

The first term in the series corresponds to the dimension-6 operator, the second one to dimension-8 and ellipses to further higher dimensional operators. Since $q^2 \ll M_{Z'}^2$, we safely concentrate only on the dimension-6 piece which is independent of q^2. Now to arrive at the effective Lagrangian, we make use of the fact that the amplitude of full theory and the effective field theory are exactly the same. Sticking with the $+i$ convention, we arrive at the following effective Lagrangian

$$\mathcal{L}_{\text{eff}} = -\left(\frac{g_\ell \times g_{bs}}{M_{Z'}^2} \right) \bar{\ell}\gamma^\mu \ell \, \bar{b}\gamma_\mu s \; . \tag{2.4.4}$$

The coupling constant of the dimension-6 operator is known as the Wilson coefficient C. Here $C = -\dfrac{g_\ell \times g_{bs}}{M_{Z'}^2}$. Hence we have illustrated an example of tree-level matching and obtained the effective Lagrangian and corresponding Wilson coefficient. Since this is obtained at tree-level, this coefficient does not have any scale dependence and is valid at all scales. Matching at loop-level introduces a parametric scale dependence on C and also often introduces new operators.

In contrast, EFTs built using bottom-up principles are arbitrary as the underlying full theory and the corresponding symmetries are not known. The higher-dimensional terms in the Lagrangian are written based on the symmetries and particle content of the low energy theory. The Lagrangian in terms of higher-dimensional operators can then be written as:

$$\mathcal{L}_{\text{tot}} = \mathcal{L}_{\text{SM}} + \sum_i \frac{C_i}{\Lambda^2} \mathcal{O}_i^{(\text{dim}=6)} + \sum_i \frac{C_i}{\Lambda^4} \mathcal{O}_i^{(\text{dim}=8)} + \dots \; , \tag{2.4.5}$$

where Λ is the scale at which NP enters. If the new physics enters only at the Planck scale i.e. $\Lambda = 10^{19}$ GeV, then the higher dimensional operators are heavily suppressed and have no effect whatsoever at the current running TeV scaled colliders. However if some new physics is present at scales much lower than the Planck scales, e.g. near the TeV scale, as motivated by the hierarchy problem, then the EFT analyses could be useful in pinpointing the correct vertex structure and eventually the full theory. This analysis although it looks arbitrary at its face value but is useful since it is not biased by any kind of underlying theory/symmetry. We exemplify this point with a recent example in the literature concerning the semileptonic B neutral decays. Few years back, an anomaly in the angular observable of $B \to K^*\mu\mu$ differential distribution was reported. During similar times, another anomaly in the observable R_K dealing with $B \to K$ transitions was also reported. Although none of the above anomalies have been seen at the 5σ-level, what is intriguing is the fact that the bottom-up EFT analysis point towards the dominant presence of new physics in the following dimension-six operator

$$\mathcal{O}_9 = \frac{\alpha_e}{4\pi}\left[\bar{s}\gamma_\mu P_L b\right]\left[\bar{\mu}\gamma^\mu \mu\right] \tag{2.4.6}$$

with the Wilson coefficient $C_9^\mu = -1$. Of course with this single operator there are still many UV-complete explanations possible but the hope is that if the anomalies are indeed genuine then the measurements in future will guide us towards a unified theory. Another place where bottom-up EFT is useful is in parametrising the anomalous contributions to the SM couplings. The electroweak sector of the SM has been well measured and the constraints on the allowed values of the corresponding anomalous couplings are quite stringent. The Higgs couplings in contrast have not been fully measured and still encompass large uncertainties as already seen in Table. 1.2. The analysis dealing with the anomalous triple gauge coupling using the bottom-up EFT technique has been performed in chapter 4.

To summarise, one can construct minimal extensions of the Standard Model which help to study real and projected deviations in the data in a focussed way. This is an easier and more practical way that the global study of deeper underlying physics, where no particular process can be studied without bringing into play a slew of theoretical and phenomenological issues. This is the approach adopted in the present thesis. We now go on to describe some of the specific analyses carried out within this broad philosophy.

Chapter 3

Neutrino mixing and R_K anomaly in class of $U(1)_X$ models

In this chapter, we present our findings on the simultaneous solutions to the anomalies seen in the recent lepton flavour universality violating observables in neutral B-meson decays and neutrino mixing data. The work has been done in collaboration with Dr. Sabyasachi Chakraborty and Prof. Amol Dighe and is published in *JHEP* **1703** (2017) 117.

3.1 Introduction

The run-I data at LHC not only succeeded in discovering a Higgs Boson but also measured one of the rarest decay predicted in the SM i.e. $B_s \to \mu\mu$ [40] with the statistical significance of more than 6σ. This sole measurement along with $B \to X_s\gamma$ and other neutral meson-mixings measurements have been responsible for constraining many well defined models like supersymmetry at the LHC [41, 42], which predicts large flavour violations in certain regions of the parameter space. Although the scales at which B decays operates occur are extremely small $\mathcal{O}(m_B)$, they have important implications in constraining the models of NP [43].

In this chapter, we focus on the recently reported indirect hints of lepton flavour universality violation by the LHCb collaboration in the $b \to s\ell\ell$ flavour observables[1]. The $b \to s$ transitions at leading order in the Standard Model proceeds through one loop penguin and box diagrams due to absence of flavour changing neutral currents. These processes are touted to be sensitive probes as NP effects here are not loop suppressed with respect to the SM contributions. Experimentally such $b \to s$ transitions could be measured as inclusive or exclusive decays of the $B_{d,s}$ mesons for instance: $B \to K^*\gamma$, $B \to X_s\gamma$, $B \to K^{(*)}\ell\ell$, $B \to X_s\ell\ell$, $B_{s,d} \to \mu\mu$ and so on. Theoretical calculation of these observables is challenging because of the presence of form factor uncertainties and non-factorizable QCD corrections. However it is still possible to construct few observables which are less vulnerable to the QCD corrections. Two such

[1] Indirect hints have also been reported in the charged B decays, but they lie outside the scope of this chapter and work.

observables are the ratios, R_K and R_{K^*} [44]. These ratios are defined as

$$R_{K^{(*)}} = \frac{\int_{q^2_{min}}^{q^2_{max}} dq^2 \dfrac{d\Gamma(H(b) \to H(s)\mu\mu)}{dq^2}}{\int_{q^2_{min}}^{q^2_{max}} dq^2 \dfrac{d\Gamma(H(b) \to H(s)ee)}{dq^2}} \,. \tag{3.1.1}$$

Here $H(b)$ and $H(s)$ refers to some hadron containing b and s valence quarks respectively. The above quantities have been measured for $B^+ \to K^+$ and $B^0 \to K^{0*}$ exclusive decays at the LHCb experiment in CERN [32, 33]. The current deviations are listed in the Table. 3.1

Observables	$R_K^{[1,6]}$ (Central q^2)	$R_{K^*}{}^{[0.045,1.1]}$ (low q^2)	$R_{K^*}{}^{[1.1,6]}$ (Central q^2)
LHCb	$0.745^{+0.090}_{-0.074} \pm 0.036$	$0.66^{+0.110}_{-0.070} \pm 0.024$	$0.685^{+0.113}_{-0.069} \pm 0.047$
Expected	1.00 ± 0.01	0.92 ± 0.02	1.00 ± 0.01
Deviation	2.6	2.3	2.6

Table 3.1: The present status of deviations in $R_{K^{(*)}}$ observables at LHCb.

Since these ratios are almost free from the hadronic uncertainties in the Standard Model, the deviations in the measurements could arise either due to statistical fluctuations or due the presence of NP. The angular observable P_5' [48] in the decays of the B mesons in $B \to K^*\mu\mu$ [30, 31] also show deviations from the SM predictions. The BELLE collaboration has also reported an anomaly in P_5' [49] which is compatible with the one observed in [30, 31]. The branching ratio measurements of $B \to K^*\mu\mu$ [50] and $B \to \phi\mu\mu$ [51] also show slight deviations from the SM predictions. While all the latter anomalies could be accounted for by form factor uncertainties and underestimated non-factorisable corrections, the $R_K^{(*)}$ measurement should be free from strong interaction effects, since such effects majorly cancel in the ratio. Therefore, if the $R_K^{(*)}$ anomaly are confirmed, they would signal a clear lepton flavour universality violation [44, 52].

Assuming that the above anomalies are due to presence of some physics beyond model, they can be addressed by invoking additional NP contributions to some of the Wilson coefficients $C_i(\mu)$ appearing in the effective Hamiltonian for $b \to s\ell\ell$. In the SM, the effective Hamiltonian for this process is [53]

$$\begin{aligned} \mathcal{H}_{\text{eff}} &= -\frac{4G_F}{\sqrt{2}} V_{tb} V_{ts}^* \times \\ &\left(\sum_{i=1,6} C_i \mathcal{O}_i + C_{7\gamma}\mathcal{O}_{7\gamma} + C_{8G}\mathcal{O}_{8G} + \sum_{i=9,10} C_i \mathcal{O}_i + \sum_{i=S,P} C_i^{(\prime)} \mathcal{O}_i^{(\prime)} \right) , \end{aligned} \tag{3.1.2}$$

where $\mathcal{O}_i$'s are the effective operators, and $'$ indicates currents with opposite chirality. The values of $C_i(m_b)$ have been calculated in [54]. At the leading order, the additional NP contributions may contribute to the operators which are already present in the SM:

$$\begin{aligned}
\mathcal{O}_{7\gamma} &= \frac{e}{16\pi^2} m_b \left(\bar{s}\sigma_{\mu\nu}P_R b\right) F^{\mu\nu} \ , \ \mathcal{O}_9 = \frac{\alpha_e}{4\pi}\left[\bar{s}\gamma_\mu P_L b\right]\left[\bar{\ell}\gamma^\mu \ell\right] \ , \\
\mathcal{O}_{10} &= \frac{\alpha_e}{4\pi}\left[\bar{s}\gamma_\mu P_L b\right]\left[\bar{\ell}\gamma^\mu \gamma_5 \ell\right] \ ,
\end{aligned} \tag{3.1.3}$$

or may enhance the effects of the operators whose contributions are normally suppressed by the lepton mass in the SM:

$$\begin{aligned}
\mathcal{O}_S &= \frac{\alpha_e}{4\pi}\left[\bar{s}P_R b\right]\left[\bar{\ell}\ell\right] \ , \qquad \mathcal{O}_P = \frac{\alpha_e}{4\pi}\left[\bar{s}P_R b\right]\left[\bar{\ell}\gamma_5 \ell\right] , \\
\mathcal{O}'_S &= \frac{\alpha_e}{4\pi}\left[\bar{s}P_L b\right]\left[\bar{\ell}\ell\right] \ , \qquad \mathcal{O}'_P = \frac{\alpha_e}{4\pi}\left[\bar{s}P_L b\right]\left[\bar{\ell}\gamma_5 \ell\right] \ ,
\end{aligned} \tag{3.1.4}$$

or may generate new operators which are absent in SM [55]:

$$\begin{aligned}
\mathcal{O}'_{7\gamma} &= \frac{e}{16\pi^2} m_b \left(\bar{s}\sigma_{\mu\nu}P_L b\right) F^{\mu\nu} \ , \ \mathcal{O}'_9 = \frac{\alpha_e}{4\pi}\left[\bar{s}\gamma_\mu P_R b\right]\left[\bar{\ell}\gamma^\mu \ell\right] \ , \\
\mathcal{O}'_{10} &= \frac{\alpha_e}{4\pi}\left[\bar{s}\gamma_\mu P_R b\right]\left[\bar{\ell}\gamma^\mu \gamma_5 \ell\right] \ .
\end{aligned} \tag{3.1.5}$$

Simultaneous explanation of the R_K and P'_5 anomalies[2] is possible if the NP effects are present in $\mathcal{O}_9, \mathcal{O}'_9, \mathcal{O}_{10}$ or $\mathcal{O}'_{10}$ operators [56]. The global fits [57–61] prefer NP effects in $\mathcal{O}^\mu_9$, i.e. additional contributions to C^μ_9. Since the observed value of $R_K(\text{obs}) = 0.745^{+0.090}_{-0.074} \pm 0.036$ [32] is less than the SM prediction, which gives R_K to be unity within an accuracy of 1% [44,52], the new physics contribution must interfere destructively with the SM, i.e. opposite to that of $C^{\text{SM}}_9(m_b) = 4.2$ [54]. This indicates that the sign of $C^{\text{NP},\mu}_9$ is negative. The best-fit value of $C^{\text{NP},\mu}_9$ is ≈ -1 [56–61]. In addition $C^{\text{NP},\mu}_9 = -C^{\text{NP},\mu}_{10}$ also gives a good fit to data [58–61]. Motivated by these results, many explanations of the anomaly using Z' [62–82] and leptoquark [56, 82–103] models have been given in the literature.

Since the flavour anomalies mentioned above mostly involve muons, and there is no clear hint of new physics effects in the electron sector apart from R_K measurement, most of the analysis have been performed assuming new physics effects in muons only. However, NP contributions in the electron sector, $C^{\text{NP},e}_9$, of the same order as those in the muon sector, are still consistent with all $b \to s$ measurements within 2σ [58–61]. The comparisons among two dimensional global fits also prefer ($C^{\text{NP},e}_9$, $C^{\text{NP},\mu}_9$) over other combinations like ($C^{\text{NP},\mu}_9$, $C^{\text{NP},\mu}_{10}$) and ($C^{\text{NP},\mu}_9$, $C'^{\text{NP},\mu}_9$), with the best fit point favouring dominant contributions to $C^{\text{NP},\mu}_9$ [61].

In this work, we build our analysis around the choice where NP contributes via the $\mathcal{O}_9$ operator. We allow both $C^{\text{NP},e}_9$ and $C^{\text{NP},\mu}_9$ to be present. Since these two contributions have to be different, the NP must violate lepton flavour universality. This may be implemented in a minimalistic way through an abelian symmetry $U(1)_X$, under which the leptons have different charges. In particular, greater NP contribution to $C^{\text{NP},\mu}_9$ than $C^{\text{NP},e}_9$ may be achieved by a higher magnitude of the X-charge for muons than for electrons. Substantial NP contributions to the flavour anomalies also require tree-level flavour-changing neutral currents (FCNC) in

[2]The time when the paper was written results of R^*_K anomaly were not known, hence the major analysis in the thesis would concern with R_K anomaly. Later in section 3.6, we will comment on the plausibility of inclusion of R_{K^*} measurement on the generality of our results.

the quark sector. These can be implemented through different X-charges for the quark generations as well, which should still allow for quark mixing, and be consistent with the flavour physics data.

A horizontal $U(1)_X$ symmetry in the lepton sector would also determine the possible textures in the mass matrix of the right-handed neutrinos. In turn, the mixing pattern of the left-handed neutrinos [27,28] will be affected through the Type-I seesaw mechanism. The possible textures of the right-handed neutrino mass matrix and the lepton flavour universality violation required for the flavour anomalies can thus have a common origin. Scenarios like an $L_\mu - L_\tau$ symmetry with X-charges given to the SM quarks [66, 78] or additional vector-like quarks [65,73], have been considered in the literature in this context. Other models with Z' also have their own X-charge assignments [67,68,70,72,77], however their connection with the neutrino mass matrix has not been explored. We build our model in the bottom-up approach, where we do not assign the X-charges a priori, but look for the X-charge assignments that satisfy the data in the quark and lepton sectors. As a guiding principle, we introduce a minimal number of additional particles, and ensure that the model is free of any gauge anomalies. Finally, we identify the horizontal symmetries that are compatible with the observed neutrino mixing pattern, and at the same time are able to generate $C_9^{\mathrm{NP},e}$ and $C_9^{\mathrm{NP},\mu}$ that explain the flavour anomalies.

The chapter is organized as follows. In section 3.2, we describe the construction of the $U(1)_X$ models from a bottom-up approach. In section 3.3, we explore the allowed ranges of the parameters that are consistent with the experimental constraints like neutral meson mixings, rare B decays, and direct collider searches for Z'. In section 3.4, we present the predictions for the CP-violating phases in the lepton sectors for specific horizontal symmetries, and project the reach of the LHC for detecting the corresponding Z'. In section 3.5, we summarize our results and present our concluding remarks.

3.2 Constructing the $U(1)_X$ class of models

We construct a class of models wherein, in addition to the SM fields, we also have three right-handed neutrinos that would be instrumental in giving mass to the left-handed neutrinos through the seesaw mechanism. We extend the SM gauge symmetry group by an additional symmetry, $U(1)_X$, which corresponds to an additional gauge boson, Z', with mass $M_{Z'}$ and gauge coupling $g_{Z'}$. To start with, we denote the X-charge for a SM field i by X_i. In this section, we shall determine the values of X_i's in a bottom-up approach.

3.2.1 Preliminary constraints on the X-charges

Since we wish to build up the model by introducing NP effects only in the $\mathcal{O}_9$ operator, we have to make sure that the NP contribution to all the other operators listed in eqs. (3.1.3), (3.1.4), and (3.1.5) should vanish. We first consider the interactions of Z' with charged leptons, ℓ, in the mass basis:

$$\mathcal{L}_{Z'}^{\ell} = g_{Z'}\,\overline{\ell_L}\,\gamma^\mu V_{\ell_L}^\dagger\,\mathcal{X}_{\ell_L}\,V_{\ell_L}\,\ell_L\,Z'_\mu + g_{Z'}\,\overline{\ell_R}\,\gamma^\mu V_{\ell_R}^\dagger\,\mathcal{X}_{\ell_R}\,V_{\ell_R}\,\ell_R\,Z'_\mu\,, \tag{3.2.1}$$

where $\mathcal{X}_{\ell_L} = \mathrm{diag}\,(X_{e_L}, X_{\mu_L}, X_{\tau_L})$ and $\mathcal{X}_{\ell_R} = \mathrm{diag}\,(X_{e_R}, X_{\mu_R}, X_{\tau_R})$, while V_{ℓ_L} and V_{ℓ_R} are the rotation matrices diagonalizing the Yukawa matrix for charged leptons. Note that the $SU(2)_L$ gauge invariance of the SM ensures $\mathcal{X}_{\ell_L} = \mathcal{X}_{\nu_{\ell L}}$.

The Lagrangian in eq. (3.2.1) may be rewritten as

$$\begin{aligned}\mathcal{L}_{Z'}^{\ell} \;&=\; \frac{1}{2}\,g_{Z'}\,\bar{\ell}\,\gamma^\mu\left(V_{\ell_L}^\dagger\mathcal{X}_{\ell_L}V_{\ell_L} + V_{\ell_R}^\dagger\mathcal{X}_{\ell_R}V_{\ell_R}\right)\ell\,Z'_\mu \\ &\quad -\frac{1}{2}\,g_{Z'}\,\bar{\ell}\,\gamma^\mu\gamma_5\left(V_{\ell_L}^\dagger\mathcal{X}_{\ell_L}V_{\ell_L} - V_{\ell_R}^\dagger\mathcal{X}_{\ell_R}V_{\ell_R}\right)\ell\,Z'_\mu\,.\end{aligned} \tag{3.2.2}$$

The second term in eq. (3.2.2) would contribute to $\mathcal{O}_{10}$ and $\mathcal{O}'_{10}$. Since we do not desire such a contribution, we require

$$V_{\ell_L}^\dagger\mathcal{X}_{\ell_L}V_{\ell_L} = V_{\ell_R}^\dagger\mathcal{X}_{\ell_R}V_{\ell_R}\;. \tag{3.2.3}$$

A straight forward solution to the eq. (3.2.3) yields $V_{\ell_L} = I$ and $V_{\ell_R} = I$ and further $\mathcal{X}_{\ell_L} = \mathcal{X}_{\ell_R}$. In such a case a non-zero Yukawa matrix would need the Higgs field, Φ, to be a singlet under $U(1)_X$. Note that with unequal vector-like charge assignments in the lepton sector, the Yukawa matrix will naturally be diagonal. This therefore is a minimal and consistent solution and we proceed with this in our analysis.

Now we turn to the Z' interactions with the d-type quarks:

$$\mathcal{L}_{Z'}^{d} = g_{Z'}\,\overline{d_L}\,\gamma^\mu V_{d_L}^\dagger\,\mathcal{X}_{d_L}\,V_{d_L}d_L\,Z'_\mu + g_{Z'}\,\overline{d_R}\,\gamma^\mu V_{d_R}^\dagger\,\mathcal{X}_{d_R}\,V_{d_R}\,d_R\,Z'_\mu\,, \tag{3.2.4}$$

where $\mathcal{X}_{d_L} = \mathrm{diag}\,(X_{d_L}, X_{s_L}, X_{b_L})$, $\mathcal{X}_{d_R} = \mathrm{diag}\,(X_{d_R}, X_{s_R}, X_{b_R})$, while V_{d_L} and V_{d_R} are the rotation matrices which diagonalize the Yukawa matrix for d-type quarks. Note that the $SU(2)_L$ gauge invariance of the SM ensures $\mathcal{X}_{d_L} = \mathcal{X}_{u_L}$.

Substantial NP effects require the X-charges to be non-universal, thereby generating both $\overline{b_L}\gamma^\mu s_L Z'_\mu$ and $\overline{b_R}\gamma^\mu s_R Z'_\mu$ transitions. The presence of $\bar{\ell}\gamma^\mu\ell Z'_\mu$ interactions from eq. (3.2.2) will potentially generate both $\mathcal{O}_9$ and $\mathcal{O}'_9$ operators. We would like the NP contributions to $\mathcal{O}'_9$ operator to be vanishing, which can be ensured if the 2-3 element of $V_{d_R}^\dagger\mathcal{X}_{d_R}V_{d_R}$ vanishes. Indeed, we would demand a stricter condition to ensure no tree-level FCNC interactions in the right handed d-type sector, i.e. $V_{d_R}^\dagger\mathcal{X}_{d_R}V_{d_R}$ is diagonal. This can be ensured if

$$V_{d_R} \approx I \quad \text{or} \quad \mathcal{X}_{d_R} \propto I\;. \tag{3.2.5}$$

The non-universal charge assignments in the quark sector will also be constrained by the observed neutral meson mixings. In particular, the constraints in the K–$\overline{K}$ oscillations are by far the most stringent, and severely constrain the flavour changing Z' interaction with the first two generation quarks. This can be accounted if we choose [66, 72]

$$X_{d_L} = X_{s_L}\;, \quad X_{d_R} = X_{s_R}\;. \tag{3.2.6}$$

Another extremely important constraint stems from the requirement that the theory be free of any gauge anomalies. If the charge assignments are vector-like, i.e.

$$\mathcal{X}_{u_L} = \mathcal{X}_{d_L} = \mathcal{X}_{u_R} = \mathcal{X}_{d_R} \equiv \mathcal{X}_Q \quad , \quad \mathcal{X}_{\ell_L} = \mathcal{X}_{\nu_{\ell L}} = \mathcal{X}_{\ell_R} = \mathcal{X}_{\nu_{\ell R}} \equiv \mathcal{X}_L \ , \tag{3.2.7}$$

and are related by the condition

$$\mathrm{Tr}\,[\,3\,\mathcal{X}_Q + \mathcal{X}_L] = 0 \ , \tag{3.2.8}$$

the theory is free of all gauge anomalies. The X-charge assignments can then be written in a simplified notation as given in table 3.2. In terms of this notation, the anomaly-free condition is

$$3\,(2x_1 + x_3) + y_e + y_\mu + y_\tau = 0 \ . \tag{3.2.9}$$

Fields	Q_1	Q_2	Q_3	L_1	L_2	L_3	Φ
$U(1)_X$	x_1	x_1	x_3	y_e	y_μ	y_τ	0

Table 3.2: Vector-like X-charge assignments after applying preliminary constraints from the vanishing of NP contributions to $\mathcal{O}_9'$, $\mathcal{O}_{10}$ and $\mathcal{O}_{10}'$ operators, and constraints from K–$\overline{K}$ mixing. Here Q_i and L_i represent the i^{th} generations of quarks and leptons, respectively.

We are now in a position to select the correct alternative in eq. (3.2.5). The NP contribution to the $\mathcal{O}_9$ operator would require x_1 and x_3 to be unequal (see section 3.2.3), i.e. $\mathcal{X}_{d_L} \neq I$. The vector-like charge assignments then imply $\mathcal{X}_{d_R} \neq I$, and the only possibility remaining from eq. (3.2.5) is $V_{d_R} \approx I$. This condition need not be automatically satisfied in our model. In addition, $\mathcal{X}_{d_L} = \mathcal{X}_{d_R} \neq I$ could create problems in generating the structure of the quark mixing matrix. We shall discuss the way to overcome these issues in section 3.2.2.

3.2.2 Enlarging the scalar sector

Additional doublet Higgs to generate the CKM matrix

The Yukawa interactions of quarks with the Higgs doublet Φ are

$$\mathcal{L}_{\text{Yuk}} = \overline{Q^{\text{f}}_L}\,\mathcal{Y}^u\,\Phi^c\,u^{\text{f}}_R + \overline{Q^{\text{f}}_L}\,\mathcal{Y}^d\,\Phi d^{\text{f}}_R \ . \tag{3.2.10}$$

where the superscript "f" indicates flavour eigenstates. The X-charge assignments given in table 3.2 govern the structure of the Yukawa matrices ($\mathcal{Y}^u$ and $\mathcal{Y}^d$) as

$$\mathcal{Y}^u = \begin{pmatrix} \times & \times & 0 \\ \times & \times & 0 \\ 0 & 0 & \times \end{pmatrix} , \quad \mathcal{Y}^d = \begin{pmatrix} \times & \times & 0 \\ \times & \times & 0 \\ 0 & 0 & \times \end{pmatrix} \ , \tag{3.2.11}$$

where $\times$ denote nonzero values. Quarks masses are obtained by diagonalizing the above $\mathcal{Y}^u$ and $\mathcal{Y}^d$ matrices using the bi-unitary transformations $V^\dagger_{u_L}\mathcal{Y}^u V_{u_R}$ and $V^\dagger_{d_L}\mathcal{Y}^d V_{d_R}$, respectively.

Clearly, the rotations would be only in 1-2 sector. Therefore the quark mixing matrix, i.e. $V_{\rm CKM} = V_{u_L}^\dagger V_{d_L}$ also would have non-trivial rotations only in the 1-2 sector, however this cannot be a complete picture as we know that all the elements of $V_{\rm CKM}$ are non-zero.

The correct form of $V_{\rm CKM}$ can be obtained if mixings between 1-3 and 2-3 generations are generated. This can be achieved by enlarging the scalar sector of SM through an addition of one more SM-like doublet, Φ_1, with X-charge equal to $\pm d$ where $d = (x_1 - x_3)$. We choose $X_{\Phi_1} = +d$, similar to that in [66].

We first show how the 1-3 and 2-3 mixings are generated with the addition of this new Higgs doublet. The generic representations for these doublets Φ_1 and $\Phi_2 \equiv \Phi$ are

$$\Phi_1 = \begin{pmatrix} \phi_1^+ \\ \frac{1}{\sqrt{2}}[{\rm Re}(\phi_1) + i{\rm Im}(\phi_1) + v_1] \end{pmatrix}, \quad \Phi_2 = \begin{pmatrix} \phi_2^+ \\ \frac{1}{\sqrt{2}}[{\rm Re}(\phi_2) + i{\rm Im}(\phi_2) + v_2] \end{pmatrix},$$

where v_1 and v_2 are vacuum expectation values of the two doublets. There are related by $v_1 = v\cos\beta$ and $v_2 = v\sin\beta$, where v is the electroweak vacuum expectation value. With this addition the Lagrangian in eq. (3.2.10) gets modified to

$$\mathcal{L}_{\rm Yuk} = \overline{Q_L^{\rm f}}\left(\mathcal{Y}_1^u \Phi_1^c + \mathcal{Y}^u \Phi_2^c\right) u_R^{\rm f} + \overline{Q_L^{\rm f}}\left(\mathcal{Y}_1^d \Phi_1 + \mathcal{Y}^d \Phi_2\right) d_R^{\rm f}\,, \tag{3.2.12}$$

where

$$\mathcal{Y}_1^u = \begin{pmatrix} 0 & 0 & 0 \\ 0 & 0 & 0 \\ \times & \times & 0 \end{pmatrix}, \quad \mathcal{Y}_1^d = \begin{pmatrix} 0 & 0 & \times \\ 0 & 0 & \times \\ 0 & 0 & 0 \end{pmatrix}. \tag{3.2.13}$$

The bi-unitary transformations would now diagonalize the quark mass matrices as

$$M_u^{\rm diag} = \frac{v}{\sqrt{2}} V_{u_L}^\dagger \left(\mathcal{Y}_1^u \cos\beta + \mathcal{Y}^u \sin\beta\right) V_{u_R}\,, \tag{3.2.14}$$

$$M_d^{\rm diag} = \frac{v}{\sqrt{2}} V_{d_L}^\dagger \left(\mathcal{Y}_1^d \cos\beta + \mathcal{Y}^d \sin\beta\right) V_{d_R}\,. \tag{3.2.15}$$

From eqs. (3.2.11), (3.2.12) and (3.2.13), it may be seen that rotations in 1-2, 1-3 as well as 2-3 sector will now be needed to diagonalize the Yukawa matrices. Appropriate choice of parameters can then reproduce the correct form of $V_{\rm CKM}$. We choose $V_{u_L} = I$, so that $V_{d_L} = V_{\rm CKM}$, which ensures that Z' does not introduce any new source of CP violation in B–$\overline{B}$ mixing.

Having fixed V_{u_L} and V_{d_L}, we now turn to V_{u_R} and V_{d_R}. The solution to eq. (3.2.14) yields $[\mathcal{Y}_1^u]_{ij} = 0$, implying the mixing angle between the 2-3 and 1-3 generation for up type quark is zero. The solution does not constrain the rotation angle between the first and the second generation, which we choose to be vanishing for simplicity. Hence, V_{u_R} in our model is I.

Note that eq. (3.2.5) and subsequent discussion near the end of section 3.2.1 led to the requirement $V_{d_R} \approx I$. We shall now see that this requirement is easily satisfied in this framework. With $V_{d_L} = V_{\rm CKM}$, eq. (3.2.15) may be written in the form

$$V_{\rm CKM} M_d^{\rm diag} V_{d_R}^\dagger = \begin{pmatrix} \times & \times & \times \\ \times & \times & \times \\ 0 & 0 & \times \end{pmatrix}. \tag{3.2.16}$$

It may be seen that V_{d_R} with small rotation angles, parametrized as

$$V_{d_R} \approx \begin{pmatrix} 1 & \theta_{d_{R12}} & \theta_{d_{R13}} e^{-i\,\delta_d} \\ -\theta_{d_{R12}} & 1 & \theta_{d_{R23}} \\ -\theta_{d_{R13}} e^{i\,\delta_d} & -\theta_{d_{R23}} & 1 \end{pmatrix} , \tag{3.2.17}$$

can lead to the above form, with

$$\theta_{d_{R23}} \approx A\lambda^2 m_s/m_b \ , \quad \theta_{d_{R13}} \approx -A\lambda^3 m_d/m_b \ , \tag{3.2.18}$$

where A and λ are the Wolfenstein parameters and m_d, m_s and m_b are the quark masses. Note that similar observation has been made in [66]. The value of $\theta_{d_{R12}}$ is not constrained, and can be chosen to be vanishing. Thus, the requirement $V_{d_R} \approx 1$ is satisfied.

Note that since V_{d_R} is only approximately equal to I, small NP contributions to C_9' are present, However as we shall see in section 3.2.3, these contributions are roughly $(A\lambda^2 m_s)/(m_b V_{tb} V_{ts}^*)$ times the NP contributions to C_9, and hence can be safely neglected.

Singlet scalar for generating neutrino masses and mixing pattern

Our model has three right handed neutrinos, ν_R's. The Dirac and the Majorana mass terms for neutrinos are

$$\mathcal{L}_\nu^{\rm mass} = -\overline{\nu_L} m_D \nu_R - \frac{1}{2}\overline{\nu_R^c} M_R \nu_R + h.c. \ , \tag{3.2.19}$$

where the basis chosen for ν_L is such that the charged lepton mass matrix is diagonal. The active neutrinos would then get their masses through the Type-I seesaw mechanism. The net mass matrix being

$$M_\nu = -m_D\, M_R^{-1}\, m_D^T \ . \tag{3.2.20}$$

Since the neutrinos are charged under $U(1)_X$ with charges (y_e,y_μ and y_τ), the (α, β) elements of the Dirac mass matrix m_D would be nonzero only when $y_\alpha = y_\beta$, while the (α, β) elements of the Majorana mass matrix M_R would be nonzero only when $y_\alpha + y_\beta = 0$. Since the X-charges of neutrinos are non-universal and vector-like, the former condition implies that m_D is diagonal. (It can have off-diagonal elements if two of the y_α's are identical. However we can always choose the ν_R basis such that m_D is diagonal.) The allowed elements of M_R are also severely restricted, and it will not be possible to have a sufficient number of nonzero elements in M_R to be able to generate the neutrino mixing pattern.

To generate the required mixing pattern, we introduce a scalar S, which is a SM-singlet, and has an X-charge $X_S = a$, as a minimal extension of our model. With the addition of this scalar, the Lagrangian in eq. (3.2.19) modifies to

$$[\mathcal{L}_\nu^{{\rm mass},S}]_{\alpha\beta} \ = \ [\mathcal{L}_\nu^{\rm mass}]_{\alpha\beta} - \frac{1}{2}[\overline{\nu_R^c}]_\alpha [\mathcal{Y}_R]_{\alpha\beta} [\nu_R]_\beta\, S + h.c. \ . \tag{3.2.21}$$

The conditions for m_D, M_R and $\mathcal{Y}_R$ elements to be non zero are

$$[m_D]_{\alpha\beta} \ \neq \ 0 \quad \text{if} \quad y_\alpha - y_\beta = 0 \ , \tag{3.2.22}$$
$$[M_R]_{\alpha\beta} \ \neq \ 0 \quad \text{if} \quad y_\alpha + y_\beta = 0 \ ,$$
$$[\mathcal{Y}_R]_{\alpha\beta} \ \neq \ 0 \quad \text{if} \quad y_\alpha + y_\beta = \pm a \ . \tag{3.2.23}$$

When S gets a vacuum expectation value v_S, it contributes to the Majorana mass term for right handed neutrinos which now becomes

$$[M_R^S]_{\alpha\beta} = [M_R]_{\alpha\beta} + \frac{v_S}{\sqrt{2}}[y_R]_{\alpha\beta} \,. \tag{3.2.24}$$

Thus an element of $[M_R^S]_{\alpha\beta}$ will be non-zero if,

$$y_\alpha + y_\beta = 0, \pm a \,. \tag{3.2.25}$$

The textures in the neutrino mass matrix, i.e. the number and location of vanishing elements therein, hold clues to the internal flavour symmetries. Only some specific textures of M_R are allowed. While no three-zero textures are consistent with data, specific two-zero textures are allowed [104–107]. In addition, most one-zero textures [108], and naturally, all no-zero textures, are also permitted. Among the allowed textures, we identify those that can be generated by a $U(1)_X$ symmetry with a singlet scalar, i.e. those for which values of y_α and a satisfying eq. (3.2.25) may be found. These combinations are listed in table 3.3, and categorized according to the ratio y_e/y_μ. Note that by the leptonic symmetry combination $p_e L_e + p_\mu L_\mu + p_\tau L_\tau$, we refer to all $U(1)_X$ charge combinations, where $p_e/y_e = p_\mu/y_\mu = p_\tau/y_\tau$ (for non zero values y_α and p_α respectively). It is to be noted that part of the list was already derived in [106, 107]. Later in section 3.2.3, we shall examine the consistency of these symmetries with the flavour data.

Note that we would like all the elements of right handed neutrino mass matrix to have similar magnitudes, so it would be natural to have $[M_R^S]_{\alpha,\beta} \sim \mathcal{O}(v_S)$. Our scenario is thus close to a TeV-scale seesaw mechanism [109].

Relating X-charges of doublet and singlet scalars

The scalar sector of our model consists of two $SU(2)_L$ doublets Φ_1 and $\Phi \equiv \Phi_2$, and a SM-singlet S, with X-charges d, 0, a, respectively. The scalar potential that respects the $SU(2)_L \times U(1)_Y \times U(1)_X$ symmetry is

$$\begin{aligned} V_{\Phi_1\Phi_2 S} \;=\; & -m_{11}^2 \Phi_1^\dagger \Phi_1 + \frac{\lambda_1}{2}(\Phi_1^\dagger \Phi_1)^2 - m_{22}^2 \Phi_2^\dagger \Phi_2 + \frac{\lambda_2}{2}(\Phi_2^\dagger \Phi_2)^2 \\ & -m_S^2 S^\dagger S + \frac{\lambda_S}{2}(S^\dagger S)^2 + \lambda_3\, \Phi_1^\dagger \Phi_1\, \Phi_2^\dagger \Phi_2 \\ & +\lambda_4\, \Phi_1^\dagger \Phi_2\, \Phi_2^\dagger \Phi_1 + \left(\lambda_{1S_1} \Phi_1^\dagger \Phi_1 + \lambda_{2S} \Phi_2^\dagger \Phi_2\right) S^\dagger S \,. \end{aligned} \tag{3.2.26}$$

The $U(1)_X$ symmetry is broken spontaneously by the vacuum expectation values of Φ_1 and S, and consequently Z' obtains a mass (see section 2.3). Since the collider bounds indicate $M_{Z'} \gtrsim$ TeV, we expect $v_s \gtrsim$ TeV (since $v_1 \lesssim$ electroweak scale).

Therefore, before electroweak symmetry breaking, $U(1)_X$ symmetry gets broken spontaneously and the singlet, S, gets decoupled. The effective potential for the doublets after

Category	y_e/a	y_μ/a	y_τ/a	Symmetries
A	0	-1	0, 1	L_μ, $L_\mu - L_\tau$
B	$\frac{1}{2}$	$-\frac{3}{2}$	$\pm\frac{1}{2}$	$L_e - 3L_\mu \pm L_\tau$
C	$-\frac{1}{2}$	$-\frac{3}{2}$	$\frac{1}{2}$	$L_e + 3L_\mu - L_\tau$
D	$\frac{1}{2}$	$-\frac{1}{2}$	$\pm\frac{1}{2}$, $\pm\frac{3}{2}$	$L_e - L_\mu \pm L_\tau$, $L_e - L_\mu \pm 3L_\tau$
E	$\frac{1}{2}$	$\frac{1}{2}$	$-\frac{1}{2}$, $-\frac{3}{2}$	$L_e + L_\mu - L_\tau$, $L_e + L_\mu - 3L_\tau$
F	$\frac{3}{2}$	$-\frac{1}{2}$	$-\frac{1}{2}$	$3L_e - L_\mu - L_\tau$
G	1	0	0	L_e

Table 3.3: The X-charges (in units of a) along with the symmetry combinations that are consistent with the neutrino oscillation data [27, 28]. Note that by the leptonic symmetry combination $p_e L_e + p_\mu L_\mu + p_\tau L_\tau$, we refer to all $U(1)_X$ charge combinations, where $p_e/y_e = p_\mu/y_\mu = p_\tau/y_\tau$ (for non zero values y_α and p_α respectively). In the list we have dropped the cases with lepton flavour universality and the one where $y_e = y_\mu = 0$.

$U(1)_X$ symmetry breaking

$$\begin{aligned} V_{\Phi_1\Phi_2} &= -\left(m_{11}^2 - \frac{\lambda_{1S_1}}{2}v_S^2\right)\Phi_1^\dagger\Phi_1 + \frac{\lambda_1}{2}(\Phi_1^\dagger\Phi_1)^2 - \left(m_{22}^2 - \frac{\lambda_{2S}}{2}v_S^2\right)\Phi_2^\dagger\Phi_2 \\ &+\frac{\lambda_2}{2}(\Phi_2^\dagger\Phi_2)^2 + \lambda_3(\Phi_1^\dagger\Phi_1)(\Phi_2^\dagger\Phi_2) + \lambda_4(\Phi_1^\dagger\Phi_2)(\Phi_2^\dagger\Phi_1). \end{aligned} \tag{3.2.27}$$

The potential, V_{Φ_1,Φ_2}, is invariant under the global transformation $U(1)_V \times U(1)_A$ such that

$$U(1)_V \times U(1)_A: \quad \Phi_1 \to e^{i(\theta_V - \theta_A)}\Phi_1, \qquad \Phi_2 \to e^{i(\theta_V + \theta_A)}\Phi_2. \tag{3.2.28}$$

Out of $U(1)_V$ and $U(1)_A$, only $U(1)_V$ can be gauged and identified as $U(1)_Y$ since both the doublets should have the same hypercharge. After electro-weak symmetry breaking, along with the gauge symmetries, $U(1)_A$ would also be broken spontaneously and would result in a Goldstone boson. This problem would not arise if the potential were not symmetric under $U(1)_A$ to begin with, i.e. if it were broken explicitly by a term

$$\Delta V_{\Phi_1\Phi_2} = -m_{12}^2\Phi_1^\dagger\Phi_2 \, + h.c. \, . \tag{3.2.29}$$

Note that this can happen naturally in our scenario: the term above can be generated by spontaneously breaking of $U(1)_X$ if X_S is equal to X_{Φ_1}, i.e., if $a = d$, we can have

$$\Delta V_{\Phi_1\Phi_2 S} = -\widetilde{m}_{12}\left[S\,\Phi_1^\dagger\Phi_2 + S^\dagger\,\Phi_2^\dagger\Phi_1\right] , \tag{3.2.30}$$

with

$$m_{12}^2 = \frac{1}{\sqrt{2}}\widetilde{m}_{12}v_S \, . \tag{3.2.31}$$

Thus the identification $X_S = X_{\Phi_1} = a$ naturally avoids a massless scalar in our model by modifying the potential as

$$V_{\Phi_1\Phi_2 S} \to V_{\Phi_1\Phi_2 S} + \Delta V_{\Phi_1\Phi_2 S} \, . \tag{3.2.32}$$

3.2.3 Selection of the desirable symmetry combinations

In this section, we combine the $U(1)_X$ symmetries identified in section 3.2.2 with the NP contribution to $\mathcal{O}_9$ needed to account for the flavour anomalies. The Lagrangian describing the Z' interactions with d-type quarks and charged leptons is

$$\begin{aligned}\mathcal{L}_{Z'} &= g_{Z'}\,\overline{d_L}\gamma^\mu\, V_{\rm CKM}^\dagger\, \mathcal{X}_Q\, V_{\rm CKM} d_L\, Z'_\mu + g_{Z'}\,\overline{d_R}\,\gamma^\mu\, V_{d_R}^\dagger\, \mathcal{X}_Q\, V_{d_R}\, d_R\, Z'_\mu \\ &\quad + g_{Z'}\,\bar{\ell}\,\gamma^\mu\, \mathcal{X}_L\, \ell\, Z'_\mu \end{aligned} \tag{3.2.33}$$

Here $\mathcal{X}_Q = \mathrm{diag}(x_1, x_1, x_3)$ and $\mathcal{X}_L = \mathrm{diag}(y_e, y_\mu, y_\tau)$. Using the above Lagrangian, the Z' contributions to the effective Hamiltonian for $b \to s\ell\ell$ processes at $M_{Z'}$ scale is

$$\mathcal{H}_{\rm eff}^{\rm NP} = -\frac{(x_1 - x_3)\, y_\ell\, g_{Z'}^2}{M_{Z'}^2} V_{tb}V_{ts}^*\,(\overline{s_L}\gamma^\mu b_L)\left(\bar{\ell}\gamma_\mu \ell\right) + \frac{(x_1 - x_3)\, y_\ell\, g_{Z'}^2}{M_{Z'}^2}\theta_{d_{R23}}^2\,(\overline{s_R}\gamma^\mu b_R)\left(\bar{\ell}\gamma_\mu \ell\right)\ . \tag{3.2.34}$$

Comparing it with the standard definition of $\mathcal{H}_{\rm eff}$ as given in eq. (3.1.2), we obtain the NP contribution to the Wilson coefficients $C_9^{\rm NP,\ell}$ and $C_9'^{\rm NP,\ell}$ as

$$C_9^{\rm NP,\ell}(M_Z') = \frac{\sqrt{2}\pi (x_1 - x_3)\, y_\ell g_{Z'}^2}{G_F M_{Z'}^2 \alpha_e}\ ,\quad C_9'^{\rm NP,\ell}(M_Z') = -\frac{\sqrt{2}\pi (x_1 - x_3)\, y_\ell g_{Z'}^2 \theta_{d_{R23}}^2}{G_F M_{Z'}^2 \alpha_e V_{tb} V_{ts}^*}\ , \tag{3.2.35}$$

The smallness of θ_{R23}, as shown in eq (3.2.18), makes the NP contribution to $\mathcal{O}'_9$ small in comparison to the corresponding contribution to $\mathcal{O}_9$:

$$\begin{aligned} C_9'^{\ell}(M_Z') &= -\frac{\theta_{D_{R23}}^2}{V_{tb}V_{ts}^*}\, C_9^{\rm NP,\ell}(M_Z') \\ &\approx -0.025\, C_9^{\rm NP,\ell}(M_Z')\ . \end{aligned} \tag{3.2.36}$$

The flavour anomalies like R_K and P_5' depend crucially on $C_9^{\rm NP,e}$ and $C_9^{\rm NP,\mu}$, and not on $C_9^{\rm NP,\tau}$. A negative value of $C_9^{\rm NP,\mu}$ is preferred [57–61] as a solution to these anomalies which can be easily obtained if, $(x_1 - x_3)\, y_\mu < 0$. The values of $C_9^{\rm NP,e}$ and $C_9^{\rm NP,\mu}$ are related by

$$C_9^{\rm NP,e}/C_9^{\rm NP,\mu} = y_e/y_\mu\ . \tag{3.2.37}$$

This ratio stays the same at all scales between $M_{Z'}$ and m_b, since the $\mathcal{O}_9$ operator does not mix with any other operator at one loop in QCD. This ratio is represented in figure 3.1 by lines corresponding to different symmetries in table 3.3.

In figure 3.1, we also show the 1σ contours in the $C_9^{\rm NP,\mu}$–$C_9^{\rm NP,e}$ plane obtained from the global fits [59–61]. For further analysis, we select only those combinations (categories A, B, C, D) which pass through the 1σ regions of any of these global fit contours. Among these possibilities, $L_\mu - L_\tau$ has already been considered in the context of R_K [65, 66, 73, 78], where the NP contribution to C_9^e is absent. We shall explore the phenomenological consequences of these symmetries in section 3.3.

Note that although we refer to the symmetries by their lepton combinations, quarks are also charged under the $U(1)_X$. These charges can be easily obtained from the anomaly eq. (3.2.9),

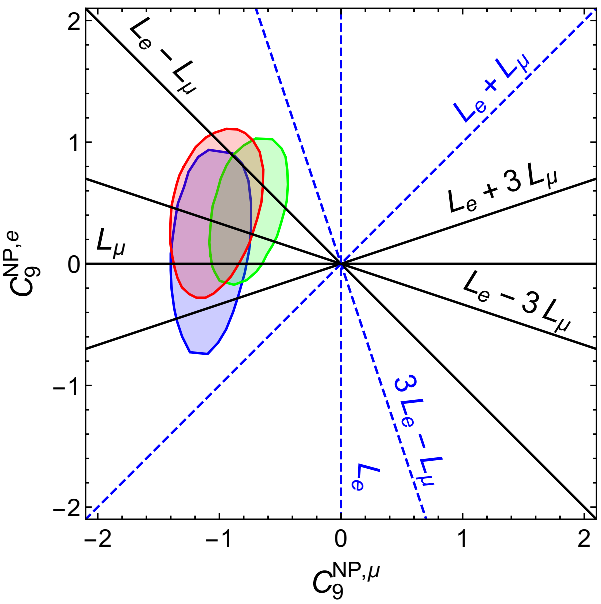

Figure 3.1: Allowed 1σ regions in $(C_9^{\mathrm{NP},e},C_9^{\mathrm{NP},\mu})$ plane using the global fit data: red contour is obtained from [59], blue from [60] and green from [61]. Lines for various $U(1)_X$ symmetries using eq. (3.2.37) have also been plotted. We do not show τ charge explicitly in the plot.

and have been given in table 3.4, in terms of the parameter a. Further, note that all the X-charges are proportional to a. As a result, a and $g_{Z'}$ always appear in the combination $ag_{Z'}$. We therefore absorb a in the definition of $g_{Z'}$:

$$g_{Z'} \to a\, g_{Z'}\ , \tag{3.2.38}$$

and consider $a = 1$ without loss of generality for our further analysis. The interactions of Z' then can be expressed in terms of two unknown parameters, $g_{Z'}$ and $M_{Z'}$. In the next section, we shall subject all the symmetry combinations in table 3.4 to tests from experimental constraints.

3.3 Experimental Constraints

Our class of models will be constrained from flavour data and direct searches at the colliders. We choose to work in the decoupling regime where the additional scalars are heavy and do not play any significant role in the phenomenology. This is easily possible by suitable choice of the parameters in eq. (3.2.32). This framework naturally induces $Z - Z'$ mixing at tree level, which can also be minimized by the choice of these parameters (section 2.3). The two parameters that are strongly constrained from the data are the mass and gauge coupling of the new vector boson, Z'. In this section, we explore the constraints on $M_{Z'}$ and $g_{Z'}$ from neutral meson mixings, rare B decays, and direct Z' searches at colliders.

Category	Symmetry/Charges	x_1/a	x_2/a	x_3/a	y_e/a	y_μ/a	y_τ/a
A	$L_\mu - L_\tau$	$\frac{1}{3}$	$\frac{1}{3}$	$-\frac{2}{3}$	0	-1	1
	L_μ	$\frac{4}{9}$	$\frac{4}{9}$	$-\frac{5}{9}$	0	-1	0
B	$L_e - 3L_\mu + L_\tau$	$\frac{7}{18}$	$\frac{7}{18}$	$-\frac{11}{18}$	$\frac{1}{2}$	$-\frac{3}{2}$	$\frac{1}{2}$
	$L_e - 3L_\mu - L_\tau$	$\frac{1}{2}$	$\frac{1}{2}$	$-\frac{1}{2}$	$\frac{1}{2}$	$-\frac{3}{2}$	$-\frac{1}{2}$
C	$L_e + 3L_\mu - L_\tau$	$\frac{1}{2}$	$\frac{1}{2}$	$-\frac{1}{2}$	$-\frac{1}{2}$	$-\frac{3}{2}$	$\frac{1}{2}$
D	$L_e - L_\mu + 3L_\tau$	$\frac{1}{6}$	$\frac{1}{6}$	$-\frac{5}{6}$	$\frac{1}{2}$	$-\frac{1}{2}$	$\frac{3}{2}$
	$L_e - L_\mu - 3L_\tau$	$\frac{1}{2}$	$\frac{1}{2}$	$-\frac{1}{2}$	$\frac{1}{2}$	$-\frac{1}{2}$	$-\frac{3}{2}$
	$L_e - L_\mu + L_\tau$	$\frac{5}{18}$	$\frac{5}{18}$	$-\frac{13}{18}$	$\frac{1}{2}$	$-\frac{1}{2}$	$\frac{1}{2}$
	$L_e - L_\mu - L_\tau$	$\frac{7}{18}$	$\frac{7}{18}$	$-\frac{11}{18}$	$\frac{1}{2}$	$-\frac{1}{2}$	$-\frac{1}{2}$

Table 3.4: Charges of the fermion fields in units of a. It can be seen that for all the allowed symmetries we have $(x_1 - x_3)\, y_\mu < 0$.

3.3.1 Constraints from neutral meson mixings and rare B decays

The FCNC couplings of Z' to d_L-type quarks (note that $V_{d_L} = V_{\rm CKM}$) will lead to neutral meson mixings as well as $b \to d$ and $b \to s$ transitions at the tree level, and hence may be expected to give significant BSM contributions to these processes.

The effective Hamiltonian in SM [110] that leads to $K - \overline{K}$, $B_d - \overline{B_d}$ and $B_s - \overline{B_s}$ mixing is

$$\begin{aligned}
\mathcal{H}_{\rm eff}^{\rm SM} &= \frac{G_F^2}{16\pi^2} M_W^2 C_K^{\rm SM}(\mu) \big[\bar{s}\gamma^\mu(1-\gamma_5)d\big]\,\big[\bar{s}\gamma_\mu(1-\gamma_5)d\big] \\
&+ \frac{G_F^2}{16\pi^2} M_W^2\,(V_{tb}V_{td}^*)^2\, C_{B_d}^{\rm SM}(\mu)\,\big[\bar{b}\gamma^\mu(1-\gamma_5)d\big]\,\big[\bar{b}\gamma_\mu(1-\gamma_5)d\big] \\
&+ \frac{G_F^2}{16\pi^2} M_W^2\,(V_{tb}V_{ts}^*)^2\, C_{B_s}^{\rm SM}(\mu)\,\big[\bar{b}\gamma^\mu(1-\gamma_5)s\big]\,\big[\bar{b}\gamma_\mu(1-\gamma_5)s\big]\ ,
\end{aligned} \tag{3.3.1}$$

where $C_P^{\rm SM}(\mu)$ are the Wilson coefficients at the scale μ for $P = K, B_d, B_s$ and the CKM factors for K–$\overline{K}$ mixing are absorbed in $C_K^{\rm SM}(\mu)$ itself.

Contributions due the Z' exchange will have the same operator form as in the SM since (i) The FCNC contributions to $\overline{d_{Ri}}\gamma^\mu d_{Rj} Z'_\mu$ operator are small as shown in eqs. (3.2.18) and (3.2.36), and (ii) we are working in the decoupling limit, where the contributions due to the exchanges of scalars H^0, A^0 and H^+ are negligible[3]. As a result, the total effective Hamiltonian can simply be written with the replacement

$$C_P^{\rm SM}(\mu) \to C_P^{\rm tot}(\mu) = C_P^{\rm SM}(\mu) + C_P^{\rm NP}(\mu)\ , \tag{3.3.2}$$

[3]The contributions due to charged Higgs are loop suppressed and the amplitude of H^0 and A^0 interferes destructively leading to vanishing contributions for the limit $\alpha - \beta \approx \frac{\pi}{2}$ and $M_{A^0} \approx M_{H^0}$.

with the Wilson coefficients $C_P^{\rm NP}$ at the $M_{Z'}$ scale given by

$$\begin{aligned} C_K^{\rm NP}(M_{Z'}) &= \frac{2\pi^2\,(x_1-x_3)^2\,g_{Z'}^2\,(V_{td}V_{ts}^*)^2}{M_{Z'}^2 G_F^2 M_W^2}\,, \\ C_{B_q}^{\rm NP}(M_{Z'}) &= \frac{2\pi^2\,(x_1-x_3)^2\,g_{Z'}^2}{M_{Z'}^2 G_F^2 M_W^2} \quad \text{where, q = d, s}\,. \end{aligned} \tag{3.3.3}$$

These Wilson coefficients at one loop in QCD run down to the M_W scale as [110]

$$C_P^{\rm NP}(M_W) = \left[\frac{\alpha_s(m_t)}{\alpha_s(M_W)}\right]^{\frac{6}{23}} \left[\frac{\alpha_s(M_{Z'})}{\alpha_s(m_t)}\right]^{\frac{2}{7}} C_P^{\rm NP}(M_{Z'})\,. \tag{3.3.4}$$

Since the form of operators corresponding to $C_P^{\rm NP}(\mu)$ and $C_P^{\rm SM}(\mu)$ is the same, the ratio $C_P^{\rm NP}(\mu)/C_P^{\rm SM}(\mu)$ stays the same for all scales below M_W. Since only this ratio is relevant for the constraints from P–$\overline{P}$ mixing, we work in terms of $C_P^{\rm NP}(M_W)/C_P^{\rm SM}(M_W)$.

The constraints from P–$\overline{P}$ measurements are generally parametrized in terms of the following quantities [111]:

$$C_{\epsilon_K} \equiv \frac{{\rm Im}\left[\langle K_0|\mathcal{H}_{\rm eff}^{\rm tot}|\bar{K_0}\rangle\right]}{{\rm Im}\left[\langle K_0|\mathcal{H}_{\rm eff}^{\rm SM}|\bar{K_0}\rangle\right]}\,, \quad C_{B_q}e^{2i\phi_{B_q}} \equiv \frac{\langle B_q|\mathcal{H}_{\rm eff}^{\rm tot}|\bar{B}_q\rangle}{\langle B_q|\mathcal{H}_{\rm eff}^{\rm SM}|\bar{B}_q\rangle}\,. \tag{3.3.5}$$

Note that the quantity $C_{\Delta m_K} \equiv {\rm Re}\left[\langle K_0|\mathcal{H}_{\rm eff}^{\rm tot}|\bar{K_0}\rangle\right]/{\rm Re}\left[\langle K_0|\mathcal{H}_{\rm eff}^{\rm SM}|\bar{K_0}\rangle\right]$ is also a relevant observable, however since it receives large long distance corrections, we do not consider it in our analysis. Since $V_{D_L} = V_{\rm CKM}$, there is no new phase contributions to $B_q - \overline{B_q}$ mixing and $\phi_{B_q} = 0$.

We combine the above measurements and show the allowed 2σ regions in the $g_{Z'}$–$M_{Z'}$ plane in figure 3.2. Note that constraints from neutral meson mixings depends on $g_{Z'}$, $M_{Z'}$ and (x_1-x_3). Since $(x_1-x_3) = a$, therefore the P–$\overline{P}$ constraints are the same in all the categories in table 3.4 (and hence for all the four panels of figure 3.2).

Figure 3.2 also shows the 2σ allowed regions that correspond to the constraints from a global fit [61] incorporating the $b \to s\ell\ell$ and $b \to s\gamma$ data. Note that these constraints have already been used in shortlisting the lepton symmetries in table 3.4, Here we find the allowed regions in the $g_{Z'}$–$M_{Z'}$ plane using eq. (3.2.35). The constraints depend on the X-charges of the electron and muon, but are independent of the charge of τ. Therefore we have displayed them in four panels, that correspond to the categories A, B, C, D, respectively.

Our model receives no constraints from $B_d \to \mu\mu$ and $B_s \to \mu\mu$ since these decays depend on $\mathcal{O}_{10}$, and our charge assignments do not introduce any NP contribution to this operator. The NP contribution will affect $b \to s\nu\nu$ decays, however the current upper limits [112] are 4-5 times larger than the SM predictions, whereas in the region that is consistent with the neutral meson mixing and global fits for the rare decays, the enhancement of this decay rate in our model is not more than 10%. We exemplify this point by working out the effect. The effective Hamiltonian for $b \to s\nu_\ell\nu_\ell$ in SM is [110, 112]

$$\mathcal{H}_{\rm eff}^{\rm SM} = -\frac{4G_F}{\sqrt{2}}\,\frac{\alpha_e}{4\pi}\,V_{tb}V_{ts}^*\,C_L^{\rm SM}\left[\overline{s_L}\gamma_\mu\,b_L\right]\left[\overline{\nu_\ell}\gamma_\mu(1-\gamma_5)\nu_\ell\right]\,, \tag{3.3.6}$$

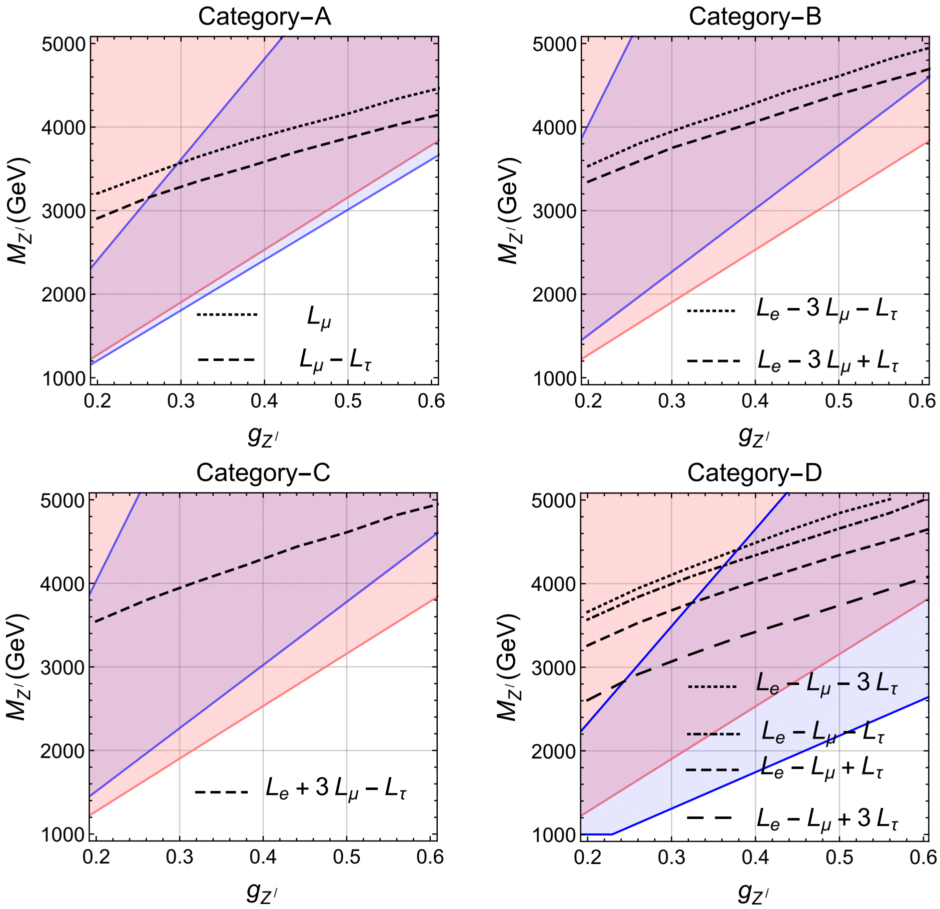

Figure 3.2: The constraints in the $g_{Z'}$ $-M_{Z'}$ plane, from neutral meson mixings, rare B decays, and collider searches for Z', for the symmetry categories in table 3.4. The 2σ regions allowed by the neutral meson mixings are shaded pink, while the 2σ regions allowed by the global fit [61] to $b \to s\ell\ell$ and $b \to s\gamma$ is shaded blue. Purple is the overlap of these two constraints. The dotted and dashed lines correspond to the collider bounds – the regions above them are allowed at 95% C. L.. The net allowed region for a given symmetry is therefore the purple region lying above the dotted / dashed line corresponding to that symmetry.

where $C_L^{\rm SM} = -X_t/s_W^2$, with $X_t = 1.469 \pm 0.017$ [112]. The Z' mediation also generates the contribution to the same operator. The combined SM and NP effect is

$$\mathcal{H}_{\rm eff}^{\rm tot} \quad = \quad -\frac{4G_F}{\sqrt{2}}\frac{\alpha}{4\pi} V_{tb}V_{ts}^* \, (C_L^{\rm SM} + C_L^{{\rm NP},\ell}) \left[\overline{s_L}\gamma_\mu \, b_L\right] \left[\overline{\nu_\ell}\gamma_\mu(1-\gamma_5)\nu_\ell\right] \,, \tag{3.3.7}$$

with $C_L^{{\rm NP},\ell} = (x_1 - x_3)\pi y_\ell g_{Z'}^2/(\sqrt{2}M_{Z'}^2 G_F \alpha_e)$ The right handed current operator contributions are small (see arguments leading to eq. (3.2.36)) and are neglected. NP can enhance the rate of an individual lepton channel $b \to s\nu_\ell\nu_\ell$ if $(x_1 - x_3)y_\ell < 0$. In experiments, the branching ratios and the decay widths corresponding to $b \to s\nu_\ell\nu_\ell$ has to summed over all the three generations of neutrinos. We consider the quantity $R_{\nu\nu}$ which gives us a measure of NP effects

$$R_{\nu\nu} = \frac{|C_L^{\rm SM} + C_L^{{\rm NP},e}|^2 + |C_L^{\rm SM} + C_L^{{\rm NP},\mu}|^2 + |C_L^{\rm SM} + C_L^{{\rm NP},\tau}|^2}{3\,|C_L^{\rm SM}|^2} \tag{3.3.8}$$

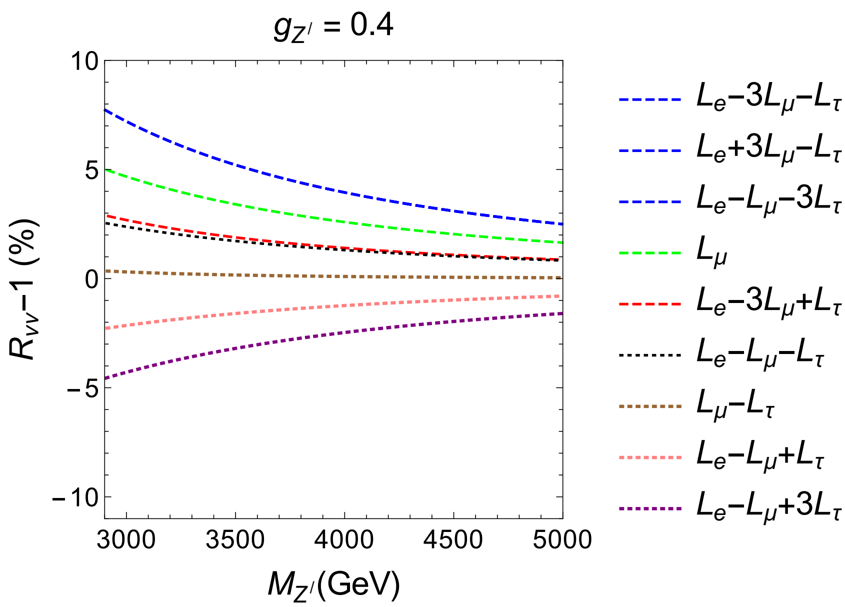

Figure 3.3: Predictions for $R_{\nu\nu}$ with different symmetries from table 3.4.

The enhancement or suppression of the branching ratio crucially depends on the combined effects of $(x_1 - x_3)y_\ell$ for the three generations.

In figure 3.3 we show the value of $R_{\nu\nu}$ as a function of $M_{Z'}$ for all the symmetries in table 3.4, where the coupling has been fixed to $g_{Z'} = 0.4$. It is observed that the net increment is not more than 10% for all symmetries. (Note that for some symmetries, the lower values of masses may not be allowed, as shown in figure 3.2, in which case the deviation would be further reduced.) The enhancement and suppression is thus too small for the current experiments to be sensitive to – The current bounds on BR($B \to K^{(*)}\nu\bar{\nu}$) are 4–5 times higher than the SM prediction [112], while Belle2 experiment is expected to reach a sensitivity close 30% from SM by 2023 [132].

3.3.2 Direct constraints from collider searches for Z'

In figure 3.2 we also show the bounds in the $g_{Z'}$–$M_{Z'}$ plane from the 95% upper limits on the $\sigma \times$ BR for the process $pp \to Z' \to \ell\ell$ [113, 114]. The bounds coming from di-jet final state [115, 116] are relatively weaker than those coming from di-leptons, hence we neglect the di-jet bounds in our analysis. The total cross-section $pp \to Z' \to \ell\ell$ depends not only on $M_{Z'}$ and g'_Z but also on the X-charges of quarks and leptons, therefore the bounds obtained differ for all the nine symmetries in table 3.4.

Note that the experimental limits in [113, 114] are given in the narrow width approximation, whereas the Z' for masses above 2 TeV has broad width for all the symmetry cases which we have considered. The constraints in the broad width case are generally weaker, therefore even lighter Z' values than those shown in the figure are allowed.

3.4 Predictions for neutrino mixing and collider signals

3.4.1 Neutrino mass ordering and CP-violating Phases

The categories A, B, C and D, in table 3.4 correspond to different texture-zero symmetries in the right-handed neutrino mass matrix M_R. Through eq. (3.2.24), these predict the light neutrino mass matrix M_ν, which can be related to the neutrino masses and mixing parameters via

$$M_\nu = -U_{\rm PMNS}\, M_\nu^{\rm diag}\, U_{\rm PMNS}^T\,, \tag{3.4.1}$$

where $U_{\rm PMNS}$ is the neutrino mixing matrix parametrized by three mixing angles θ_{12}, θ_{13}, θ_{23}, and the Dirac phase δ_{cp}. The diagonal mass matrix $M_\nu^{\rm diag} = (e^{2i\alpha_1}m_1, e^{2i\alpha_2}m_2, m_3)$ incorporates the Majorana phases α_1 and α_2, in addition to the magnitudes of the masses, m_1, m_2 and m_3. Since the symmetries restrict the form of M_R, they are expected to restrict the possible values of neutrino mixing parameters. While the neutrino mixing angles are reasonable well-measured, the values of unknown parameters like α_1, α_2 and $\delta_{\rm CP}$ may be restricted in each of the scenario. In addition, whether the neutrino mass ordering is normal ($m_2^2 < m_3^2$) or inverted ($m_2^2 > m_3^2$) is also an open question, and some of the symmetries may have strong preference for one or the other ordering. The symmetries in table 3.4 that yield two-zero textures for M_R, viz. $L_\mu - L_\tau$, $L_e - 3L_\mu - L_\tau$, $L_e + 3L_\mu - L_\tau$ and $L_e - L_\mu \pm 3L_\tau$ have already been explored in this context and the allowed parameter values determined [66, 104–106, 117].

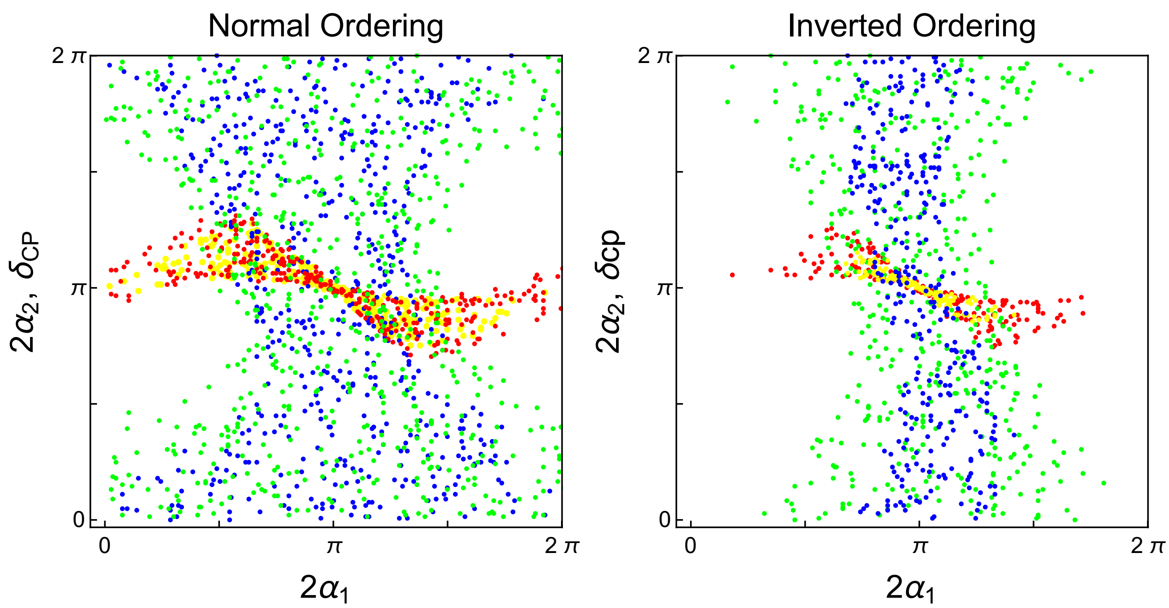

Figure 3.4: The scatter plots of allowed values of the CP phases α_2 and $\delta_{\rm CP}$ with the those of α_1. The left (right) panel shows the results for normal (inverted) mass ordering. The yellow (red) points correspond to $(2\alpha_1, 2\alpha_2)$ values for $m_{\rm light} = 0.05(0.2)$ eV, while the blue (green) points correspond to $(2\alpha_1, \delta_{\rm CP})$ values for $m_{\rm light} = 0.05(0.2)$ eV.

We exemplify the point in the context of the symmetries that yield one-zero texture for M_R, viz. L_μ and $L_e - 3L_\mu + L_\tau$. These two also happen to be the ones that are consistent with all the global fits [58–61] to the $b \to s\ell\ell$ and $b \to s\gamma$ data to within 1σ. Both of these symmetries lead to $[M_R]_{22} = 0$. Equation (3.2.24) then leads to the condition of one vanishing minor in the M_ν mass matrix [118], i.e. $[M_\nu]_{11}[M_\nu]_{33} - [M_\nu]_{13}^2 = 0$. In terms of masses and elements of the $U_{\rm PMNS}$ matrix,

$$\begin{aligned}(U_{13}U_{32} - U_{12}U_{33})^2\, m_2 m_3 e^{2i\alpha_2} \quad = \quad & -(U_{12}U_{31} - U_{11}U_{32})^2\, m_1 m_2 e^{2i(\alpha_1+\alpha_2)} \\ & -(U_{13}U_{31} - U_{11}U_{33})^2\, m_1 m_3 e^{2i\alpha_1}\ , \end{aligned} \tag{3.4.2}$$

where U_{ij} are elements of the $U_{\rm PMNS}$ matrix. Requiring the neutrino masses and mixings to satisfy the above relation, we show the allowed values of the CP-violating phases α_1, α_2 and $\delta_{\rm CP}$ in figure 3.4, for two fixed values of the lightest neutrino mass $m_{\rm light}$ (i.e. m_1 for normal ordering and m_3 for inverted ordering). We let the other neutrino parameters (mixing angles and mass squared differences) to vary within their 3σ ranges [27, 28]. The figure shows that the allowed value of α_2 with the L_μ or $L_e - 3L_\mu + L_\tau$ symmetry is restricted to be rather close to $\pi/2$. For lower $m_{\rm light}$ values, α_2 is more severely restricted and for inverted ordering, the value of α_1 also is restricted to be close to $\pi/2$.

Another set of predictions may be obtained by relating the lightest neutrino mass $m_{\rm light}$ to the effective mass measured by the neutrinoless double beta decay experiments [119] if the neutrinos are Majorana, i.e.

$$\langle m_{ee}\rangle = \left| m_1 e^{2i\alpha_1}\cos^2\theta_{12}\cos^2\theta_{13} + m_2 e^{2i\alpha_2}\sin^2\theta_{12}\cos^2\theta_{13} + m_3 e^{-2i\delta_{\rm CP}}\sin^2\theta_{13}\right| \ . \tag{3.4.3}$$

We show the allowed region (with mixing angles and mass squared differences varied within their 3σ ranges [27, 28]) in the $m_{\rm light}$–$\langle m_{ee}\rangle$ plane in figure 3.5. Bounds from the non-observation of neutrinoless double beta decay [119] and conservative limits coming from cosmology ($\sum m_\nu < 0.6$ eV) [120] have also been shown. The figure shows that the symmetries L_μ or $L_e - 3L_\mu + L_\tau$ restrict the allowed values of $m_{\rm light}$ and $\langle m_{ee}\rangle$ significantly in the case of inverted ordering: $m_{\rm light} \gtrsim 0.045$ eV and $\langle m_{ee}\rangle \gtrsim 0.055$ eV. With the cosmological bounds on the sum of neutrino masses becoming stronger, the inverted hierarchy in these scenarios would get strongly disfavoured.

The symmetries in table 3.4 that do not lead to a zero-texture in M_R, i.e. $L_e - L_\mu \pm L_\tau$, will not give any predictions for the neutrino mass ordering or CP-violating phases; model parameters can always be tuned to satisfy the data.

3.4.2 Prospects of detecting Z' at the LHC

In our model apart from Z', there are additional scalars and three heavy majorana neutrinos. Note that the parameters in our model have been chosen such that we are in the decoupling limit, i.e. the additional scalars $H, A, H^\pm, S$ are too heavy to affect any predictions in the model. The three right handed neutrinos in our model have masses of the order of a TeV and

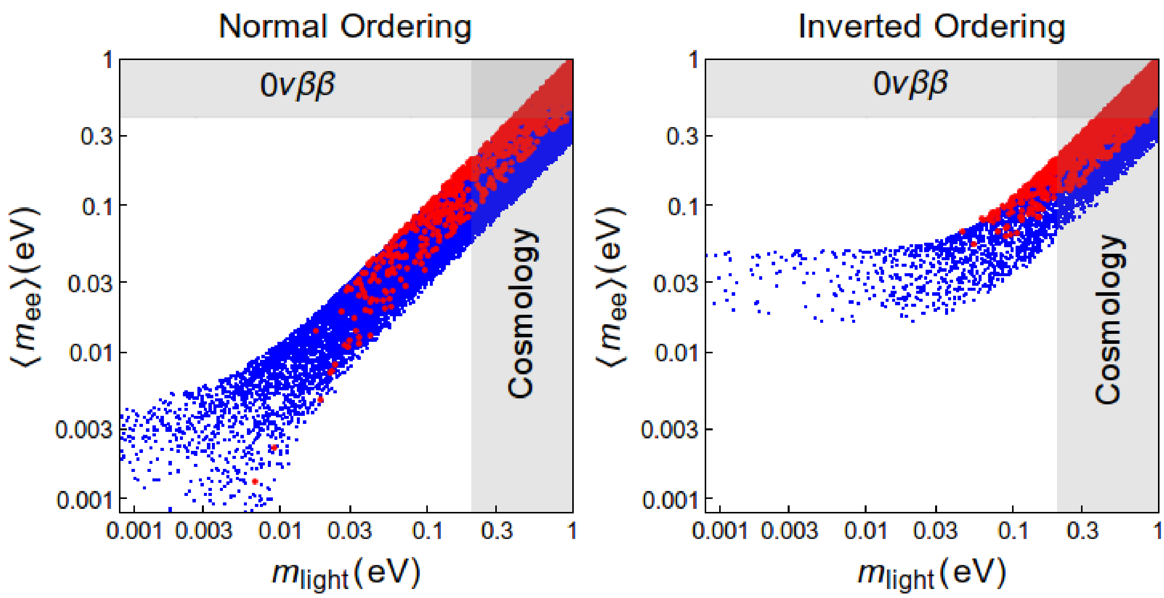

Figure 3.5: The scatter plots of allowed values of m_{light} and $\langle m_{ee}\rangle$. The red (blue) points correspond to the allowed values with (without) the symmetry (L_μ or $L_e - 3L_\mu + L_\tau$). The left (right) panel shows the results for normal (inverted) mass ordering. The regions disallowed by the non-observations of neutrinoless double beta decay ($0\nu\beta\beta$) and cosmological constraints have also been shown.

hence can be looked at the collider-based experiments. The recent analyses for the detection of the heavy right handed neutrinos can be found in [121]. We however choose $M_R \gtrsim M_{Z'}/2$, hence do not consider the phenomenology of the right handed neutrinos.

We shall now explore the possibility of a direct detection of the Z' gauge boson in the 13 TeV LHC run. The cleanest probe for this search is $pp \to Z' \to \ell\ell$ [113, 114]. In such a search, one looks for a peak in the invariant mass spectrum of the dilepton pair.

As an example, we choose the $L_e - 3L_\mu + L_\tau$ symmetry. We use `FeynRules` [122] to generate the model files and then interface the `Madgraph` [123] output of the model with `PYTHIA 6.4` [124] for showering and hadronisation with parton distribution function `CTEQ-6` [125]. The output is then fed into `Delphes 3.3` [126,127] which gives the output in the `ROOT` [128] format for a semi-realistic detector simulation while using the default ATLAS card. In our detector analysis jets are constructed from particle flow algorithm using the anti-k_T jet algorithm with $R = 0.5$ and $p_T^{\text{min}} = 50$ GeV. We retain events only with a pair of isolated opposite-sign muons with highest p_T in each event. Care has been taken to reject any isolated electron in the event sample. A rough p_T cut on the muons is set at $p_T^\mu > 25$ GeV which roughly matches the ATLAS cuts [113]. The dominant SM background for this di-muon channel comes from the Drell-Yann process. Other factors contributing to the SM background are diboson and top quarks in the final state. In the left panel of figure 3.6 we show the dimuon invariant mass distribution of the SM backgrounds as well as the signal for a fixed benchmark scenario satisfying all the flavour and collider constraints (see figure 3.2) with $M_{Z'} = 4$ TeV and

$g_{Z'} = 0.36$. Although the production cross section for such a heavy Z' gauge boson is small, close to 1.49 fb, the SM background is also minuscule in that regime. Therefore, the $Z' \to \mu\mu$ is a natural probe to look for BSM signals. We note in passing that a Z' associated with a hard jet in the final state should increase the signal significance further [129]. However, we only select events with opposite sign di-muon pair and a hard jet veto.

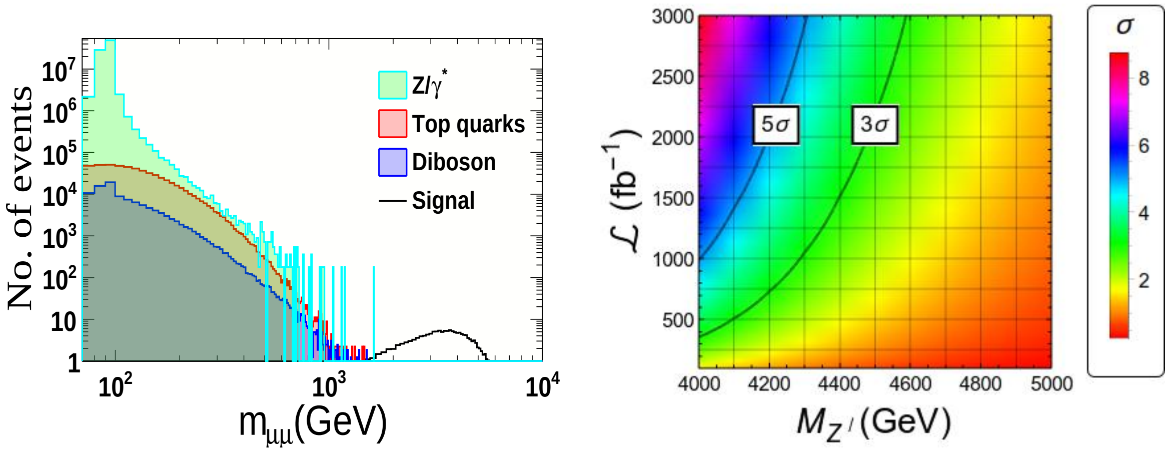

Figure 3.6: The left panel shows the dimuon invariant mass distribution for the signal originating from Z' (with $M_{Z'} = 4$ TeV and $g_{Z'} = 0.36$) and the various SM backgrounds at 13 TeV, with $\mathcal{L} = 100\,\text{fb}^{-1}$. The right panel shows the discovery significance $S/\sqrt{S+B}$ as a function of $M_{Z'}$ (with $g_{Z'} = 0.36$) and integrated luminosity. The 5 σ and 3 σ contours are also shown explicitly.

To further calculate the reach of the LHC for the Z' discovery via $Z' \to \mu\mu$, we use a signal specific cut on the dimuon invariant mass $m_{\mu\mu} > 700$ GeV which renders all the SM backgrounds to be very small whereas the signal hardly gets affected. We keep the coupling $g_{Z'}$ fixed at 0.36, and illustrate in the right panel of figure 3.6, the reach of the LHC in the $M_{Z'}$– integrated luminosity ($\mathcal{L}$) plane, in the form of a density plot of the significance $S/\sqrt{S+B}$ [130]. (Here S, B are the number of signal and background events after the cut, respectively.) The figure indicates that detecting a Z' of mass 4000 GeV at 3 σ (5 σ) significance requires an integrated luminosity close to 400 fb^{-1} (1000 fb^{-1}) in the 13 TeV run of the LHC.

3.5 Summary and concluding remarks

In this chapter, we have looked for a class of models with an additional possible $U(1)_X$ symmetry that can explain the flavour anomalies (R_K and P_5') and neutrino mixing pattern. The models are built around the phenomenological choice where NP effects are dominant only in the $\mathcal{O}_9$ operator, as indicated by the global fits to the $b \to s$ data. One salient feature of our analysis is that the assignment of X-charges of fields is done in a bottom-up approach. I.e., we do not start with a pre-visioned symmetry, but look for symmetry combinations consistent with both the flavour data and neutrino mixing.

In order to generate neutrino masses through the Type-I seesaw mechanism, we add three right-handed neutrinos to the SM field content. This also allows us to assign vector-like X-charges to the SM fermions, so that the anomaly cancellation can be easily achieved. This choice also makes NP contributions to $\mathcal{O}_{10}$ and $\mathcal{O}'_{10}$ vanish. While the different X-charge assignments to the SM generations introduce the desired element of lepton flavour non-universality at tree level, it also introduces the problem of generating mixings in both quark and lepton sector. This is alleviated by adding an additional doublet Higgs Φ_1 that generates the required quark mixing, and a scalar S that generates lepton mixing. The choice of rotation matrices $V_{u_L} = V_{u_R} = 1$, $V_{d_L} = V_{\rm CKM}$ and $V_{d_R} \approx 1$ also ensures that the NP contribution to $\mathcal{O}'_9$ is negligible. The scalar S also helps in avoiding the possible problem of a Goldstone boson appearing from the breaking of a symmetry in the doublet Higgs sector.

Our model is thus rather parsimonious, with the introduction of only the two additional scalar fields Φ_1 and S. The symmetry breaking due to the vacuum expectation values of these scalars gives mass to the new gauge boson Z', at the same time keeping its mixing with the SM Z boson under control.

With the X-charges of quark and lepton generations connected through anomaly cancellation, the X-charge assignments may be referred to in terms of the corresponding symmetries in the lepton sector. We identify those leptonic symmetries that would give rise to the required structure in the neutrino mass matrix, at the same time are consistent with the global fits to the $b \to s$ data. We find nine such symmetries, viz. $L_\mu - L_\tau$, L_μ, $L_e - 3L_\mu \pm L_\tau$, $L_e + 3L_\mu - L_\tau$, $L_e - L_\mu \pm 3L_\tau$, and $L_e - L_\mu \pm L_\tau$. We find the allowed regions in the $g_{Z'}$–$M_{Z'}$ parameter space that satisfy the bounds from neutral meson mixings, rare B decays, and direct Z' collider searches.

The lepton symmetries give rise to specific textures in the right-handed neutrino mass matrix M_R, and hence, through seesaw, to patterns in the light neutrino mass matrix. The consequent neutrino masses and mixing parameters are hence restricted by these symmetries. In order to exemplify this, we have focussed on the symmetries L_μ and $L_e - 3L_\mu + L_\tau$ that give rise to one zero-texture in M_R, and are also the most favoured symmetries according to all the $b \to s$ global fits. We have analyzed the correlations among the CP-violating phases $\alpha_1, \alpha_2, \delta_{\rm CP}$, and also explored the allowed region in the parameter space of the lightest neutrino mass $m_{\rm light}$ and the effective neutrino mass $\langle m_{ee} \rangle$ measured in the neutrinoless double beta decay. For $L_e - 3L_\mu + L_\tau$, we also calculate the reach of the LHC for direct detection of Z' through the di-muon channel. We find that discovery of Z' with the required mass and gauge coupling is possible with a few hundred fb^{-1} integrated luminosity at the 13 TeV run.

Note that the parameters in our minimal model have been chosen such that we are in the decoupling limit, i.e. the additional scalars $H, A, H^\pm, S$, and the three right-handed neutrinos are too heavy to affect any predictions in the model. Our model thus does not try to account for the flavour anomalies indicated in the semileptonic $b \to c$ decays [131]. These anomalies may be addressed in the extensions of this minimal model to include non-decoupling scenarios (for example, where the charged Higgs is light), or additional charged $W'^\pm$ gauge bosons.

While the former scenario needs to satisfy additional constraints from flavour and collider data, the latter will need mechanisms for giving masses to the new gauge bosons.

In this chapter we have presented a class of symmetries that are consistent with the current data, and not applied any aesthetic biases among them. As more data come along, some of these symmetries are sure to be further chosen or discarded. We have chosen the symmetries in the bottom-up approach, and have not tried to explore their possible origins. A curious pattern applicable for some of the symmetries (L_μ, $L_e - 3L_\mu + L_\tau$ and $L_e - L_\mu + L_\tau$) is that the non-universality of X-charges is displayed only by the third generation quarks and the second generation leptons. Such patterns may provide further hints in the search for the more fundamental theory governing the mass generation of quarks and leptons.

3.6 Afterword

In this section, we comment on the implications of including R_{K^*} measurements and on the possibility of having simultaneous solutions of R_K and R_{K^*}. In previous sections, we had seen that most favourable solution explaining the $b \to s$ anomalies was

$$C_9^{\mathrm{NP},\mu} \approx -1 \, , C_9^{\mathrm{NP},e} \approx 0 \, . \tag{3.6.1}$$

This same solution, however, is unable to explain R_{K^*} measurement in low q^2 bin. To see this, let us note the expressions of R_K and R_{K^*} measurements in detail [44,133].

$$R_K = \frac{\int_{q^2_{\min}}^{q^2_{\max}} dq^2 \dfrac{d\Gamma(B \to K\mu\mu)}{dq^2}}{\int_{q^2_{\min}}^{q^2_{\max}} dq^2 \dfrac{d\Gamma(B \to Kee)}{dq^2}} \, , \qquad R_{K^*} = \frac{\int_{q^2_{\min}}^{q^2_{\max}} dq^2 \dfrac{d\Gamma_{(0+\perp)}(B \to K^*\mu\mu)}{dq^2}}{\int_{q^2_{\min}}^{q^2_{\max}} dq^2 \dfrac{d\Gamma_{(0+\perp)}(B \to K^*ee)}{dq^2}} \tag{3.6.2}$$

where,

$$\begin{aligned}
\frac{d\Gamma(B \to K\ell\ell)}{dq^2} &\propto \left(|C_{10}^\ell + C_{10}^{\ell\prime}|^2 + \left| C_9^\ell + C_9^{\ell\prime} + \frac{2m_b}{m_b + m_K} C_7 \frac{f_T(q^2)}{f_+(q^2)} \right|^2 \right) \\
\frac{d\Gamma_0(B \to K^*\ell\ell)}{dq^2} &\propto \left(|C_{10}^\ell - C_{10}^{\ell\prime}|^2 + \left| C_9^\ell - C_9^{\ell\prime} + \frac{2m_b}{m_B} C_7 \frac{T_0(q^2)}{V_0(q^2)} \right|^2 \right) \\
\frac{d\Gamma_\perp(B \to K^*\ell\ell)}{dq^2} &\propto \left(|C_{10}^\ell|^2 + |C_{10}^{\ell,\prime}|^2 + |C_9^{\ell\prime}|^2 + \left| C_9^\ell + \frac{2m_b m_B}{q^2} C_7 \frac{T_-(q^2)}{V_-(q^2)} \right|^2 \right)
\end{aligned} \tag{3.6.3}$$

Observing the above equations, it is certain that if we introduce a NP contribution in C_9^μ, i.e. $C_9^{\mu,\mathrm{NP}}$, then the observables R_K and R_{K^*} will have values lesser than their SM expectation. However, due to photon pole enhancement of R_{K^*} in the low q^2 bin, large negative values of C_9^μ (much larger than -1) will be required. Such large values are undesirable for R_K measurement as they push its value outside the 2-σ range.

To analyze the plausibility of simultaneous solutions, say within 1-σ of the experimental deviation, we plot $\sigma = \dfrac{(R_H^{\text{theory}} - R_H^{\text{measured}})}{\sigma^{\text{exp}}}$ for different values of $C_9^{\mu,\text{NP}}$ in fig. 3.7. Here $R_H = R_K$ or R_{K^*}. Note that $\sigma = 0$ in the plot implies that the theoretically predicted value of R_K or R_{K^*} exactly matches the measured value at the experiment. Clearly simultaneous solutions does not exist between R_K and R_{K^*} (both) as there is no-overlap within 1-σ. However, if we ignore R_{K^*} measurement in the low q^2, then simultaneous solution is possible between R_K and central q^2 bin measurement of R_{K^*} anomaly.

Note that although we have examined only a particular case of new physics but the result is generic and holds for all the symmetries. There is no neat simultaneous explanation of R_K and R_{K^*} anomaly possible, if the effects of both the bins in R_{K^*} measurement are included.

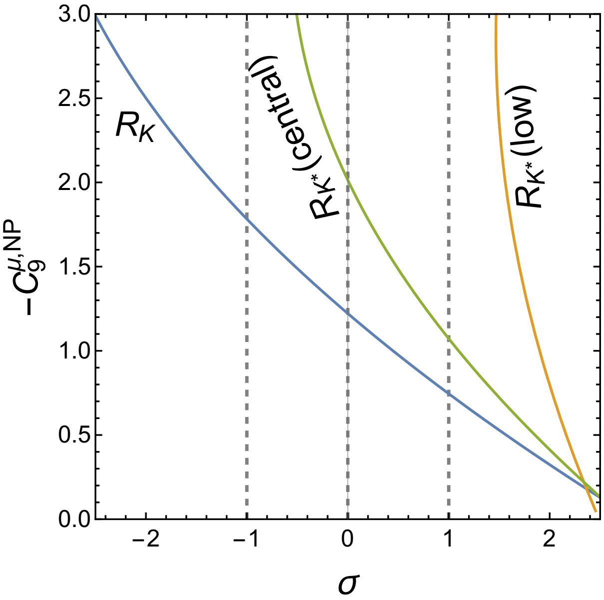

Figure 3.7: A plot in the plane of (σ, C_9^{μ}) to check the possibility of simultaneous explanations of R_K and R_{K^*} measurements.

Many papers after the announcement of R_{K^*} measurement either discarded low q^2 bin solution or predicted light mass particles, which could in principle explain low q^2 solutions, see for example [134, 135]. However in the current situation, both approaches look contrived and it is perhaps better for us to wait for next results.

Chapter 4

Pinning down the anomalous triple gauge boson couplings at the LHC

This chapter deals with the analysis concerning the presence of NP interactions in triple gauge boson couplings. The work has been done in collaboration with Dr. Ushoshi Maitra and Prof. Sreerup Raychaudhuri and is there on Phys. Rev. D **99**, no. 9, 095017 (2019).

4.1 Introduction

In chapter 2, we discussed effective field theory in detail. The broad picture of effective field theories in bottom-up approach is perhaps not the best approach to probe of physics beyond the SM because of presence of large number of operators consistent with the symmetries. The focus in recent times has been, therefore, on a more minute examination of the operators, and on measurables which depend significantly on only a limited set of these operators, rather than the whole set – an exercise which goes under the misnomer of *simplified models* – though it is the examination rather than the model which is simplified. Perhaps one of the earliest of these focussed examinations has been that of *anomalous* triple gauge-boson couplings (TGCs) [139, 140], which started from the days of the LEP collider [141] and have acquired new relevance in the present climate [142–144]. These are anomalous, of course, only in the sense of being absent in the SM at tree level. The TGC's which have been considered are possible modifications to the $W^+W^-\gamma$ and W^+W^-Z vertices, and possible new $ZZ\gamma$, $Z\gamma\gamma$ and ZZZ vertices [145].

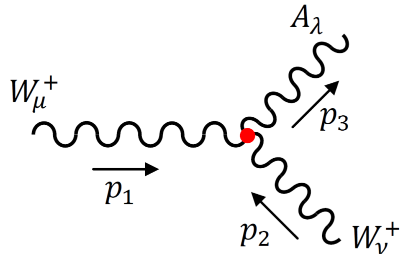

This chapter takes precisely one of these vertices, viz, the $W^+W^-\gamma$ vertex illustrated on the left and considers a specific final state which is affected by only changes to this vertex. The process in question is

$$p + p \to W^\pm + \gamma$$

where the $W^\pm \to \ell^\pm \nu_\ell(\bar{\nu}_\ell)$ for $\ell = e, \mu$ and perhaps τ.

If we denote the $W^+_\mu W^-_\nu A_\lambda$ vertex by $i\Gamma^{(WW\gamma)}_{\mu\nu\lambda}$, then the most general CP-conserving form consistent with the gauge and Lorentz symmetries of the SM can be parametrised [139] in the form of three separate terms, viz.

$$i\Gamma^{WW\gamma}_{\mu\nu\lambda}(p_1,p_2,p_3) = ie\left[T^{(0)}_{\mu\nu\lambda}(p_1,p_2,p_3) + \Delta\kappa_\gamma T^{(1)}_{\mu\nu\lambda}(p_1,p_2,p_3) + \frac{\lambda_\gamma}{M_W^2}T^{(2)}_{\mu\nu\lambda}(p_1,p_2,p_3)\right] \tag{4.1.1}$$

where the $T_{\mu\nu\lambda}$ tensors are, respectively,

$$\begin{aligned} T^{(0)}_{\mu\nu\lambda} &= g_{\mu\nu}\left(p_1-p_2\right)_\lambda + g_{\nu\lambda}\left(p_2-p_3\right)_\mu + g_{\lambda\mu}\left(p_3-p_1\right)_\nu \\ T^{(1)}_{\mu\nu\lambda} &= g_{\mu\lambda}p_{3\nu} - g_{\nu\lambda}p_{3\mu} \\ T^{(2)}_{\mu\nu\lambda} &= p_{1\lambda}p_{2\mu}p_{3\nu} - p_{1\nu}p_{2\lambda}p_{3\mu} - g_{\mu\nu}\left(p_2\cdot p_3\ p_{1\lambda} - p_3\cdot p_1\ p_{2\lambda}\right) \\ &- g_{\nu\lambda}\left(p_3\cdot p_1\ p_{2\mu} - p_1\cdot p_2\ p_{3\mu}\right) - g_{\mu\lambda}\left(p_1\cdot p_2\ p_{3\nu} - p_2\cdot p_3\ p_{1\nu}\right) \end{aligned} \tag{4.1.2}$$

The tensor $T^{(0)}_{\mu\nu\lambda}$ in Eq. (4.1.3) corresponds to the Standard Model coupling, while the tensors $T^{(1)}_{\mu\nu\lambda}$ and $T^{(2)}_{\mu\nu\lambda}$ give rise to *anomalous* TGC's. It may be noted that the dimension-4 tensor $T^{(1)}_{\mu\nu\lambda}$ can be absorbed in $T^{(0)}_{\mu\nu\lambda}$ with a coefficient $\kappa_\gamma = 1 + \Delta\kappa_\gamma$. However, in our work we have kept these tensors distinct as representing the SM and beyond-SM parts. Thus $\Delta\kappa_\gamma$ and λ_γ parametrise the beyond-SM contributions — which agrees with the common usage by most experimental collaborations[1]. It is reasonable to assume that $\Delta\kappa_\gamma$ will not be more than a few percent, for otherwise these corrections would have been detected when the W itself was discovered. It is also traditional to parametrise the mass-suppression of the dimension-6 operator $T^{(2)}_{\mu\nu\lambda}$ with a factor M_W^{-2}. If the operator arises from new physics at a scale Λ, the corresponding coefficient should have been ξ/Λ^2, and hence, we can identify

$$\lambda_\gamma = \xi\left(\frac{M_W}{\Lambda}\right)^2 \tag{4.1.3}$$

Setting $\xi = 1$, and $\Lambda = 1$ TeV, we get $\lambda_\gamma \simeq 0.0065$. We may thus expect λ_γ to lie an order of magnitude below $\Delta\kappa_\gamma$, and, in fact, we shall see below that this is indeed true for the experimental constraints.

We remark in passing that there are also CP-violating contributions to the $W^+W^-\gamma$ vertex, which can be parametrised in terms of two coupling constants $\tilde{\kappa}_\gamma$ and $\tilde{\lambda}_\gamma$. However, these are constrained to be very small from the measurement of the electric dipole moment of the neutron [150], and hence we will not consider them further in this chapter. It is also possible – in fact, plausible – that if the photon has anomalous couplings with a W^+W^- pair, then the Z boson may also have such anomalous couplings, which may be related in some way by the gauge invariance of the SM [139]. However, the philosophy adopted in this chapter is that these will not affect the measurement in question, and can therefore, be kept outside the scope of the discussion.

[1]Strictly speaking, there are SM contributions to $\Delta\kappa_\gamma$ and λ_γ at higher orders. For example, at the one-loop level, there could be contributions of the order of (few)$\times 10^{-4}$ at a centre-of-mass energy of TeV strength [146]. These are negligible in the current experimental studies, which, till date, only put constraints at the level of 10^{-2}.

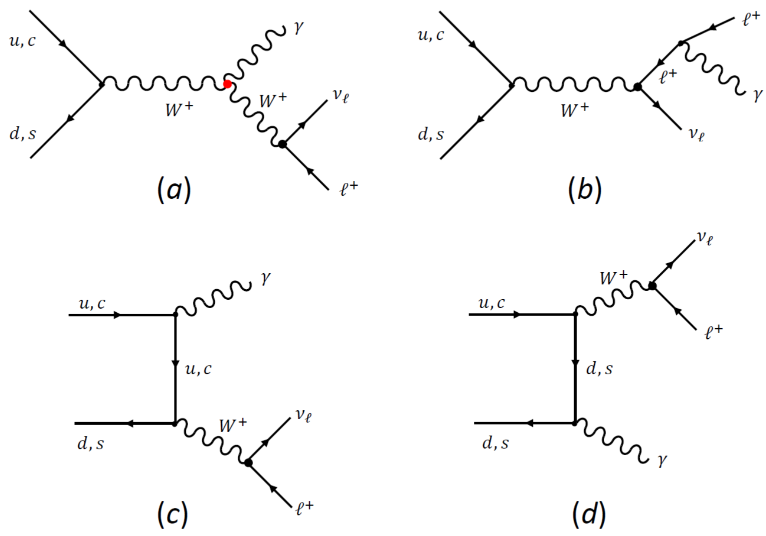

Figure 4.1: Feynman diagrams contributing to the final state $\gamma\ell^+\nu_\ell$ at a hadron collider, with initial $u\bar{d}$ (or the more suppressed $c\bar{s}$) partonic states. These diagrams correspond to both the signal and the background, since the $W^+W^-\gamma$ vertex, indicated by the red dot in diagram (a), has both SM and anomalous contributions.

4.2 Collider Analysis

The production of a $W^\pm$ associated with a hard transverse photon is one of the most standard processes which one considers at a hadron collider [153, 154]. It occurs through a pair of dissimilar quarks, e.g. u and d, as the initial-state partons, which are required for single W boson production. A photon can then be radiated off any of the internal or external legs of the corresponding diagram. However, if we allow the $W^\pm$ to decay further into a charged lepton $\ell^\pm$ and the corresponding neutrino ν_ℓ, we will have one more diagram where a photon is radiated off the charged lepton. The final state consists, then, of a photon, a lepton and missing energy from the neutrino. One would also require a jet veto to keep the process hadronically quiet. The four diagrams at leading order are illustrated in Fig. 4.1.

When these diagrams are evaluated, the Feynman amplitude can be written

$$\mathcal{M}(\Delta\kappa_\gamma, \lambda_\gamma) = \mathcal{M}_{\rm SM} + \Delta\kappa_\gamma \mathcal{M}_\kappa + \lambda_\gamma \mathcal{M}_\lambda \tag{4.2.1}$$

squaring which, it follows that the cross-section will be a combination of terms

$$\begin{aligned} \sigma(\Delta\kappa_\gamma, \lambda_\gamma) \quad &= \quad \sigma_{\rm SM} + \left(\Delta\kappa_\gamma\right)^2 \sigma_\kappa + \lambda_\gamma^2 \sigma_\lambda \\ &\quad\quad + \Delta\kappa_\gamma \sigma_{\kappa,{\rm SM}} + \lambda_\gamma \sigma_{\lambda,{\rm SM}} + \Delta\kappa_\gamma \lambda_\gamma \sigma_{\kappa,\lambda} \end{aligned} \tag{4.2.2}$$

where the terms on the first line of Eq. (4.2.2) arise from the squares of the corresponding terms in Eq. (4.2.1), while the terms on the second line are the respective interference terms. Since $\Delta\kappa_\gamma$ and λ_γ are small, it is clear that $\sigma_{\rm SM}$ will be the dominant term – or dominant background – while the other terms in Eq. (4.2.2) will constitute a small signal. Of these, the terms linear in $\Delta\kappa_\gamma$ and λ_γ will generally be the largest. The challenge is, therefore, to isolate the extremely small signal from the large SM background by the judicious use of kinematic cuts and distributions. At this point, we note that QCD corrections to the $W\gamma$ process may increase [155] the overall cross-section by $30-40\%$. However, these may be expected to be rather similar for both signal and background, and hence are not taken into account in our analysis.

In the experimental situation, our concern is with a hadronically-quiet final state consisting of a hard transverse photon, a hard transverse lepton and substantial missing energy. This is a very clean signal and, barring issues like pileup and multiple interactions at the LHC, may be expected to constitute a strong probe for the underlying physics – in this case, the TGC concerned. Since the final state is so simple, there exists only a small number of kinematic variables which are invariant under longitudinal boosts, and these, together with the cuts we have imposed on them, are listed below.

(A) The magnitude of the transverse momentum of the photon ($p_{T\gamma}$), which we require to satisfy $p_{T\gamma} \geq 60$ GeV.

(B) The pseudorapidity of the photon (η_γ), which we require to satisfy $\eta_\gamma \leq 2.5$.

(C) The magnitude of the transverse momentum of the lepton ($p_{T\ell}$), which we require to satisfy $p_{T\ell} \geq 40$ GeV.

(D) The pseudorapidity of the lepton (η_ℓ), which we require to satisfy $\eta_\ell \leq 2.5$.

(E) The magnitude of the missing transverse momentum ($\not{p}_T$), which we require to satisfy $\not{p}_T \geq 40$ GeV.

(F) The so-called angular separation between photon and lepton ($\Delta R_{\gamma\ell}$), which we require to satisfy $\Delta R_{\gamma\ell} \geq 0.4$.

The cuts in (A) – (E) are driven more by ease of identification of the final state and the detector coverage, while (F) is included to suppress the collinear photons which are preferred by the SM diagram in Fig 4.1(b).

In addition to the above, if we consider the vector momenta in the transverse plane, which we denote $\vec{p}_{T\gamma}$, $\vec{p}_{T\ell}$ and $\vec{\not{p}}_T$, we can construct three more variables which are invariant under longitudinal boosts. These are

$$\Delta\varphi_{\gamma\ell} = \cos^{-1}\left(\frac{\vec{p}_{T\gamma}\cdot\vec{p}_{T\ell}}{p_{T\gamma}\;p_{T\ell}}\right) \qquad \Delta\varphi_{\gamma\not{p}_T} = \cos^{-1}\left(\frac{\vec{p}_{T\gamma}\cdot\vec{\not{p}}_T}{p_{T\gamma}\;\;\not{p}_T}\right) \qquad \Delta\varphi_{\ell\not{p}_T} = \cos^{-1}\left(\frac{\vec{p}_{T\ell}\cdot\vec{\not{p}}_T}{p_{T\ell}\;\;\not{p}_T}\right) \tag{4.2.3}$$

These angular variables are known to be highly sensitive to momentum-dependent operators [142] and since the tensors $T^{(1,2)}_{\mu\nu\lambda}$ are of this kind, we may expect them to carry some signs of the anomalous TGCs. In fact, we find that the only variables which are sensitive to these are the transverse momenta in (A), (C) and (E) above, and these angular variables in Eq. (4.2.3).

Finally, to ensure good convergence of our Monte Carlo simulations, we construct [153, 154]

Cut	σ_{SM}	σ_κ	σ_λ
$p_{T\gamma} \geq 60$ GeV	430.11 fb	737.82 fb	41.89 pb
$p_{T\gamma} \geq 60$ GeV	100.0 %	100.0 %	100.0 %
$p_{T\ell} \geq 40$ GeV	70.25 %	75.70 %	85.55 %
$\not{p}_T \geq 40$ GeV	22.82 %	52.34 %	70.77 %
$M_{TW} \geq 30$ GeV	20.68 %	43.13 %	55.11 %
$\eta_\gamma \leq 2.5$	15.89 %	36.88 %	53.50 %
$\eta_\ell \leq 2.5$	12.28 %	32.61 %	52.24 %
$\Delta R_{\gamma\ell} \geq 0.4$	11.30 %	32.60 %	52.26 %
	48.57 fb	240.52 fb	21.89 pb

Table 4.1: Cut flow table showing the effect of different kinematic cuts on the principal terms in the cross-section. As may be expected, the SM contribution is brought down to about one tenth, whereas the others are reduced to roughly a third and a fifth respectively. The large value of σ_λ is due to the inappropriate choice of M_W^2 as the suppression factor — if we had chosen $\Lambda = 1$ TeV instead, these cross-sections would be suppressed by a factor $(M_W/1\text{ TeV})^2 \approx 6.4 \times 10^{-3}$, which would bring them on par with the previous columns.

the variable M_{TW}, where

$$M_{TW}^2 = 2\, p_{T\ell}\, \not{p}_T\, (1 - \cos\Delta\varphi_{\ell\not{p}_T}) \tag{4.2.4}$$

and impose a cut $M_{TW} \geq 30$ GeV. The effect of these successive kinematic cuts on the terms in the cross-section is shown in Table 4.1. Any stronger cuts would result in severe loss in the TGC signal, both for $\Delta\kappa_\gamma$ and λ_γ.

4.3 Results

4.3.1 1D LO analysis

In this section, we perform the one-dimensional analysis considering leading order results. We derive the limits by considering one of the TGCs at a time, viz., either $\Delta\kappa_\gamma \neq 0, \lambda_\gamma = 0$, or $\Delta\kappa_\gamma = 0, \lambda_\gamma \neq 0$.

If we consider the total cross-section, as given above, the limits one can put on the parameters $\Delta\kappa_\gamma$ and λ_γ are already strong. The actual number of signal events (in thousands) expected are shown in the panels marked (a) and (b) in Fig. 4.2, assuming an integrated luminosity of 100 fb^{-1}. The abscissa in (a) and (b) shows, respectively, the values of $\Delta\kappa_\gamma$ and λ_γ, each assuming that the other is zero. The region marked in grey corresponds to the 95%

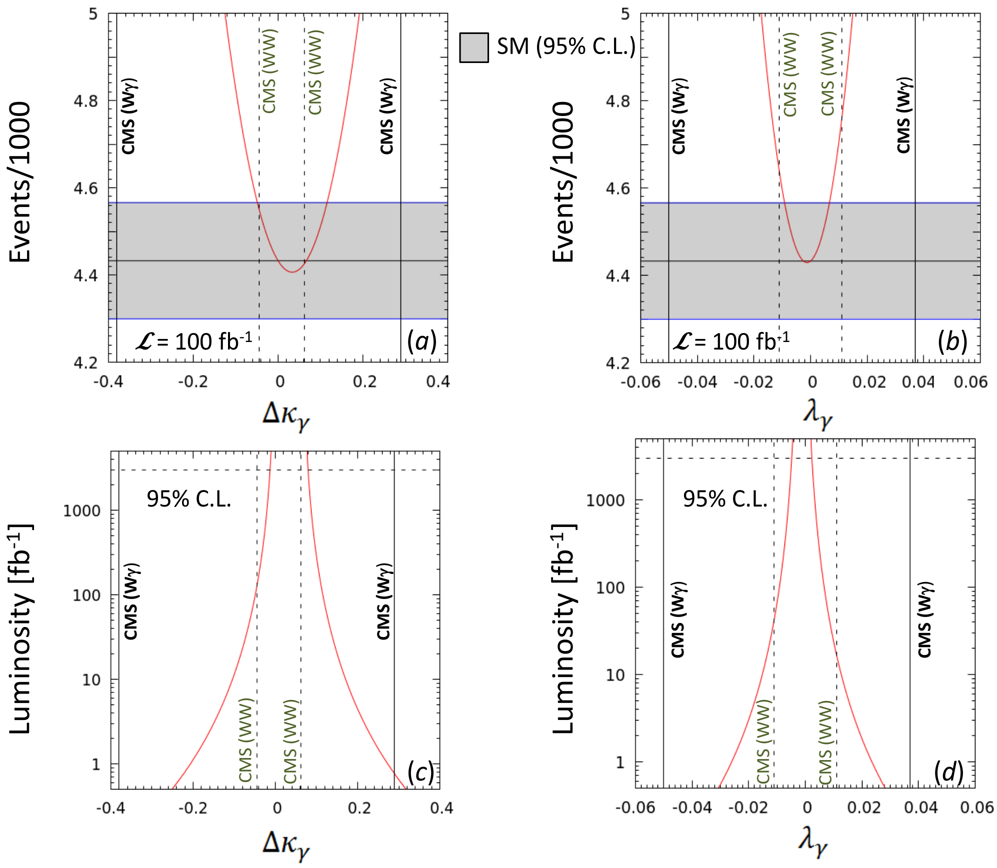

Figure 4.2: Constraints on the anomalous $WW\gamma$ couplings from consideration of the total cross-section, assuming an integrated luminosity of 100 fb^{-1}. The upper panels correspond to the variation in the excess in events per thousand over the SM prediction for the cases (a) $\Delta\kappa_\gamma \neq 0, \lambda_\gamma = 0$ and (b) $\Delta\kappa_\gamma = 0, \lambda_\gamma \neq 0$. The horizontal line shows the SM prediction and the shaded portion corresponds to its variation at 95% C.L. Solid vertical lines marked 'CMS(Wγ)' correspond to the Run-1 CMS bounds on the corresponding anomalous coupling from $W\gamma$ production [154] and broken verticals marked 'CMS(WW)' correspond to similar bounds obtained from WW production [152], assuming that $WW\gamma$ and WWZ anomalous couplings are related through $SU(2)$ symmetry. The lower panels, marked (c) and (d) respectively, show the corresponding 95% C.L. search limits (see text) when the luminosity is varied up to 5 ab^{-1}, with a horizontal broken line to indicate the machine limit of 3 ab^{-1} for the HL-LHC.

confidence level (C.L.) fluctuation in the SM prediction. Solid vertical lines indicate the current experimental bounds[2] from $W\gamma$ production at the LHC [153, 154], which directly constrains the $WW\gamma$ vertex, whereas broken vertical lines indicate the bounds from WW production [151,152], where there are contributions from both $WW\gamma$ and WWZ vertices. As explained above, these constraints are not as solid as those obtained from $W\gamma$ production.

[2]The constraints from ATLAS [151,153] and CMS [152,154] are not obtained from the total cross-section, but from a study of the p_T distributions of the final states. However, they are included here for purposes of comparison.

However, it is immediately obvious that the signal considered in this work can achieve the 95% C.L. level even at values which are comparable with the WW constraints, and certainly far smaller than the current $W\gamma$ constraints.

If the plots in the upper panels of Figure 4.2 indicate strong constraints with a luminosity of 100 fb^{-1}, it is relevant to ask what may be achieved at the high-luminosity upgrade of the LHC (HL-LHC), where the integrated luminosity may go as high as 3 ab^{-1}. To determine the search limits, we can determine the signal significance $\chi^2(L, \Delta\kappa_\gamma, \lambda_\gamma)$ as a function of luminosity L as

$$\chi^2(L, \Delta\kappa_\gamma, \lambda_\gamma) = \left[\frac{L\{\sigma(\Delta\kappa_\gamma, \lambda_\gamma) - \sigma_{SM}\}}{\sqrt{L\sigma_{SM}}}\right]^2 \tag{4.3.1}$$

assuming Gaussian random fluctuations in the background $\delta(L\sigma_{SM}) = \sqrt{L\sigma_{SM}}$. For this study, we ignore systematic errors, or, more properly, assume that they will be small enough to be ignored, compared to the statistical error. Now if, for a given value of L, the value(s) of $\Delta\kappa_\gamma$ and/or λ_γ satisfies $\chi^2(L, \Delta\kappa_\gamma, \lambda_\gamma) > 1.96$, we qualify the signal for an anomalous TGC as observable at 95% C.L. The corresponding variations, for the cases (c) $\Delta\kappa_\gamma \neq 0, \lambda_\gamma = 0$ and (d) $\Delta\kappa_\gamma = 0, \lambda_\gamma \neq 0$ are plotted in the lower panels of Figure 4.2. It may immediately be seen that even with a very low integrated luminosity, the 13 TeV LHC does immensely better than the Run-1 data, and with an integrated luminosity of 1 ab^{-1}, the direct constraints which may be obtained from the total cross-section are better than those even from WW production (which involve the WWZ couplings), except for one case $\Delta\kappa_\gamma > 0, \lambda_\gamma = 0$. At this juncture it is relevant to note the asymmetry of the curves in each panel about the zero point, which can be attributed to large interference terms between the anomalous $WW\gamma$ operators and the SM ones.

We now address the principal question for which this work was taken up, and that is whether the study of differential cross-sections instead of the total cross-section can help better in identifying anomalous $WW\gamma$ couplings. We have made a careful study of practically all the straightforward kinematic variables it is possible to construct with a $\gamma\ell \not{p}_T$ final state. It turns out that the ones which are sensitive to the anomalous couplings, i.e. the ones for which the anomalous operators behave differently than the SM operators, are those listed below:

$X =$	(a)	(b)	(c)	(d)	(e)	(f)
$v_X =$	$p_{T\gamma}$	$p_{T\ell}$	$\not{p}_T$	$\Delta\varphi_{\gamma\ell}$	$\Delta\varphi_{\gamma\not{p}_T}$	$\Delta\varphi_{\ell\not{p}_T}$

Table 4.2: List of kinematic variables whose distributions are sensitive to anomalous TGCs.

The effect of the anomalous TGCs on these is, of course, different for different observables, and this is illustrated in Figures 4.3 and 4.4. In Figure 4.3 we show three histograms in each panel, for the bin-wise quantity

$$N_{\text{excess}} = L\left(\frac{d\sigma}{dv_X} - \frac{d\sigma_{\text{SM}}}{dv_X}\right) , \tag{4.3.2}$$

where L is the integrated luminosity and v_X is the corresponding variable in Table 4.2. In each panel of Figure 4.3, the red histogram corresponds to the excess events as per Eqn. (4.3.2) for $\Delta\kappa_\gamma = +0.063$, i.e. the more stringent CMS upper limit arising from the WW cross-section [152], and the blue histogram indicates the corresponding lower limit $\Delta\kappa_\gamma = -0.063$. The solid shaded region represents the 95% C.L. fluctuations in the SM prediction, denoted δ(SM). In each case, the kinematic cuts listed in the text above are shown by a vertical line and hatching. For these plots, we have set $L = 3$ ab^{-1}, i.e., the maximum envisaged value of the HL-LHC.

If we consider the case of $\Delta\kappa_\gamma > 0$, i.e. the red histograms in Figure 4.3, we can see that the number of excess events is substantially above the SM fluctuation for a significant number of bins, especially as one goes towards higher magnitudes of p_T and for back-to-back vectors in the transverse plane, except for the opening angle in the transverse plane between the decay products of the W, which tend to be aligned for the signal. In fact, in some of the bins, the deviation is rather large. One the other hand, if we consider the case of $\Delta\kappa_\gamma < 0$, i.e. the blue histograms in Figure 4.3, the deviations are large only for really high magnitudes of p_T and even more extreme angles in the transverse plane than in the case of positive $\Delta\kappa_\gamma$.

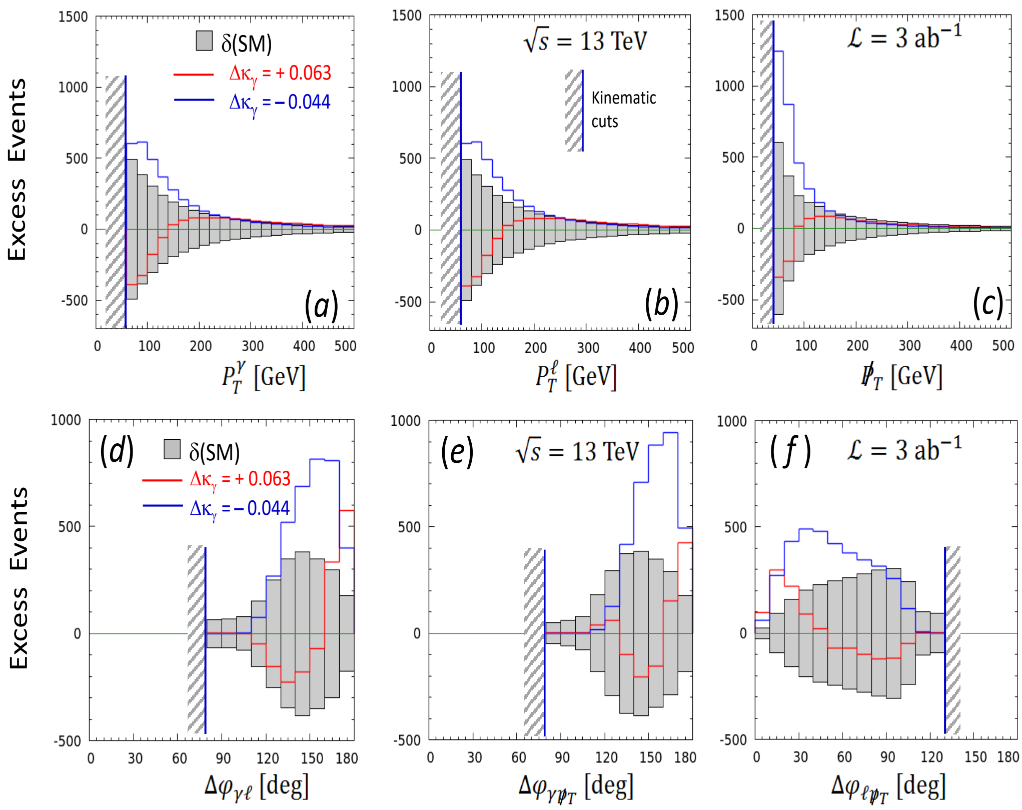

Figure 4.3: Background-subtracted kinematic distributions for the different variables listed above in the case of $\Delta\kappa_\gamma \neq 0$ with $\lambda_\gamma = 0$. The panels are marked (a), (b), etc. according to the legend in the text. Red histograms correspond to the signal with a positive value (marked) of $\Delta\kappa_\gamma$ and blue histograms correspond to negative values of $\Delta\kappa_\gamma$, while the shaded histograms correspond to the 95% C.L. fluctuations in the SM background. Vertical lines with hatching indicate the kinematic cuts listed in the text.

Some of the salient features of the histograms in Figure 4.3 are listed below.

- In all the panels, the signal histograms for negative $\Delta\kappa_\gamma$ change sign over the selected range, whereas for positive $\Delta\kappa_\gamma$ they are monotone.
- Of the upper three panels, clearly the best signal will come from a study of the missing p_T, for, even for negative $\Delta\kappa_\gamma$, there are significant deviations over 100 GeV.
- In the lower three panels, all show large deviations from the SM background. It is not clear by inspection which of these three variables is best suited to find the signal. For this, we must develop a suitable numerical metric.

We then turn to the other anomalous coupling λ_γ, in the case when $\Delta\kappa_\gamma = 0$. This is illustrated in Figure 4.4, where we show the same three histograms in each panel as for Figure 4.3, for the bin-wise quantities as defined in Eqn. (4.3.2) and the table below it. The notations and conventions of Figure 4.4 are therefore identical with those of Figure 4.3. Obviously the range of values of λ_γ is smaller, but this is, as explained before, due to the artificial scaling with M_W instead of some higher scale. Thus, the red (blue) histograms correspond to $\lambda_\gamma = +0.011(-0.011)$, which are, as before, the CMS limits from WW production [152]. Qualitatively, the deviations are rather similar to those in Figure 4.3, and one cannot tell, just by inspection, which of the parameters is preferable. Thus, if indeed, a deviation in these distributions from the SM prediction is found, we will encounter a difficult *inverse problem*, i.e. separation of signals from $\Delta\kappa_\gamma$ from those for λ_γ. In the present chapter, however, we feel that it is premature to address this problem. Instead, we focus on whether it will be possible to extend the discovery reach of the LHC by considering these distributions, rather than the total cross-section. The time to address this distinction will come when a deviation is actually found.

In order to see if a distribution has enough deviation from the SM prediction to be observable at, say, 95% C.L., we need to construct a suitable numerical metric. We choose a simple-minded extension of the one in Eqn. (4.3.1), in the form

$$\chi^2_X(L, \Delta\kappa_\gamma, \lambda_\gamma) = \sum_{n=1}^{N_X} \left(\frac{N^{(n)}_{\text{excess}}}{\sqrt{N^{(n)}_{\text{SM}}}} \right)^2 \tag{4.3.3}$$

where the index n runs over all the bins, and

$$N^{(n)}_{\text{SM}} = L \frac{d\sigma^{(n)}_{\text{SM}}}{dv_X} \tag{4.3.4}$$

is the SM prediction in that bin. N_{excess} is defined in Eqn. (4.3.2), but here it carries a bin index n, and L is, as usual, the integrated luminosity. The total number of bins N_X is not the same for all the different variables v_X, as a glance at Figures 4.3 and 4.4 will show. We can now compare the calculated values of $\chi^2_X(L, \Delta\kappa_\gamma, \lambda_\gamma)$ with $\chi^2(N_X, 95\%)$ which is the probability that the SM cross-section with N_X bins will undergo a 95% Gaussian fluctuation,

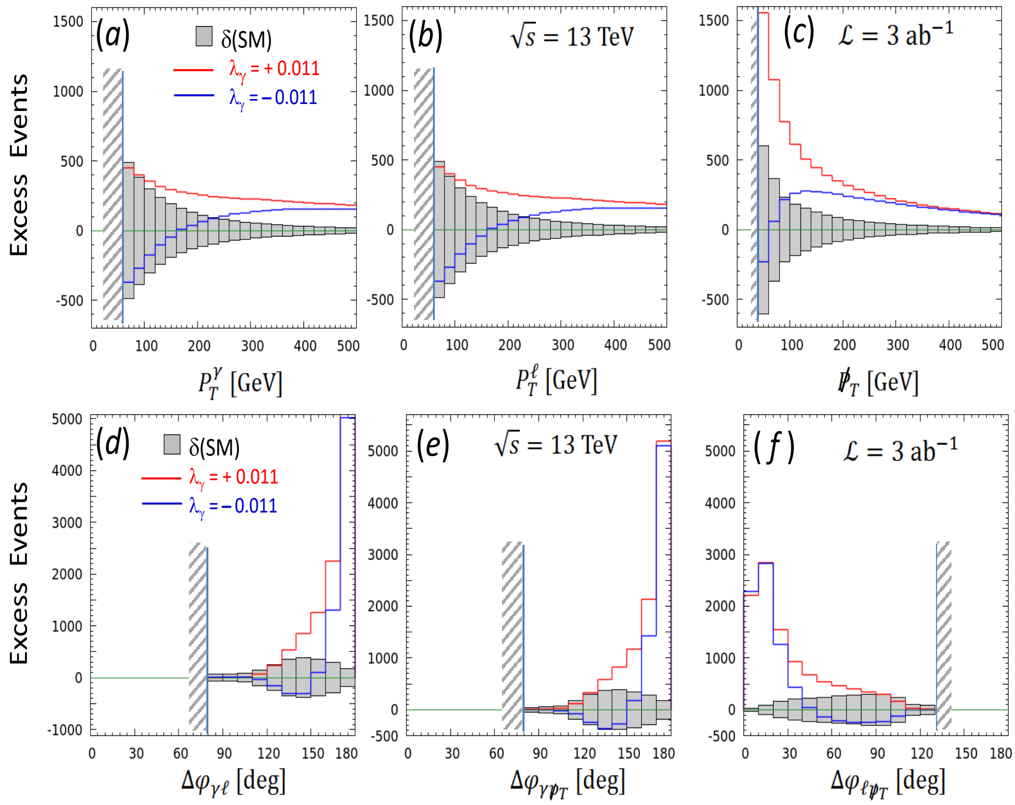

Figure 4.4: Background-subtracted kinematic distributions for the different variables listed above in the case of $\lambda_\gamma \neq 0$ with $\Delta\kappa_\gamma = 0$. The panels are marked (a), (b), etc. according to the legend in the text. Red histograms correspond to the signal with a positive value (marked) of λ_γ and blue histograms correspond to negative values of λ_γ, while the shaded histograms correspond to the 95% C.L. fluctuations in the SM background. Vertical lines with hatching indicate the kinematic cuts listed in the text.

faking a signal. If, for a given set of arguments, $\chi^2_X(L, \Delta\kappa_\gamma, \lambda_\gamma) > \chi^2(N_X, 95\%)$, we will assume the corresponding anomalous TGC to be discoverable at the LHC.

Our results for the different variables are shown in Figure 4.5. The upper panels, marked (a) and (c) show the discovery limits for the transverse momentum variables p_T^γ, p_T^ℓ and $\not{p}_T$ in the two cases (a) $\Delta\kappa_\gamma \neq 0, \lambda_\gamma = 0$ and (c) $\Delta\kappa_\gamma = 0, \lambda_\gamma \neq 0$ respectively. Corresponding limits for the azimuthal angle variables $\Delta\varphi_{\gamma\ell}$, $\Delta\varphi_{\gamma\not{p}_T}$ and $\Delta\varphi_{\ell\not{p}_T}$ are similarly shown in the lower panels, marked (b) and (d) respectively. As before, the CMS limits from $W\gamma$ production [154], as well as those from WW production [152] are shown by solid and broken vertical lines respectively. As in Figure 4.2, a broken horizontal line represents the maximum integrated luminosity envisaged at the HL-LHC, and therefore, its intersections with the different curves indicates the discovery limit of the machine.

If we now inspect the discovery limits in Figure 4.5 and compare then with those in Figure 4.2, the following conclusions emerge.

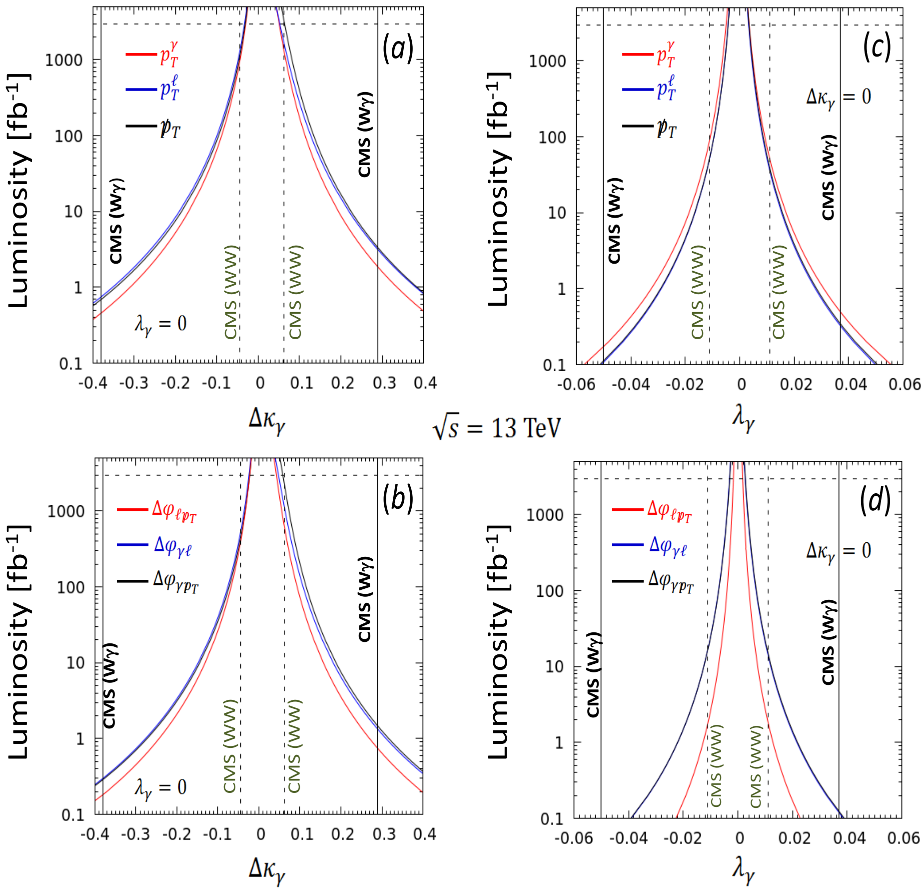

Figure 4.5: 95% C.L. discovery limits for the case $\Delta\kappa_\gamma \neq 0, \lambda_\gamma = 0$ in the panels on the left, marked (a) and (b), and the case $\Delta\kappa_\gamma = 0, \lambda_\gamma \neq 0$ in the panels on the right, marked (c) and (d). Only three variables at a time have been shown in each panel to avoid clutter. The upper panels, marked (a) and (c) show the discovery limits for transverse momentum variables, while the lower panels, marked (b) and (d) show the discovery limits for azimuthal angle variables.

- For $\Delta\kappa_\gamma < 0, \lambda_\gamma = 0$, the discovery limits from the total cross-section are better than those from the distributions; among the distributions, the best constraints arise from $\Delta\varphi_{\ell\not{p}_T}$.
- For $\Delta\kappa_\gamma > 0, \lambda_\gamma = 0$, the discovery limits from the total cross-section are no longer better; instead the p_T distributions are more efficient, especially as the luminosity increases above 100 fb^{-1}. The $\Delta\varphi_{\ell\not{p}_T}$ distribution can be used to get discovery limits comparable to those from the different p_T distributions, but not better.
- For $\Delta\kappa_\gamma = 0, \lambda_\gamma < 0$, the total cross-section and the p_T distributions give similar discovery limits, while the discovery limits from the $\Delta\varphi_{\ell\not{p}_T}$ are significantly better and obviously improve as the integrated luminosity increases.
- For $\Delta\kappa_\gamma = 0, \lambda_\gamma > 0$, the total cross-section gives better discovery limits than the p_T distributions, whereas the $\Delta\varphi_{\ell\not{p}_T}$ distribution always gives better sensitivity.

It is also interesting to note that of the three p_T distributions, the best results are obtained from different distributions in different regimes, whereas for the $\Delta\varphi$ distributions, $\Delta\varphi_{\ell \not{p}_T}$ is always the most sensitive. This sensitivity is likely to be due to interference between different helicity amplitudes [147], though that is not explicit in our calculations.

There is a very important lesson to learn from the above observations, viz., that there is no unique variable whose study will provide the maximum sensitivity to anomalous TGCs. A proper experimental study should, therefore, include *all* the variables considered above, including the total cross-section. Currently, experimental results are mostly based on transverse momentum studies [148, 153, 154], but these, as our results indicate, are not always the most sensitive variables.

NLO analysis

As all of the above results are considered at the leading order (LO) with a fixed set of parton distribution functions (PDFs), viz. the CTEQ-6L set, it is relevant to ask how robust these results are against QCD effects, such as scale variation, next-to-leading order (NLO) effects and PDF uncertainties. One could also ask whether detector effects will lead to degeneration in the bounds obtainable from these variables. A complete analysis of these questions, we feel, is beyond the scope of the present work, and hence we have only made some preliminary studies in this regard.

To estimate these effects, as well as to validate our LO analyses, we have simulated the processes in questions using a combination of the following public domain softwares: MadGraph (version MG5-aMC-v2.4.2 [156]) to calculate cross-sections, Pythia (version Pythia8219 [157]) for the simulation including fragmentation effects and Delphes (version Delphes-3.4.1 [158]) as a toy detector simulation. In this simulation, we trigger on a final state with a hard transverse photon and a hard transverse lepton, with a significant amount of missing p_T. In addition, we require our process to be hadronically quiet, i.e. we put a strong jet veto.

At the very outset, let us note that with the requirement of high-p_T, the detector effects, simulated by using the Delphes package, with standard levels of smearing for the final state photon and the lepton, are very small, and may be safely neglected. The QCD effects are simulated by running the package MadGraph, which permit (a) the inclusion of NLO corrections, (b) variation of the factorisation scale Q, which we set to $M_W/2$, M_W and $2M_W$ to cover the expected range, and (c) two PDF sets, the CTEQ-6 set [159] and the NNPDF-2.3 set [160]. Even though a large portion of these are removed by the jet veto and the hard p_T cuts, the residual effects are still not small, especially for the SM background where the change can be as much as a factor of 2. The new operators associated with the anomalous couplings $\Delta\kappa_\gamma$ and λ_γ are also changed, but by not much more than 20 - 30% after application of the jet veto. However, all this does have an effect on the χ^2. As mentioned above, a full study of the detailed effects for all the distributions is beyond the scope of this work, though it

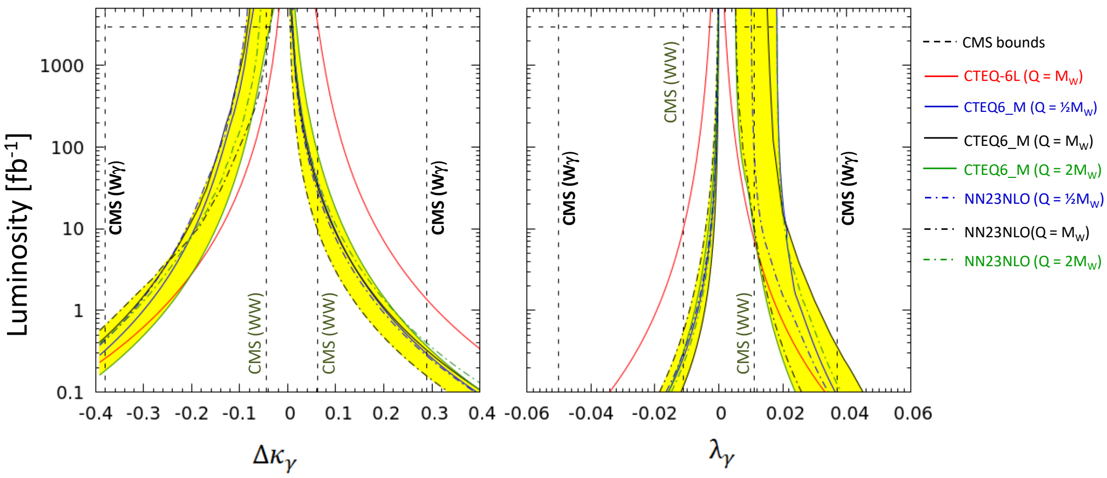

Figure 4.6: QCD smearing of 95% C.L. discovery limits for the case $\Delta\kappa_\gamma \neq 0, \lambda_\gamma = 0$ in the panel on the left, marked (a), and the case $\Delta\kappa_\gamma = 0, \lambda_\gamma \neq 0$ in the panel on the right, marked (b). Only the variable $\Delta\varphi_{\ell \not{p}_T}$ has been considered. Solid (dot-dash) lines correspond to CTEQ-6 and NNPDF-2.3 parton densities and the colour scheme is as follows: red for LO and blue; back and green for NLO with $Q = \frac{1}{2}M_W, M_W$ and $2M_W$ respectively. The region shaded yellow is the envelope of the different QCD uncertainties. As in the previous figures, dashed lines indicate the CMS constraints.

should certainly be taken up before the experimental data come in. However, our preliminary findings can be summarised as follows. Despite the smearing in distributions due to QCD effects, the variable $\Delta\varphi_{\ell \not{p}_T}$ remains the most sensitive of the azimuthal angle variables. We have exhibited our results for the χ^2 analysis using the $\Delta\varphi_{\ell \not{p}_T}$ variable in Figure 4.6.

In Figure 4.6, we have plotted the graphs for integrated luminosity versus the minimum accessible values of (a) $\Delta\kappa_\gamma$ and (b) λ_γ respectively, taking into account the QCD effects in the distribution of $\Delta\varphi_{\ell \not{p}_T}$. The LO contributions, with $Q = M_W$, as used in all the other plots, are shown as solid red lines. The solid curves correspond to CTEQ-6 PDFs, and the dot-dashed curves to NNPDF choices. Blue, black and green colours correspond to $Q = \frac{1}{2}M_W$,M_W and $2M_W$ respectively. The yellow-shaded region is the envelope of all these curves and may be taken as an indicator of the overall smearing due to QCD effects.

A glance at the QCD effects shows that they are clearly asymmetric, and hence arise principally from the interference terms. This is consistent with the maximum change happening in the SM contribution. For $\Delta\kappa_\gamma$, it leads to dilution of the LO results for negative $\Delta\kappa_\gamma$, but to a strengthening for positive $\Delta\kappa_\gamma$. On the other had, for λ_γ, we have a strengthening (and very little spread) for negative λ_γ, but a large smearing as well as dilution for positive λ_γ. We may expect all the χ^2 analyses for different distributions to have such effects. This underlines the importance of considering all the variables, as mentioned above, before the potential of the LHC to probe anomalous TGC's is fully realised.

4.4 2D LO analysis

Thus far, we have only considered one of the TGCs at a time, viz., either $\Delta\kappa_\gamma \neq 0, \lambda_\gamma = 0$, or $\Delta\kappa_\gamma = 0, \lambda_\gamma \neq 0$. While convenient from a purely phenomenological standpoint, this is hard to justify from a top-down approach, for the same new physics which creates nonzero $\Delta\kappa_\gamma$ could very well generate nonzero λ_γ as well. We now turn, therefore, to the study of this more realistic case of joint variation of the two parameters. The formulae in Eqns. (4.3.1) and (4.3.3) are naturally geared to handle this joint variation, so all that is required is to numerically vary both the parameters and perform the same kind of analysis as we have described above.

Our results for joint variation are shown in Figure 4.7. The left panel, marked (a) shows the discovery limits that can be obtained using the total cross-section. The inaccessible region at the 13 TeV LHC, assuming an integrated luminosity of 10(1000) fb^{-1} is shaded in pink(red). For comparison, on the same panel we give the constraints from LEP-2 (black), and from the CMS (blue) and ATLAS (green) Collaborations at the LHC Run-1. In each case the inside of the ellipse is not accessible and the region outside is ruled out. It is immediately obvious that, as was the case with one parameter at a time, the total cross-section is a reasonably sensitive probe of anomalous TGCs, and in fact, even with 10 fb^{-1} of data, it is as sensitive as the use of the WW production data (modulo the WWZ caveat). Sensitivity improves dramatically for 1000 fb^{-1} luminosity, as the tiny red shaded region indicates. However – and here lies the rub – the inaccessible region is star-shaped, with four arms which stretch to possible large values of one of the parameters at a time. It is easy to see why these arise, for the significance is based on a single parameter, viz., the total cross-section, and there will always be regions where the contributions to this from $\Delta\kappa_\gamma$ cancel with those from λ_γ, making the signal small or vanishing. Thus, although the total cross-section can be used to probe the anomalous TGCs quite efficiently, there remain these four narrow wedges of the parameter space which are inaccessible to the LHC.

The situation can be radically improved by using a distribution, rather than the total cross-section, for it is almost inconceivable that the extra contributions from $\Delta\kappa_\gamma$ will undergo a bin-by-bin cancellation with those from λ_γ, given that the distributions are somewhat different, as shown in Figures 4.3 and 4.4. To be precise, the same pair of values which cause cancellation of anomalous effects in one bin, may not cause cancellation in another bin, and hence, the overall value of χ^2 will not be rendered small. This is illustrated in the right panel, marked (b) of Figure 4.7, where we use the distribution in $\Delta\varphi_{\ell \not{p}_T}$ to obtain 95% C.L. discovery limits. Here, corresponding to different values of the integrated luminosity, we show the discovery limits as elliptic regions in the same way as shown by the experimental collaborations. As usual, the interior of each ellipse is inaccessible to the LHC with the luminosity in question. The experimental constraints are given exactly as in the left panel, marked (a). It hardly needs to be commented that at the HL-LHC, very stringent constraints

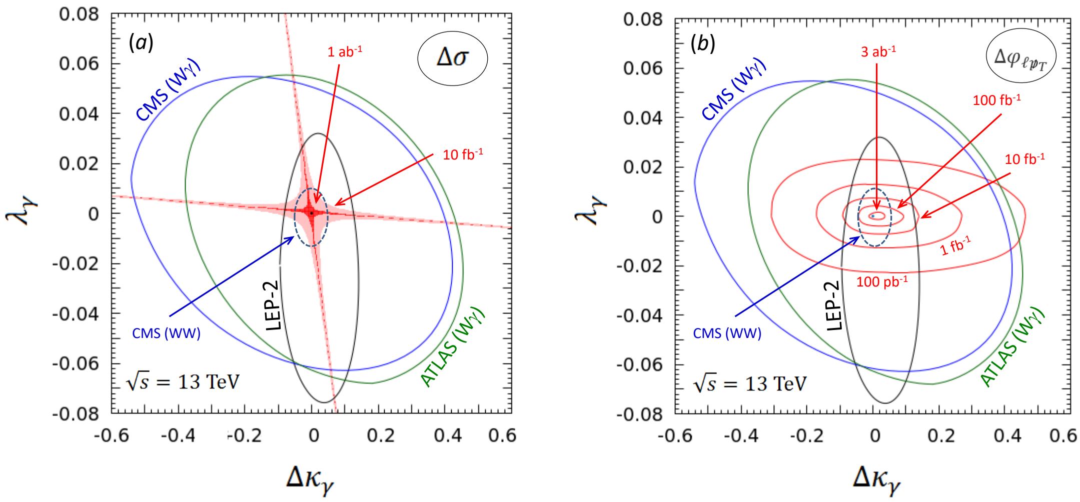

Figure 4.7: Joint discovery limits at 95% C.L. on the anomalous couplings $\Delta\kappa_\gamma$ and λ_γ. The measurables used are (a) the total cross-section, and (b) the azimuthal angle variable $\Delta\varphi_{\ell \not{p}_T}$ respectively. In the left panel, marked (a) the regions shaded pink (red) are inaccessible to the LHC with 10 (1000) fb^{-1} of integrated luminosity. Similar inaccessible regions lie inside the oblate ellipses (in red) on the right panel, marked (b). Experimental constraints from LEP-2 and from the Run-1 of LHC are shown as prolate ellipses in both panels. The tiny black dot at the centre is, of course, the SM prediction at tree-level.

indeed could be obtained in case no deviation from the SM is seen. It may be noted, however, that even with this accuracy of measurement, the one-loop SM effects will not be accessible, though effects from new physics such as the MSSM, may be [146] . The above results will also be both strengthened and diluted by QCD effects, as shown for the single-parameter analyses above. We may thus expect the ellipses in Figure 4.7 to get distorted (though retaining their ellipticity) and smeared out on the same pattern as the curves in Figure 4.6.

4.5 Summary

We have considered the process $pp \to \gamma W^* \to \gamma\, \ell\, \not{p}_T$ at the 13 TeV run of the LHC, and studied possible implications of having anomalous (CP-conserving) $WW\gamma$ vertices in the theory. The choice of this process (which has a lower cross-section than, say, W^+W^- pair production) is because the tagging of a final-state photon ensures that there is no contamination of the new physics contribution with possible anomalous effects in the WWZ vertex. We have shown that the anomalous $WW\gamma$ couplings may be constrained by considering not one, but seven independent observables, viz. the total cross-section, three different p_T distributions and three different azimuthal angle variables. The relative efficacy of each of these has been studied in detail, making certain simplifying assumptions, such as the absence of initial/final state radiation, pileup effects, systematic errors and detector effects. The first two we expect to be essentially eliminated by the rather severe kinematics cuts chosen for our analysis, but the latter ones can only be estimated by a thorough experimental analysis, which is beyond the scope of this work. Similarly, we have assumed that the kinematic cuts suggested by us will be effective in controlling backgrounds from W + jet events (with a jet faking a photon). Under these assumptions, we have shown that the judicious use of the variables studied, especially the azimuthal angle variable $\Delta\varphi_{\ell \not{p}_T}$, can be used to pinpoint anomalous effects in the process in question, to a great degree of accuracy, as the statistics collected by the LHC (and its HL upgrade) grow larger. QCD effects will cause some dilution or strengthening of these results, depending on the values of the TGC's, but the overall pattern will not change too radically. Such measurements would eventually probe not just large electoweak corrections in the TGC sector, but could also effectively constrain new physics involving modifications and mixings in the gauge sector. Of course, the most exciting scenario would be to see an unambiguous deviation from the SM prediction in any of the variables (or more than one variable) in the upcoming runs of the LHC, and it is on this hopeful note that we conclude this chapter.

Chapter 5

Light CP-even Higgs Boson in type-I 2HDM at LHC

This chapter deals with the phenomenology of a scalar lighter than the observed 125-GeV Higgs Boson in the final states $\gamma\gamma$ and $b\bar{b}$. The results of this chapter are based on the work: D. Bhatia, U. Maitra and S. Niyogi, "Discovery prospects of a light Higgs boson at the LHC in type-I 2HDM, Phys. Rev. D **97**, no. 5, 055027 (2018)". Note that most parts of the $b\bar{b}$ analysis were performed by Dr. Ushoshi Maitra. Our analysis has become important in the context of recent diphoton excess of 2.8σ (global 1.3 σ)in the $\gamma\gamma$ channel around 95 GeV [161]. Although at this stage, the deviation is not significant but is certainly of importance simply because LEP had also indicated a possibility of observing an excess of Higgs-like events in similar mass region [17].

5.1 Introduction

Despite the overwhelming success of the SM, the current measurements [21] at LHC still do not rule out the possibility of the observed particle belonging to an enlarged scalar sector of a beyond-SM scenario. Usually the additional scalars are considered to be heavy, and in some cases, they are even decoupled from the low-energy effective theory. However, there may exist scenarios where some of the new physics particles are lighter than the observed Higgs. We explore this possibility in context of the type-1 two-Higgs-doublet model, which is least constrained by the data.

As already discussed in Chapter. 2, two Higgs doublet models (2HDM's) are one of the simplest extensions of the SM with an additional scalar doublet charged under $SU(2)_L$, where in type-I only one of the Higgs doublets interacts with the fermions in the gauge basis. Since the Higgs boson discovered at the LHC is CP even [162,163], amongst the five scalars predicted in the 2HDM viz., the light CP-even scalar h, the heavier CP-even scalar H, the CP-odd scalar A and the charged scalar $H^{\pm}$, we can identify only one of the CP-even scalars with the observed scalar at the LHC. Since we are interested in studying light CP-even scalar scenarios, we identify H with the observed 125-GeV Higgs and study the phenomenology of the lighter Higgs. Furthermore we choose its mass range from $70-110$ GeV to avoid decay of $H \to hh$. As a result, the bounds coming from the total decay width measurement of the observed scalar [164], the measurement of Higgs signal rate [21], and direct decay of the observed Higgs to a pair of light Higgses, i.e., $H \to hh$ [165] becomes irrelevant in our case (see Refs. [166, 167] for an analysis with additional scalars lighter than $m_h/2$).

To study the discovery prospects of the light CP even scalar, a suitable choice of production and decay channels is essential. In our scenario, the light Higgs decays dominantly to $b\bar{b}$, except in the fermiophobic limit. Here its decay to bosons (mainly photons) becomes important. We therefore examine the light Higgs decays in the $b\bar{b}$ and $\gamma\gamma$ final states at the LHC. Note that the search for such low mass scalars decaying to diphotons has already been performed at LHC Run-1 [168, 169]. For the diphoton channel, we consider the production of the scalar through gluon fusion and in association with gauge bosons. The production of the light scalar in association with gauge boson/top pair is considered for the $b\bar{b}$ mode. Owing to a clean environment, the diphoton final state is one of the favorite channels to search for new resonances at the LHC. In contrast, the $b\bar{b}$ state is plagued by the huge SM multijet backgrounds. Therefore, the light Higgs has been considered in the boosted regimes for this channel, where the jet substructure techniques enable the efficient suppression of the SM backgrounds [170, 171]. Note that since $b\bar{b}$ analysis was not explicitly performed by me, I will focus only on the diphoton analysis in the chapter.

This chapter is organized in the following manner. We begin with a brief introduction to the 2HDM in section 5.2, followed by a discussion of plausible channels which can be used to probe the light Higgs at the LHC in section 5.3. In section 5.4, we briefly review various constraints on the 2HDM parameter space arising from the LEP and LHC measurements, in the context of Type-I 2HDM. A dedicated collider analysis of the light Higgs in the allowed parameter space at the LHC is performed in section 5.5. Finally in section 5.6, we summarize our results. Further in appendix A.1, we discuss the light Higgs couplings to diphotons. In appendix A.2, the implications of the light charged Higgs boson on our results is analyzed, and in appendix A.3, the tagging methods used to reconstruct boosted objects are discussed. Finally, in appendix A.4, we tabulate the behaviour of the total cross section of the selected modes with respect to the 2HDM parameters.

5.2 2HDM: a brief review

The Z_2-symmetric 2HDM Lagrangian with two $SU(2)_L$ Higgs doublets (Φ_1 and Φ_2)[1] can be parametrized as [37]:

$$\mathcal{L}_{\rm 2HDM} = (D_\mu \Phi_1)^\dagger \, D^\mu \Phi_1 + (D_\mu \Phi_2)^\dagger \, D^\mu \Phi_2 + \mathcal{L}_{\rm Yuk}(\Phi_1, \Phi_2) - V(\Phi_1, \Phi_2) \, , \tag{5.2.1}$$

[1]Under Z_2 transformation, $\Phi_1 \to \Phi_1$ and $\Phi_2 \to -\Phi_2$

where $\mathcal{L}_{\rm Yuk}$ represents the Yukawa interactions and $V(\Phi_1, \Phi_2)$ is the scalar potential given as

$$\begin{aligned} V(\Phi_1,\Phi_2) &= m_{11}^2\,\Phi_1^\dagger\Phi_1 + \frac{\lambda_1}{2}\,(\Phi_1^\dagger\Phi_1)^2 + m_{22}^2\,\Phi_2^\dagger\Phi_2 + \frac{\lambda_2}{2}\,(\Phi_2^\dagger\Phi_2)^2 - \left[m_{12}^2\Phi_1^\dagger\Phi_2 + h.c\right] \\ &\quad +\lambda_3\,\Phi_1^\dagger\Phi_1\,\Phi_2^\dagger\Phi_2 + \lambda_4\,\Phi_1^\dagger\Phi_2\,\Phi_2^\dagger\Phi_1 - \left[\frac{1}{2}\lambda_5\left(\Phi_1^\dagger\Phi_2\right)^2 + H.c.\right]\,. \end{aligned} \tag{5.2.2}$$

Here m_{12} is the soft Z_2 symmetry-breaking parameter. Note that in our analysis, we have assumed $V(\Phi_1, \Phi_2)$ to be invariant under CP (i.e., charge and parity transformations) and consequently the parameters of the scalar potential are real. The spontaneous breaking of $SU(2)_L \times U(1)_Y$ symmetry results in five physical scalar fields h, H, A and $H^\pm$ (with masses m_h, m_H, m_A and $m_{H^\pm}$, respectively) and three Goldstone bosons G and $G^\pm$, which appear as the longitudinal modes for Z and $W^\pm$ bosons. The mass spectra of the particles are obtained by minimizing the scalar potential $V(\Phi_1, \Phi_2)$ in Eq. (5.2.2).

The doublets in terms of the physical fields and the Goldstone bosons can be expressed as:

$$\begin{aligned} \Phi_1 &= \begin{pmatrix} G^+\cos\beta + H^+\sin\beta \\ \frac{1}{\sqrt{2}}\left[h\sin\alpha - H\cos\alpha + i\,(G\cos\beta + A\sin\beta) + v_1\right] \end{pmatrix}, \\ \Phi_2 &= \begin{pmatrix} G^+\sin\beta - H^+\cos\beta \\ \frac{1}{\sqrt{2}}\left[-h\cos\alpha - H\sin\alpha + i\,(G\sin\beta - A\cos\beta) + v_2\right] \end{pmatrix}, \end{aligned} \tag{5.2.3}$$

where α and β are the rotation angles which diagonalize the mass matrices for the neutral CP even Higgs and the charged Higgs/CP odd Higgs respectively. The parameters of the scalar potential $(m_{11}, m_{22}, \lambda_i\ )$ can be expressed in terms of the rotation angles (α, β), the Z_2 symmetry breaking parameter (m_{12}), and the masses of the scalars (m_h, m_H, m_A, $m_H^\pm$) as [37]:

$$m_{11}^2 = \frac{1}{4}\left(m_h^2 + m_H^2 - 4m_{12}^2\tan\beta + \left(m_H^2 - m_h^2\right)\sec\beta\cos(2\alpha-\beta)\right), \tag{5.2.4}$$

$$m_{22}^2 = \frac{1}{4}\left(m_h^2 + m_H^2 - 4m_{12}^2\cot\beta + \left(m_H^2 - m_h^2\right)\csc\beta\sin(2\alpha-\beta)\right), \tag{5.2.5}$$

$$\lambda_1 = \frac{1}{2v^2}\sec^2\beta\left(m_h^2 + m_H^2 + (m_H^2 - m_h^2)\cos 2\alpha - 2m_{12}^2\tan\beta\right)\,, \tag{5.2.6}$$

$$\lambda_2 = \frac{1}{2v^2}\csc^2\beta\left(m_h^2 + m_H^2 - (m_H^2 - m_h^2)\cos 2\alpha - 2m_{12}^2\cot\beta\right)\,, \tag{5.2.7}$$

$$\lambda_3 = \frac{1}{v^2}\csc 2\beta\left(-2m_{12}^2 + (m_H^2 - m_h^2)\sin 2\alpha + 2m_{H^\pm}^2\sin 2\beta\right)\,, \tag{5.2.8}$$

$$\lambda_4 = \frac{1}{v^2}\left(m_A^2 - 2m_{H^\pm}^2 + m_{12}^2\csc\beta\sec\beta\right)\,, \tag{5.2.9}$$

$$\lambda_5 = \frac{1}{v^2}\left(m_{12}^2\csc\beta\sec\beta - m_A^2\right)\,, \tag{5.2.10}$$

$$v_1 = v\cos\beta \quad \text{and} \quad v_2 = v\sin\beta\,. \tag{5.2.11}$$

The couplings λ_i $(i = 1, 5)$ are constrained by the perturbativity, vacuum stability [172], and unitarity [173] bounds, which in turn, restrict the allowed values of the scalar masses for a given value of α and β [37, 174]. The masses of the additional scalars also get constrained from the well measured flavour and electroweak observables [175–177]. The combined effect of these constraints on the 2HDM parameter space is discussed in appendix. A.2, in the context of type-I 2HDM. Note that the free parameter α remains unaffected after imposition of above constraints (see Fig. A.1 in appendix. A.2).

In our analysis, we identify the heavier CP even Higgs with the discovered scalar by fixing $m_H = 125$ GeV and study the phenomenology of the light CP even scalar h. At this stage we have following free parameters — α, β, $m_{H^\pm}$, m_A, m_{12} and m_h. However, we confine ourselves to that part of the allowed parameter space, where the masses of the charged and pseudoscalar Higgs bosons are heavy i.e. $\mathcal{O}(500)$ GeV and do not affect our analysis. The Z_2 breaking parameter in this case becomes irrelevant for the light Higgs phenomenology and can be suitably chosen to have any value less than 100 GeV (see appendix. A.2). Note that although we have chosen the charged Higgs to be heavy for most of our analysis, we do analyze the implications of having a low-mass charged scalar in appendix. A.2.

We now discuss the couplings of the scalar particles with fermions and gauge bosons. In the type-I 2HDM, fermions couple only to one of the doublets i.e. Φ_2 and $\mathcal{L}_{\rm Yuk}$ is given as

$$\begin{aligned}
\mathcal{L}_{\rm Yuk}^{\rm Type-I} &= \overline{Q_L}\,\mathcal{Y}^d\Phi_2 d_R + \overline{Q_L}\mathcal{Y}^u\Phi_2^c u_R + \overline{Q_L}\mathcal{Y}^e\Phi_2^c e_R + h.c.\,, \\
&= -\sum_{f=u,d,\ell}\frac{m_f}{v}\left(\xi_h^f\overline{f}f\,h + \xi_H^f\overline{f}f\,H - i\xi_A^f\overline{f}\gamma_5 f\,A\right) \\
&- \frac{\sqrt{2}V_{ud}}{v}\overline{u}\left(m_u\xi_A^u P_L + m_d\xi_A^d P_R\right)d\,H^+ - \frac{\sqrt{2}m_\ell}{v}\xi_A^\ell\overline{\nu}P_R\ell\,H^+ + h.c. \quad (5.2.12)
\end{aligned}$$

where $\mathcal{Y}^{u,d,e}$ are 3×3 Yukawa matrices, V_{ud} is the Cabibbo-Kobayashi-Maskawa matrix element, m_f is the mass of a fermion (f) and

$$\xi_h^{u,d,\ell} = \cos\alpha/\sin\beta\,,\ \xi_H^{u,d,\ell} = \sin\alpha/\sin\beta\,,\ \xi_A^u = \cot\beta\,,\ \xi_A^{d,\ell} = -\cot\beta\,. \quad (5.2.13)$$

We list some of the couplings of gauge bosons with scalars that are relevant for our analysis (see Refs. [178], [179] for a complete list):

$$\begin{aligned}
\mathcal{L}_{\rm Gauge-int} &= \frac{m_Z^2}{v}\xi_h^V Z_\mu Z^\mu h + \frac{m_Z^2}{v}\xi_H^V Z_\mu Z^\mu H + 2\frac{m_W^2}{v}\xi_h^V W_\mu W^\mu h + 2\frac{m_W^2}{v}\xi_H^V W_\mu W^\mu H \\
&+ \frac{\alpha_{em}}{8\pi v}\,\xi_h^\gamma h\,F_{\mu\nu}F^{\mu\nu} + \frac{\alpha_{em}}{8\pi v}\,\xi_H^\gamma\,HF_{\mu\nu}F^{\mu\nu}\,, \quad (5.2.14)
\end{aligned}$$

where

$$\xi_h^V = \sin(\beta-\alpha) \quad , \quad \xi_H^V = \cos(\beta-\alpha)\,, \quad (5.2.15)$$

and the expressions for ξ_h^γ and ξ_H^γ are listed in appendix A.1. Based on the above couplings of the scalars with fermions and gauge bosons, two interesting limits arise:

1. Alignment limit ($\alpha \to \beta$): Here the couplings of the heavier CP even Higgs exactly match those of the SM Higgs.

2. Fermiophobic limit ($\alpha \to \pi/2$) : In this limit, the tree-level couplings of the light Higgs with fermions (ξ_h^f) vanish [see Eq. (5.2.13)] and its loop-induced couplings with fermions are also negligible. The light Higgs in this case behaves as a fermiophobic scalar.

We shall see later that these limits have interesting implications in our analysis. As an aside, note that the condition $\alpha \equiv \beta \to \pi/2$ corresponds to the case where the alignment and fermiophobic limits occurs simultaneously. In this case, the couplings of the light Higgs with both fermions and gauge bosons vanish [see Eqns. 5.2.13, 5.2.15] and the type-I 2HDM maps to the inert 2HDM model.

After discussing the couplings of the light Higgs boson, we are now in a position to predict its phenomenological consequences. In the next section, we identify the promising channels which could be useful in probing the light Higgs at the LHC. Keeping a large QCD background in mind, a suitable choice of the production channel and decay mode would be essential for the discovery of a light scalar like the SM Higgs.

5.3 Promising channels to explore at the LHC

The light Higgs boson, just like the SM Higgs, can be produced at the LHC via gluon fusion (ggF), vector-boson fusion (VBF), and in association with SM gauge bosons (Vh), as well as with a top pair ($t\bar{t}h$). The ratio of the production cross section of the light Higgs and that of the SM-like Higgs (h_{SM}) as a function of α is plotted in the left panel of Fig. 5.1. Here, by "SM-like Higgs" we mean a hypothetical scalar whose couplings are exactly same as those of the SM Higgs but whose mass is equal to that of the light Higgs i.e. $m_{h_{SM}} = m_h$. Note that m_h is chosen to be 80 GeV in Fig. 5.1 for illustrative purposes. The gluon fusion as well as the $t\bar{t}h$ production cross section of the light Higgs in the type-I model scale as $(\xi_h^f)^2$ with respect to the SM-like Higgs. Similarly, the cross sections for the light Higgs produced in

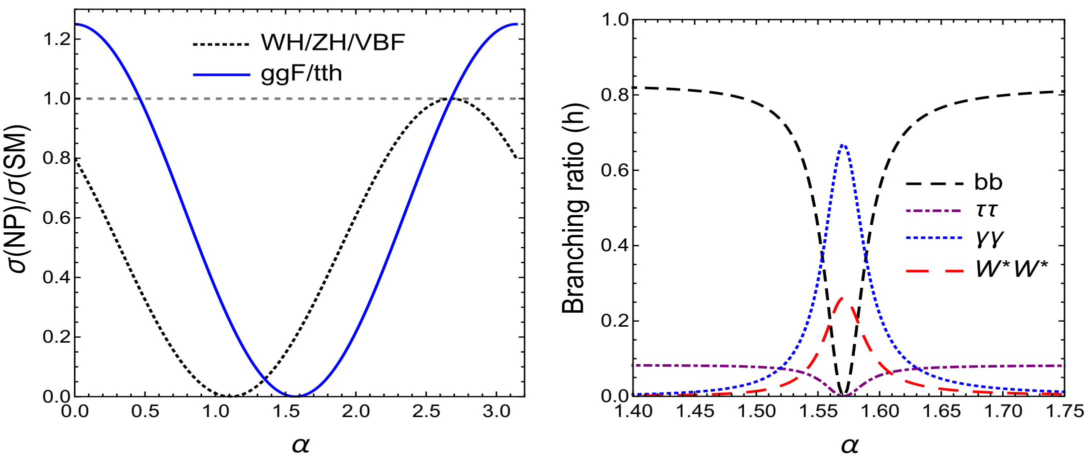

Figure 5.1: A representative plot for $m_h = 80$ GeV and $\tan\beta = 2$. The left panel illustrates the variation of the ratio of the cross sections of the light Higgs (h) and the SM-like Higgs (h_{SM}) with α. The right panel shows the branching ratios of the light Higgs as a function of α (the range of α is restricted near $\pi/2$ to signify the behavior around the fermiophobic limit). Note that the Vh/VBF and ggF/$t\bar{t}h$ production modes are able to probe a similar parameter space. In a similar fashion, the variations of the $b\bar{b}$ and $\tau\bar{\tau}$ decay modes are identical with α.

association with gauge bosons or through vector-boson fusion scale as $(\xi_h^V)^2$. Therefore, the ordinate in Fig. 5.1 essentially shows the variation of $(\xi_h^i)^2$ against α. The scaling has been illustrated for $\tan\beta = 2$ in Fig. 5.1. It can be seen from Eqn. (5.2.13) and (5.2.15) that for large values of $\tan\beta$, all production channels scale identically as $\cos^2\alpha$.

The right panel of Fig. 5.1 represents various branching fractions of the light Higgs again as a function of α. In most of the parameter space, the light Higgs decays dominantly to a pair of bottom quarks. However, near $\alpha \to \pi/2$ (the fermiophobic limit), it decays maximally to a pair of gauge bosons. We therefore choose $b\bar{b}$ and $\gamma\gamma$ as the light Higgs decay modes for our analysis. We must stress that the branching ratio of h to a τ pair is also significant ($\sim 10\%$). Since the parameter space probed by it is similar to that of $b\bar{b}$, we restrict ourselves to the analysis of $b\bar{b}$ in this manuscript.

Now our task is to determine the suitable production mode for a light Higgs decaying to a pair of bottom quarks and photons. Note that analyzing $b\bar{b}$ channel in the ggF or VBF mode is challenging due to the presence of large QCD background. However, the presence of a lepton(s) in addition to the $b\bar{b}$ in Vh or $t\bar{t}h$ production modes could help to suppress these backgrounds. Hence, we choose light Higgs production in association with a W boson and top pair for $b\bar{b}$ analysis.[2] On the other hand, the diphoton channel is one of the cleanest probes for discovering new resonances at the LHC. This channel is also comes with the additional advantage of enhanced sensitivity near the fermiophobic limit in the type-I 2HDM. In this limit, i.e., $\alpha \to \pi/2$, the decay of h to $\gamma\gamma$ becomes prominent and can only be probed through the Vh/VBF production mode as shown in Fig. 5.1. We have considered only the Wh process in our analysis as the parameter space probed by VBF and Zh are exactly the same as that of Wh. The diphoton channel can also be used to probe regions away from the fermiophobic limit through ggF/$t\bar{t}h$ production mode. Since the production cross section of $t\bar{t}h$ is roughly 100 times smaller than that of ggF, we have not considered this for the diphoton analysis. To summarize, we have chosen the following channels[3] for probing the light Higgs at the LHC:
Channel 1: $pp \to h \to \gamma\gamma$.
Channel 2: $pp \to Wh \to W\gamma\gamma$.
Channel 3: $pp \to Wh \to b\bar{b}$.
Channel 4: $pp \to t\bar{t}h \to t\bar{t}b\bar{b}$.
The phenomenological consequences of these channels will be examined in section 5.5.

5.4 Experimental constraints

In this section, we discuss the experimental constraints on the 2HDM parameter space i.e. α, $\tan\beta$ and m_h from the observed Higgs signal strength measurements and the direct searches

[2] Zh production mode is neglected as leptonic branching ratio in case of Z is smaller than W and the parameter space probed by Wh and Zh are exactly the same.

[3] The behavior of the total cross section with respect to α and β corresponding to the four selected channels is discussed in appendix A.4.

of light scalars at LEP and LHC. In our analysis, we have varied α in its full range i.e., $[0 : \pi]$ and $\tan\beta$ in the restricted range of $[1 : 10]$. While the lower value of $\tan\beta$ is chosen to account for the constraints from the flavor observables (as discussed in appendix. A.2, the higher value is restricted to 10 for interesting phenomenology.[4] The organization of this section is as follows. In Secs. 5.4.1 and 5.4.2 we discuss the individual constraints from the signal strength measurements and the direct searches for light scalars, respectively. Towards end of section 5.4.2, the combined effect of the above constraints on the parameter space is presented.

5.4.1 LHC constraints: Signal strength measurements of the 125 GeV Higgs

Since we have identified the heavier CP even Higgs with the observed Higgs boson, its couplings with fermions and gauge bosons – which are different from that of the SM by the factors ξ_H^f, ξ_H^V, ξ_H^γ, get constrained by the signal strength measurements [21]. If the observed Higgs is produced through channel i and decays to j, then the signal strength (μ_j^i) (assuming narrow-width approximation) is defined as [21, 180]

$$\mu_j^i = \frac{\sigma(i \to H)}{\sigma(i \to H_{\rm SM})} \times \frac{{\rm BR}(H \to j)}{{\rm BR}(H_{\rm SM} \to j)} \; = \; \xi_H^{{\rm prod},i} \times \xi_H^{{\rm decay},j} \frac{\Gamma_{H_{\rm SM}}^{\rm tot}}{\Gamma_H^{\rm tot}} \,, \tag{5.4.1}$$

where

$$\xi_H^{{\rm prod},i} = \frac{\sigma(i \to H)}{\sigma(i \to H_{\rm SM})} \,, \quad \xi_H^{{\rm decay},j} = \frac{\Gamma(H \to j)}{\Gamma(H_{\rm SM} \to j)} \,, \quad \Gamma_H^{\rm tot} = \sum_k \xi_H^{{\rm decay},k} \Gamma_H^{k,{\rm SM}} \,.$$

In Table 5.1 we list the production and decay scaling factors for the observed Higgs. Note that these factors are exact only at the leading order. However, the deviations after including the higher-order corrections are small [181] and hence are neglected in the analyses.

Production	$ggF/t\bar{t}H$	VBF/VH	Decay	$f\bar{f}$	VV^*	$\gamma\gamma$
$\xi_H^{\rm prod}$	$(\xi_H^f)^2$	$(\xi_H^V)^2$	$\xi_H^{\rm decay}$	$(\xi_H^f)^2$	$(\xi_H^V)^2$	$(\xi_H^\gamma)^2$

Table 5.1: Scaling factors for the production and decay processes. See Eqs. (5.2.13), (5.2.14) and (A.1.3) for the definitions of ξ_H^f, ξ_H^V and ξ_H^γ respectively.

The measured signal strengths i.e. $(\mu_j^i)^{\rm exp}$ used in our analysis are listed in Table 5.2. Note that these measurements do not constrain the mass of the light Higgs due to the absence of $H \to hh$ the decay mode as we have considered $m_h > m_H/2$ in our analysis. Hence the parameters that are constrained by Higgs signal strength measurements are α and β. In Fig. 5.2, we present the allowed regions in the $(\sin(\beta - \alpha), \tan\beta)$ plane after incorporating constraints from the Higgs signal strength measurements. These regions are determined by

[4]With an increase in $\tan\beta$, the couplings of the light Higgs in the type-I 2HDM with fermions decrease, and for gauge bosons, they become independent of β.

Signal Strength $(\mu_j^{\rm ggF})^{\rm exp}$	ATLAS-CMS (7 − 8 TeV) (combined)	Signal Strength $(\mu_j^{\rm VBF})^{\rm exp}$	ATLAS-CMS (7 − 8 TeV) (combined)
$\mu^{\rm ggF}_{\gamma\gamma}$	$1.10^{+0.23}_{-0.22}$	$\mu^{\rm VBF}_{\gamma\gamma}$	$1.3^{+0.5}_{-0.5}$
$\mu^{\rm ggF}_{ZZ}$	$1.13^{+0.34}_{-0.31}$	$\mu^{\rm VBF}_{ZZ}$	$0.1^{+1.1}_{-0.6}$
$\mu^{\rm ggF}_{WW}$	$0.84^{+0.17}_{-0.17}$	$\mu^{\rm VBF}_{WW}$	$1.2^{+0.4}_{-0.4}$
$\mu^{\rm ggF}_{\tau\bar{\tau}}$	$1.0^{+0.6}_{-0.6}$	$\mu^{\rm VBF}_{\tau\bar{\tau}}$	$1.3^{+0.4}_{-0.4}$

Table 5.2: The combined measured values of $(\mu_j^i)^{\rm exp}$ from ATLAS and CMS using 7 and 8 TeV data [21], used in our analysis. The allowed regions in the parameter space are determined by allowing individual μ_j^i predicted in the type-I 2HDM to lie within $\pm 2\sigma$ from the central values of the measured signal strengths i.e. $(\mu_j^i)^{\rm exp}$.

allowing individual μ_j^i predicted in the type-I 2HDM to lie within $\pm 2\sigma$ of the central values of $(\mu_j^i)^{\rm exp}$ obtained from the combined ATLAS and CMS 7 and 8 TeV data [21]. However, we must mention that we have not employed the χ^2 minimization technique while deriving such allowed regions using data.

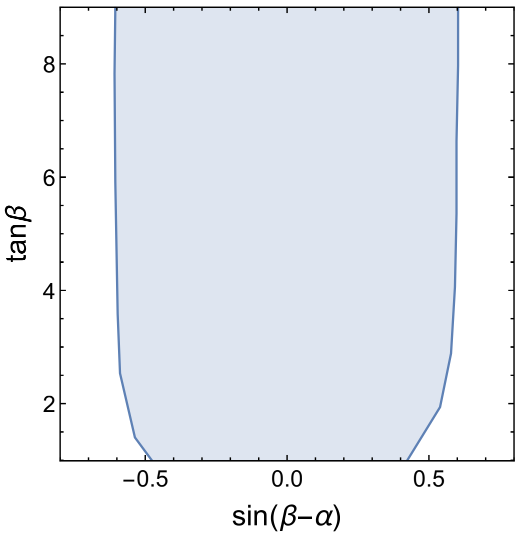

Figure 5.2: The allowed region (shaded in blue) is determined by allowing individual μ_i^j predicted in the type-I 2HDM to lie within $\pm 2\sigma$ of the central values of $(\mu_j^i)^{\rm exp}$ obtained from the combined ATLAS and CMS 7 and 8 TeV data [21]. The signal strengths considered for the analysis are listed in Table 5.2. Note that we have not employed the χ^2 minimization technique in our analysis for determining the allowed regions of the parameter space.

We now discuss the qualitative features of Fig. 5.2. The constraints from the Higgs signal strength measurements force us to remain close to the alignment limit as the heavier CP even Higgs here behaves exactly like the SM Higgs. In Fig. 5.2, one could notice that for $\tan\beta \approx 1$, negative values of $\sin(\beta-\alpha)$ are slightly less constrained than positive ones. In this region, $\sin(\beta-\alpha) > 0$ implies $\alpha < \pi/4$ and $\sin(\beta-\alpha) < 0$ implies $\alpha > \pi/4$. As a result, the Yukawa couplings of the SM-like Higgs which scale as (ξ_H^f) decrease for increasing positive

Light Higgs mass	Maximum allowed $\lvert\sin(\beta-\alpha)\rvert$ from LEP
70 GeV	0.165
80 GeV	0.21
90 GeV	0.39
100 GeV	0.49
110 GeV	0.54

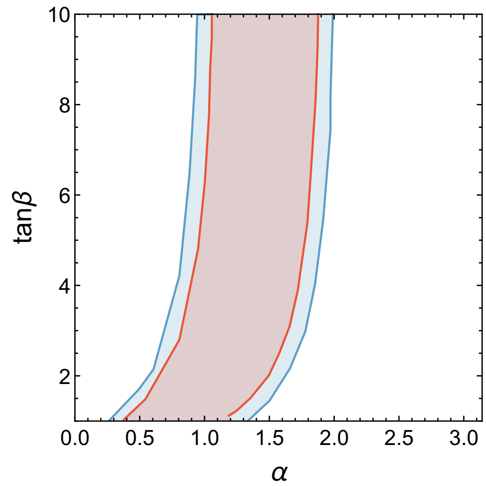

Figure 5.3: In the left panel we list the upper bounds on $|\sin(\beta-\alpha)|$ at 95% C.L. obtained from the LEP direct search measurements [182] for different light Higgs masses. In the right panel we translate these bounds into allowed regions at 95% C.L. in the $(\alpha, \tan\beta)$ plane. The regions shaded in blue(pink) correspond to $m_h = 90$ (100) GeV. Note that the effect of the LEP constraint limits the allowed range of α for a given $\tan\beta$ and light Higgs mass.

values of $\sin(\beta-\alpha)$. Therefore, the signal strength μ_j^{ggF} (which depends on ξ_H^f) drops quickly below the allowed range for positive values of $\sin(\beta-\alpha)$, making this region relatively more constrained. For larger values of $\tan\beta$, $\sin(\beta-\alpha)$ is approximately equal to $\cos\alpha$. Hence, the allowed region in Fig. 5.2 becomes symmetric in $\sin(\beta-\alpha)$ as well as independent of $\tan\beta$. Although, we have plotted effect of signal strength constraints in the $(\sin(\beta-\alpha), \tan\beta)$ plane, this can be easily translated to the $(\alpha,\ \tan\beta)$ plane. The net effect is only to restrict the allowed range of α to be less than π for a given value of $\tan\beta$.

5.4.2 Light Higgs direct search bounds

A CP even scalar has been searched for in the channel $e^+e^- \to Zh$ [182] at LEP. The cross section for this process scales as $(\xi_h^V)^2$, i.e., $\sin^2(\beta-\alpha)$. The absence of any excess in this process has severely constrained $|\sin(\beta-\alpha)|$. In the left panel of Fig. 5.3, we list the upper limits on $|\sin(\beta-\alpha)|$ at 95%C.L. for different masses of the light Higgs [182].

Note that as the center-of-mass energy at LEP was limited to 209 GeV, the production cross section of the light Higgs for the heavier masses faced severe phase-space suppression. As a result, these masses are less constrained by the LEP data. In the right panel of Fig. 5.3, we project the LEP bounds listed in the left panel onto the allowed regions at 95% C.L. in the $(\alpha, \tan\beta)$ plane for $m_h = 90$ GeV (pink) and $m_h = 100$ GeV (blue) for illustrative purposes. Note that the LEP constraint – just like the Higgs signal strength – restricts the allowed range of α to be less than π, for a given $\tan\beta$ and m_h. We must mention that the Tevatron also searched for such a light Higgs in the Vh production mode [183]. However, the Tevatron

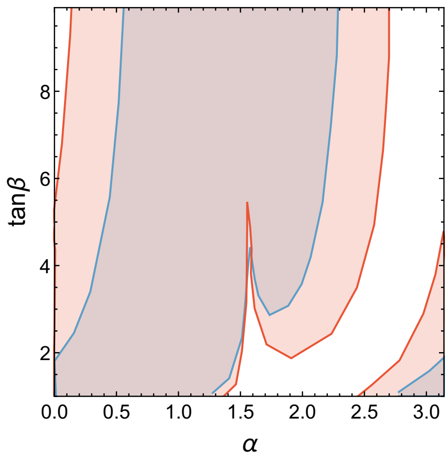

Figure 5.4: We demonstrate the allowed regions by incorporating constraints only from the light scalar searches at the LHC [161, 168, 169] in the (α, $\tan\beta$) plane for $m_h = 90$ GeV (pink band) and 100 GeV (blue band). The masses have been chosen for illustrative purposes as before.

bounds are much less stringent than LEP and hence are not considered in the analysis.

LEP has also searched for a CP odd scalar in the process $e^+e^- \to hA$ [184, 185]. This search is complimentary to $e^+e^- \to hZ$ as the former depends on $\cos^2(\beta-\alpha)$ and the latter on $\sin^2(\beta-\alpha)$. The null results in both production modes significantly constrain both $\sin(\beta-\alpha)$ and $\cos(\beta-\alpha)$ and require them to be much less than unity. If both h and A are light at the same time such that $m_A + m_h < 209$ GeV, then the combined direct search constraints of h and A rule out a significant part of the parameter space including the regions which satisfy the alignment limit. Therefore, our choice of demanding a heavy pseudoscalar is in sync with the requirement of a light Higgs.

Both the ATLAS and CMS collaborations have searched for additional light scalars in the diphoton final state [161, 168, 169]. While CMS has placed 95% C.L. upper bounds on the total cross section for a light scalar decaying to $\gamma\gamma$ for the production modes ggF+$t\bar{t}h$ and VBF+Vh. On the other hand, ATLAS instead provides an inclusive bound for the combination of all of the production modes. To understand the effect of these measurements on the parameter space of the 2HDM, let us note the behavior of the total cross section of the light Higgs decaying to a pair of photons. We now know that the light Higgs branching ratio to a pair of photons is large near the fermiophobic limit and could be probed in the VBF+Vh production mode. However, in this case, the total cross section, i.e., $\sigma \times$ BR is large only for smaller values of $\tan\beta$ and tends to zero for larger values of $\tan\beta$ (see Table A.1 in appendix A.4). For regions away from the fermiophobic limit, although the branching ratio of the light Higgs to a diphoton is not large, this decay could still be probed in the ggF mode owing to its large production cross section.

The effect of the LHC direct detection constraints [161, 168, 169] are displayed in Fig. 5.4, where we plot the allowed parameter space in the $(\alpha, \tan\beta)$ plane for $m_h = 90$ GeV (pink

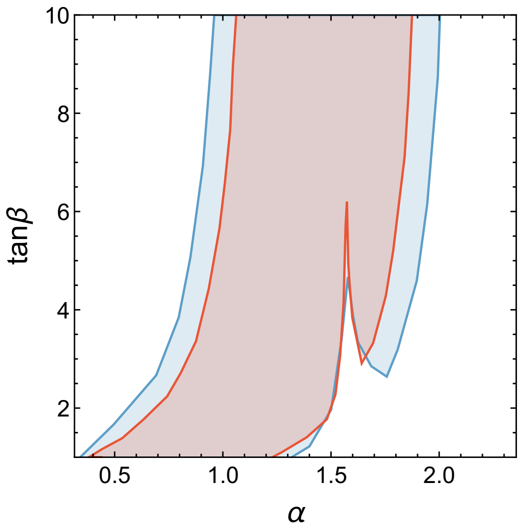

Figure 5.5: The net allowed parameter space for the type-I 2HDM in the $(\alpha, \tan\beta)$ plane for $m_h = 90$ GeV (pink band) and 100 GeV (blue band) after combing measurements from the Higgs signal strength [21] and the direct searches for light scalar at LEP and LHC [161, 168, 169, 182]. The wedge-like disallowed region around $\alpha \approx \pi/2$ arises from the direct searches for the light Higgs decaying to the a diphoton at the LHC. This constraint gets relaxed for larger values of $\tan\beta$ and with increasing mass of the light Higgs due to suppression in the production cross section.

band) and 100 GeV (blue band). The masses have been chosen for illustrative purposes as before. The combined bounds from ATLAS and CMS near the fermiophobic limit are sensitive only to the VBF+Vh production mode, where the total cross section is large for smaller $\tan\beta$ values. Consequently, this region gets severely constrained and results in a wedge-like exclusion around $\alpha \approx \pi/2$ as can be seen in Fig. 5.4. For regions away from the fermiophobic limit, the combined constraints from ATLAS and CMS [161, 168, 169] are far more stringent for $m_h = 100$ GeV than 90 GeV, hence rule out a significant part of the parameter space for the same.

Now we combine the individual constraints from the Higgs signal strength measurements [21] and the direct searches of the low mass scalars at LEP and LHC [161, 168, 169, 182]. The results are shown in Fig. 5.5 in the $(\alpha, \tan\beta)$ plane for $m_h = 90$ GeV (pink band) and 100 GeV (blue band). As already noted, the effect of the direct detection constraints from LEP and the Higgs signal strength measurements is to restrict the allowed range of α to be less than π. In our case, the LEP constraints are far more stringent than those arising from the Higgs signal strength. In Fig. 5.5, we can see that the allowed range of α increases with as the light Higgs mass increases. This happens due to the relaxed LEP constraints for heavier light Higgs mass (see left panel of Fig. 5.3). In contrast, the direct search for a light Higgs at the LHC rules out a wedge-like region around the fermiophobic limit and some regions away from the fermiophobic limit. However, the constraints for the latter from the LHC are much weaker than the LEP constraints and consequently are masked in the combination (see Fig. 5.5). Note that the LHC constraint around the fermiophobic limit gets relaxed for larger values of $\tan\beta$ and with increasing mass of the light Higgs due to suppression in the production cross section.

5.5 Future prospects at LHC Run-2

In this section, we discuss the prospects of observing a light Higgs boson in the following channels: $pp \to h \to \gamma\gamma$, $pp \to Wh \to W\gamma\gamma$, $pp \to Wh \to b\bar{b}$, and $pp \to t\bar{t}h \to t\bar{t}b\bar{b}$. The signal and background processes[5] corresponding to each channel are generated using the event generators `Madgraph` [123] or `Pythia-8` [186] (depending on the number of final-state hard particles at the parton level) with the `NN23LO1` [187] parton distribution function. The generated events are then showered and hadronized using `Pythia-8`. Note that the collider analysis has been carried out in `Pythia`. We have not performed any detector simulation in the analysis. We now describe the basic cuts used in our analysis.

1. A minimum cut of 20 GeV is imposed on the transverse momentum of photons, electrons, muons, and missing energy.

2. Owing to the finite resolution of the electomagnetic calorimeter, photons and electrons (muons) are accepted for further analysis if their pseudorapidities are less than 2.5 (2.7).

3. Photons and leptons (electrons and muons) are required to be isolated, meaning free from the dominant jet activity in their nearby regions.

4. In experiments, there is a typical 5% probability for an electron to fake a photon, due to track mismeasurements. Since this feature is not present in `Pythia`, we take this into account in our analysis with the help of a random number. We randomly select 5% events, where an electron is mistagged as a photon.

5. The hadrons are clustered into jets with jet radius $R = 0.4$ using anti-k_T algorithm [188]. The jets that satisfy — $p_T^{\text{jet}} > 30$ GeV and $|\eta| < 4.5$ are retained for further analysis.

6. For the topologies which require b tagging, ΔR is computed between a b parton and each of the anti-k_T jets. If it happens to be less than 0.1, we convolute it with an additional 70% b-tag efficiency factor.

Note that the above cuts (criteria) imposed on the final-state objects in `Pythia` are extremely generic and not specific to any process under consideration. Hence these fall under the category of preselection cuts. In the coming sections, we discuss the detailed collider analysis

[5] Note that there are two types of backgrounds associated with a particular signal topology: reducible and irreducible. While the irreducible backgrounds consist of exactly the same final states, the reducible backgrounds are somewhat different and contribute to a particular signal topology because of the misidentification of objects.

of observing the light Higgs boson. The signal significance[6] is computed over the allowed parameter space as a function of α, $\tan\beta$, and m_h.

5.5.1 Channel 1: $pp \to h \to \gamma\gamma$

We begin with the analysis of the light Higgs boson decaying to the diphoton final state. For our signal topology, the irreducible background arises from the tree-level quark-antiquark as well as loop-induced gluon-gluon annihilation to $\gamma\gamma$. The reducible backgrounds arise from $j\gamma$, jj and e^+e^- final states, respectively, where a jet(s) or lepton(s) fakes a photon(s). The QCD backgrounds can be considerably reduced by demanding the final-state photons to be isolated (see Table. 5.3). The background due to the Z-pole contributions in the Drell-Yan ($Z \to ee$) process also dilutes the diphoton signal for light Higgs masses around m_Z due to its large cross section, even though the mistagging rate for an electron to fake a photon is small.

The preselection criteria discussed in the previous section are extremely generic and cannot aid in effective signal-background separation. Additional cuts on the kinematic variables i.e., the transverse momentum (p_T) and the invariant mass of the diphoton pair are necessary for further reduction in the background processes. To illustrate this point, in Fig. 5.6, we plot the normalized transverse momentum distributions for the leading isolated photon (p_T^γ) corresponding to the signal (with $m_h = 110$ GeV) and the SM backgrounds. The p_T for the signal distribution peaks approximately at $m_h/2$ and for backgrounds processes (e.g., $\gamma\gamma$, $j\gamma$, and jj) it peaks at much lower values (although in the plot only the $\gamma\gamma$ background is shown). Therefore, suitable choice of the cuts on the leading and subleading isolated photon candidates and the invariant mass of the diphoton pair can enhance the signal significance. The selection cuts used for the diphoton analysis are as follows:

$$p_T \,\text{selection} \;:\; p^\gamma_{T_\text{lead}} > 40 \text{ GeV} \;, p^\gamma_{T_\text{sub}} > 30 \text{ GeV} . \tag{5.5.1}$$

$$m^{\gamma\gamma}_\text{inv} \,\text{selection} \;:\; |m^{\gamma\gamma}_\text{inv} - m_h| < 2.5 \text{ GeV} . \tag{5.5.2}$$

Here $p^\gamma_{T_\text{lead}}$ and $p^\gamma_{T_\text{sub}}$ correspond to the transverse momentum of the leading and subleading photon, respectively and $m^{\gamma\gamma}_\text{inv}$ corresponds to the invariant mass of the diphoton pair. Table 5.3 shows the efficiencies of the preselection and selection cuts on the signal and background processes, where the efficiency of a cut is defined as

$$\text{Efficiency} \equiv \frac{\text{Number of events after imposing the cut}}{\text{Number of events before imposing the cut}} \tag{5.5.3}$$

After imposing the preselection and selection cuts on the signal and background processes, we are in a position to determine the signal significance for the light Higgs boson as a function

[6]The significance S of observing signal over background is defined as $\dfrac{s}{\sqrt{s+b}}$, where s and b are the number of signal and background events respectively.

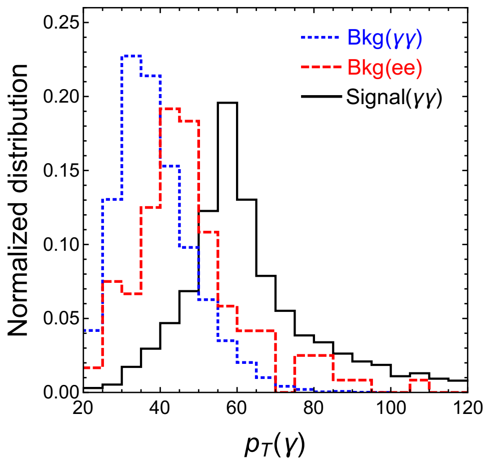

Figure 5.6: The figure illustrates the normalized p_T distributions of the leading isolated photon in the channel $\gamma\gamma$ for the signal and background processes. Here Signal ($\gamma\gamma$) corresponds to the light Higgs boson of mass $m_h = 110$ GeV, which is produced in the gluon-fusion process and decays to a pair of photons, Bkg($\gamma\gamma$) corresponds to the irreducible diphoton background and Bkg(ee) corresponds to reducible background where both electrons fake a photon

.

Cuts	Efficiency				
	Signal	Backgrounds			
		$\gamma\gamma$	$j\gamma$	jj	ee
Preselection	0.59	0.377	0.019	1.0×10^{-6}	1.0×10^{-3}
p_T selection	0.84	0.28	0.21	~ 0	0.45
$m_{\text{inv}}^{\gamma\gamma}$ selection	0.99	0.082	0.024	0	$\sim 10^{-4}$

Table 5.3: The efficiencies of the signal and background processes against different cuts are listed for Channel 1. The light Higgs mass is chosen to be 110 GeV for illustration. The dijet background becomes negligible after imposing all of the cuts.

of its mass and mixing angles α and β. In Fig. 5.7 (a), we plot the significance of observing h i.e. $S(\gamma\gamma)$ with respect to α for $m_h = 100$ GeV and an integrated luminosity $\mathcal{L} = 300$ fb^{-1} for different values of $\tan\beta$. In Fig. 5.7 (b) we repeat the exercise with $m_h = 110$ GeV. Note that the significance for smaller masses is negligible, and hence it is not shown in the plot. We now discuss the qualitative features of Fig. 5.7 with respect to α and $\tan\beta$. The discontinuities in Fig. 5.7 (a) for $\tan\beta = 3$ and 4 near the fermiophobic limit, correspond to the excluded regions from the direct searches of the light Higgs at the LHC as discussed in section 5.4.2. In addition, the constraints from LEP has limited the allowed range of α to be less than π for a given light Higgs mass and $\tan\beta$ (see discussions in section 5.4.2). The dip in the significance signifies the regions where the total cross section proportional to $\xi_h^f \times \xi_h^\gamma$ vanishes. The first minimum occurs where ξ_h^γ vanishes due to cancellation of the top and W loop contribution[7] in $h \to \gamma\gamma$ whereas the second minimum corresponds to the

[7] For large values of $\tan\beta$, the dip corresponding to $\xi_h^\gamma \to 0$ shifts towards $\alpha \approx \pi/2$ [see Eq. (A.1.3)].

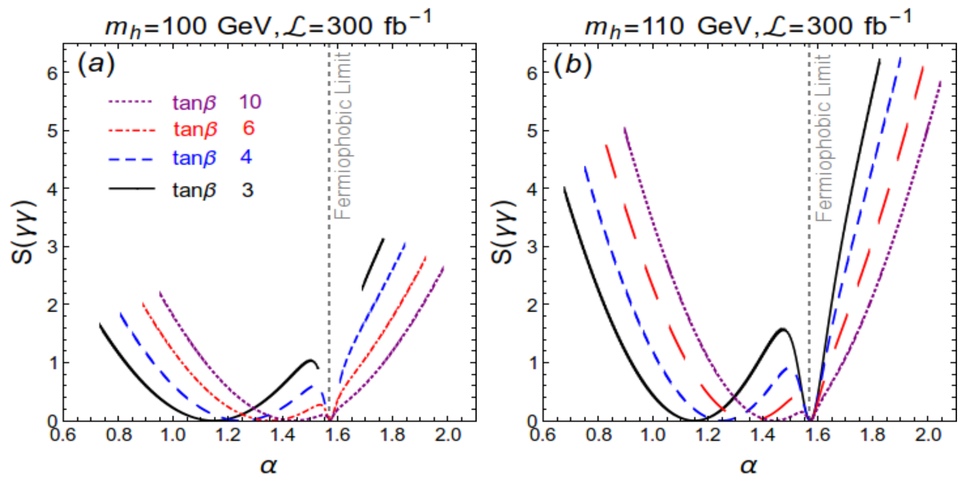

Figure 5.7: Variation of the signal significance $S(\gamma\gamma)$ with α for $m_h = 100\,,110$ GeV and $\mathcal{L} = 300$ fb^{-1} for different values of $\tan\beta$. Panel (a) corresponds to $m_h = 100$ GeV and panel (b) to 110 GeV. The vertical gray dashed line corresponds to $\alpha = \pi/2$ i.e., the fermiophobic limit. Here the signal significance drops to zero as expected. Hence, the light Higgs produced in gluon fusion is insensitive to the alignment limit. The discontinuities in panel (a) for $\tan\beta = 3$ and 4 near the fermiophobic limit, correspond to the excluded regions from the direct searches of the light Higgs at LHC as discussed in section 5.4.2.

fermiophobic limit ($\xi_h^f \to 0$). Hence, this channel is ineffective in probing the regions close to the fermiophobic limit. The significance of observing the signal in this channel is larger for $\alpha > \pi/2$ as $\sin(\beta - \alpha)$ is negative in this region. As a consequence, the top- and W loop interfere constructively and enhance the diphoton rate.

5.5.2 Channel 2: $pp \to Wh \to W\gamma\gamma$

In this section, we analyze the discovery prospects of the light Higgs boson in the channel $W\gamma\gamma$ at 13 TeV center-of-mass energy, where the leptonic decays (only e and μ) of W are considered. The SM backgrounds arises from $pp \to W\gamma\gamma$, $pp \to Wj\gamma$, $pp \to Wjj$ and $pp \to WZ\,(Z \to e^+e^-)$. The background reduction methods are exactly the same as the ones discussed in section 5.5.1, and hence we refrain from discussing them in this section.

The signal is characterized by the presence of at least one isolated lepton, two isolated photons and missing energy. The selection cuts used in the analysis are

$$\begin{aligned} p_T\,\text{selection} &: \; p_T^\ell > 30 \text{ GeV}\,, \mathrm{E}_\mathrm{T}^\mathrm{miss} > 30 \text{ GeV}\,, p_{T_\mathrm{lead}}^\gamma > 40 \text{ GeV}\,, p_{T_\mathrm{sub}}^\gamma > 30 \text{ GeV}\,. \\ m_\mathrm{inv}^{\gamma\gamma}\,\text{selection} &: \; |m_\mathrm{inv} - m_h| < 2.5 \text{ GeV}\,. \end{aligned}$$

Here p_T^ℓ corresponds to the transverse momentum of leptons (e and μ) and $\mathrm{E}_\mathrm{T}^\mathrm{miss}$ denotes the total missing transverse energy. We refer to Table 5.4 for the effect of preselection and selection cuts on the signal and background processes. This channel allows us to probe the regions close to fermiophobic limit where production via the gluon-fusion process loses its

Cuts	Efficiency			
	Signal	Backgrounds		
		$W\gamma\gamma$	$Wj\gamma$	Wee
Preselection	0.29	0.042	0.032	4.9×10^{-3}
p_T selection	0.55	0.186	0.36	0.308
$m_{\rm inv}^{\gamma\gamma}$ selection	0.98	0.028	0.023	6×10^{-3}

Table 5.4: The efficiencies of the signal and background processes against different cuts for Channel 2. The light Higgs mass is chosen to be 110 GeV for illustration.

sensitivity. In Fig. 5.8, the significance $S(\ell\nu\gamma\gamma)$ of the signal with respect to α for 100 fb^{-1} integrated luminosity is plotted for four different values of mass of the light Higgs. We now summarize the distinctive features of Fig. 5.8 below:

1. For a given light Higgs mass, the significance in this channel decreases as $\tan\beta$ increases, as the production cross section (proportional to ξ_h^V) decreases for large values of $\tan\beta$.

2. The branching ratio of $h \to WW^*$ increases significantly for larger values of m_h. Furthermore the decay, $h \to Z\gamma$ also opens up for $m_h > m_Z$. As a result, the branching ratio of the light Higgs to diphotons decreases with increase in m_h. This reduces the signal significance substantially.

3. The discontinuities in Fig. 5.8 correspond to the disallowed regions from the LEP, and LHC direct search measurements. The chopped-off upper half of the curves in Fig. 5.8 (a) for $\tan\beta = 4, 6$, Fig. 5.8 (b) for $\tan\beta = 3, 4, 6$ and Fig. 5.8 (c) for $\tan\beta = 3, 4$ near $\alpha \approx \pi/2$ are due to the LHC constraint. These are exactly the disallowed wedge-shaped regions in Fig. 5.5. Note that the bounds from the LHC become insignificant for larger values of $\tan\beta$ and m_h. The direct search bounds from LEP on the other hand, constrain the minimum and the maximum values of α. This restricts the net allowed range of α to be less than π. Since in Fig. 5.8 we highlight regions close to the fermiophobic limit, the net effect of the LEP constraints is not visible.

To conclude, regions around the fermiophobic limit can be best explored at the 13 TeV LHC for lower masses of the light Higgs and intermediate $\tan\beta$ values.

5.5.3 Channel 3: $pp \to Wh \to W\, b\bar{b}$

In this section, we analyze the discovery prospects of the light Higgs in the $Wb\bar{b}$ channel, where we consider leptonic decays of W. The signal is characterized by $Wb\bar{b}$, where we tag the leptonic (e and μ) decays of W. The signal is categorized by the presence of two b-tagged jets, an isolated lepton and missing energy. In spite of the fact that it is the dominant decay channel in most of the parameter space, the $b\bar{b}$ mode is difficult to probe because of the presence of the enormous QCD background. The SM irreducible background arises from

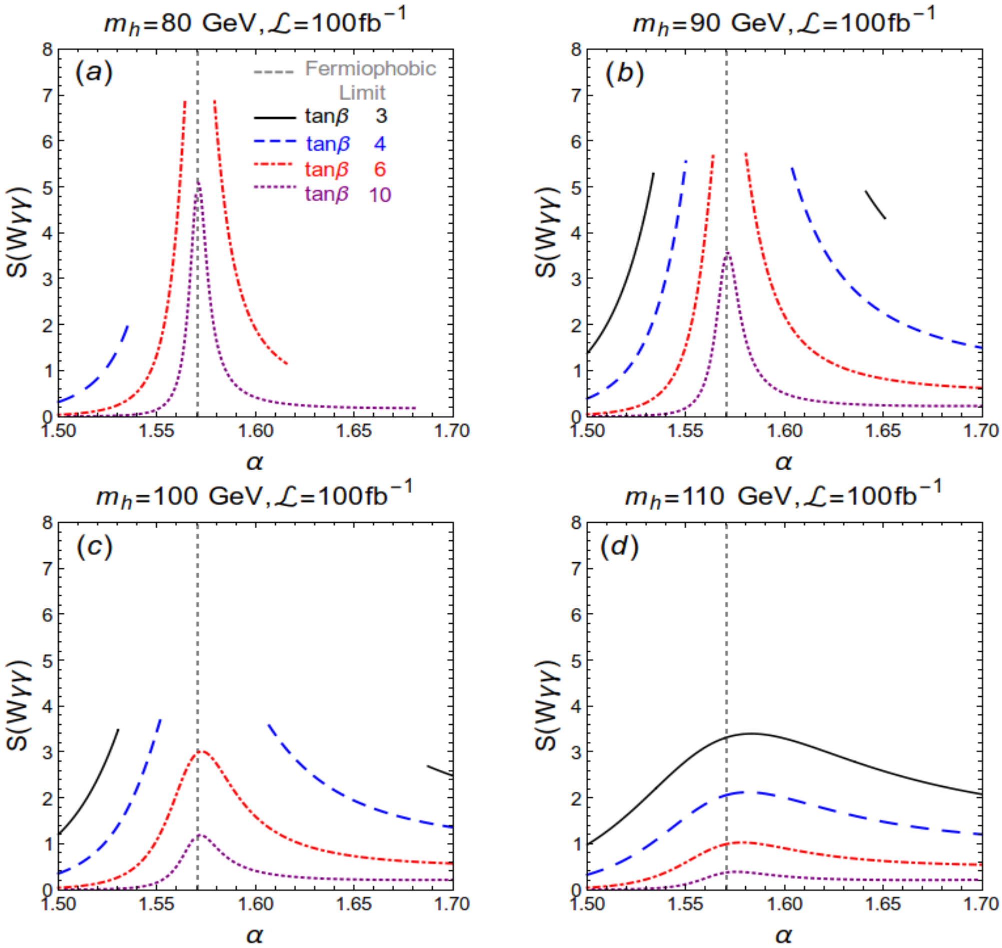

Figure 5.8: Variation of the signal significance $S(W\gamma\gamma)$ with α for $m_h = 80, 90, 100, 110$ GeV for $\mathcal{L} = 100$ fb^{-1} for different values of $\tan\beta$. The color code is the same as in Fig. 5.7. Note that the range of α is restricted in the plot to signify the regions with reasonable significance. The discontinuities in panel (a) for $\tan\beta = 4$ and 6, panel (b) for $\tan\beta = 3$, 4 and 6, panel (c) for $\tan\beta = 3$ and 4 near the fermiophobic limit correspond to the excluded regions from the direct searches of the light Higgs at LHC-I as discussed in section 5.4.2. The absence of the $\tan\beta = 3$ line in panel (a) is attributed to constraints from LEP which set an upper limit on α and require it to be less than 1.5 for $\tan\beta = 3$ and $m_h = 80$ GeV.

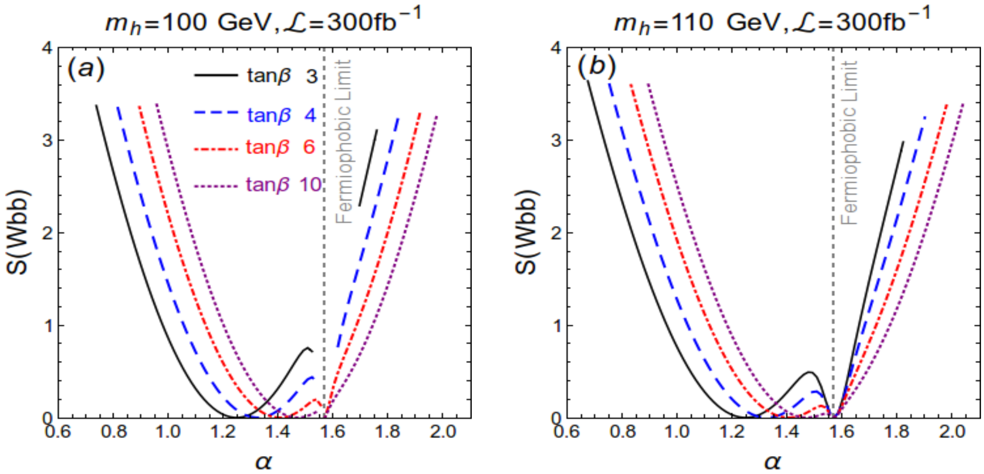

Figure 5.9: Variation of the signal significance $S(Wbb)$ with α for m_h = 80, 90, 100, 110 GeV for $\mathcal{L} = 300$ fb^{-1} for different values of $\tan\beta$. The color code is the same as in Figs. 5.7 5.8. This channel is also insensitive around the fermiophobic limit.

$pp \to WZ$. The reducible background arise from $pp \to t\bar{t}$ where one of the W's is along the beam line and hence escapes detection, and W+jets where light-quark jets are mistagged as b-jets. The Wh production rate is governed by the magnitude of ξ_h^V and is small in the favored parts of the parameter space. With a small signal cross section in comparison to large backgrounds, it is difficult to isolate signal events from huge SM backgrounds in the $2b + \ell + E_T^{\rm miss}$ final state at the LHC. In order to achieve appreciable significance at the LHC, we follow the analysis of Ref. [170] and consider the Wh process in the boosted regime. Although we lose a significant number of events by demanding boosted Higgs ($p_T^h > 200$ GeV), it enables us to overcome huge SM backgrounds quite efficiently. We reconstruct a fat jet with radius parameter $R_J = 0.8$ and transverse momentum $p_T^J > 200$ GeV. We then tag the fat jet as a Higgs using the mass-drop technique discussed in appendix A.3.

The analysis is performed with 14 TeV centre-of-mass energy for m_h = 70, 80, 100 and 110. We have not considered m_h = 90 GeV in our analysis as it is difficult to isolate the signal from the huge $Z \to b\bar{b}$ background. We summarize our selection criteria as follows:

$$\begin{aligned}
&p_T^\ell > 30 \text{ GeV}\,, \mathrm{E_T^{miss}} > 30 \text{ GeV}\,, \mathrm{p_T^W} = |\mathrm{p_T^\ell} + \mathbf{p_T^{miss}}| > 200\mathrm{GeV}\,, \mathrm{R_J} = 0.8\,,\\
&p_T^J > 200 \text{ GeV}\,, |\mathrm{m_h} - \mathrm{m_J}| < 5 \text{ GeV} \quad \left(\text{for } \mathrm{m_h} \leq 90 \text{ GeV}\right)\,,\\
&p_T^J > 250 \text{ GeV}\,, |m_h - m_J| < 8 \text{ GeV} \quad \left(\text{for } m_h > \ 90 \text{ GeV}\right)\,,
\end{aligned}$$

where p_T^W is the magnitude of the vector sum of the momentum of the lepton and missing energy in the transverse plane. The efficiencies of these cuts are displayed in Table. 5.5. We can see that by demanding at least one fat jet and anti-k_T jet reduces $Wb\bar{b}$ and $W3j$ backgrounds. Also, by invoking a fat jet with no jet activity outside and MassDrop with a double b-tag, we are able to suppress the $t\bar{t}b\bar{b}$ process very effectively.

After imposing the above cuts, we compute the signal significance for the light Higgs boson as a function of its mass and mixing angles α and β. In Fig. 5.9 we plot the significance of observing the light Higgs as a function of α. Figures 5.9 (a) and 5.9 (b) represent the significance with an integrated luminosity of 300 fb^{-1} for $m_h = 100$ and 110 GeV respectively. Again, the discontinuities in Fig. 5.9 arise due to direct detection constraints from LEP and LHC. It is interesting to note the behavior of the signal significance in Fig. 5.9. The dip in the plot signifies the points where the total cross section proportional to $\xi_h^V \times \xi_h^f$ vanishes. The first dip corresponds to $\xi_h^V \to 0$ and the second dip represents $\xi_h^f \to 0$ (fermiophobic limit). Hence, this channel is useful in probing regions away from the fermiophobic limit.

Cuts	Efficiency			
	Signal	Backgrounds		
		Wbb	$W3j$	$t\bar{t}b\bar{b}$
At least one fat jet and anti-k_T jet	0.45	0.11	0.10	0.47
Isolated leptons	0.86	0.71	0.68	0.21
One fat jet with no anti-k_T jet	0.5	0.27	0.16	0.019
$E_T^{\rm miss} > 30$ GeV	0.987	0.93	0.93	0.99
$p_T^W > 200$ GeV	0.93	0.88	0.85	0.77
MassDrop with double b-tag	0.32	0.299	0.0037	0.031
Inv. mass	0.79	0.077	0.077	0.11

Table 5.5: The efficiencies of the different cuts used for the analysis of Channel 3 for both signal and background processes. The numbers are for a light Higgs mass of 110 GeV.

5.5.4 Channel 4: $pp \to t\bar{t}\,h \to t\bar{t}\,b\bar{b}$

Continuing with the discussion of a light Higgs decaying to $b\bar{b}$, we now focus our attention on the $t\bar{t}h$ production mode, where semileptonic decays of top-pair are considered The irreducible background here arises from the $t\bar{t}b\bar{b}$ final state and the reducible background arises from $t\bar{t}+$jets, where a jet fakes the bottom quark. Due to the presence of four b quarks in the final state, it is difficult to reconstruct the light Higgs accurately due to the various possible combinations. This problem can be addressed by resorting to boosted scenarios where the decay products of the hadronically decaying top and light Higgs are enclosed within a single jet of large radius parameter. Therefore, our signal essentially comprises of two fat jets, an isolated lepton, missing energy and one anti-kT b tagged jet. To tag the top and Higgs jets, we first construct the fat jets with $p_T^J > 125$ GeV and $\Delta R = 1.2$. The jets satisfying $p_T^J > 250$ GeV are tagged as top-jet if they satisfy the prescription described in appendix. A.3. Similarly the remaining jets are tagged as the Higgs jets if they satisfy the mass drop criteria and the filtered jet mass, $m_J^{\rm Higgs}$, lies within 5/10 GeV window about the light Higgs mass (see appendix. A.3 for more details). In addition, we demand a b-tagged jet outside the top and Higgs fat jet. This helps in further eliminating the $t\bar{t}$+jets background. We summarize

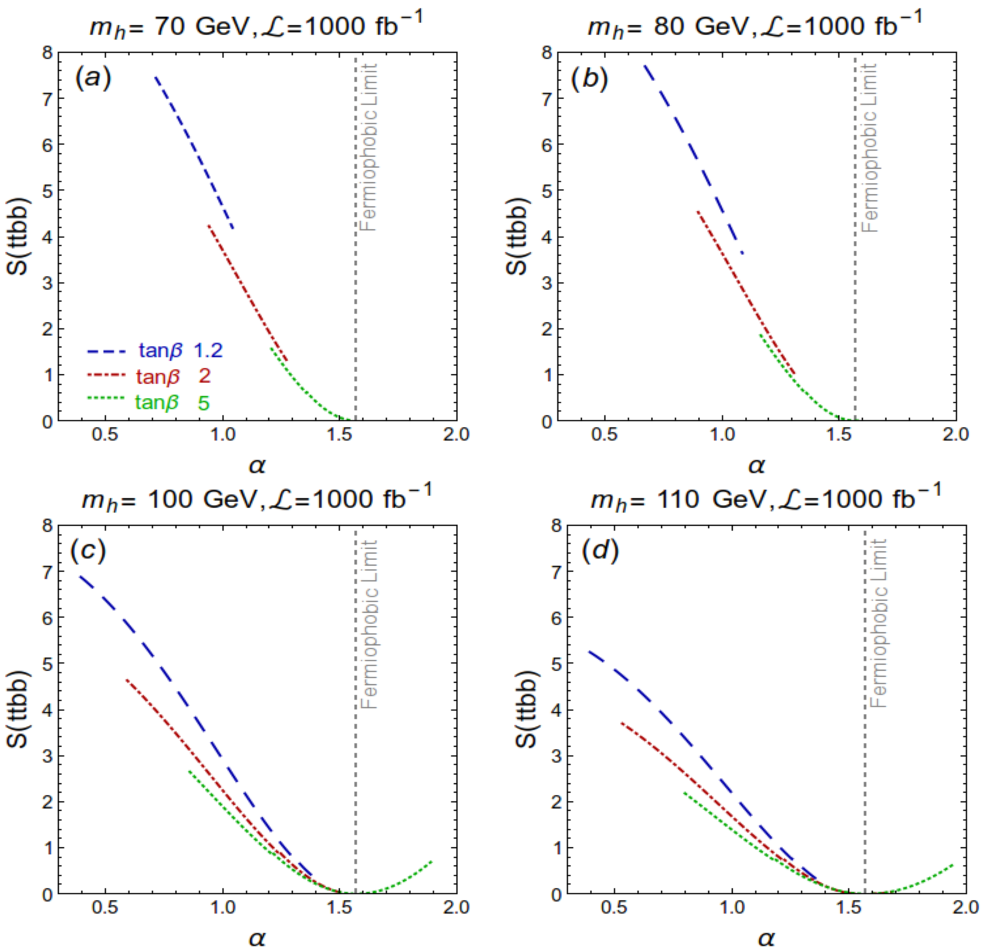

Figure 5.10: Variation of the signal significance $S(t\bar{t}b\bar{b})$ in the channel $t\bar{t}b\bar{b}$ with α for different values of m_h at 1000 fb^{-1} integrated luminosity. While the dark blue, dark red, and dark green dashed lines correspond to $\tan\beta = 1.2$, 2, and 5, respectively, the dashed gray vertical line for $\alpha = \pi/2$ illustrates the fermiophobic limit. Owing to enhanced sensitivity of $\sigma(pp \to t\bar{t}h \to t\bar{t}b\bar{b})$ for low $\tan\beta$, we have chosen slightly lower values of $\tan\beta$ for this channel.

the cuts used in the analysis below:

$$\begin{aligned}
&p_T^{\ell} > 30 \text{ GeV} , \mathrm{E_T^{miss}} > 30 \text{ GeV} , \mathrm{p_T^{top}} > 250 \text{ GeV}, \ 150 \text{ GeV} < \mathrm{m_J^{top}} < 200 \text{ GeV} , \\
&p_T^{\rm Higgs} > 125 \text{ GeV} , |m_J^{\rm Higgs} - m_h| < 5 \text{ GeV} \qquad \big(\text{for } m_h \leq 90\text{GeV}\big) \\
&p_T^{\rm Higgs} > 160 \text{ GeV} , |m_J^{\rm Higgs} - m_h| < 10 \text{ GeV} \qquad \big(\text{for } m_h > 90 \text{ GeV}\big) .
\end{aligned}$$

The efficiencies of the individual cuts are listed in Table 5.6. We are now in a position to estimate the signal significance i.e., $S(t\bar{t}b\bar{b})$ as a function of α, $\tan\beta$, and m_h. In Fig. 5.10 we plot the significance of observing a light Higgs for four different light Higgs masses: $m_h =$ 70, 80, 100, and 110 GeV. We have not considered $m_h = 90$ GeV for the analysis because in that case it will be difficult to isolate the signal events from the large $t\bar{t}Z$ background. Note that we have chosen smaller $\tan\beta$ values as the total cross section decreases with increase in β (see Table. A.1). The significance is higher for lower values of α. Hence this channel is effective for probing lower $\tan\beta$ and α regions. This particular mode for probing the light Higgs does not work out in the fermiophobic limit as both the production cross section and decay branching ratio are negligible.

Cuts	Efficiency		
	Signal	Backgrounds	
		$ttbb$	$tt+3j$
Isolated leptons	0.53	0.56	0.57
Two fat jets	0.31	0.17	0.20
$p_T^\ell > 30$ GeV, $E_T^{\text{miss}} > 30$ GeV	0.76	0.65	0.63
Top tagged	0.11	0.088	0.13
Mass drop with double b-tag and inv mass	0.056	0.011	0.0009
anti-kT b-jet outside top and Higgs jet	0.28	0.25	0.50

Table 5.6: We list the efficiencies of the different cuts used for the analysis of Channel-4 for both signal and background processes. The numbers are for light Higgs mass 110 GeV.

5.6 Summary and concluding remarks

To summarize, we study the prospects of observing a CP-even scalar lighter than the observed 125 GeV Higgs at the LHC, in the context of Type-I 2HDM. We identify the heavier CP-even Higgs in the 2HDM with the discovered Higgs. We also consider the charged and pseudoscalar Higgs bosons to be heavy. This choice simplifies the 2HDM parameter space and leaves α, $\tan\beta$, and mass of the light Higgs (m_h) as the relevant free parameters. We consider various theoretical and experimental constraints to determine the allowed regions in the parameter space. The mass of the light Higgs is taken to be greater than 62.5 GeV to avoid $H \to hh$ decay.

To study the phenomenology of the light Higgs at the LHC, we determine the suitable production and decay modes. In most parts of the parameter space, the light Higgs in Type-I 2HDM decays dominantly to $b\bar{b}$. However, for regions close to the fermiophobic limit, its decay to bosons, mainly photons, becomes dominant. Therefore, we focus on the light Higgs decay to $b\bar{b}$ and $\gamma\gamma$ in this analysis. Analyzing $b\bar{b}$ in the ggF or VBF production mode is challenging due to the large QCD background. We choose the light Higgs production in association with the W boson and top pair for the $b\bar{b}$ analysis. Furthermore, we tag the light Higgs in the boosted regimes, for better signal significances. The choice of the production mode for $\gamma\gamma$ channel is much simpler because of its better reconstruction properties. We choose the Wh production mode for analyzing regions close to the fermiophobic limit, and the ggF production mode for regions away from the fermiophobic limit.

We analyze the discovery prospects of the light Higgs boson in four channels viz. $pp \to h \to \gamma\gamma$, $pp \to Wh \to W\gamma\gamma$, $pp \to Wh \to Wb\bar{b}$, and $pp \to t\bar{t}h \to t\bar{t}b\bar{b}$ at the LHC. We find interesting regions in the parameter space of 2HDM which could be probed at the future

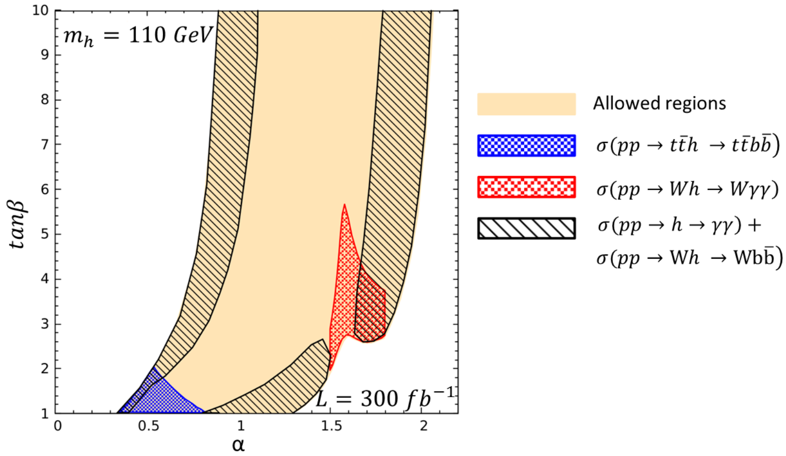

Figure 5.11: The plot illustrates the regions of the allowed parameter space, which could be probed/excluded in different channels with significances greater than 2σ for the light Higgs boson of mass 110 GeV at the LHC with 300 fb^{-1} of integrated luminosity. While the contour shaded in yellow illustrates the total allowed region in the $(\alpha, \tan\beta)$ plane for $m_h = 110$ GeV, we can probe only the hatched regions with significances greater than 2σ, leaving behind regions which satisfy the alignment limit, $\alpha \approx \beta$. Here, we have combined the allowed regions for $pp \to h \to \gamma\gamma$ and $pp \to Wh \to Wb\bar{b}$ due to their similar behaviour.

runs of the LHC with a few hundred fb^{-1} of Luminosity. We summarize our findings in Fig. 5.11 for $m_h = 110$ GeV and $\mathcal{L} = 300$ fb^{-1}. In this plot, the contour shaded in yellow illustrates the total allowed region for $m_h = 110$ GeV. The hatched portions denote the regions where the above channels could be probed with significances greater than 2σ at the LHC. The un-hatched regions in the allowed contour correspond to $\alpha \approx \beta$ and approximately satisfy the alignment limit. As already noted, such regions would be difficult to probe/rule-out in near future. For the purpose of the plot, we have combined the allowed regions for $pp \to h + X \to \gamma\gamma + X$ and $pp \to Wh + X \to Wb\bar{b} + X$ as they probe almost similar parts of the parameter space (see appendix A.4).

Searches of physics beyond the Standard Model till date have yielded neither any significant results nor specific directions to follow. However, the current measurements still do not rule out the possibility of the observed 125 GeV scalar belonging to some enlarged sector. In this chapter, we examined a possible scenario in context of Type-I 2HDM and studied the prospects of observing a light CP-even scalar at the future runs of LHC. Our aim in the study was to put together all the relevant information and provide an optimized search strategy for the light Higgs at the LHC. The discovery of such a light scalar would not only open doors to the new physics but also help us to understand the mechanism of electroweak symmetry breaking better.

Chapter 6

Dissecting Multi-Photon Resonances at the Large Hadron Collider

This chapter deals with the analysis concerning disentanglement of multi-photon topologies with the diphoton ones. The work has been done in collaboration with Dr. Abhishek Iyer and Prof. B.C. Allanach and is published in Eur. Phys. J. C 77, no. 9, 595 (2017).

6.1 Introduction

In this chapter, we consider a hypothetical new boson X, with mass around a TeV-scale, decaying dominantly to photons, which can potentially give rise to an excess in the diphoton final state.

There are mainly two kind of topologies which could result in such an effect viz., the standard and the non-standard ones. In the standard case, the decay proceeds in the conventional manner i.e. $pp \to X \to \gamma\gamma$. The non-standard topologies result in multi-photon[1] final states, but the decay products appear to be diphotons from the detector point of view. Here the heavy resonance X decays first to lighter particles n, which further decay into diphotons, thereby leading to a multi-photon final state. Since $m_n << m_X$, photons from n are highly collimated and this creates an illusion of a diphoton final state in the detector.

We are interested in the disentanglement of the standard versus the non-standard topologies in our analysis. To perform this segregation, we have ignored the SM backgrounds. For this to be a good approximation, we require the backgrounds to be smaller than the signal cross-section. Figure 6.1 shows viable regions for $m_X \geq 1200$ GeV where this is the case, i.e. $\sigma(pp \to X) \times \mathrm{BR}(X \to \gamma\gamma)$ is well above the background but below the current experimental limits [34, 35].

Disentanglement of the standard versus the non-standard topologies crucially depends on the mass of the lighter resonance n. Photons deposit their energies in the electromagnetic calorimetric cells, where the granularity of each ECAL cell is approximately 0.02×0.02 in the $\eta - \varphi$

[1] more than two

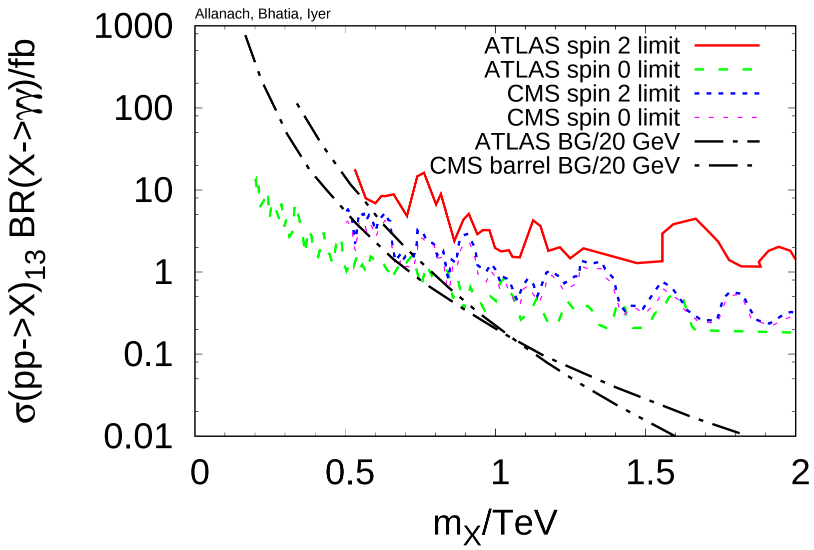

Figure 6.1: The plot displays the upper 95% C.L., obtained from both ATLAS and CMS collaborations, on the total cross-section for the diphoton final state considering spin-0 and spin-2 resonance. The curves labelled "BG" shows central values of the fitted diphoton mass spectrum at 13TeV LHC collisions.

direction for both ATLAS and CMS detectors. In the limit of extremely small m_n, where each apparent photon deposits its energy within a single cell of the electromagnetic calorimeter, the separation between the two topologies is challenging. However, when m_n is large enough for the photons (from n) to be detected by different cells of the electromagnetic calorimeter, but small enough so that they produce the illusion of a single photon, discrimination using photon jet substructure properties is possible. One has to disregard the photon isolation in such cases and form photon jets instead [189, 190].

As a case study, we study bosonic extensions of the standard model which could give rise to the standard/non-standard topologies. Using λ_J variable, we attempt to disentangle not just the toplogies but also the spin of the prototype resonance considered. The lighter particle i.e. n is assumed to have spin-0 in the analysis, as an example.

This chapter is organised as follows: in section 6.2 we set up extensions to the SM Lagrangian which can predict heavy di-photon or multi-photon resonances. The finite photon resolution of the detector is discussed in section 6.3. In section 6.4, isolation criteria are removed and photon-jets are adopted. Substructure and kinematic observables are then used to distinguish the different scenarios. In section 6.5 we introduce the statistics which tell us how many measured signal events will be required to discriminate one set of spins from another, whereas we cover how one can constrain the mass of the intermediate particle n in section 6.6. We conclude in section 6.7.

6.2 Model description

In this section we describe the minimal addition to the SM Lagrangian which can give rise to heavy resonant final states made of photons. We make no claims of generality: various couplings not relevant for our final state or production will be neglected. However, we shall insist on SM gauge invariance. Beginning with the di-photon final state, a minimal extension involves the introduction of a SM singlet heavy resonance X. We assume that any couplings of new particles such as the X (and the n, to be introduced later) to Higgs fields or $W^{\pm}, Z^0$ bosons are negligible. Eq. 6.2.1 gives an effective field theoretic interaction Lagrangian for the coupling of X to a pair of photons, when X is a scalar (first line) or a graviton (second line).

$$\begin{aligned}
\mathcal{L}^{int}_{X=\text{spin }0} &= -\eta_{GX}\frac{1}{4}G^a_{\mu\nu}G^{\mu\nu a}X - \eta_{\gamma X}\frac{1}{4}F_{\mu\nu}F^{\mu\nu}X, \\
\mathcal{L}^{int}_{X=\text{spin }2} &= -\eta_{T\psi X}T^{\alpha\beta}_{fermion}X_{\alpha\beta} - \eta_{TGX}T^{\alpha\beta}_{gluon}X_{\alpha\beta} - \eta_{T\gamma X}T^{\alpha\beta}_{photon}X_{\alpha\beta}.
\end{aligned} \tag{6.2.1}$$

where $T^{\alpha\beta}_i$ is the stress-energy tensor for the field i and the η_j are effective couplings of mass dimension -1. $F_{\mu\nu}$ is the field strength tensor of the photon (this may be obtained in a SM invariant way from a coupling involving the field strength tensor of the hypercharge gauge boson), whereas $G^a_{\mu\nu}$ is the field strength tensor of a gluon of adjoint colour index $a \in \{1, \ldots, 8\}$. As noted earlier, the direct decay of a vector boson into two photons is forbidden by the Landau-Yang theorem [191, 192]. Since X is assumed to be a SM singlet, there are no couplings to SM fermions, which are in non-trivial chiral representations when it is a scalar.

The presence of an additional light scalar SM singlet in the theory (n), with masses such that $m_n < m_X$, opens up another decay mode: $X \to nn$. Lagrangian terms for these interactions are

$$\mathcal{L}^{int}_{X=\text{spin }0,n} = -\frac{1}{2}A_{Xnn}Xnn, \qquad \mathcal{L}^{int}_{X=\text{spin }2,n} = -\eta_{TnX}X_{\alpha\beta}T^{\alpha\beta}_n, \tag{6.2.2}$$

where A_{Xnn} has mass dimension 1. n may further decay into a pair of photons leading to a multi-photon final state through a Lagrangian term

$$\mathcal{L}^{int}_{n\gamma\gamma} = -\frac{1}{4}\eta_{n\gamma\gamma}F_{\mu\nu}F^{\mu\nu}n. \tag{6.2.3}$$

Although we assume that n is electrically neutral, it may decay to two photons through a loop-level process (as is the case for the Standard Model Higgs boson, for instance). Alternatively, if X is a spin 1 particle, it could be produced by quarks in the proton and then decay into $n\gamma$. The Lagrangian terms would be

$$\mathcal{L}^{int}_{X=\text{spin }1,n} = -(\lambda_{\bar{q}Xq}\bar{q}_R\gamma_\mu X^\mu q_R + \lambda_{\bar{Q}XQ}\bar{Q}_L\gamma_\mu X^\mu Q_L + H.c.) - \frac{1}{4}\eta_{nX\gamma}n\tilde{X}_{\mu\nu}F^{\mu\nu}, \tag{6.2.4}$$

where λ_i are dimensionless couplings, q_R is a right-handed quark, Q_L is a left-handed quark doublet and $\tilde{X}_{\mu\nu} = \partial_\mu X_\nu - \partial_\mu X_\nu$. The decay $X_{spin=1} \to n\gamma$ would have to be a loop-level process, as explicitly exemplified in Ref. [193], since electromagnetic gauge invariance forbids it at tree level.

Spin of X	Spin of n	Number of photons
0	0	$\gamma\gamma$+$\gamma\gamma$
	2	$\gamma\gamma$+$\gamma\gamma$
1	0	γ+$\gamma\gamma$
	2	γ+$\gamma\gamma$
2	0	$\gamma\gamma$+$\gamma\gamma$
	2	$\gamma\gamma$+$\gamma\gamma$

Table 6.1: Different possibilities for spin assignments leading to an apparent di-photon state from other multi-photon final states. The one or two photon states have been grouped into terms which may only be resolved as one photon when m_n/m_X is small.

For scalar n then, we have a potential four photon final state if X is spin 0 or spin 2 and a potential three photon final state if X is spin 1 as shown in Eq. 6.2.5:

$$\begin{aligned} p\,p \to X_{spin=0,2} &\;\to\; n\,n \to \gamma\gamma + \gamma\gamma \\ p\,p \to X_{spin=1} &\;\to\; n\,\gamma \to \gamma\gamma + \gamma \end{aligned} \tag{6.2.5}$$

If the mass of the intermediate scalar n is such that $m_n \ll m_X$, its decay products are highly collimated because the n is highly boosted. It thereby results in a photon pair resembling a single photon final state. This opens up a range of possibilities with regards to the interpretation of the apparent di-photon channel. Above, we have assumed the intermediate particle n to be a scalar while considering different possibilities for the spin of X. Table 6.1 gives possible spin combinations for the heavy resonance X and the intermediate particle n leading to a final state made of photons. The third column gives the number of photons for each topology, grouped in terms of collimated photons that may experimentally resemble a single photon in the $m_n/m_X \to 0$ limit. The spin 1 X example was already proposed as a possible explanation [193] for a putative 750 GeV apparent di-photon excess measured by the LHC experiments (this subsequently turned out to be a statistical fluctuation).

In this work, we shall focus on the case where n is a scalar. However, the techniques developed in this chapter can be extended to cases where n is spin 2 as well (but not spin 1, since $n \to \gamma\gamma$ would then be forbidden by the Landau-Yang theorem). In the next section we will describe the scenario under which the process in Eq. 6.2.5 can mimic a truly di-photon signal.

6.3 The size of a photon

In a collider environment, any given process can be characterised by a given combination of final states. These final states correspond to different combinations of photons, leptons (electrons and muons), jets and missing energy. They can be distinguished by the energy deposited by them in different sections of the detector. In a typical high energy QCD jet, most of the final state particles (roughly 2/3) are charged pions whereas neutral pions make up much of the remaining 1/3 [190]. The constituents of a jet primarily deposit their energy in the hadronic calorimeter (HCAL) while the $\pi^0 \to 2\gamma$ decay of a neutral pion ensures that it shows up in the electromagnetic calorimeter (ECAL). Thus most of the constituents of the jet pass through the ECAL and deposit their energy in the HCAL. Photons and electrons deposit their energy in the ECAL, on the other hand. They can be distinguished by mapping the energy deposition to the tracker (which precedes the calorimeters). Apart from the tracker, electrons and photons are similar in appearance, from a detector point of view. Muons are detected by the muon spectrometer on the outside of the experiment.

The experimental sensitivity to detect a single photon is subject to the following two criteria:
(a) **Dimensions of the ECAL cells**: The ATLAS and CMS detectors have slightly different dimensions for the ECAL cells. ATLAS has a slightly coarser granularity with a crystal size of (0.0256, 0.0254) in (η, ϕ). In comparison, CMS has a granularity of (0.0174, 0.0174) in $(\eta,\ \phi)$. CMS and ATLAS have a pre-shower layer in the electromagnetic calorimeter with finer η segmentation, which should also be employed in analyses looking for resonances into multi-photon final states. The details of this layer are not available to us, and so we do not discuss it further. However, we bear in mind that information from the pre-shower layer may be used in addition to the techniques developed in this chapter. Any estimates of sensitivity (which come later) are therefore conservative in the sense that additional information from the pre-shower layer should improve the sensitivity. High energy photons will tend to shower in the ECAL: this is taken into account by clustering the cells into cones of size $R_{cone} = \Delta R = 0.1$. Thus if two high energy signal photons are separated a distance $\Delta R < R_{cone}$, they are typically not considered to be resolved by the ECAL since it could be a single photon that is simply showering.
(b) **Photon isolation**: In ATLAS and in CMS, a photon is considered to be isolated if the magnitude of the vector sum of the transverse momenta (p_T) of all objects with $\Delta R \in [R_{cone},\ 0.4]$ is less than 10% of its p_T. Qualitatively, this corresponds to the requirement that most of the energy is carried by the photon around which the cone is constructed. This criterion is required in order to distinguish a hard photon from a photon from a π^0 decay.

However, it is possible that certain signal topologies may give rise final state photons that are separated by a distance $\Delta R \in [R_{cone},\ 0.4]$. For instance, consider the process given in Eq. 6.2.5. The particle X can either be a scalar or a graviton. For concreteness, let us assume that n is a scalar. In this case, a four photon final state resulting from $X \to nn \to \gamma\gamma + \gamma\gamma$ would appear to be a di-photon final state. However, as m_n increases, eventually $\Delta R > 0.4$ and the number of resolved final state photons will increase. Similar arguments hold for the case where particle X is a spin 1 state. For a given mass of n, the eventual number of detected, isolated and resolved photons depends on the granularity of the detector and is expected to be slightly different for both the CMS and ATLAS.

To approximate the acceptance and efficiency of the detectors for our signal process, we perform a Monte-Carlo simulation using the following steps:

- The matrix element for our signal process is generated in `MadGraph5 aMC@NLO` [123] by generating the Feynman rules for the process with `FEYNRULES` [194]. We set $\eta_i = \mathcal{O}(20\text{ TeV})^{-1}$, $A_{Xnn} = M_X/100$ and $\lambda_i = 0.5$ in the model file. `MadGraph5` then calculates the width of the X: $\Gamma_X \sim 1-2$ GeV depending on the model, so the heavy resonance is narrow[2]. Events are generated at 13 TeV centre of mass energy using the `NNLO1` [187] parton distribution functions.

- For showering and hadronisation, we use `PYTHIA 8.2.1` [186]. The set of final state particles is then passed through the `DELPHES 3.3.2` detector simulator [127].

We use the `DELPHES 3.3.2` isolation module for photons and we impose a minimum p_T requirement of 100 GeV on each isolated photon.

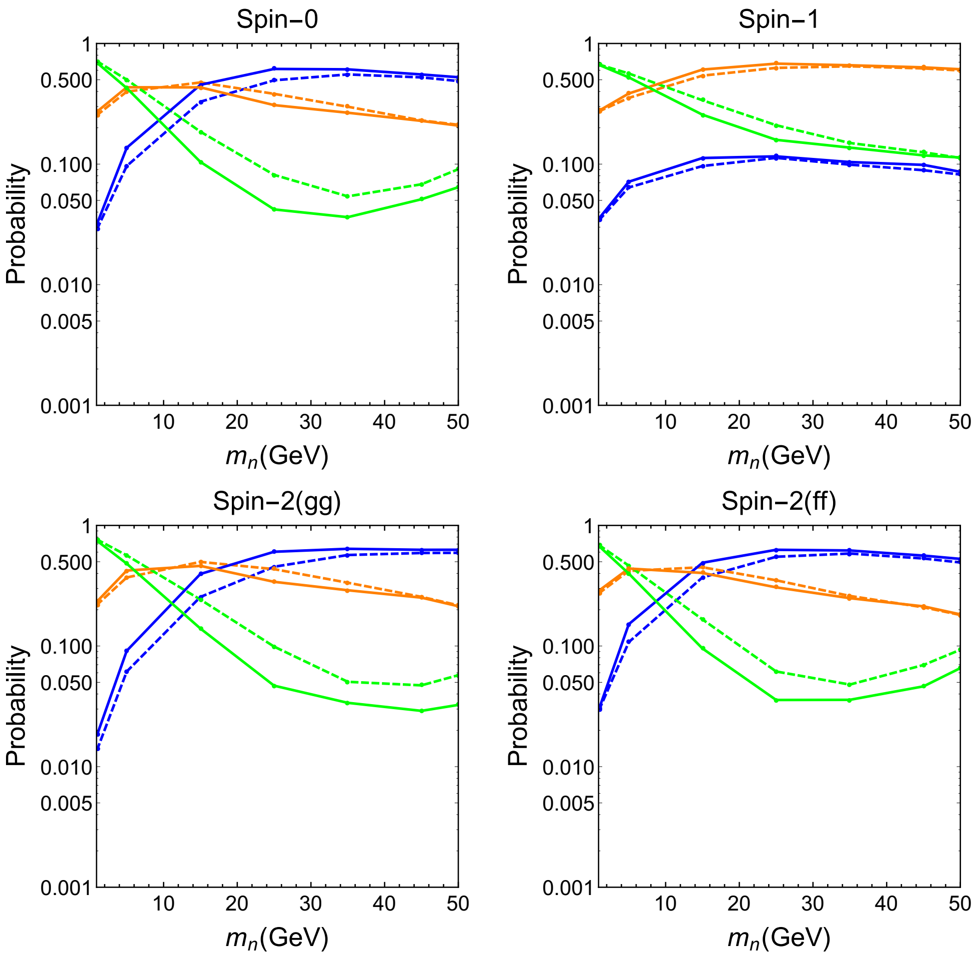

Figure 6.2: Probabilities of detecting different numbers of isolated, resolved photons for a 1200 GeV $X \to$ multi-photon decay as a function of m_n, the mass of the intermediate particle. We show the probabilities for 0 (blue), 1 (orange) or 2 (green) photons for each X produced. The probabilities for detecting 3 or 4 isolated, resolved photons for the signal are very small for this range of m_n and are not shown. Solid lines correspond to CMS, and dashed lines to ATLAS.

[2]The light resonance is also narrow, since $\Gamma_n = m_n^3|\eta_{n\gamma\gamma}|^2/(64\pi)$.

Figure 6.2 shows the probabilities of detecting the different number of detected, resolved, isolated photons in the final state for a produced X for ATLAS (dashed) and CMS (solid). If $p_T(\gamma) < 10$ GeV or $|\eta(\gamma)| > 2.5$, `DELPHES` records a zero efficiency for the photon, and it is added to the '0 photon' line. In the rest of the detector, `DELPHES` assigns between a 85% and a 95% weight for the photon (the difference from 100% is also added to the '0 photon' line in the figure). A few of the simulated photons from the X additionally fail the $p_T > 100$ GeV cut: these are not counted in the figure, and so the curves do not add exactly to 1.

The probabilities are shown for different possibilities of the spin of X, as shown by the header in each case. The bottom row corresponds to spin 2 when it is produced by gg fusion (left) and $\bar{q}q$ annihilation (right). Spin 1 corresponds to $X \to n\gamma \to \gamma\gamma + \gamma$, whereas the other cases all correspond to a $X \to nn \to \gamma\gamma + \gamma\gamma$ decay chain. The effective number of detected photons can be reduced by them not appearing in the fiducial volume of the detector (i.e. $|\eta(\gamma)| < 2.5$), or by them not being isolated (in which case both photons are rejected) or resolved (in which they count as one photon). We note that for each spin case, in the low m_n limit, the X is most likely to be seen as two resolved, isolated photons because each photon pair is highly collimated.

We note first that the probability for detecting 0, 1 or 2 resolved, isolated photons for the spin 2 case does not depend much on whether it is produced by a hard gg collision or a hard $\bar{q}q$ collision. An interesting trend is observed for the spin 0 and spin 2 cases, where the two photon probability has a minimum at $m_n \approx 40$ GeV. At $m_n = 40$ GeV, the photon pair from an n are often separated by $\Delta R \in [R_{cone},\ 0.4]$ and fail the isolation criterion because the two photons have similar p_T. Fig. 6.3 gives the distribution of ΔR between the photon pair coming from n as a function of its mass, and illustrates the preceding point. For light masses ($m_n = 1$ GeV) it is clear that both signal photons are within $\Delta R < R_{cone}$. For intermediate masses $m_n \in \{25,\ 50\}$ GeV, most photons are within $\Delta R \in [R_{cone},\ 0.4]$, whereas for $m_n = 100$ GeV, a good fraction are already isolated photons, having $\Delta R > 0.4$. Using an estimate $m_n \sim M_X \Delta R/4$ from following equation

$$\Delta R = \frac{m_n}{M_X} \frac{2\cosh\eta(n)}{\sqrt{z(1-z)}}. \tag{6.3.1}$$

we deduce that events with four isolated signal photons are expected to be evident only in the $m_n \gtrsim 120$ GeV region for $M_X = 1200$ GeV.

The spin 1 case in comparison, has a significantly lower zero photon rate for $m_n < 50$ GeV, as the process is characterised by a single photon and two collimated photons. Thus, unless the single photon is lost in the barrel or lost because of tagging efficiency, it will be recorded even if the collimated photons fail the isolation criterion.

6.4 Photon Jets

Since we wish to describe collimated and non-isolated photons in more detail (since, as the previous section shows, these are the main mechanisms by which signal photons are lost), we

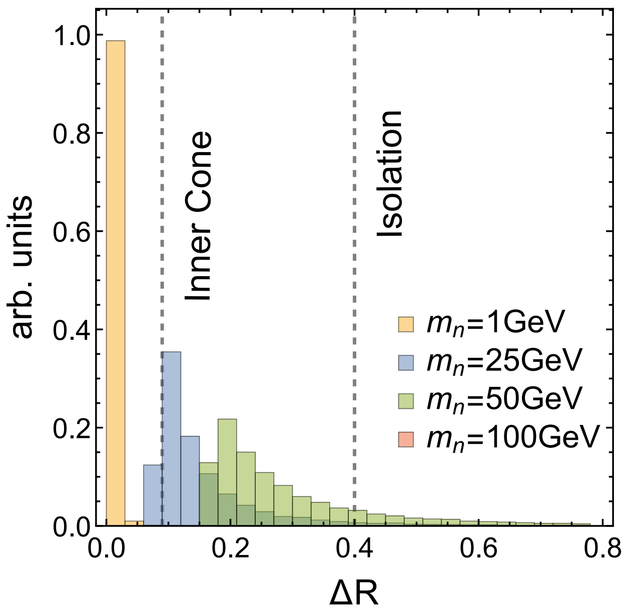

Figure 6.3: ΔR distribution for photon pairs originating from $n \to \gamma\gamma$ for different values of m_n. Photon pairs to the left hand side of the 'ECAL Prescription' line are considered to be one photon, whereas those between the ECAL prescription and the 'Isolation' line are rejected because of the photon isolation criteria.

follow refs. [189,190] and define photon-jets. For this, we relax the isolation criteria and work with the detector objects, i.e. the calorimetric and track four vectors. The calorimetric four vectors for each event are required to satisfy the following acceptance criteria:

$$E_{ECAL} > 0.1 \text{ GeV} \quad , \quad E_{HCAL} > 0.5 \text{ GeV}, \tag{6.4.1}$$

while only tracks with $p_T > 2$ GeV are accepted. These calorimetric and track four vectors are clustered using `FASTJET 3.1.3` [195] using the anti-k_T [188] clustering algorithm with $R = 0.4$. The tracks' four vectors are scaled by a small number and are called 'ghost tracks': their directions are well defined, but this effectively scales down their energies to negligible levels to avoid over counting them (the energies are then defined from the calorimetric deposits). The photon jet size $R = 0.4$ is chosen to coincide with the isolation separation of the photon described in Section 6.3. The anti-k_T clustering algorithm ensures that the jets are well defined cones (similar to the isolation cone) and clustered around a hard momentum four vector, which lies at the centre of the cone. Thus for our signal events, the jets are constructed around the photon(s). These typically have a large p_T, since they are produced from a massive resonance.

Since these jets are constructed out of the calorimetric (and ghost track) four vectors, they constitute a starting point for our analysis. At this stage, while a QCD-jet (typically initiated by a quark or gluon) is on the same footing as a photon jet, they can be discriminated from each other[3] by analysing different observables:

- **Invariant mass cut:** We would demand the invariant mass of the two leading photon

[3] Here we have not implemented such cuts, since we only simulated signal.

jets to be close to the mass of the observed resonance, reducing continuum backgrounds.

- **Tracks:** QCD jets are composed of a large number of charged mesons which display tracks in the tracker before their energy is deposited in the calorimeter[4] [196]. The track distribution for a QCD jet typically peaks at higher values of the number of tracks compared to a photon jet which peaks at zero tracks.

- **Logarithmic hadronic energy fraction ($\log \theta_J$):** This variable is a measure of the hadronic energy fraction of the jet. For a photon jet most of the energy is carried by the hard photon(s). As a result, this jet will deposit almost all of its energy into the ECAL, which is in stark contrast with a QCD jet. This can be quantified by constructing the following substructure observable [189, 190]:

$$\theta_J = \frac{1}{E^{total}} \sum_i E_i^{HCAL}, \tag{6.4.2}$$

  where E^{total} is the total energy in the jet deposited in the HCAL plus that deposited in the ECAL, whereas E_i^{HCAL} is the energy of each jet sub-object i that is deposited in the HCAL. $\log(\theta_J)$ is large and negative for a photon jet, while it peaks close to $\log[2/3] = -0.2$ for a QCD jet, since charged pions constitute around (2/3) of the jet constituents. We would require the leading jet to have $\log(\theta_J) < -0.5$, corresponding to very low hadronic activity.

Under these cuts, the QCD fake rate should reduce to less than 10^{-5} [189, 190]. Removing photon isolation and instead describing the event in terms of photon jets is advantageous because it helps discriminate the standard di-photon decay from the decay to more than two photons in Eq. 6.2.5. However, it still fails in the limit $m_n/M_X \to 0$, as we shall see later. Taking photon jets as a starting point, we shall devise strategies where we may discern the nature of the topology and glean information about the spins of the particles involved.

6.4.1 Nature of the topology

In this section we identify variables that aid in identifying the topology of the signal process and the spin of X. We begin by listing different cases we would like to discriminate between in Table 6.2. In the event of an observed excess in an apparent di-photon final state, we would relax the isolation criteria and define photon jets. Analysing the photon jets' substructure will help measure the number of hard photons within each jet. The difference in substructure for a photon jet with a single hard photon as opposed to several hard photons can be quantified by [189, 190]:

$$\lambda_J = \log\left(1 - \frac{p_{T_L}}{p_{T_J}}\right). \tag{6.4.3}$$

This can be understood as follows:

- Hard photon jets are re-clustered into sub-jets.

[4] A gluon initiated jet typically has a larger track multiplicity than a quark initiated jet.

Model	Process
$S2$	$pp \to S \to \gamma\gamma$
$S4$	$pp \to S \to nn \to \gamma\gamma + \gamma\gamma$
$V3$	$pp \to Z' \to n\gamma \to \gamma + \gamma\gamma$
$G2_{ff}$	$q\bar{q} \to G \to \gamma\gamma$
$G4_{gg}$	$gg \to G \to nn \to \gamma\gamma + \gamma\gamma$
$G4_{ff}$	$\bar{q}q \to G \to nn \to \gamma\gamma + \gamma\gamma$

Table 6.2: Cases to discriminate with a scalar n and a heavy resonance which is: scalar (S), spin 1 (Z') or spin 2 (G). We have listed the main signal processes to discriminate between in the second column, ignoring any proton remnants. The notation used for a given model is Xk: $X = S, V, G$ labels the spin of the resonance and k denotes the number of signal photons at the parton level in the final state.

- p_{T_L} denotes the p_T of the leading sub-jet (i.e. the sub-jet with the largest p_T) within the jet in question, whilst p_{T_J} is the p_T of the parent jet.
- For a 'single pronged' photon jet, $p_{T_L} \sim p_{T_J}$. Thus λ_J is negative, with a large magnitude.
- For a double-prong photon jet, $p_{T_L} < p_{T_J}$, resulting in λ_J closer to zero than the single pronged jets. We expect a peak where $p_T(n)$ is shared equally between the two photons, i.e. $p_{T_L}/p_{T_J} = 1/2$, or $\lambda_J = -0.3$.

There exist other substructure variables one could use in place of λ_J, such as $N-$Subjettiness [197, 198] or energy correlations [199] which are a measure of how pronged a jet is. Here, we prefer to use λ_J because it is particularly easily implemented and understood, and is robust in the presence of pile-up [200].

Fig. 6.4 shows the distribution of λ_J for the di-photon heavy resonance S2 (solid) and a multi[5]-photon S4 topology $m_n = 1$ GeV (dot-dashed). It is evident from the figure that the λ_J distribution is similar for the two cases, since they both peak at highly negative λ_J. This can be attributed to the fact that for such low masses of n in S4, the decay photons are highly collimated with $\Delta R < R_{\text{cell}}$. They therefore should resemble a single photon. However, the appearance of a small bump like feature on the right of the plot for $m_n = 1$ GeV S4 is interesting and unexpected prima facie since the opening angle between the photons in this case is less than the dimensions of an ECAL cell. However, this is explained by the fact that the energy of a photon becomes smeared around the cell where it deposits most of its energy. When a single (or two closely spaced photons) hit the centre of the cell, the smearing is almost identical for both cases. However, there exist a small fraction of cases for the collimated S4 topologies, where the two photons hit a cell near its edge such that they get deposited in adjacent cells, leading to the small double-pronged jet peak at $\lambda_J = -0.3$. One would require both good statistics and a very good modelling of the ECAL in order to be able to claim

[5]In this article, we refer to three or more hard signal photons as a multi-photon state.

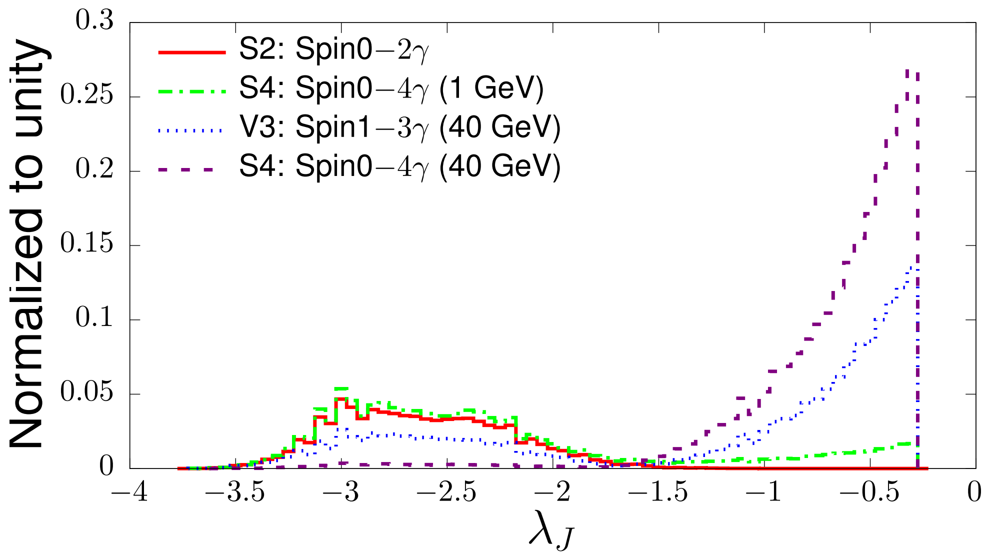

Figure 6.4: Distribution of λ_J for $S2$ and some multi-photon topologies $S4$ for $m_n = 1$ GeV and $V3$ and $S4$ for $m_n = 40$ GeV in the ATLAS detector. Double photon jets dominantly appear at $\lambda_J \sim -0.3$. If a single hard photon in a jet radiates, it often appears in the bump $\lambda_J \in [-3.5, -2]$, but there is a possibility for the photon jet to really only contain one photon: here, λ_J is strictly minus infinity. We do not show such events here on the figure, but they will count toward model discrimination.

discrimination of the two cases S2 and S4 (1 GeV), and for now we assume that they will not be. On the other hand, by the time that m_n reaches 40 GeV, the multi-photon topologies V3 and S4 are easily discriminated from S2, due to the large double-photon peak at $\lambda_J = -0.3$. They should also be easily discriminated from each other since V3 has a characteristic double peak due to its $\gamma + \gamma\gamma$ topology.

Using the λ_J distribution of the apparent di-photon signal, we then segregate the different scenarios into two classes:

- **Case A: a peak in signal photons at $\lambda_J = -0.3$:** Here, the distribution in Fig. 6.4 points to the presence of intermediate particles n and intermediate masses (of say $m_n > 15$ GeV) which lead to well resolved photons inside the photon jet, e.g. V3 (40 GeV) and S4 (40 GeV) in Fig. 6.5. There are 4 possibilities under this category: $S4, V3, G4_{gg}, G4_{ff}$ (see Table 6.2). Due to the double-peak structure $V3$ can be distinguished from $S4, G4_{ff}, G4_{gg}$ using the λ_J distribution.

- **Case B: no sizeable peak at $\lambda = -0.3$:** Here, we can either have S2 or intermediate particles n with a low mass. Most photon pairs coming from n appear as one photon since each from the pair hits the same ECAL cell. Thus, signal events resemble a conventional di-photon topology. All seven cases in Table 6.5 ($S2, S4, V3, G2_{gg}, G4_{gg}, G2_{ff}, G4_{ff}$) can lie in this category, depending on m_n/M_X.

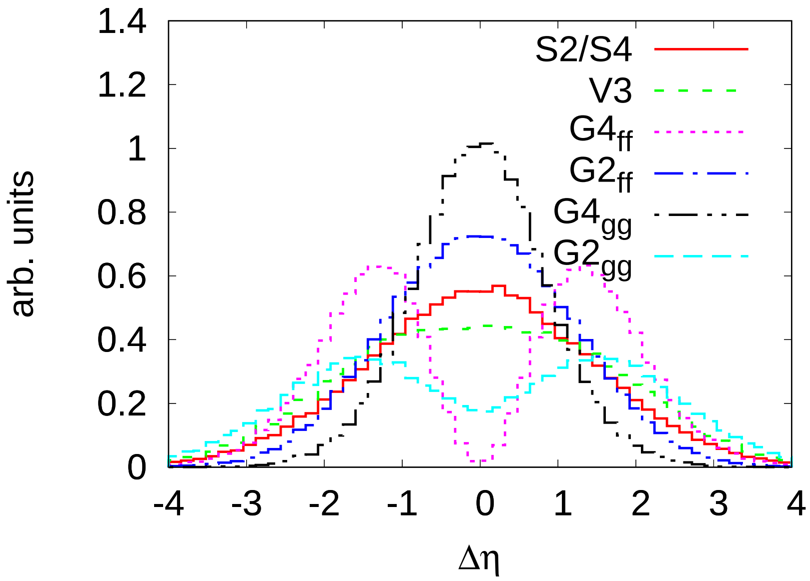

Figure 6.5: $\Delta\eta$ distribution between the two leading photon jets for the various models. There was very little difference between the S2 and S4 distributions by eye and so we have plotted them as one histogram.

Model	$S2$	$S4$	$V3$	$G4_{gg}$	$G2_{ff}$	$G2_{gg}$	$G4_{ff}$
$\Delta\eta$	Central					Non central	

Table 6.3: Classification of the $\Delta\eta$ distributions of models (listed in Table 6.2) as either central or non-central.

Once the nature of the topology is confirmed by the λ_J distribution (i.e. a classification into case A or B), we then wish to determine the spin of the resonance X responsible for the excess.

Consider case A for instance: as shown in Fig 6.6, the three remaining scenarios in case A, $S4, G4_{ff}, G4_{gg}$, can be distinguished from one another by constructing the $\Delta\eta$ distribution between the leading signal photon jets. We classify $\Delta\eta$ for a given scenario as either central (peaking at zero) or non-central (two distinct peaks away from zero) as shown in Table 6.3. We show the various distributions in Fig. 6.5. In the case where two scenarios can have the same $\Delta\eta$ distribution classification (e.g. $S4$ and $G4_{gg}$), one must examine differences in the precise shapes of these distributions to distinguish them. This will be discussed in the next section. In case B, all seven models listed in Table 6.5 are possibly indicated if m_n/M_X is very small. As shown in Fig 6.6, $\Delta\eta$ will be needed to distinguish the various models.

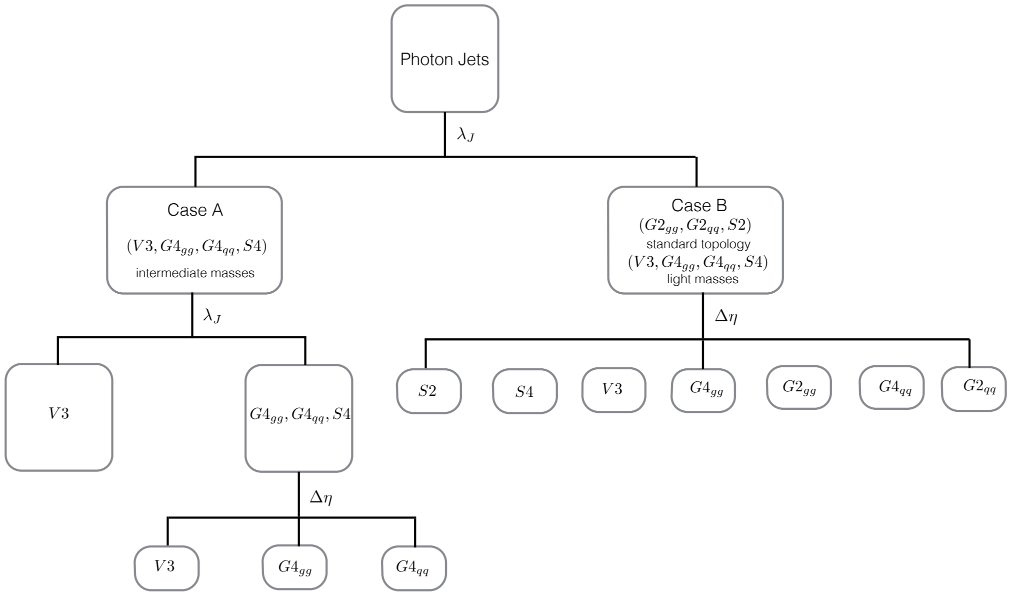

Figure 6.6: Flow chart representing the analysis strategy, beginning with photon jets, to discern the spin of the parent resonance X. After defining photon jets, the λ_J distribution is used to select different possibilities: Case A, where the λ_J distribution indicates the presence of intermediate n particles in the decay with an intermediate mass. Case B indicates that either the intermediate particles are very light or absent. A double bump structure in the λ_J distribution indicates the spin 1 ($V3$) topology.

6.5 Spin Discrimination

The discussion in the previous section illustrates the role of the substructure variables λ_J and $\Delta\eta$. While λ_J is useful in determining whether a given process results in well resolved photons in the calorimeter, $\Delta\eta$ helps discriminate the different spin hypotheses from one another. The signal $\Delta\eta$ distribution changes depending upon which spins are involved in the chain and they are invariant with respect to longitudinal boosts. They should therefore be less subject to uncertainties in the parton distribution functions (PDFs), which determine the longitudinal boost in each case[6].

We wish to calculate how much luminosity we expect to need in order to be able to discriminate the different spin possibilities in the decays, i.e. the different rows of Table 6.2. For this, we assume that one particular Hypothesis H_T, is true. Following Ref. [201] (which did a continuous spin discrimination analysis for invariant mass distributions of particle decay chains and large N), we require N signal events to disfavour a different spin hypothesis H_S to some factor R. We solve

$$\frac{1}{R} = \frac{p(H_S|N \text{ events from } H_T)}{p(H_T|N \text{ events from } H_T)} \tag{6.5.1}$$

[6]We note that whether the photon is in the fiducial volume or not does depend upon the longitudinal boost, and is therefore subject to PDF errors.

for N, for some given R (here we will require $R = 20$, i.e. that some spin hypothesis H_S is disfavoured at 20:1 odds over another H_T). We are explicitly assuming that background contributions B are negligible to make our estimate, but in practice, they could be included in the $\Delta\eta$ distributions in which case $H_S \to H_S + B$ and $H_T \to H_T + B$ in Eq. 6.5.1.

We characterise the 'N events from H_T' by the values of a particular observable (or set of observables) o_i. In the present chapter, we shall consider the pseudrapidity difference $\Delta\eta$ between the leading and next-to-leading photon jet, $o_i^{(T)}$ (for $i \in \{1, 2, \ldots, N\}$) that are observed in those events, although the observables could easily be extended to include other observables, for example λ_J. By Bayes' Theorem, we rewrite Eq. 6.5.1 as

$$\frac{1}{R} = \frac{p(H_S)}{p(H_T)} \frac{p(N \text{ events from } H_T|H_S)}{p(N \text{ events from } H_T|H_T)} = \frac{p(H_S)}{p(H_T)} \frac{\prod_{i=1}^{N} p(o_i^{(T)}|H_S)}{\prod_{i=1}^{N} p(o_i^{(T)}|H_T)}. \tag{6.5.2}$$

Binned data measured in the o distribution $\{n_j^{(T)}\}$ (for $j \in \{1, 2, \ldots, K\}$, K being the number of bins), will be Poisson distributed[7] based on the expectation $\mu_j^{(X)}$ for bin j:

$$p(n_j|H_X) = \text{Pois}(n_j|\mu_j^{(X)}), \tag{6.5.3}$$

where $X \in \{S, T\}$ and $\text{Pois}(n|\mu) = \frac{\mu^n e^{-\mu}}{n!}$. Substituting this into Eq. 6.5.2, we obtain

$$\log\left(\frac{1}{R}\right) = \log\left(\frac{p(H_S)}{p(H_T)}\right) + \sum_{j=1}^{K} \left[n_j^{(T)} \log \frac{\mu_j^{(S)}}{\mu_j^{(T)}} + \mu_j^{(T)} - \mu_j^{(S)} \right], \tag{6.5.4}$$

where $\mu_j^{(T)}$ is the expectation of the number of events in bin j from H_T and $n_j^{(T)}$ is a random sample of observed events obtained from $p(n_j|H_T)$. There is a (hopefully small) amount of information lost in going between unbinned data in Eq. 6.5.2 and binned data in Eq. 6.5.4. The first term on the right hand side contains the ratio of prior probabilities of H_T and H_S: this ratio we will set to one, having no particular a priori preference. Then taking the expectation over many draws, $\langle n_j^{(T)} \rangle = \mu_j^{(T)}$ and so

$$\log\left(\frac{1}{R}\right) = \sum_{i=1}^{K} \left[\mu_j^{(T)} \log \frac{\mu_j^{(S)}}{\mu_j^{(T)}} + \mu_j^{(T)} - \mu_j^{(S)} \right]. \tag{6.5.5}$$

We notice that Eq. 6.5.5 is not antisymmetric under $T \leftrightarrow S$, but this is expected since we are assuming that H_T is the true hypothesis, in contrast to H_S. As the data come in, at some integrated luminosity, the distribution will be sufficiently different from the prediction of some other hypothesis, H_S, to discriminate against it at the level of 20 times as likely. Each term on the right-hand side is proportional to the integrated luminosity collected $\mathcal{L}$,

$$\mu_j^{(X)} = \mathcal{L}\sigma_{tot}^{(X)}\epsilon_j^{(X)}, \tag{6.5.6}$$

[7]As argued above, we work in kinematic régimes where backgrounds can be neglected. We are also neglecting theoretical errors in our signal predictions. It would be straightforward to extend our analysis to the case where some smearing due to theoretical uncertainties is included, where we would convolute Eq. 6.5.3 with a Gaussian distribution.

where $\sigma_{tot}^{(X)}$ is the assumed total signal cross-section (i.e. the X production cross section) before cuts for H_X and $\epsilon_j^{(X)}$ is the probability that a signal event makes it past all of the cuts and into bin j, under hypothesis X. Assuming that $\sigma_{tot}^S = \sigma_{tot}^T \equiv \sigma_{tot}$, we may solve Eq. 6.5.5 and Eq. 6.5.6 for $N_R = \mathcal{L}\sigma_{tot}$, the expected number of total signal events required to disfavour H_S over H_T to an odds factor of R:

$$N_R = \frac{\log R}{\sum_{j=1}^K \left[\epsilon_j^{(T)} \log \frac{\epsilon_j^{(T)}}{\epsilon_j^{(S)}} + \epsilon_j^{(S)} - \epsilon_j^{(T)} \right]}. \tag{6.5.7}$$

One property of this equation is that if $\epsilon_j^{(T)} = \epsilon_j^{(S)}\ \forall\, j$, then $\mathcal{L}_R \to \infty$. This makes sense: there is no luminosity large enough such that it can discriminate between identical distributions. Eq. 6.5.7 works for multi-dimensional cases of several observables: one simply gets more bins for the multi-dimensional case. If one works in the large statistics limit, for continuous data (rather than binned data), one obtains a required number of events that is related [201] to the Kullback-Leibler divergence instead [202]. The Kullback-Leibler divergence is commonly used when one has analytic expressions for distributions of the observables (see Ref. [201]), and has the advantage of utilizing the full information in o. We do not have analytic expressions, partly because they depend upon parton distribution functions, which are numerically calculated. Our method loses some information by binning, but it has the considerable advantage that it includes kinematical selection and detector effects (all contained within the ϵ_j). Eq. 6.5.7 has the property that: if one halves the total X production cross-section, one requires double the luminosity to keep the discrimination power (measured by R) constant.

Since we shall estimate $\epsilon_j^{(X)}$ numerically via Monte-Carlo event generation, there is a potential problem we have to deal with: a bin might end up with no generated events and so one encounters divergences from the logarithm in the denominator of Eq. 6.5.7. This is due, however, to not using enough Monte Carlo statistics, where M signal events are simulated in total for each parameter choice and for each hypothesis pairing. We restrict the range of o and use large enough Monte Carlo statistics ($M = 200000$) such that no bins (that are set to be wide enough) contain zero events.

6.5.1 Event Selection and Results

Using the statistic developed in Eq. 6.5.7, we first first discriminate Case A from B defined in Section 6.4.1. Thus, in the event of an apparent di-photon excess in a certain invariant mass bin say $m_{\gamma\gamma}^{(0)}$, we propose the following steps:

- We relax the isolation criteria and re-analyse the events by constructing photon jets.
- The invariant mass $m_{j_1 j_2}$ of the two leading photon jets for each events are required to lie around $m_{\gamma\gamma}^{(0)}$: we require $1100 < m_{j_1 j_2}/\text{GeV} < 1300$.
- Photon jets from pions are eliminated by requiring that leading jet to have no tracks ($n_T = 0$) and by requiring $\log\theta_J < -0.5$. We also take into account the photon

conversion factor. This depends on whether the photon converts before or after exiting the pixel detector. This conversion probability is a function of the number of radiation lengths (a) a photon passes through before it escapes the first pixel detector and is given by [190]

$$P(\eta) = 1 - \exp(-\frac{7}{9}a(\eta)). \tag{6.5.8}$$

We approximate this by an η independent conversion probability $P(\eta) = 0.2$.

- The substructure of each jet is analysed using λ_J to determine whether it is in Case A or B.

Fig.6.6 gives a pictorial representation of these steps. We use $m_n = 40$ GeV and $m_n = 1$ GeV as examples for the model hypotheses to be tested. We simulate 2×10^5 events for the topologies predicted by H_T and H_S and compute λ_J for the all events which pass the basic selection criteria. To avoid any zero event bins, λ_J is binned between $[-4, 0]$ with a bin size of 0.6 and the efficiency for each particular bin is extracted for both distributions from the simulation. Owing to the distinct nature of the λ_J distribution for both the cases, 3-4 events is sufficient to discriminate between case A and case B. The $m_n = 1, 40$ GeV cases both have a post-cut acceptance efficiency of $\sim 55\%$. For a cross-section of 0.5 fb, we can accumulate some five signal events with $\sim$18 fb^{-1} of integrated luminosity. Once the nature of the topology (corresponding to a given case) is identified, our next step is to discriminate the different possibilities within it. Both of the scenarios are handled independently as follows:
CASE A: In this case there are only four possibilities corresponding to a multi-photon topology (i.e. proceeding through an intermediate n). As discussed earlier, we do not impose the requirement of two isolated photons, since the photons from n tend to fail isolation cuts. We compute $\Delta\eta$ between the two leading photon jets. In order to discriminate V3 from the other cases, the twin-peaked structure of $V3$ under λ_J (as shown in Fig 6.4.3) can be employed to discriminate it collectively from $S4, G4_{gg}, G4_{ff}$. In this case one requires a minimum of 20 signal events to disfavour the other three at a 20 : 1 odds. All samples are characterised by a minimum of $\sim 55\%$ acceptance efficiency. With this information then, one can disfavour $S4, G4_{gg}, G4_{ff}$ in favour of $V3$ with ~ 72 fb^{-1} of integrated luminosity for a 0.5 fb signal cross-section.

$S4, G4_{gg}, G4_{ff}$ can then be discriminated from one another using $\Delta\eta$ between the two leading jets. Table 6.4 computes the minimum number events required for pairwise discrimination of the three cases for $m_n = 40$ GeV and is computed using Eq. 6.5.7 To avoid zero event bins in the $\Delta\eta$ distribution, we restrict the a priori range of $|\Delta\eta| \in [-5, 5]$ to $[-4, 4]$. As shown in the Table 6.4, disfavouring $S4$ as compared to $G4_{gg}$ constitutes the largest expected number of required signal events *i.e.* 29. This can be achieved with a luminosity of ~ 105 fb^{-1}. Thus in the event of a discovery corresponding to Case A, it is possible to get exact nature of the spin of X within 105 fb^{-1} of data.

CASE B: This constitutes the more complicated of the two cases. Since the two hard photons inside the photon-jet for the multi-photon topologies can not be well resolved, the substructure is similar to the conventional single photon jet from the standard di-photon topology. Thus

N_R	$S4$	$G4_{gg}$	$G4_{ff}$
$S4$	∞	22	13
$G4_{gg}$	29	∞	4
$G4_{ff}$	19	5	∞

Table 6.4: Spin discrimination: $N_R = \mathcal{L}\sigma_{tot}^{(X)}$, the expected number of total signal events required to be produced to discriminate against the 'true' row model versus a column model by a factor of 20 at the 13 TeV LHC for $m_n = 40$ GeV.

there are more cases to distinguished in this case. We compute the $\Delta\eta$ between the leading two jets of the event. To avoid zero event bins in the $\Delta\eta$ distribution, we restrict the a priori range of $\Delta\eta$ from $[-5, 5]$ to $[-4, 4]$.

The signal models here are characterised by an acceptance efficiency of at least 55%. Using the cross-section of 0.5 fb, we find that the cases $S2$ and $S4$ are virtually indistinguishable owing to the similar shapes of their $\Delta\eta$ distributions. They thus cannot be distinguished on the basis of the $\Delta\eta$ distribution. However, as shown in Fig. 6.4, the presence of secondary bump for the collimated case will help in distinguishing these two cases. In this case, the same technology we have developed for the $\Delta\eta$ distribution could be employed for the λ_J distribution.

Distinguishing $S2, S4$ from $V3$ requires a maximum expected number of events of 250-300. This is achievable with 1.1 ab^{-1} of integrated luminosity, assuming an acceptance of ~ 55 % and a signal production cross-section of 0.5 fb. Distinguishing scenarios like $S2$ from $G4_{ff}$ or $G4_{gg}$ requires 23 events or less: these could be discriminated with $\sim$84 fb^{-1} for our reference cross-section of 0.5 fb, whereas the rest of the pairs of spin hypotheses can be distinguished within 364 fb^{-1} of data.

N_R	$S2$	$S4$	$V3$	$G2_{gg}$	$G4_{gg}$	$G2_{ff}$	$G4_{ff}$
$S2$	∞	> 2000	272	27	15	91	14
$S4$	> 2000	∞	255	26	15	96	13
$V3$	260	248	∞	54	9	37	21
$G2_{gg}$	32	31	65	∞	5	13	38
$G4_{gg}$	23	24	14	6	∞	54	4
$G2_{ff}$	102	110	44	12	40	∞	8
$G4_{ff}$	19	18	28	37	5	12	∞

Table 6.5: Spin discrimination of two models: $N_R = \mathcal{L}\sigma_{tot}^{(X)}$, the expected number of total signal events required to be produced to discriminate against the 'true' row model versus a column model by a factor of 20 at the 13 TeV LHC for $m_n = 1$ GeV.

6.6 Mass of the intermediate scalar

A multi-photon topology is indicative of the presence of two scales in the theory: m_X and m_n. While the scale of the heavier resonance is evident from the apparent di-photon invariant mass distribution, extracting the mass of the lighter state may be more difficult. From Fig. 6.2, we see that for low to intermediate masses, one does not obtain isolated photons from n which may be used to reconstruct its mass. We therefore examine the invariant mass of photon jets. The decay constituents of n retain its properties such as its p_T, pseudo-rapidity η, mass *etc.*. Fig. 6.7 shows a comparison of the mass of the leading jet for $S4$ and a few different values of m_n. The peak of each distribution, which can be fitted, clearly tracks with the mass of n.

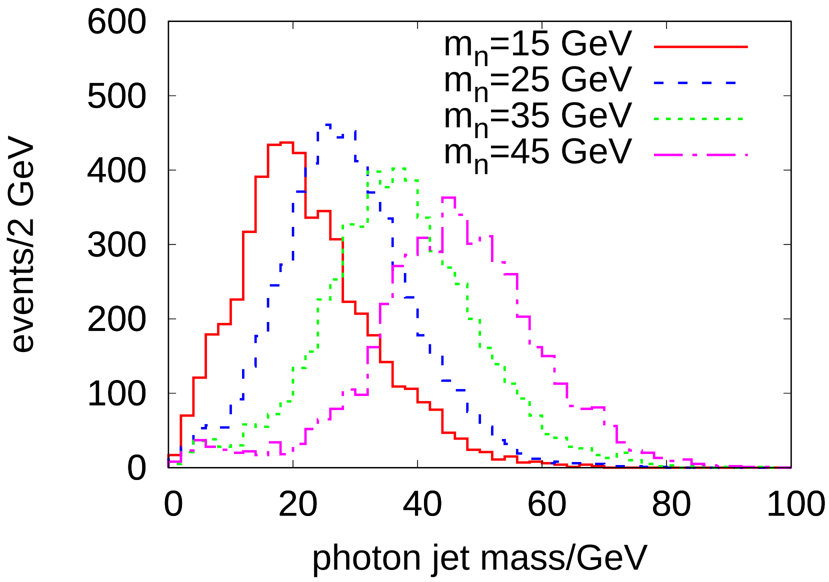

Figure 6.7: Comparison of the S4 photon jet mass distributions for the leading photon jets and various m_n.

Using an estimate based on the statistical measure introduced in section 6.5, we calculate that 25 signal events would be required to discriminate the 35 GeV from the 45 GeV hypothesis, for instance: i.e. $\sim$91 fb^{-1} of integrated luminosity and a signal cross-section of 0.5 fb. Thus, for intermediate masses and reasonable amounts of integrated luminosity, a fit to the peak should usefully constrain m_n, at least for $m_n \gtrsim 10$ GeV.

6.7 Conclusion

In the event of the discovery of a resonance at high di-photon invariant masses, it will of course be important to dissect it and discover as much information about its anatomy as possible. Here, we have provided a use case for Refs. [189, 190], where photon jets, photon sub-jets and simple kinematic variables were defined that might provide this information. The apparent di-photon signals may in fact be multi-photon (i.ė greater than two photons), where several photons are collinear, as is expected when intermediate particles have a mass much less than the mass of the original resonance. We identified useful variables for this purpose: the pseudo-rapidity difference between the photon jets helps discriminate different spin combinations of the two new particles in the decays. We quantify an estimate for how many signal events are expected to be required to provide discrimination between different spin hypotheses, setting up a discrete version of the Kullback-Leibler divergence for the purpose. For the discovery of a 1200 GeV resonance with a signal cross-section of 05 fb, many of the spin possibilities can be discriminated within the expected total integrated luminosity expected to be obtained from the LHC. A simple sub-jet variable λ_J provides a good discriminant between the di-photon and multi-photon cases. The invariant mass of the individual photon jets provides useful information about the intermediate resonance mass.

Chapter 7

Summary and concluding remarks

The present searches at the Large Hadron Collider have witnessed no success in determining any signs of new physics apart from few glitches in the charged and neutral B meson decays. With more and more statistics, the SM seems to be emerging as the sole winner. Since the race is not yet over, however, we cannot be sure of its outcome. There is still much room for new physics and it is in this context that we have studied four different new physics scenarios. These scenarios have mostly dealt with the determination of direct and indirect hints of new bosonic physics[1] at the Large Hadron Collider.

Probes of new physics depend on the scales at which observable effects emerge. While lighter particles could be probed as resonances at the colliders, the heavier particles rely on the indirect hints where for instance a well-measured observable significantly differs from its SM prediction. Note that the definition of lighter and heavier is relative and depends on the center of mass energy probed by a particular collider.

Given the lack of experimental evidences and with well-motivated models failing to show their mark at the collider, the strategy followed in the thesis has been primarily to understand the fluctuations in the data and eventually make predictions by either constructing or considering simple extensions of SM in a bottom-up approach. The advantage of this approach is that it is mostly unbiased and could help to point towards the full UV-complete theory in future. Till then our job is essentially to collect the missing pieces of the puzzle.

A wide range of analyses have been performed using these techniques ranging from determining class of $U(1)_X$ models to explain the hints of lepton flavour universality violation in neutral B-decays to finding signs of new physics in diphoton resonances to probing the well-measured gauge boson vertices. In performing these analyses, a number of "clean" final states have been analyzed ranging from $\gamma\gamma$ to di-muons to $W\gamma$, where leptonic decays of W are considered, for different NP scenarios. The interesting regions/channels which could be probed at the recent runs of the LHC have been identified Luminosity. Now it remains to be

[1]The choice of bosonic signals is partly motivated by the fact that more fermions generally lead to anomalies, but this is not a very strong argument. It is more fair to say that in the present climate bosonic signals seemed to be the ones that suggested themselves to us more strongly.

seen which of these scenarios would survive at the future runs of LHC.

Since the nature of the new physics is not known, this creates confusion in finding a particular direction and probing it further. We may hope that the situation will change with more running years of the LHC and other futuristic colliders like BELLE-II, CLIC and ILC. Till that time our work will be to persevere in trying to find smart methods to probe the undetectable. On this note the present thesis may be properly ended.

Appendix A

This appendix is devoted to analysis performed in chapter 5. Here we list the some of the important formulas and implications of the low mass charged Higgs on the diphoton analysis. We also discuss the fat-jet tagging techniques used for $h \to \bar{b}b$ analysis. The behaviour of the total cross-section with respect to mixing angles α and β are also noted.

A.1 Diphoton loop

The effective interactions of $h(H)$ with $\gamma\gamma$ are given as [178]:

$$L = \frac{\alpha_{em}}{8\pi v} \xi_h^\gamma h \, F_{\mu\nu}F^{\mu\nu} + \frac{\alpha_{em}}{8\pi v} \xi_H^\gamma \, HF_{\mu\nu}F^{\mu\nu} \, . \tag{A.1.1}$$

Correspondingly the decay width is

$$\Gamma(h(H) \to \gamma\gamma) = \frac{\alpha^2 g^2}{1024\pi^3} \frac{m_{h(H)}^3}{m_W^2} |\xi_{h(H)}^\gamma|^2 \, . \tag{A.1.2}$$

For Type-I 2HDM, the effective couplings $\xi_{h(H)}^\gamma$ receives dominant contributions from W-boson, charged Higgs and top loop, and is given as

$$\xi_{h(H)}^\gamma = N_c Q_t^2 \, \xi_{h(H)}^t F_{1/2}(\tau_t) + \xi_{h(H)}^W F_1(\tau_W) + \frac{m_W^2}{M_{H^\pm}^2} \xi_{h(H)}^{H^\pm} F_0(\tau_{H^\pm}) \, . \tag{A.1.3}$$

The form factors are given as:

$$F_0(\tau_{H^\pm}) = \tau_{H^\pm} \left[1 - \tau_{H^\pm} f(\tau_{H^\pm})\right] \, , \quad F_{1/2}(\tau_t) = -2\tau_t \left[1 + (1-\tau_t) f(\tau_t)\right] \, , \tag{A.1.4}$$

$$F_1(\tau_W) = 2 + 3\tau_W + 3\tau_W(2 - \tau_W) f(\tau_W) \, , \tag{A.1.5}$$

where

$$\begin{aligned} f(\tau) &= \left(\sin^{-1} \frac{1}{\sqrt{\tau}}\right)^2 \text{ for } \tau > 1 \, , \qquad f(\tau) = -\frac{1}{4}\left(\log \frac{\eta_+}{\eta_-} - i\pi\right)^2 \text{ for } \tau < 1 \, , \\ \eta_\pm &= 1 \pm \sqrt{1-\tau} \, , \qquad \tau = 4\left(m/m_{h(H)}\right)^2 \, . \end{aligned} \tag{A.1.6}$$

The couplings of $h(H)$ with $t\bar{t}$, W^+W^- and H^+H^- in Type-I 2HDM:

$$\xi_h^t = \cos\alpha/\sin\beta \,, \xi_H^t = \sin\alpha/\sin\beta \,, \xi_h^W = \sin(\beta-\alpha) \,, \xi_H^W = \cos(\beta-\alpha) \,, \tag{A.1.7}$$

$$\begin{aligned}\xi_h^{H^\pm} &= \frac{1}{4m_W^2\sin^2(2\beta)}\Bigg[8m_{12}^2\cos(\alpha+\beta) - \sin(2\beta)\Bigg((m_h^2 - 2m_{H^\pm}^2)\cos(\alpha-3\beta) \\ &\quad +(2m_{H^\pm}^2 + 3m_h^2)\cos(\alpha+\beta)\Bigg)\Bigg] \,,\end{aligned} \tag{A.1.8}$$

$$\begin{aligned}\xi_H^{H^\pm} &= \frac{1}{4m_W^2\sin(2\beta)}\Bigg[(2m_{H^\pm}^2 - m_H^2)\sin(\alpha-3\beta) + \sin(\alpha+\beta)\Bigg(\frac{4m_{12}^2}{\sin\beta\cos\beta} \\ &\quad -2m_{H^\pm}^2 - 3m_H^2\Bigg)\Bigg] \,.\end{aligned} \tag{A.1.9}$$

A.2 Charged Higgs analysis

In this section, we revisit some of our analyses by considering effect of low mass charged Higgs. We will see that our results will remain more-or-less unaltered. The independent 2HDM parameters are varied in the following ranges[1]:

$$\begin{aligned}\alpha = [0,\pi] \,, \tan\beta = [1,10] \,, m_{12} = [0.01, 1000]\ \text{GeV} \,, \\ M_A = [80, 2000]\ \text{GeV} \,, M_{H^\pm} = [80, 2000]\ \text{GeV} \,.\end{aligned} \tag{A.2.1}$$

As in Type-I 2HDM, couplings decrease with increase in $\tan\beta$, we have fixed the upper limit on $\tan\beta$ to be 10. We first determine the allowed parameter space by incorporating following constraints:

- Perturbativity: We demand the Higgs self couplings i.e. λ_i and the Yukawa couplings to be less than 4π, for the perturbative expansion to remain valid.
- Vacuum stability: This condition ensures the scalar potential to be bounded from below by restricting λ_i's in the following ranges :
  $\lambda_{1,2} > 0$, $\lambda_3 > -\sqrt{\lambda_1\lambda_2}$ and $\lambda_3 + \lambda_4 - |\lambda_5| > -\sqrt{\lambda_1\lambda_2}$ [172]
- Unitarity: This arise from the requirement of unitarity of scattering amplitudes such that the amplitudes do not grow with the increase in center of mass energies. The unitary bounds for 2HDM can be found in Ref. [173]
- ρ-parameter $\left(\dfrac{m_W^2}{m_Z^2\cos\theta_W}\right)$: Its value in SM is predicted to be unity at tree-level (the renormalization scheme is chosen such that this relation even holds after including higher order corrections [203]). Experimental prediction of ρ parameter is in agreement with the SM and constraints the masses of new scalars introduced in the theory [175].
- Flavour observables: Although the tree-level FCNC in 2HDM are absent due to the Z_2 symmetry, the charged scalars can affect these processes through higher order diagrams. In general, the flavour observables in these models are sensitive to the $m_{H^\pm}$ and $\tan\beta$.

[1] The lower range of M_A has been kept same as that of $M_{H^\pm}$ for simplicity.

- Direct charged Higgs searches at LEP: The charged Higgs has been searched in the channel $e^+e^- \to H^+H^-$ at LEP. The null observation of the signal has put a lower bound of 80 GeV on the mass of charged Higgs [204, 205]. This bound has been derived assuming $H^\pm$ decays only to the $\tau\bar{\nu}$ and $c\bar{s}$ modes. However, in the alignment limit the decay $H^\pm \to hW^\pm$ becomes significant. Hence, the bound on the charged Higgs mass gets relaxed in the regions close to the alignment limit [206].

The effect of above constraints on the parameter space is shown in Fig. A.1 . The allowed regions are shown in the panels (a), (b) and (c) of Fig. A.1 in $(M_A, M_{H^\pm})$, (α, m_{12}) and $(M_{H^\pm}, m_{12})$ planes respectively. For Type-I model, the bounds from flavour physics are weak and allows almost all values of $m_{H^\pm} \gtrsim 80$ GeV for $\tan\beta \gtrsim 2$ [176, 177, 207]. Hence we haven't shown the effect in the plot.

The important inferences which we can make from Fig. A.1 are following:

1. It can be seen from Fig. A.1 (a) that there exists upper bounds on the masses of the charged Higgs and the pseudoscalar Higgs. These bounds arise primarily due to the unitarity constraints. Furthermore bounds from the ρ parameter force the mass of pseudoscalar to be approximately equal to that of charged Higgs for $m_{H^\pm} \gtrsim 200$ GeV, and for $m_{H^\pm} \lesssim 200$ GeV, the pseudoscalar mass remains unconstrained.

2. The Z_2 symmetry breaking parameter m_{12} is also restricted to be less than 100 GeV (see Fig. A.1 (b) and (c)). These bounds arise from the vacuum stability requirements.

3. The mixing angle α is not constrained at all by any of the above constraint as can be seen in Fig. A.1 (c).

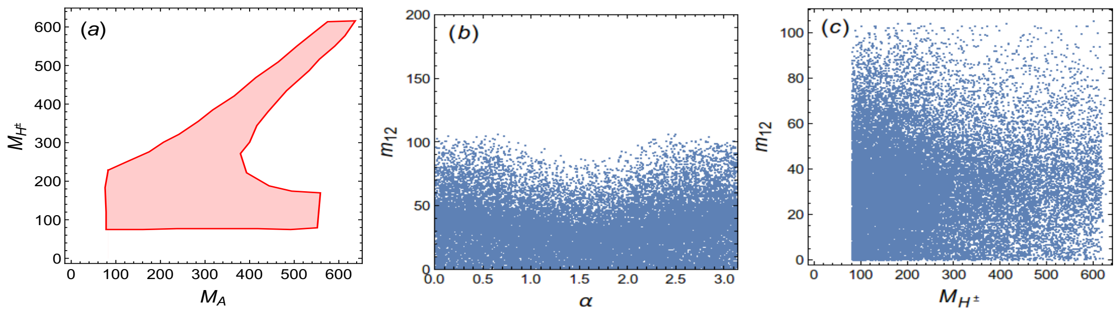

Figure A.1: Allowed range of M_A and $M_{H^\pm}$ after imposing constraints from perturbativity, vacuum stability, tree-level unitarity, ρ-parameter, LEP and flavour data.

After determining the allowed parameter space from theoretical and few experimental constraints, we proceed to examine the effect of light charged Higgs on the allowed parameter space from the Higgs signal strength measurements (for earlier analyses of this kind Ref. [208]). For illustration purpose, we have fixed the mass of charged Higgs to be 200 GeV and $m_{12}^2 = 100$ GeV. The charged Higgs boson will affect the signal strength measurements through its contribution in $H \to \gamma\gamma$ decay. It can be seen from Fig A.2 that the deviations in the high $\tan\beta$ regions are dramatic while for low $\tan\beta$, the increment in the allowed range of $\sin(\beta - \alpha)$ is slight. Furthermore, for the low $\tan\beta$ regions, the LEP measurements are far more constraining (see Fig. 5.5). Therefore, the allowed parameter space for $\tan\beta < 10$ which is our region of interest, remains same even after including effects from the low mass charged Higgs.

A light charged Higgs boson could also affect the significance of observing light Higgs h in the $\gamma\gamma$ channel. It is however found that the significance only increases slightly for larger values $|\sin(\beta-\alpha)|$. The effect is depicted in the right panel of Fig A.2. Although the plot is shown for a particular choice of m_h and $\tan\beta$, the qualitative result is independent of their values. Hence the effect of considering light charged Higgs boson only mildly affects our analyses.

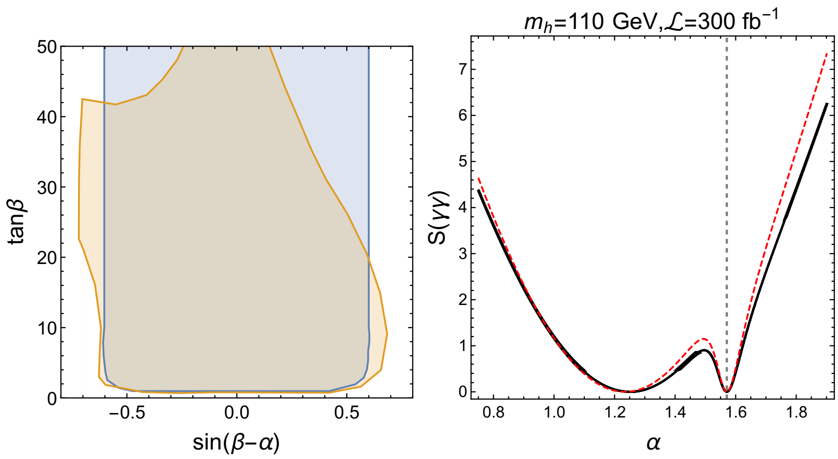

Figure A.2: In the left panel, the allowed parameter space from the signal strength data is plotted with and without charged Higgs. The blue contour shows the allowed parameter space without $H^{\pm}$ and the brown contour is with $H^{\pm}$ of mass 200 GeV. In the parameter region we are considering *i.e.*, $\tan\beta < 10$, the effect of adding charged Higgs is miniscule. In the right panel, we show the effect of the charged Higgs on the significance of observing $\gamma\gamma$ final state. The charged Higgs is found to enhance the significance for large values of $\sin(\beta-\alpha)$. The Black (red dashed) line corresponds to the diphoton analysis without (with) the charged Higgs effects.

A.3 Fat jet tagging techniques

In this section, we summarize the fat jet tagging methods for Higgs and top quark jets [170, 171]. We begin with the discussion on the reconstruction of a Higgs fat jet. To start with, we combine all the momentum four-vectors (j_i) within $\Delta R = 0.8$ to form a fat jet (J) using Cambridge-Aachen algorithm. The fat jets with $p_T > 200$ GeV are considered for further analysis.

- The fatjet (J) is broken into two subjets (j_1 and j_2) and the heavier jet is labelled as j_1.
- The two subjets are considered if the mass of j_1 has sufficient mass drop i.e. $m_{j_1} < \mu m_J$

and the splitting between two jets defined as $y = \dfrac{\min(p_{T_1}, p_{T_2})}{\max(p_{T_1}, p_{T_2})}$ is greater than y_{cut}[2]. This is a powerful cut to reduce the contaminations due to the QCD background. We have considered $\mu = 0.67$ and $y_{cut} = 0.09$ for our analysis [170].

- If the previous condition is not satisfied then j_1 is identified as J and the procedure is repeated until both of the above conditions are satisfied.
- The final jet is considered as the Higgs if both subjets are b-tagged and the mass of the filtered[3] fat jet (m_J) is close to the Higgs mass.

Now we discuss the reconstruction of top jet. We combine all the momentum four-vectors (j_i) within $\Delta R = 1.2$ to form a fat jet (J) using Cambridge-Achen algorithm. The fat jets with $p_T > 250$ GeV are considered for further analysis.

- Inside a fat jet, a lose massdrop criteria is employed such that $J \to j_1 j_2$, $m_{j_2} < m_{j_1}$ and $m_{j_2} > 0.2 m_J$. The splitting takes place iteratively till $m_{j_1} > 30$ GeV. A fat jet is retained if it has atleast three such subjets.
- The three subjets are then filtered with $\Delta R = 0.3$ into five subjets. Only those fatjets with total jet mass close to the top quark mass are considered. The subjets which reconstruct the top mass are then reclustered into three subjets.
- These subjets are then required to satisfy decay kinematics. Among three pair of invariant mass with these subjets, two of them are independent (as one of them satisfies W-mass criteria). In a two dimensional space where the coordinates represent two independent invariant mass, top-like jets represent a thin triangular annulus whereas QCD jet is localized in the region of small pair-wise invariant mass.

A.4 Cross section

The dependency of the total cross section ($\sigma \times$ BR) on α and $\sin(\beta - \alpha)$ are listed in Table. A.1 and also displayed in Fig. A.3.

It can be easily seen from the expressions of the cases A and D listed in the Table A.1, that the behaviour of total cross section for $pp \to h \to \gamma\gamma$ and $pp \to Wh \to Wb\bar{b}$ becomes identical with respect to α in the large $\tan\beta$ regions. The same can also be verified from $\tan\beta = 6$ line Fig. A.3.

[2] This is to ensure not too asymmetric splitting between j_1 and j_2.

[3] To eliminate underlying events in the fatjet, it is filtered with $R_{\text{filter}} = 0.3$ and three hard subjets are retained.

	Total cross section	Parametric dependence	Limit where the cross section vanishes
A	$\sigma(pp \to h \to \gamma\gamma)$	$\left(\frac{\cos\alpha}{\sin\beta}\right)^2 \times \lvert\xi_h^\gamma\rvert^2 \times \frac{1}{\Gamma_h^{\rm tot}}$	$\alpha \to \pi/2$, $\lvert\xi_h^\gamma\rvert \to 0$
B	$\sigma(pp \to Vh \to V\gamma\gamma)$	$\sin(\beta-\alpha)^2 \times \lvert\xi_h^\gamma\rvert^2 \times \frac{1}{\Gamma_h^{\rm tot}}$	$\alpha \to \beta$, $\lvert\xi_h^\gamma\rvert \to 0$
C	$\sigma(pp \to t\bar{t}h \to t\bar{t}b\bar{b})$	$\left(\frac{\cos\alpha}{\sin\beta}\right)^4 \times \frac{1}{\Gamma_h^{\rm tot}}$	$\alpha \to \pi/2$
D	$\sigma(pp \to Vh \to Vb\bar{b})$	$\sin(\beta-\alpha)^2 \times \left(\frac{\cos\alpha}{\sin\beta}\right)^2 \times \frac{1}{\Gamma_h^{\rm tot}}$	$\alpha \to \pi/2$, $\alpha \to \beta$

Table A.1: The dependency of total cross section for various processes with respect to coupling scale factors are tabulated. The limits where the total cross section vanishes are also listed. The behaviour of the total cross section for all four cases with respect to α for $\tan\beta = 2$ and 6 is plotted in Fig.A.3.

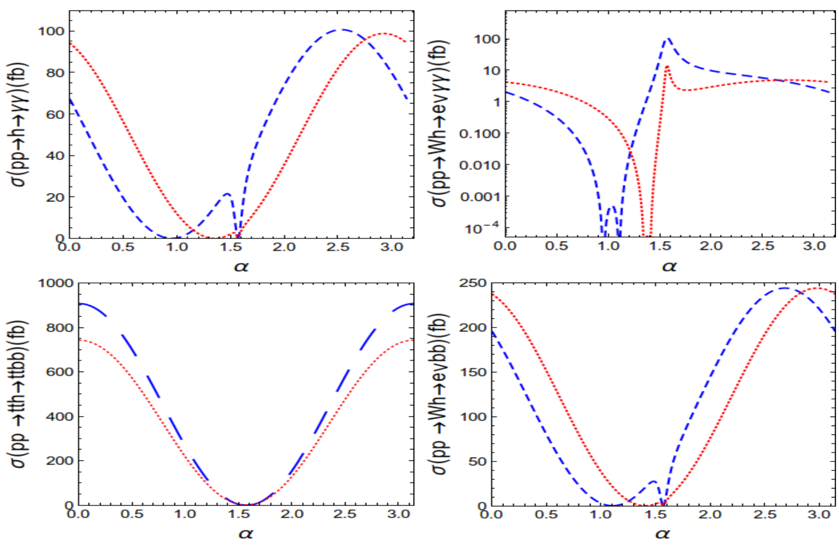

Figure A.3: A representative plot of ($\sigma\times$ BR) for light Higgs decaying to $\gamma\gamma$ and $b\bar{b}$ for $m_h = 100$ GeV. The dashed line in blue corresponds to $\tan\beta = 2$ while the dotted line in red corresponds to a $\tan\beta = 6$.

Bibliography

[1] S. L. Glashow, Nucl. Phys. **22**, 579 (1961).

[2] S. Weinberg, Phys. Rev. Lett. **19**, 1264 (1967).

[3] Abdus Salam, Nobel Lecture, https://www.nobelprize.org/prizes/physics/1979/salam/lecture.

[4] D. J. Griffiths, "Introduction To Elementary Particles".

[5] M. E. Peskin and D. V. Schroeder, "An Introduction to quantum field theory".

[6] T. P. Cheng and L. F. Li, "Gauge Theory Of Elementary Particle Physics".

[7] M. D. Schwartz, "Quantum Field Theory and the Standard Model".

[8] Palash B. Pal, "An Introductory Course of Particle Physics".

[9] F. Englert and R. Brout, Phys. Rev. Lett. **13**, 321 (1964).

[10] P. W. Higgs, Phys. Rev. Lett. **13**, 508 (1964).

[11] G. 't Hooft, Nucl. Phys. B **35**, 167 (1971).

[12] T. D. Lee and C. N. Yang, Phys. Rev. **104**, 254 (1956).

[13] R. P. Feynman and M. Gell-Mann, Phys. Rev. **109**, 193 (1958).

[14] E. C. G. Sudarshan and R. e. Marshak, Phys. Rev. **109**, 1860 (1958).

[15] F. J. Hasert *et al.* [Gargamelle Neutrino Collaboration], Phys. Lett. B **46**, 138 (1973) [Phys. Lett. **46B**, 138 (1973)].

[16] F. J. Hasert *et al.*, Phys. Lett. B **46**, 121 (1973) [Phys. Lett. **46B**, 121 (1973)].

[17] R. Barate *et al.* [ALEPH and DELPHI and L3 and OPAL Collaborations and LEP Working Group for Higgs boson searches], Phys. Lett. B **565**, 61 (2003) [hep-ex/0306033].

[18] C. E. Gerber *et al.* [TeV4LHC-Top Collaboration and Electroweak Working Group], arXiv:0705.3251 [hep-ph].

[19] A. J. Bevan *et al.* [BaBar and Belle Collaborations], Eur. Phys. J. C **74**, 3026 (2014).

[20] G. Aad *et al.* [ATLAS Collaboration], Phys. Lett. B **716**, 1 (2012) ;
S. Chatrchyan *et al.* [CMS Collaboration], Phys. Lett. B **716**, 30 (2012).

[21] G. Aad *et al.* [ATLAS and CMS Collaborations], JHEP **1608**, 045 (2016).

[22] https://twiki.cern.ch/twiki/bin/view/CMSPublic/PhysicsResultsCombined, https://twiki.cern.ch/twiki/bin/view/AtlasPublic/StandardModelPublicResults.

[23] See, for example, J. Ellis, Phil. Trans. Roy. Soc. Lond. A **370**, 818 (2012).

[24] R. K. Kaul, arXiv:0803.0381 [hep-ph].

[25] https://pitp.ias.edu/sites/pitp/files/craig.pdf.

[26] R. Barbieri and A. Strumia, hep-ph/0007265.

[27] F. Capozzi, E. Lisi, A. Marrone, D. Montanino and A. Palazzo, "Neutrino masses and mixings: Status of known and unknown 3ν parameters," Nucl. Phys. B **908**, 218 (2016). [arXiv:1601.07777 [hep-ph]].

[28] I. Esteban, M. C. Gonzalez-Garcia, M. Maltoni, I. Martinez-Soler and T. Schwetz, "Updated fit to three neutrino mixing: exploring the accelerator-reactor complementarity," arXiv:1611.01514 [hep-ph].

[29] http://pdg.lbl.gov/2018/reviews/rpp2018-rev-dark-matter.pdf.

[30] R. Aaij *et al.* [LHCb Collaboration], "Measurement of Form-Factor-Independent Observables in the Decay $B^0 \to K^{*0}\mu^+\mu^-$," Phys. Rev. Lett. **111**, 191801 (2013).

[31] R. Aaij *et al.* [LHCb Collaboration], "Angular analysis of the $B^0 \to K^{*0}\mu^+\mu^-$ decay using 3 fb^{-1} of integrated luminosity," JHEP **1602**, 104 (2016).

[32] R. Aaij *et al.* [LHCb Collaboration], "Test of lepton universality using $B^+ \to K^+\ell^+\ell^-$ decays," Phys. Rev. Lett. **113** (2014) 151601.

[33] R. Aaij *et al.* [LHCb Collaboration], JHEP **1708**, 055 (2017).

[34] V. Khachatryan *et al.* [CMS Collaboration], Phys. Lett. B **767**, 147 (2017).

[35] The ATLAS collaboration [ATLAS Collaboration], ATLAS-CONF-2016-059.

[36] V. Barger, P. Langacker, M. McCaskey, M. Ramsey-Musolf and G. Shaughnessy, Phys. Rev. D **79**, 015018 (2009).

[37] G. C. Branco, P. M. Ferreira, L. Lavoura, M. N. Rebelo, M. Sher and J. P. Silva, "Theory and phenomenology of two-Higgs-doublet models," Phys. Rept. **516**, 1 (2012).

[38] P. Langacker, "The Physics of Heavy Z' Gauge Bosons," Rev. Mod. Phys. **81**, 1199 (2009).

[39] See for example, http://www.people.fas.harvard.edu/ hgeorgi/review.pdf.

[40] V. Khachatryan *et al.* [CMS and LHCb Collaborations], Nature **522**, 68 (2015).

[41] A. Arbey, M. Battaglia, F. Mahmoudi and D. Martnez Santos, Phys. Rev. D **87**, no. 3, 035026 (2013).

[42] A. Dighe, D. Ghosh, K. M. Patel and S. Raychaudhuri, Int. J. Mod. Phys. A **28**, 1350134 (2013).

[43] G. Isidori, Y. Nir and G. Perez, Ann. Rev. Nucl. Part. Sci. **60**, 355 (2010)

[44] C. Bobeth, G. Hiller and G. Piranishvili, "Angular distributions of $\bar{B} \to \bar{K}\ell^+\ell^-$ decays," JHEP **0712**, 040 (2007).

[45] R. Aaij *et al.* [LHCb Collaboration], Phys. Rev. Lett. **118**, no. 19, 191801 (2017).

[46] A. J. Buras, In *Lake Louise 1999, Electroweak physics* 1-83 [hep-ph/9905437].

[47] V. Ilisie,

[48] S. Descotes-Genon, J. Matias, M. Ramon and J. Virto, "Implications from clean observables for the binned analysis of $B- > K * \mu^+\mu^-$ at large recoil," JHEP **1301**, 048 (2013). [arXiv:1207.2753 [hep-ph]].

[49] S. Wehle *et al.* [Belle Collaboration], "Lepton-Flavor-Dependent Angular Analysis of $B \to K^*\ell^+\ell^-$," arXiv:1612.05014 [hep-ex].

[50] R. Aaij *et al.* [LHCb Collaboration], "Differential branching fractions and isospin asymmetries of $B \to K^{(*)}\mu^+\mu^-$ decays," JHEP **1406**, 133 (2014).

[51] R. Aaij *et al.* [LHCb Collaboration], "Differential branching fraction and angular analysis of the decay $B_s^0 \to \phi\mu^+\mu^-$," JHEP **1307**, 084 (2013).

[52] M. Bordone, G. Isidori and A. Pattori, "On the Standard Model predictions for R_K and R_{K^*}," Eur. Phys. J. C **76**, no. 8, 440 (2016).

[53] G. Buchalla, A. J. Buras and M. E. Lautenbacher, "Weak decays beyond leading logarithms," Rev. Mod. Phys. **68**, 1125 (1996) [hep-ph/9512380].

[54] W. Altmannshofer, P. Ball, A. Bharucha, A. J. Buras, D. M. Straub and M. Wick, "Symmetries and Asymmetries of $B \to K^*\mu^+\mu^-$ Decays in the Standard Model and Beyond," JHEP **0901**, 019 (2009).

[55] G. Hiller and F. Kruger, "More model independent analysis of $b \to s$ processes," Phys. Rev. D **69**, 074020 (2004) [hep-ph/0310219].

[56] G. Hiller and M. Schmaltz, "R_K and future $b \to s\ell\ell$ physics beyond the standard model opportunities," Phys. Rev. D **90**, 054014 (2014).

[57] S. Descotes-Genon, J. Matias and J. Virto, "Understanding the $B \to K^*\mu^+\mu^-$ Anomaly," Phys. Rev. D **88**, 074002 (2013).

[58] D. Ghosh, M. Nardecchia and S. A. Renner, "Hint of Lepton Flavour Non-Universality in B Meson Decays," JHEP **1412**, 131 (2014).

[59] W. Altmannshofer and D. M. Straub, "New physics in $b \to s$ transitions after LHC run 1," Eur. Phys. J. C **75**, no. 8, 382 (2015).

[60] S. Descotes-Genon, L. Hofer, J. Matias and J. Virto, "Global analysis of $b \to s\ell\ell$ anomalies," JHEP **1606**, 092 (2016).

[61] T. Hurth, F. Mahmoudi and S. Neshatpour, "On the anomalies in the latest LHCb data," Nucl. Phys. B **909**, 737 (2016).

[62] R. Gauld, F. Goertz and U. Haisch, "On minimal Z' explanations of the $B \to K^* \mu^+ \mu^-$ anomaly," Phys. Rev. D **89**, 015005 (2014).

[63] S. L. Glashow, D. Guadagnoli and K. Lane, "Lepton Flavor Violation in B Decays?," Phys. Rev. Lett. **114**, 091801 (2015).

[64] B. Bhattacharya, A. Datta, D. London and S. Shivashankara, "Simultaneous Explanation of the R_K and $R(D^{(*)})$ Puzzles," Phys. Lett. B **742**, 370 (2015).

[65] A. Crivellin, G. D'Ambrosio and J. Heeck, "Explaining $h \to \mu^\pm \tau^\mp$, $B \to K^* \mu^+ \mu^-$ and $B \to K \mu^+ \mu^- / B \to K e^+ e^-$ in a two-Higgs-doublet model with gauged $L_\mu - L_\tau$," Phys. Rev. Lett. **114**, 151801 (2015).

[66] A. Crivellin, G. D'Ambrosio and J. Heeck, "Addressing the LHC flavor anomalies with horizontal gauge symmetries," Phys. Rev. D **91**, no. 7, 075006 (2015).

[67] A. Crivellin, L. Hofer, J. Matias, U. Nierste, S. Pokorski and J. Rosiek, "Lepton-flavour violating B decays in generic Z' models," Phys. Rev. D **92**, no. 5, 054013 (2015).

[68] A. Celis, J. Fuentes-Martin, M. Jung and H. Serodio, "Family nonuniversal Z' models with protected flavor-changing interactions," Phys. Rev. D **92**, no. 1, 015007 (2015).

[69] D. Aristizabal Sierra, F. Staub and A. Vicente, "Shedding light on the $b \to s$ anomalies with a dark sector," Phys. Rev. D **92**, no. 1, 015001 (2015).

[70] G. Blanger, C. Delaunay and S. Westhoff, "A Dark Matter Relic From Muon Anomalies," Phys. Rev. D **92**, 055021 (2015).

[71] B. Gripaios, M. Nardecchia and S. A. Renner, "Linear flavour violation and anomalies in B physics," JHEP **1606**, 083 (2016).

[72] B. Allanach, F. S. Queiroz, A. Strumia and S. Sun, "Z' models for the LHCb and $g-2$ muon anomalies," Phys. Rev. D **93**, no. 5, 055045 (2016).

[73] K. Fuyuto, W. S. Hou and M. Kohda, "Z' -induced FCNC decays of top, beauty, and strange quarks," Phys. Rev. D **93**, no. 5, 054021 (2016).

[74] C. W. Chiang, X. G. He and G. Valencia, "Z' model for $b \to s\bar{\ell}\ell$ flavor anomalies," Phys. Rev. D **93**, no. 7, 074003 (2016).

[75] S. M. Boucenna, A. Celis, J. Fuentes-Martin, A. Vicente and J. Virto, "Non-abelian gauge extensions for B-decay anomalies," Phys. Lett. B **760**, 214 (2016).

[76] S. M. Boucenna, A. Celis, J. Fuentes-Martin, A. Vicente and J. Virto, "Phenomenology of an $SU(2) \times SU(2) \times U(1)$ model with lepton-flavour non-universality," JHEP **1612**, 059 (2016).

[77] A. Celis, W. Z. Feng and M. Vollmann, "Dirac Dark Matter and $b \to s\ell^+\ell^-$ with $\mathbf{U(1)}$ gauge symmetry," arXiv:1608.03894 [hep-ph].

[78] W. Altmannshofer, S. Gori, S. Profumo and F. S. Queiroz, "Explaining dark matter and B decay anomalies with an $L_\mu - L_\tau$ model," JHEP **1612**, 106 (2016).

[79] A. Crivellin, J. Fuentes-Martin, A. Greljo and G. Isidori, "Lepton Flavor Non-Universality in B decays from Dynamical Yukawas," Phys. Lett. B **766**, 77 (2017).

[80] I. Garcia Garcia, "LHCb anomalies from a natural perspective," arXiv:1611.03507 [hep-ph].

[81] D. Beirevi, O. Sumensari and R. Zukanovich Funchal, "Lepton flavor violation in exclusive $b \to s$ decays," Eur. Phys. J. C **76**, no. 3, 134 (2016).

[82] B. Bhattacharya, A. Datta, J. P. Guvin, D. London and R. Watanabe, "Simultaneous Explanation of the R_K and $R_{D^{(*)}}$ Puzzles: a Model Analysis," arXiv:1609.09078 [hep-ph].

[83] S. Biswas, D. Chowdhury, S. Han and S. J. Lee, "Explaining the lepton non-universality at the LHCb and CMS within a unified framework," JHEP **1502**, 142 (2015).

[84] B. Gripaios, M. Nardecchia and S. A. Renner, "Composite leptoquarks and anomalies in B-meson decays," JHEP **1505**, 006 (2015).

[85] S. Sahoo and R. Mohanta, "Scalar leptoquarks and the rare B meson decays," Phys. Rev. D **91**, no. 9, 094019 (2015).

[86] D. Beirevi, S. Fajfer and N. Konik, "Lepton flavor nonuniversality in $b \to s\ell^+\ell^-$ processes," Phys. Rev. D **92**, no. 1, 014016 (2015).

[87] R. Alonso, B. Grinstein and J. Martin Camalich, "Lepton universality violation and lepton flavor conservation in B-meson decays," JHEP **1510**, 184 (2015).

[88] L. Calibbi, A. Crivellin and T. Ota, "Effective Field Theory Approach to $b \to s\ell\ell'$, $B \to K * \nu\overline{\nu}$ and $B \to D^*\tau\nu$ with Third Generation Couplings," Phys. Rev. Lett. **115**, 181801 (2015).

[89] W. Huang and Y. L. Tang, "Flavor anomalies at the LHC and the R-parity violating supersymmetric model extended with vectorlike particles," Phys. Rev. D **92**, no. 9, 094015 (2015).

[90] H. Ps and E. Schumacher, "Common origin of R_K and neutrino masses," Phys. Rev. D **92**, no. 11, 114025 (2015).

[91] M. Bauer and M. Neubert, "Minimal Leptoquark Explanation for the $\mathrm{R}_{D^{(*)}}$, R_K , and $(g-2)_g$ Anomalies," Phys. Rev. Lett. **116**, no. 14, 141802 (2016).

[92] S. Fajfer and N. Konik, "Vector leptoquark resolution of R_K and $R_{D^{(*)}}$ puzzles," Phys. Lett. B **755**, 270 (2016).

[93] R. Barbieri, G. Isidori, A. Pattori and F. Senia, "Anomalies in B-decays and $U(2)$ flavour symmetry," Eur. Phys. J. C **76**, no. 2, 67 (2016).

[94] S. Sahoo and R. Mohanta, "Lepton flavor violating B meson decays via a scalar leptoquark," Phys. Rev. D **93**, no. 11, 114001 (2016).

[95] I. Dorner, S. Fajfer, A. Greljo, J. F. Kamenik and N. Konik, "Physics of leptoquarks in precision experiments and at particle colliders," Phys. Rept. **641**, 1 (2016).

[96] D. Das, C. Hati, G. Kumar and N. Mahajan, "Towards a unified explanation of $R_{D^{(*)}}$, R_K and $(g-2)_\mu$ anomalies in a left-right model with leptoquarks," Phys. Rev. D **94**, 055034 (2016).

[97] S. Sahoo and R. Mohanta, "Effects of scalar leptoquark on semileptonic Λ_b decays," New J. Phys. **18**, no. 9, 093051 (2016).

[98] C. H. Chen, T. Nomura and H. Okada, "$B \to K^*\mu^+\mu^-$, muon $g-2$, and 750 GeV diphoton excesses in a leptoquark model," Phys. Rev. D **94**, no. 11, 115005 (2016).

[99] D. Beirevi, N. Konik, O. Sumensari and R. Zukanovich Funchal, "Palatable Leptoquark Scenarios for Lepton Flavor Violation in Exclusive $b \to s\ell_1\ell_2$ modes," JHEP **1611**, 035 (2016).

[100] D. Beirevi, S. Fajfer, N. Konik and O. Sumensari, "Leptoquark model to explain the B-physics anomalies, R_K and R_D," Phys. Rev. D **94**, no. 11, 115021 (2016).

[101] S. Sahoo, R. Mohanta and A. K. Giri, "Explaining the R_K and $R_{D^{(*)}}$ anomalies with vector leptoquarks," Phys. Rev. D **95**, no. 3, 035027 (2017).

[102] R. Barbieri, C. W. Murphy and F. Senia, "B-decay Anomalies in a Composite Leptoquark Model," Eur. Phys. J. C **77**, no. 1, 8 (2017).

[103] P. Cox, A. Kusenko, O. Sumensari and T. T. Yanagida, "SU(5) Unification with TeV-scale Leptoquarks," arXiv:1612.03923 [hep-ph].

[104] L. Lavoura, "Zeros of the inverted neutrino mass matrix," Phys. Lett. B **609**, 317 (2005).

[105] E. I. Lashin and N. Chamoun, "Zero minors of the neutrino mass matrix," Phys. Rev. D **78**, 073002 (2008).

[106] T. Araki, J. Heeck and J. Kubo, "Vanishing Minors in the Neutrino Mass Matrix from Abelian Gauge Symmetries," JHEP **1207**, 083 (2012).

[107] J. Heeck, "Gauged Flavor Symmetries," Nucl. Phys. Proc. Suppl. **237-238**, 336 (2013).

[108] E. I. Lashin and N. Chamoun, "One vanishing minor in the neutrino mass matrix," Phys. Rev. D **80**, 093004 (2009).

[109] D. Atwood, S. Bar-Shalom and A. Soni, Phys. Rev. D **76**, 033004 (2007).

[110] A. J. Buras, "Weak Hamiltonian, CP violation and rare decays," hep-ph/9806471.

[111] UTFIT collaboration, summer 2016 results, `http://www.utfit.org`

[112] A. J. Buras, J. Girrbach-Noe, C. Niehoff and D. M. Straub, "$B \to K^{(*)} \nu\overline{\nu}$ decays in the Standard Model and beyond," JHEP **1502**, 184 (2015).

[113] The ATLAS collaboration [ATLAS Collaboration], "Search for new high-mass resonances in the dilepton final state using proton-proton collisions at $\sqrt{s} = 13$ TeV with the ATLAS detector," ATLAS-CONF-2016-045.

[114] CMS Collaboration [CMS Collaboration], "Search for a high-mass resonance decaying into a dilepton final state in 13 fb^{-1} of pp collisions at $\sqrt{s} = 13$ TeV," CMS-PAS-EXO-16-031.

[115] G. Aad *et al.* [ATLAS Collaboration], "Search for new phenomena in dijet mass and angular distributions from *pp* collisions at $\sqrt{s} = 13$ TeV with the ATLAS detector," Phys. Lett. B **754**, 302 (2016).

[116] A. M. Sirunyan *et al.* [CMS Collaboration], "Search for dijet resonances in proton-proton collisions at $\sqrt{s} = 13$ TeV and constraints on dark matter and other models," [arXiv:1611.03568 [hep-ex]].

[117] H. Fritzsch, Z. z. Xing and S. Zhou, "Two-zero Textures of the Majorana Neutrino Mass Matrix and Current Experimental Tests," JHEP **1109**, 083 (2011).

[118] E. Ma, "Connection between the neutrino seesaw mechanism and properties of the Majorana neutrino mass matrix," Phys. Rev. D **71**, 111301 (2005).

[119] M. Agostini *et al.* [GERDA Collaboration], "Results on Neutrinoless Double-β Decay of ^{76}Ge from Phase I of the GERDA Experiment," Phys. Rev. Lett. **111**, no. 12, 122503 (2013).

[120] Particle Data Group webpage, `http://pdg.lbl.gov/2016/listings/rpp2016-list-neutrino-prop.pdf`

[121] S. Antusch, E. Cazzato and O. Fischer, arXiv:1612.02728 [hep-ph].

[122] A. Alloul, N. D. Christensen, C. Degrande, C. Duhr and B. Fuks, "FeynRules 2.0 - A complete toolbox for tree-level phenomenology," Comput. Phys. Commun. **185**, 2250 (2014).

[123] J. Alwall *et al.*, "The automated computation of tree-level and next-to-leading order differential cross sections, and their matching to parton shower simulations," JHEP **1407**, 079 (2014).

[124] T. Sjostrand, S. Mrenna and P. Z. Skands, "PYTHIA 6.4 Physics and Manual," JHEP **0605**, 026 (2006).

[125] J. Pumplin, D. R. Stump, J. Huston, H. L. Lai, P. M. Nadolsky and W. K. Tung, "New generation of parton distributions with uncertainties from global QCD analysis," JHEP **0207**, 012 (2002).

[126] S. Ovyn, X. Rouby and V. Lemaitre, "DELPHES, a framework for fast simulation of a generic collider experiment," arXiv:0903.2225 [hep-ph].

[127] J. de Favereau *et al.* [DELPHES 3 Collaboration], "DELPHES 3, A modular framework for fast simulation of a generic collider experiment," JHEP **1402**, 057 (2014).

[128] I. Antcheva *et al.*, "ROOT: A C++ framework for petabyte data storage, statistical analysis and visualization," Comput. Phys. Commun. **180**, 2499 (2009).

[129] V. Khachatryan *et al.* [CMS Collaboration], "Measurements of the differential production cross sections for a Z boson in association with jets in pp collisions at $\sqrt{s} = 8$ TeV," [arXiv:1611.03844 [hep-ex]].

[130] D. G. d'Enterria *et al.* [CMS Collaboration], "CMS physics technical design report: Addendum on high density QCD with heavy ions," J. Phys. G **34**, 2307 (2007).

[131] Y. Amhis *et al.* [Heavy Flavor Averaging Group (HFAG)], "Averages of b-hadron, c-hadron, and τ-lepton properties as of summer 2014," arXiv:1412.7515 [hep-ex].

[132] T. Aushev *et al.*, "Physics at Super B Factory," arXiv:1002.5012 [hep-ex].

[133] C. Bobeth, G. Hiller and G. Piranishvili, JHEP **0807**, 106 (2008).

[134] D. Ghosh, Eur. Phys. J. C **77**, no. 10, 694 (2017).

[135] A. Datta, J. Kumar, J. Liao and D. Marfatia, Phys. Rev. D **97**, no. 11, 115038 (2018)

[136] ATLAS Collaboration, Summary Plot for SUSY,
https://atlas.web.cern.ch/Atlas/GROUPS/PHYSICS/CombinedSummaryPlots/
SUSY/ATLAS_SUSY_Summary/
ATLAS_SUSY_Summary.png ;
ATLAS Collaboration, Summary Plot for Exotics,
https://atlas.web.cern.ch/Atlas/GROUPS/PHYSICS/CombinedSummaryPlots/EXOTICS/ATLAS_Exotics_Summary/
ATLAS_Exotics_Summary.png ;
CMS Combined Summary Plot,
https://twiki.cern.ch/twiki/pub/CMSPublic/PhysicsResultsCombined/exo-limits_ICHEP_2016.001.png.

[137] J. Hewett, Theory Summary, delivered at the 53rd Recontres de Moriond (La Thuile, Italy), March 2018.

[138] W. Büchmuller and D. Wyler, Nucl. Phys. B **268**, 621 (1986).
For a more recent review, see S. Dawson, TASI 2016 Lectures, arXiv:1712.07232 [hep-ph].

[139] K. Hagiwara, R. D. Peccei, D. Zeppenfeld and K. Hikasa, Nucl. Phys. B **282**, 253 (1987).

[140] K. Hagiwara, S. Ishihara, R. Szalapski and D. Zeppenfeld, Phys. Lett. B **283**, 353 (1992).

[141] U. Baur and D. Zeppenfeld, Phys. Lett. B **201**, 383 (1988).

[142] S. S. Biswal, R. M. Godbole, B. Mellado and S. Raychaudhuri, Phys. Rev. Lett. **109**, 261801 (2012) ;
S. S. Biswal, M. Patra and S. Raychaudhuri, arXiv:1405.6056 [hep-ph] ;
A. Azatov, J. Elias-Miro, Y. Reyimuaji and E. Venturini, JHEP **1710**, 027 (2017) ;
R. Li, X. M. Shen, K. Wang, T. Xu, L. Zhang and G. Zhu, arXiv:1711.05607 [hep-ph].

[143] G. Buchalla, O. Cata, R. Rahn and M. Schlaffer, Eur. Phys. J. C **73**, 2589 (2013) ;
L. Bian, J. Shu and Y. Zhang, JHEP **1509**, 206 (2015) ;
A. Rosca, Nucl. Part. Phys. Proc. **273-275**, 2226 (2016) ;
J. D. Wells and Z. Zhang, Phys. Rev. D **93**, 034001 (2016) ;
S. M. Etesami, S. Khatibi and M. Mohammadi Najafabadi, Eur. Phys. J. C **76**, 533 (2016) ;
R. Rahaman and R. K. Singh, arXiv:1711.04551 [hep-ph] ;
A. Falkowski *et al.*, JHEP **1702**, 115 (2017) ;
Z. Zhang, Phys. Rev. Lett. **118**, 011803 (2017).

[144] T. Corbett *et al.*, Phys. Rev. Lett. **111**, 011801 (2013) ;
A. Butter, *et al*, JHEP **1607**, 152 (2016).

[145] D. R. Green, P. Meade and M. A. Pleier, Rev. Mod. Phys. **89**, 035008 (2017).

[146] G. Gounaris *et al.*, hep-ph/9601233.

[147] G. Panico, F. Riva and A. Wulzer, Phys. Lett. B **776**, 473 (2018).

[148] See, for example, S. Schael *et al.* [ALEPH, DELPHI, L3 and OPAL, LEP Electroweak Collaborations], Phys. Rept. **532**, 119 (2013).

[149] See, for example, C. E. Gerber *et al.* [TeV4LHC-Top Collaboration and Electroweak Working Group], arXiv:0705.3251 [hep-ph].

[150] F. Boudjema, K. Hagiwara, C. Hamzaoui and K. Numata, Phys. Rev. D **43**, 2223 (1991) ;
D. Choudhury, J. Kalinowski and A. Kulesza, Phys. Lett. B **457**, 193 (1999).

[151] M. Aaboud *et al.* [ATLAS Collaboration], Eur. Phys. J. C **77**, 563 (2017).

[152] A. M. Sirunyan *et al.* [CMS Collaboration], Phys. Lett. B **772**, 21 (2017).

[153] G. Aad *et al.* [ATLAS Collaboration], Phys. Rev. D **87**, 112003 (2013) ;
Erratum: Phys. Rev. D **91**, 119901 (2015).

[154] S. Chatrchyan *et al.* [CMS Collaboration], Phys. Lett. B **701**, 535 (2011) ;
S. Chatrchyan *et al.* [CMS Collaboration], Phys. Rev. D **89**, 092005 (2014).

[155] J. Ohnemus, Phys. Rev. D **47**, 940 (1993) ;
A. Denner, S. Dittmaier, M. Hecht and C. Pasold, JHEP **1504**, 018 (2015).

[156] J. Alwall, M. Herquet, F. Maltoni, O. Mattelaer and T. Stelzer, JHEP **1106**, 128 (2011).

[157] T. Sjstrand, S. Mrenna and P. Skands, JHEP05 (2006) 026, Comput. Phys. Comm. 178 (2008) 852.

[158] J. de Favereau *et al.* [DELPHES 3 Collaboration], JHEP **1402**, 057 (2014)

[159] J. Pumplin *et al.*, JHEP **0207**, 012 (2002).

[160] R. D. Ball *et al.*, Nucl. Phys. B **867**, 244 (2013).

[161] CMS Collaboration [CMS Collaboration], CMS-PAS-HIG-17-013.

[162] G. Aad *et al.* [ATLAS Collaboration], Phys. Lett. B **726**, 120 (2013).

[163] S. Chatrchyan *et al.* [CMS Collaboration], Phys. Rev. D **89**, no. 9, 092007 (2014).

[164] V. Khachatryan *et al.* [CMS Collaboration], Phys. Rev. D **92**, no. 7, 072010 (2015).

[165] V. Khachatryan *et al.* [CMS Collaboration], JHEP **1710**, 076 (2017).

[166] J. Bernon, J. F. Gunion, Y. Jiang and S. Kraml, Phys. Rev. D **91**, no. 7, 075019 (2015).

[167] R. Aggleton, D. Barducci, N. E. Bomark, S. Moretti and C. Shepherd-Themistocleous, JHEP **1702**, 035 (2017).

[168] CMS Collaboration [CMS Collaboration], CMS-PAS-HIG-14-037.

[169] G. Aad *et al.* [ATLAS Collaboration], Phys. Rev. Lett. **113**, no. 17, 171801 (2014).

[170] J. M. Butterworth, A. R. Davison, M. Rubin and G. P. Salam, Phys. Rev. Lett. **100**, 242001 (2008).

[171] T. Plehn and M. Spannowsky, J. Phys. G **39**, 083001 (2012).

[172] S. Nie and M. Sher, Phys. Lett. B **449**, 89 (1999).

[173] A. G. Akeroyd, A. Arhrib and E. M. Naimi, Phys. Lett. B **490**, 119 (2000).

[174] G. Bhattacharyya and D. Das, Pramana **87**, no. 3, 40 (2016).

[175] S. Schael *et al.* [ALEPH and DELPHI and L3 and OPAL and SLD Collaborations and LEP Electroweak Working Group and SLD Electroweak Group and SLD Heavy Flavour Group], Phys. Rept. **427**, 257 (2006).

[176] F. Mahmoudi and O. Stal, Phys. Rev. D **81**, 035016 (2010).

[177] M. Aoki, S. Kanemura, K. Tsumura and K. Yagyu, Phys. Rev. D **80**, 015017 (2009).

[178] J. F. Gunion, H. E. Haber, G. L. Kane and S. Dawson, Front. Phys. **80**, 1 (2000).

[179] V. D. Barger and R. J. N. Phillips, “Collider Physics,” REDWOOD CITY, USA: ADDISON-WESLEY (1987) 592 P. (FRONTIERS IN PHYSICS, 71).

[180] S. Dawson *et al.*, arXiv:1310.8361 [hep-ex].

[181] G. Cacciapaglia, A. Deandrea, S. Gascon-Shotkin, S. Le Corre, M. Lethuillier and J. Tao, JHEP **1612**, 068 (2016).

[182] S. Schael *et al.* [ALEPH and DELPHI and L3 and OPAL Collaborations and LEP Working Group for Higgs Boson Searches], Eur. Phys. J. C **47**, 547 (2006).

[183] T. Aaltonen *et al.* [CDF Collaboration], Phys. Rev. D **87**, 052008 (2013).

[184] [ALEPH and DELPHI and L3 and OPAL Collaborations and LEP Higgs Working Group], hep-ex/0107030.

[185] J. Abdallah *et al.* [DELPHI Collaboration], Eur. Phys. J. C **35**, 313 (2004).

[186] T. Sjstrand *et al.*, Comput. Phys. Commun. **191**, 159 (2015).

[187] R. D. Ball *et al.* [NNPDF Collaboration], Nucl. Phys. B **877**, 290 (2013).

[188] M. Cacciari, G. P. Salam and G. Soyez, JHEP **0804**, 063 (2008).

[189] S. D. Ellis, T. S. Roy and J. Scholtz, Phys. Rev. Lett. **110**, no. 12, 122003 (2013).

[190] S. D. Ellis, T. S. Roy and J. Scholtz, Phys. Rev. D **87**, no. 1, 014015 (2013).

[191] L. D. Landau, Dokl. Akad. Nauk Ser. Fiz. **60**, no. 2, 207 (1948).

[192] C. N. Yang, Phys. Rev. **77**, 242 (1950).

[193] M. Chala, M. Duerr, F. Kahlhoefer and K. Schmidt-Hoberg, Phys. Lett. B **755**, 145 (2016).

[194] N. D. Christensen and C. Duhr, Comput. Phys. Commun. **180**, 1614 (2009).

[195] M. Cacciari, G. P. Salam and G. Soyez, Eur. Phys. J. C **72**, 1896 (2012).

[196] B. Bhattacherjee, S. Mukhopadhyay, M. M. Nojiri, Y. Sakaki and B. R. Webber, JHEP **1504**, 131 (2015).

[197] J. Thaler and K. Van Tilburg, JHEP **1103**, 015 (2011).

[198] J. Thaler and K. Van Tilburg, JHEP **1202**, 093 (2012).

[199] A. J. Larkoski, G. P. Salam and J. Thaler, JHEP **1306**, 108 (2013).

[200] A. Chakraborty, A. M. Iyer and T. S. Roy, Nucl. Phys. B **932**, 439 (2018).

[201] C. Athanasiou, C. G. Lester, J. M. Smillie and B. R. Webber, JHEP **0608**, 055 (2006).

[202] S. Kullback and R.A. Leibler, The annals of mathematical statistics, 22, 1, 79 (1951).

[203] D. A. Ross and J. C. Taylor, Nucl. Phys. B **51**, 125 (1973) Erratum: [Nucl. Phys. B **58**, 643 (1973)].

[204] [ALEPH and DELPHI and L3 and OPAL Collaborations and LEP Higgs Working Group for Higgs boson searches], hep-ex/0107031.

[205] P. Abreu *et al.* [DELPHI Collaboration], Phys. Lett. B **507**, 89 (2001).

[206] A. Arbey, F. Mahmoudi, O. Stal and T. Stefaniak, Eur. Phys. J. C **78**, no. 3, 182 (2018).

[207] A. Arbey and F. Mahmoudi, Comput. Phys. Commun. **182**, 1582 (2011).

[208] P. Posch, Phys. Lett. B **696**, 447 (2011).